UNIVERSITÀ DEGLI STUDI DI PAVIA
DOTTORATO DI RICERCA IN FISICA – XXIII CICLO

Design of the Central Tracker of the $\overline{\text{P}}$ANDA experiment

Susanna Costanza

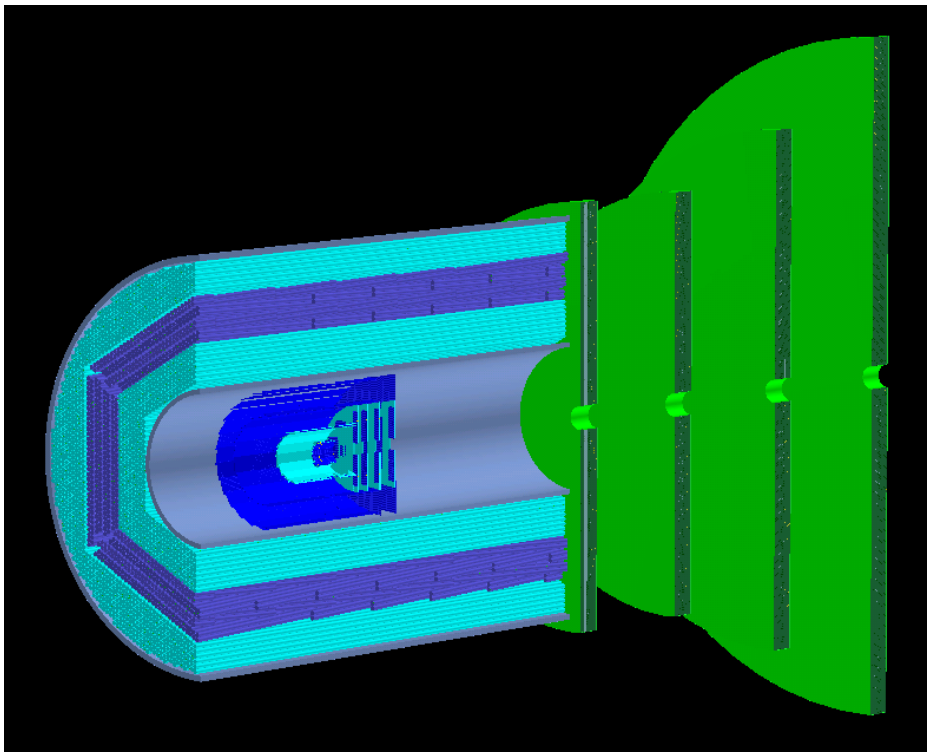

Supervisor: Prof. Alberto Rotondi

Tesi per il conseguimento del titolo

Università degli Studi di Pavia

Dipartimento di Fisica Nucleare e Teorica

Istituto Nazionale di Fisica Nucleare

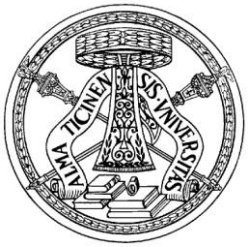

DOTTORATO DI RICERCA IN FISICA – XXIII CICLO

DESIGN OF THE CENTRAL TRACKER OF THE $\overline{\text{P}}$ANDA EXPERIMENT

dissertation submitted by

Susanna Costanza

to obtain the degree of

DOTTORE DI RICERCA IN FISICA

Supervisor: Prof. Alberto Rotondi (Università degli Studi di Pavia)

Referee: Dr. Peter Wintz (Forschungszentrum Jülich)

Cover: *Section of the tracking devices of the $\overline{P}$ANDA Target Spectrometer: the Micro-Vertex Detector (the innermost), the Straw Tube Tracker (the cylindrical one with light blue and violet straw tube layers) and the GEM chambers (the green planes).*
The image has been realised with the PandaRoot display.

ISBN 978-88-95767-38-3

Dottorato di Ricerca in Fisica
Università di Pavia, Italy
Printed by Print Service, Pavia
December 2010

La teoria è quando si sa tutto
ma non funziona niente.
La pratica è quando funziona tutto
ma non si sa il perchè.
In ogni caso si finisce sempre
con il coniugare la teoria con la pratica:
non funziona niente e non si sa il perchè.

A. Einstein

Contents

Introduction

Although more than forty years have passed since the discovery of the J/ψ, the charmonium and open charm physics are still interesting and exciting research fields. The phenomena of the confinement of quarks, the existence of glueballs and hybrids and the origin of the mass of strongly interacting, composite systems are long–standing puzzles and represent a challenge in our attempt to understand the nature of the strong interaction and of the hadronic matter.
Both theoretical and experimental activities have been stimulated by the recent discovery of narrow charmed–strange states. New capabilities for the quest of the missing resonances in the charmonium region are provided by the B factories, which represent rich sources of charmonium states.
Despite this thrust, many years of intense experimentation are still required in order to reach a precise knowledge of mass, width, decay modes and spin–parity of all the states.
Significant progresses can be attained only if the statistics and precision of the new data will exceed the past efforts by several orders of magnitude. This is presently done by the high statistics experiments in e^+e^- annihilations, but in these experiments only states with the quantum numbers of the photon $J^{PC} = 1^{--}$ can be directly formed. On the contrary, with antiproton beams all the $\overline{q}q$ quantum numbers are accessible.
The $\overline{\mathrm{P}}$ANDA experiment, that will be installed at the international FAIR facility in the site of the GSI laboratory (Darmstadt, Germany), will take advantage of the physics potential available using the high–intensity, phase space cooled antiproton beams provided by the high–energy storage ring HESR.
The $\overline{\mathrm{P}}$ANDA detector will be optimised for the physics goals presented above and will be able, at the same time, to accomodate additional physics aspects, like Drell–Yan and $\mathcal{CP}$–violating processes. So it will enable the FAIR facility to play a significant role in strong interaction physics, providing a link between nuclear physics and hadron physics.
The design of the $\overline{\mathrm{P}}$ANDA detector is based on the previous experience in antiproton experiments and takes advantage of ongoing detector developments performed at the laboratories for high–energy experiments.
A first sketch of the detector that fulfils the physics requirements was laid out

in the $\overline{\text{P}}$ANDA Letter of Intent (2004). Its operation is planned to start after 2015, after a delay due to some financial problems; nevertheless, extensive R&D programs for the subdetector design and cost optimisation have already started and are in progress.

This thesis fits in the scenario presented above: here the results of the work devoted to the simulation and design of the tracking system of the $\overline{\text{P}}$ANDA detector, together with the study of its physics performances, are collected.
The tracking system is the set of subdetectors sensitive to the passage of charged particles, that provide the spatial coordinates of the points where the energy has been deposited. By joining all the pieces of information from the whole tracking system and applying devoted track fitting algorithms, the full particle trajectory can be reconstructed.
Part of this work has been focused on the Straw Tube Tracker (STT), one of the two options proposed for the $\overline{\text{P}}$ANDA Central Tracker.
Since it has to fulfil strict requirements in order for $\overline{\text{P}}$ANDA to achieve high–precision results in the physics topics presented above, systematic studies have been performed to determine the best detector design and to test the performances of the foreseen layout. The design parameters of the detector have been extensively tested with Monte Carlo simulations.
Concerning the experimental tests, an R&D program which foresees the construction of a complete full–scale prototype of the STT is ongoing, but such a prototype is not yet ready for experimental tests. Nevertheless, a small one is available at the Institut für Kernphysik (IKP) at the Jülich Forschungszentrum (FZJ): the author spent about six months at the research center to develop a dedicated algorithm for the analysis of the cosmic ray data collected with this prototype.

All the results are presented and discussed in the thesis. It is divided into four parts:

- **PART I:** in the first part, the $\overline{\text{P}}$ANDA experiment is presented. In particular, in Chap. 1 the main points of the $\overline{\text{P}}$ANDA physics program are summarised. In Chap. 2 an overview of the foreseen detector layout is provided; a more detailed description of the Straw Tube Tracker design and of the characteristics of the straw tubes it is made of is also given.

- **PART II:** this section is dedicated to the study of a single straw tube, both from the simulation and from the experimental point of view.
  In Chap. 3 the physical processes that govern the functioning of a straw tube are reviewed. A detailed description of how these processes are implemented in the simulation is also reported in this chapter.
  The real functioning of straw tubes is studied in Chap. 4, which is devoted to a detailed description of the results of the analysis of the experimental data collected with the straw tube prototype of the IKP–FZJ. In partic-

ular, it is explained how the spatial resolution has been obtained through a dedicated autocalibration procedure.

- **PART III:** this part is dedicated to the study of the performances of the Straw Tube Tracker through the simulation of single track events. After a brief description of the simulation environment and of the track fitting methods developed in the software, Chap. 5 reports in detail the results of systematic studies of the tracker performances: the momentum resolution and tracking efficiency have been studied as a function of the particle momentum and angular range, of the geometry design (straw tube length, skew angle of the tilted tubes) and of the input single tube resolution curve.

- **PART IV:** in the last part, the capabilities of the $\overline{\mathrm{P}}$ANDA detector to fulfil the physics requirements have been studied through the simulation of two physics channels: the reactions $\overline{p}p \rightarrow \Psi(3770) \rightarrow D^+D^-$ and $\overline{p}p \rightarrow \eta_c(2979) \rightarrow K^0_S K^+\pi^-$ have been chosen as benchmark processes. Chap. 6 reports the results of the analysis of the simulated events and the invariant mass resolutions that have been obtained.
  In addition, a new proposal for a study of antiproton annihilations on light nuclei like ^{4}He has been presented, together with the resolution the apparatus would need in order to study this kind of events.

Part I

$\overline{\text{P}}$ANDA: antiProton ANnihilations at DArmstadt

Chapter 1

The $\overline{\text{P}}$ANDA experiment

$\overline{\text{P}}$ANDA [1, 4], the acronym for anti$\overline{\text{P}}$roton ANnihilation at DArmstadt, is one of the major projects of the international Facility for Antiproton and Ion Research (FAIR) at Darmstadt (Germany), an extension of the existing Heavy Ion Research Lab GSI (Helmholtzzentrum für Schwerionenforschung) [3].
The FAIR facility (Fig. 1.1) will consist of a series of accelerators, among which there is the High Energy Storage Ring (HESR) for the antiproton accumulation.
The antiproton beam of unprecedented quality provided by the HESR will allow to make high precision and high statistic measurements of QCD in the charmonium mass regime and of other aspects of particle and nuclear physics (the physics motivations and the research program of $\overline{\text{P}}$ANDA are treated in more details in Sec. 1.2).
In order to explore these items, the $\overline{\text{P}}$ANDA detector will be built as a general purpose fixed target detector that will study $\overline{p}p$ and $\overline{p}A$ annihilations. It will consist of a set of systems surrounding an internal proton or nuclear target placed in one of the two straight sections of the HESR.

1.1 High Energy Storage Ring

The HESR is dedicated to supply $\overline{\text{P}}$ANDA with high–quality antiproton beams over a broad momentum range from 1.5 to 15 GeV/c.
In storage rings, the complex interplay of many processes like beam–target interaction and intra–beam scattering determines the final equilibrium distribution of the beam particles. Electrons and stochastic cooling systems are required to ensure that the specified beam quality and luminosity for experiments at the HESR are achieved.
Two different modes of operation have been worked out to fulfil the experimental requirements:

- high resolution mode (HR) for high precision physics;

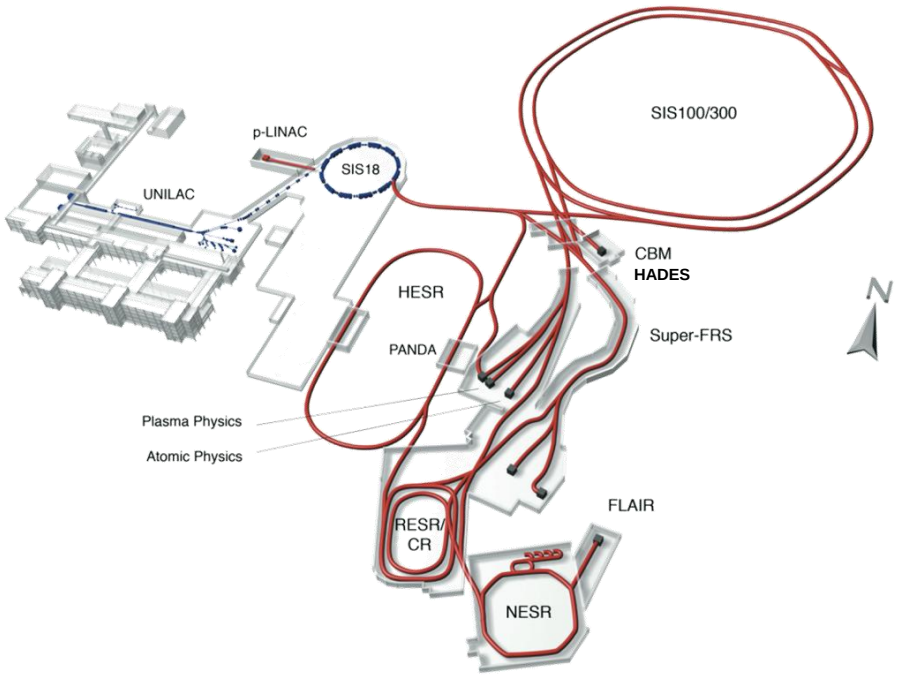

Figure 1.1: Layout of the FAIR facility. The existing facilities are depicted in blue; in red the new ones. Figure taken from Ref. [3].

- high luminosity mode (HL) for high statistic physics.

For more detailed information about these operation modes, see Tab. 1.1.

Table 1.1: Parameters of the operation modes.

Operation Modes	
High resolution (HR)	Peak luminosity of 2×10^{31} cm^{-2} s^{-1} for 10^{10} $\overline{p}$
	RMS momentum spread $\sigma_p/p \leq 4 \times 10^{-5}$
	1.5 to 9 GeV/c
High luminiosity (HL)	Peak luminosity of 2×10^{32} cm^{-2} s^{-1} for 10^{11} $\overline{p}$
	RMS momentum spread $\sigma_p/p \sim 10^{-4}$
	1.5 to 15 GeV/c

1.2 Physics motivations

The modern theory of strong interactions is Quantum Chromodynamics (QCD), the quantum field theory of quarks and gluons based on the non–abelian gauge group SU(3), which is part of the Standard Model of particle physics together with the SU(2)×U(1) electroweak theory.

QCD is a well tested theory at high energies, where the strong coupling constant becomes small and perturbation theory is used; on the contrary, in the low–energy regime QCD becomes a strongly coupled theory and it is not yet completely understood. There are still open questions like: is it possible to bring order into the wide variety of phenomena in the low energy QCD? Are there effective degrees of freedom allowing us to understand the resonances and bound states of QCD? Does QCD generate exotic structures so far undiscovered?
The $\overline{\text{P}}$ANDA experiment will be in a unique position to provide answers to such important questions about non–perturbative QCD. In fact, the experiment has been designed in order to fully exploit the physics potential arising from the availability of high–intensity cooled antiproton beams. $\overline{\text{P}}$ANDA will allow a significant progress in the understanding of the strong interaction and hadron structure thanks to the improvements in statistics and precision of the data.
The available energy in the antiproton–proton annihilations at $\overline{\text{P}}$ANDA opens a series of possible measurements (Fig. 1.2):

- study of the QCD bound states;
- non–perturbative QCD dynamics;
- study of hadrons in nuclear matter;
- hypernuclear physics;
- electromagnetic processes;
- electroweak physics.

In this chapter, the various topics of the $\overline{\text{P}}$ANDA physics program, extensively described in Ref. [4], will be presented in detail.

1.2.1 QCD bound states

1.2.1.1 The charmonium spectroscopy

Charmonium spectroscopy is one of the main items of the experimental program of the $\overline{\text{P}}$ANDA experiment; the design of the detector and of the accelerator are optimised to be well suited for this kind of physics. In particular, $\overline{\text{P}}$ANDA will represent a great improvement with respect to the Fermilab experiments E760 and E835:

- the instantaneous luminosity will be up to ten times higher ($L = 2 \times 10^{32}$ cm^{-2}s^{-1} in high–luminosity mode, vs. 2×10^{31} cm^{-2}s^{-1} at Fermilab);
- the resolution of the beam momentum will be better ($\Delta p/p = 10^{-5}$ in high–resolution mode vs. 10^{-4} at Fermilab);

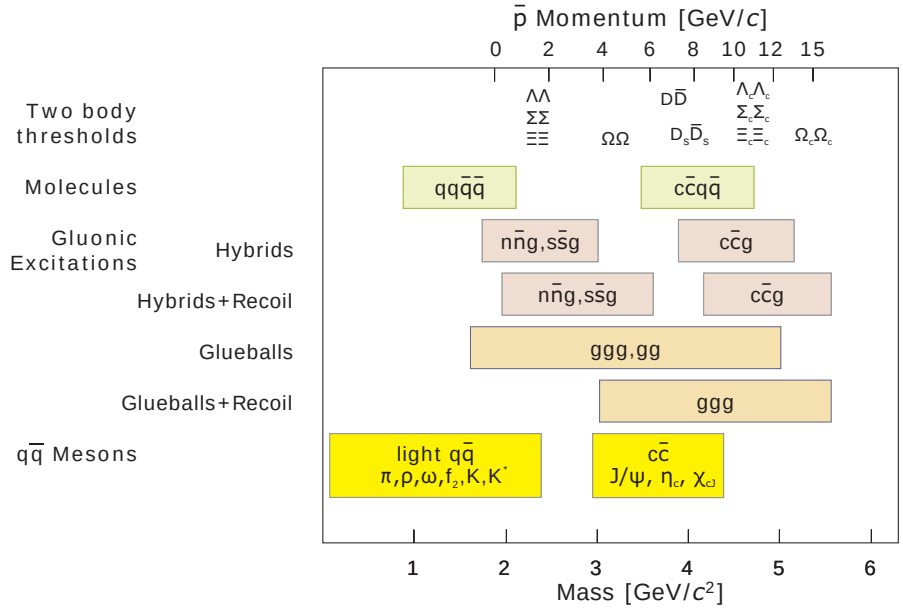

Figure 1.2: Physics topics available at $\overline{\text{P}}$ANDA. Figure taken from Ref. [4].

- the $\overline{\text{P}}$ANDA detector will have a higher angular coverage, magnetic field and so will be able to better detect the hadronic decay modes.

At full luminosity $\overline{\text{P}}$ANDA will be able to collect several thousands of $c\bar{c}$ states per day. Through fine scans, it will be possible to measure masses with accuracies of the order of 100 keV and widths up to 10% or even better.
The main problem in the experimental study of charmonium spectroscopy at $\overline{\text{P}}$ANDA (as well as in all the experiments with $\bar{p}p$ annihilations) is the high hadronic background.
The spectrum of the charmonium states is shown in Fig. 1.3. It consists of eight narrow states below the open charm threshold (3.73 GeV) and several tens of states above the threshold.

Narrow charmonium Concerning the narrow states, the triplets are well established with very good accuracy; it is not the same for the singlet states.

The η_c $(1S)$ is the state with the lowest mass of the bound $c\bar{c}$ states; it has the same quantum numbers as the η, i.e. $I^G(J^{PC}) = 0^+(0^{-+})$.
It is very interesting to be studied because it is the pseudoscalar partner of the charmonium vector state 1^3S_1, that is J/ψ. It was discovered almost thirty years ago and a lot of measurements of its mass and width have been obtained in the last few years, but the reached precision is still far from satisfactory.
The J/ψ mass value given by the Particle Data Group (PDG) [5] is 2980.5 ± 1.2 MeV/c^2, an average of thirteen measurements with an internal confidence level of 0.014; the error on the η_c mass is still large compared with few tens of keV/c^2

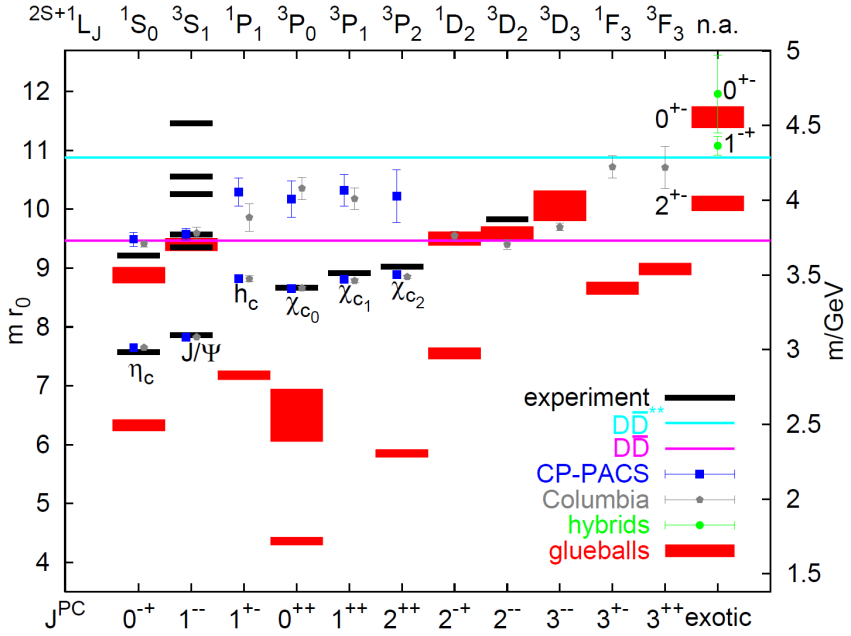

Figure 1.3: Charmonium spectrum from Lattice QCD (LQCD). Figure taken from Ref. [4].

for the J/ψ and ψ' and few hundreds of keV/c^2 for the χ_{cJ} states. The situation is even worse for the total width: the PDG average is 27.4 ± 2.9 MeV/c^2 with an overall confidence level smaller than 0.0001 but with individual measurements ranging from 7 MeV to 48 MeV. The most recent measurements [6, 7, 8] show that the η_c width is larger than previously believed, with values which are difficult to accomodate within the quark models.
This situation points out the need for new high–precision measurements of the η_c parameters: thanks to the very high statistics, $\overline{\text{P}}$ANDA could determine the mass value with an error almost comparable with the $M(J/\psi)$ value.

Since the radial excitations of charmonium resonances are far from being simple recursions of the ground states, as shown by the ψ', it is necessary and interesting to study the first radial excitation of the charmonium ground state, $\eta_c(2S)$.
Its first experimental evidence was stated by the Crystal Ball collaboration [9], but this discovery was not confirmed by subsequent searches in $p\overline{p}$ or e^+e^- experiments. The $\eta_c(2S)$ was finally discovered by the Belle Collaboration [10] in the hadronic decay of the B meson $B \to K + \eta_c(2S) \to K + (K_s K^- \pi^+)$ but with a mass incompatible with the Crystal Ball candidate. The Belle finding was confirmed by CLEO [11] and BaBar [12] which observed the state in two–photon fusion.
The PDG value of the mass is 3637 ± 4 MeV/c^2, leading to a surprisingly small hyperfine splitting of 49 ± 4 MeV/c^2.

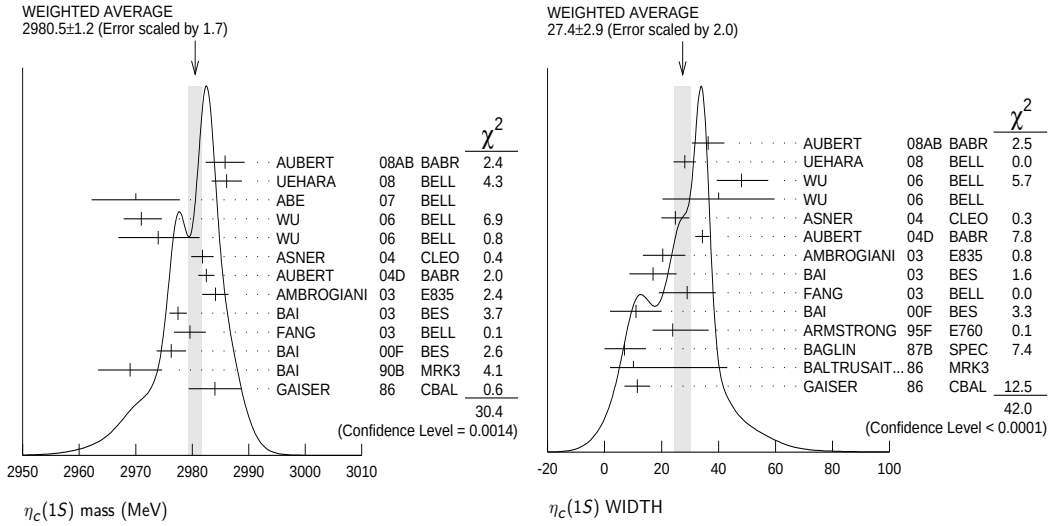

Figure 1.4: Present knowledge about $\eta_c(1S)$ mass (left) and width (right). Figures taken from Ref. [5].

The study of this state has just started and the precision of the measurements at $\overline{\text{P}}$ANDA could take advantage of the high yield of charmonium production in $\overline{p}p$ annihilations.

The singlet–P resonance of charmonium, $h_c(1P)$, is extremely important in determining the spin dependent components of the $q\overline{q}$ confinement potential. The h_c was first observed and identified by the E760 Collaboration in the decay channel $J/\psi\pi^0$ [13] with a mass of $3526.2 \pm 0.15 \pm 0.2$ MeV/c^2. The h_c was not confirmed by the E835 experiment, which just recorded an enhancement in the $\eta_c\gamma$ final state at an energy of $3525.8 \pm 0.2 \pm 0.2$ MeV/c^2 [14]. It was finally observed by the CLEO Collaboration in the decay mode $h_c \rightarrow \eta_c\gamma$, with the η_c decaying into hadrons [15], with a mass value of $3524.4 \pm 0.6 \pm 0.4$ MeV/c^2. The mass values found by these experiments agree with each other; it is clear that the study of this state has just started and many measurements are needed to determine its properties, in particular the width. It should be pointed out that, due to the narrowness of the state and to the expected low yields, only a $\overline{p}p$ formation experiment like $\overline{\text{P}}$ANDA will be able to measure the h_c width with high precision and to carry out a systematic study of its decay modes.

Open charm The region above $D\overline{D}$ threshold is rich in interesting new physics. In particular, close to the threshold value four $1D$ states are expected: of these, only the 1^3D_1 resonance has been identified with the $\psi(3770)$. The $J = 2$ states (1^1D_2 and 1^3D_2) are predicted to be narrow, because parity conservation forbids their decay to $D\overline{D}$. In addition to the D states, the radial excitations of the S and P states are predicted to occur above the open charm threshold.

It must be considered indeed that while below the open charm threshold all the narrow states have been observed and match predictions, above it almost all conventional charmonium states are missing.
Nowadays, a lot of new states have recently been discovered at the B–factories, mainly in the hadronic decays of the B mesons: these states are associated with charmonium because they decay predominantly into charmonium states such as J/ψ or ψ', but their interpretation is far from being obvious, since they do not match regular spectroscopy, but are rather candidates for bound states with additional quarks or gluons. An updated review of the experimental and theoretical state of the art on heavy quarkonium spectroscopy can be found in Ref. [16].
The new measured charmonium states are:

- $X(3872)$, the first state that was found not to fit charmonium spectroscopy and, by far, the state for which the most information is available;

- the 3940 family, three different states observed by the Belle Collaboration with masses close to 3940 MeV/c^2 ($X(3940)$, $Y(3940)$ and $Z(3940)$);

- a cluster of $C = +$ states with masses close to 4150 MeV/c^2: $X(4140)$, $X(4160)$, $X(4350)$ and $Z(4250)$;

- the 1^{--} family, consisting in the $Y(4260)$, $Y(4350)$ and $Y(4660)$ states observed via e^+e^- annihilation, hence with $J^{PC} = 1^{--}$;

- the three charged states $Z(4430)$, $Z_1(4050)$ and $Z_2(4250)$.

Fig. 1.5 shows the observed states overlaid on the regular charmonium states as predicted by the potential models [17]; the most likely J^{PC} assignment is shown.
Colours identify the grouping of the states: red for the individual states, green for the 3940 family, blue for the states around $M = 4140$ MeV, purple for the 1^{--} states and orange for the charged states. Black states are traditionally considered as regular charmonium, although $\psi(4040)$ seems to behave as an exotic particle, since it does not match any potential model and is close in mass to a charged state with the same J^P. In summary, of the observed states above open charm threshold only the $X(4160)$, $Z(3940)$, $Y(3940)$ and $\psi(3770)$ are good candidates for regular charmonium: $\eta_c(3S)$, $\chi_{c,2}(2P)$, $\chi_{c,0}(2P)$ and $\psi(1D)$ respectively.
Nevertheless, the possibility is still open of at least a fraction of them being ordinary charmonium with an incorrect J^{PC} assignment or for which the potential model predictions do not hold.
The states recently discovered suggest in particular the possibility to observe states with two or three quarks and two or three anti–quarks. There are two possibilities to form bound states out of two quarks and two anti–quarks:

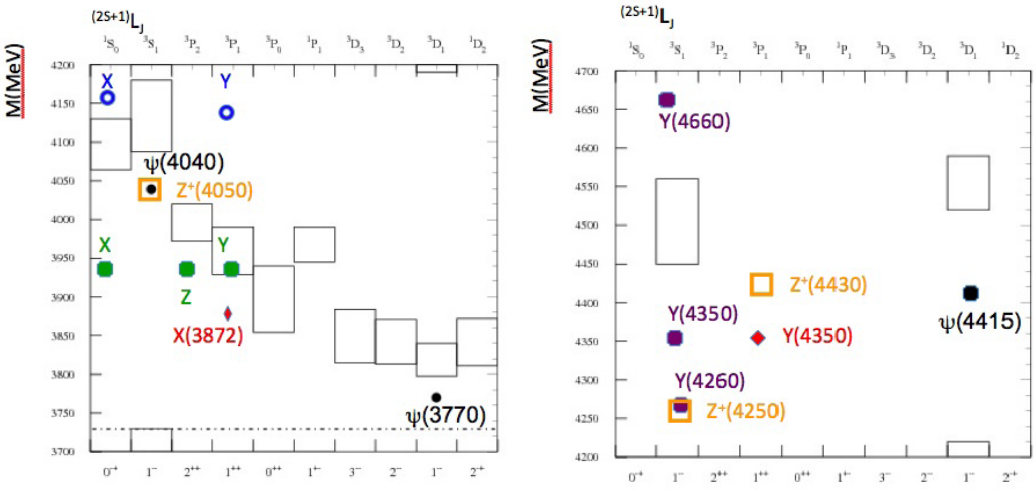

Figure 1.5: Observed states with hidden charm above the open charm threshold. Figure taken from Ref. [16].

- tetraquark, binding the two quarks in a coloured configuration called diquark $[qq]_\alpha$ or antidiquark $[\bar{q}\bar{q}]^\alpha$, such that colour charge is neutralized by the interaction diquark–antidiquark;

- molecular bound state, binding each quark to an anti–quark $[q_\alpha \bar{q}^\alpha]$ and allowing interaction between the two color neutral pairs $[q_\alpha \bar{q}^\alpha][q_\beta \bar{q}^\beta]$. This configuration is very close to the one with two interacting mesons.

Expected tetraquark spectra were derived, under assumption which lead to uncertainties $O(100$ MeV$)$. Besides the $X(3872)$ which is assumed to be a tetraquark when building the model and that would naturally be constituted by two states close in mass, the following states have a match within 100 MeV: $Y(4350)$, $Z(4430)$, $X(4160)$, $Y(4260)$, $Y(4350)$ and $Y(4660)$. Such a small number of matched states is opposed to the large number of needed states: 18 (27) for each of the $J = 0(1)$ multiplets. While it can be argued that the production and decay mechanism can distinguish between the states and that experimental sensitivity differs significantly between final states, one striking observation is that no attempt is made to search for the strange states, that would decay into charmonium plus a kaon.
Predictions in the case of molecules are more difficult. It is easy to classify the masses around which a molecule could possibly lay by computing all sums of the masses of two mesons with correct quantum numbers. Each case should be considered separately to estimate the production cross sections and the binding energies. Since the molecules have masses lower than the sum of the constituent mesons, it is interesting to search for their decays in the final states at lower masses.
So we are still far from having clear assignments for each of the states between

different possible interpretations. Moreover, a new spectroscopy implies the existence of a large number of states, whose absence would have to be justified. A perception of the status of the global picture and an indication on where to search can be obtained from a comparison between possible spectra and observed states.

1.2.1.2 Gluonic excitations

The quark model from its beginning [18] contemplate the existence of other aggregations than $q\bar{q}$ pairs or qqq triplets. In fact, the QCD Lagrangian contains also the gluons: besides being the particles which mediate strong interactions, they can act as dynamical degrees of freedom and as principal components of entirely new types of hadrons, the "gluonic hadrons". They are bound states of gluons and quarks and can be classified in two categories: the glueballs, which are bound states of only gluons, and the hybrids which are $q\bar{q}g$ bound states, i.e. $q\bar{q}$ states with a gluonic excitation.
The additional degrees of freedom carried by the gluons allow glueballs and hybrids to have spin–exotic quantum numbers J^{PC} that are forbidden for normal mesons and other fermion–antifermion systems. Exotic quantum numbers (e.g. J^{PC}=0^{--}, 0^{+-}, 1^{-+}, 2^{+-}) provide the best opportunity to discriminate between gluonic hadrons and $q\bar{q}$ states.
The properties of glueballs and hybrids are determined by the long–distance features of QCD; so their study will yield fundamental insight into the structure of the QCD vacuum.

Hybrids The existence of hybrid mesons was suggested in 1976 by Jaffe and Johnson [19] and Vainsthein and Okun [20]. Hybrids have been studied using different approaches: (i) the MIT bag model [21, 22], (ii) an adiabatic heavy–quark bag model [23, 24], (iii) constituent gluon models [25, 26, 27, 28, 29, 30], (iv) heavy quark lattice gauge theory [31] and (v) the flux tube model [32].
In the simplest scenario, hybrids can be described by adding the quantum numbers of a gluon ($J^P = 1^+$ or 1^-, depending on if it is a colour–electric or colour–magnetic excitation) to a simple $q\bar{q}$ pair. Hybrids which exhibit quantum numbers which can not be formed by a normal $q\bar{q}$ pair are called exotic; thus, they could be more easily identified experimentally.
The average mass obtained for the lightest hybrid with light quarks is about 1.5-2 GeV/c^2. Concerning the charmonium family, hybrids are predicted in the mass region around 4.3 GeV/c^2, with an estimated uncertainty of $100 - 200$ MeV/c^2. Four of the low–lying charmonium hybrids ($J^{PC} = 1^{--}$, 0^{-+}, 1^{-+}, 2^{-+}) correspond to a $c\bar{c}$ pair with $J^{PC} = 0^{-+}$ or 1^{--} coupled to a gluon in the lightest mode with $J^{PC} = 1^{--}$. The other four states ($J^{PC} = 1^{++}$, 0^{+-}, 1^{+-}, 2^{+-}) with the gluon mode $J^{PC} = 1^{-+}$ are probably heavier.
In $\overline{p}p$ annihilations, production experiments are the only way to obtain charmonium hybrids with exotic quantum numbers. At $\overline{\text{P}}$ANDA, as a first step, all possible production channels will be studied with production measurements

at the highest antiproton energy available ($E_{\overline{p}} = 15$ GeV), in order to cover exotic and non–exotic states. The next step would consist of formation experiments, by scanning the antiproton energy in small steps in the region where production measurements give hints about the possible presence of hybrids.

Glueballs A detailed prediction for the glueball mass spectrum can be obtained from LQCD calculations in the quenched approximation disregarding light quark loops [33]; as an example, the calculated width of about 100 MeV/c^2 [34] for the ground state glueball is in agreement with the experimental results. According to LQCD, 15 glueballs are predicted, some with exotic quantum numbers in the mass range accessible by the HESR (Fig. 1.6).
Like charmonium hybrids, they can be formed directly in the $\overline{p}p$ annihilation process or can be produced together with another particle.
Glueballs with exotic quantum numbers are called oddballs and they cannot mix with normal mesons; consequently, they are predicted to be rather narrow and they should be easily identified experimentally [35].
The lightest oddball, with $J^{PC} = 2^{+-}$ and a predicted mass of 4.3 GeV/c^2, would be in the range of the proposed experimental program.
It is worth noting that the $\overline{p}p$ annihilations offer a unique chance to search for heavier glueballs since alternative methods have severe limitations; since the study of glueballs is a key to understand long–distance QCD, every effort should be made to identify them.

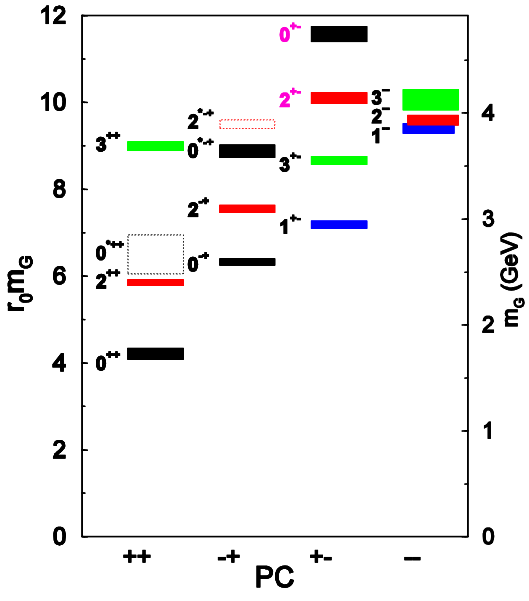

Figure 1.6: Glueball predictions from LQCD calculations. Spin–exotic glueballs with $J^{PC} = 0^{+-}$ and 2^{+-} are important research topics for $\overline{\text{P}}$ANDA. Figure taken from Ref. [4].

1.2.2 Hadrons in nuclear medium

The in–medium properties of charmonium states and D mesons have been studied theoretically in different approaches [36].
At present, the investigation of medium modifications of hadrons embedded in hadronic matter is one of the main activities at GSI. The aim is to understand the origin of hadron masses in the context of spontaneous chiral symmetry breaking in QCD and their modification due to chiral dynamics and partial restoration of chiral symmetry in hadronic environment.
In general, the picture of spontaneous symmetry breaking involves a hot system respecting a given symmetry. As the system cools below its critical temperature T_c, the expectation value of the order parameter associated with the system symmetry attains a nonzero value, indicating that spontaneous symmetry breaking has occurred. In the case of QCD, the relevant symmetry that is spontaneously broken is chiral symmetry and the associated order parameter is the quark–antiquark condensate $\langle\overline{q}q\rangle$. The nonzero vacuum expectation value of the $\overline{q}q$ condensate $\langle 0|\overline{q}q|0\rangle$ turns out to be related to the quark and hadron masses (see Refs. [38, 39, 40] and references quoted therein).
Due to the limitations in the available energy, up to now the studies on in–medium properties have been focused on the sector of light quarks. In particular, the in–medium modifications of the light vector mesons ρ, ω, ϕ, for which substantial changes of spectral functions in the medium are predicted to occur at normal nuclear matter density [37], are the main research goal of the HADES experiment [41] at GSI.
Thanks to the high intensity antiproton beam up to 15 GeV/c that will be available at $\overline{\mathrm{P}}$ANDA, it will be possible to extend this research program to the charm sector, both for hadrons with hidden and with open charm.
Concerning the charmonium states, since their mass is dominated by the large mass of the charm quark pair, it is expected to have only small changes in the quark condensate but major modifications of the gluon condensate. So the investigation of the interaction of $c\bar{c}$ mesons with nucleons and nuclei will allow to explore fundamental aspects of gluon dynamics in QCD.
According to recent calculations [42], the in–medium mass reductions for the low lying charmonium states like J/ψ and η_c will be of the order of $5-10$ MeV/c^2; in the case of excited charmonium states, the effect should be larger, since it is expected to scale with the volume occupied by the $c\bar{c}$ pair. Large attractive mass shifts of 40 MeV/c^2 for χ_{cJ}, 100 MeV/c^2 for ψ' and 140 MeV/c^2 for $\psi(3770)$ are predicted by modelling a QCD second order Stark–effect [43, 44].
Concerning D mesons, the situation is different: since they are made of a heavy c quark and a light antiquark, the D mesons will provide the unique chance to study the in–medium dynamics of a system with a single light quark.
According to recent phenomenological studies, a mass splitting for D mesons in nuclear matter is predicted, although there is no agreement on the predicted size of the splitting and on the sign of the D^- mass shift (the values can be

found in Refs. [36, 45, 46, 47]).
It is also predicted an in–medium reduction of the $D\overline{D}$ threshold, that would result in an increased D and $\overline{D}$ production in antiproton annihilation on nuclei, in particular at sub–threshold energies [45]. This would allow to identify the D mesons via their hadronic decay with K and $\overline{K}$ in the final state. Cross sections of $\sim$ nb near threshold lead to about 100 events per day at a luminosity of 10^{31} cm^{-2}s^{-1}, which allows to perform a D meson physics program.
In addition, the lowering of the $D\overline{D}$ threshold in the nuclear medium could open this decay channel or increase its partial width for the decay of the excited charmonium states lying close to the free $D\overline{D}$ mass, as long as the reduction of the in–medium mass of these states is sufficiently small [46, 48].
In conclusion, it should be pointed out that the availability of antiproton beams up to 15 GeV/c opens new opportunities to investigate the nuclear potential of strange atoms.

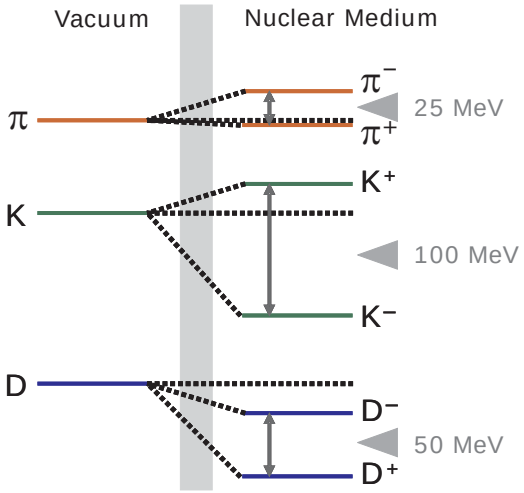

Figure 1.7: Mesons shift in the nuclear medium. The shifts of pions and kaons have been already discovered at GSI. Figure taken from Ref. [49].

1.2.3 Hypernuclear physics

A hypernucleus can be formed by replacing an up or down quark with a strange quark in a nucleon, which is bound in the nucleus.
The hypernuclei physics represents an interdisciplinary science, since it has many interesting links to different fields of physics: for example, it is important to understand how nuclear physics can be derived in a rigorous way from Quantum Chromo Dynamics (QCD) and how nuclear structures, like nuclei on the small scale, are formed. It is interesting also for the astrophysics field: in fact, up to now there is no clear picture regarding what kind of matter is present in the cores of neutron stars.

The advantage of the hypernuclei is that the hyperon bound into the nucleus, usually a Λ particle, is not subject to the Pauli principle in populating all possible nuclear states, unlike protons and neutrons. This allows the formation of deeply bound hypernuclear states that are directly accessible in the experiments.
The presence of the hyperon itself inside the nuclear medium may cause some dramatical modifications of the nucleus in which it is implanted, giving rise to new nuclear structures that cannot be seen in normal nuclei composed of only nucleons.
In addition, the description of the hyperons occupying the allowed single–particle states is without the complications encountered in ordinary nuclei, like pairing interactions. For this reason, a hypernucleus represents a sensitive probe of the hadronic many–body problem.
A comparison with ordinary matter may also give chances to reveal key questions in nuclear physics, like the origin of the nuclear spin–orbit force.
One of the goals is to measure the level spectra and decay properties of hypernuclei, in order to test the energies and wave functions from microscopic structure models. Furthermore, there is the hope that the detailed knowledge of the hyperons excitation spectra and structure could provide unique information on the hyperon–nucleon (YN) and hyperon–hyperon (YY) interaction.
Direct experimental investigation for the YN interactions are still very rare, due to the short lifetime of hyperons that makes hyperon targets impossible. In addition, it is very difficult to produce low–momentum hyperons and hyperon–proton scattering is only feasible via the double–scattering technique. There are only a few hundreds low–momentum $\Lambda - N$ and $\Sigma^{\pm} - N$ scattering events available and there is essentially no data on $\Xi - N$ or $\Omega - N$ scattering.
The different $S = -2$ systems, like Ξ^-–atoms and single Ξ^-–hypernuclei on one side and double $\Lambda\Lambda$ hypernuclei on the other side, provide complementary information on the baryon force. Hyperatoms created during the capture process of the hyperon will supply additional information on the hyperon–nucleus interaction.
At the same time, the YN weak interactions can be studied where the Pauli principle acts in the opposite way: for example, the decay $\Lambda \rightarrow N\pi$ into a nucleus is suppressed, since all nucleon states in the nucleus are occupied. On the contrary, processes like $\Lambda N \rightarrow NN$ are allowed, opening a unique window for four–baryon, strangeness non–conserving interactions.
Moreover, the non mesonic weak decays $\Lambda\Lambda \rightarrow \Lambda N$ and $\Lambda\Lambda \rightarrow \Sigma n$ are possible in double hypernuclei [50, 51, 52], allowing to access the $\Lambda\Lambda K$ coupling.
In order to succeed in having a detailed and consistent understanding of the quark aspect of the baryon–baryon forces, it is necessary to have experimental information on the hyperon–hyperon channel. Since scattering experiments are not possible between two hyperons, the precise spectroscopy of multistrange hypernuclei at $\overline{\text{P}}$ANDA will provide a unique approach to explore the hyperon–hyperon interaction. It will be possible by using a dedicated nuclear target

station and additional detectors (Sec. 2.1.1.7).
At $\overline{\text{P}}$ANDA, it will be possible to study not only Ξ^- atoms, but also Ω^- atoms, thus providing unique information on the nuclear optical potential of Ω^- baryons. The Ω hyperon is particularly interesting because, due to its long lifetime and its spin 3/2, it is the only "elementary" baryon with a non–vanishing spectroscopic quadrupole moment. Since it is mainly determined by the one–gluon exchange contribution to the quark–quark interaction, its measurement represents a unique benchmark for our understanding of the quark–quark interaction.
Finally, another challenging topic of $\Lambda\Lambda$ hypernuclear physics is the possible existence of a $S = -2$ six quarks ($uuddss$) H–dibaryon. Although some theories predict that the H–dibaryon is stable, the observation of several double hypernuclei makes the existence of a strongly bound free H–dibaryon unlikely. However, since the mass of that particle might drop inside a nucleus and due to hyperon mixing, a detailed study of the energy levels in double hypernuclei might succeed in observing traces of a H–dibaryon even if it is unbound in free space.

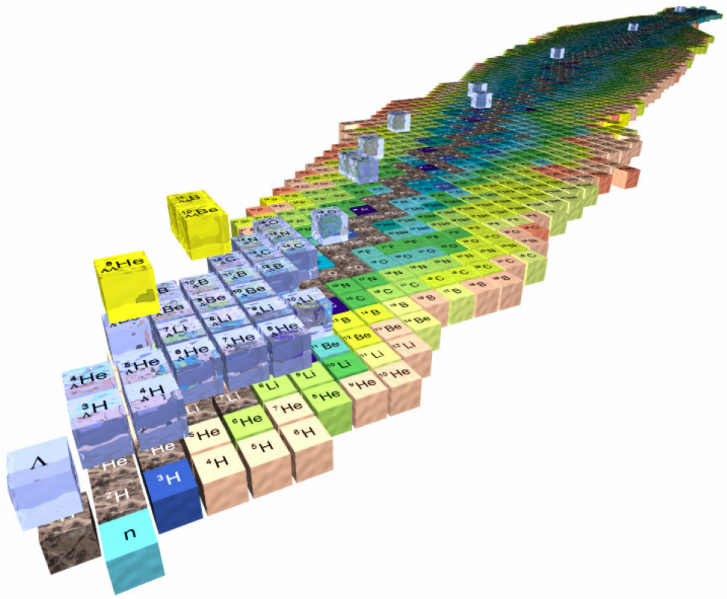

Figure 1.8: Present knowledge of hypernuclei: just few events of double hypernuclei have been detected and identified up to now. Figure taken from Ref. [4].

1.2.4 Antibaryon–baryon production in $p\overline{p}$ annihilation

The $p\overline{p} \to Y\overline{Y}$ baryon–antibaryon production processes allow to study in a particularly clean way the quark rearrangement and the annihilation and creation of quark–antiquark pairs [57].
In the absence of polarization, the angular distribution of the final products of the reaction can be written as:

$$I(\theta_i, \theta_j) \propto 1 + \alpha P_Y + \overline{\alpha} P_{\overline{Y}} + \alpha\overline{\alpha} \sum_{i,j} C_{ij} \cos\overline{\theta}_i \cos\theta_j \ ,$$

where $i, j = x, y, z$ and α is the decay asymmetry parameter. The angles refer to the decay directions in the $Y, \overline{Y}$ rest frame.
This distribution has been extensively studied for the $p\overline{p} \to \Lambda\overline{\Lambda} \to p\pi^-\overline{p}\pi^+$ reaction by the PS185 experiment at the LEAR accelerator at CERN [58].
The study of the polarization and of the spin correlation coefficients C_{ij}, showing that the $s\overline{s}$ pairs are predominantly produced with parallel spin, put severe constraints to the quark–gluon and meson exchange models. Concerning the depolarization coefficient, data from a polarized target do not match at present with any model [58].
If $\mathcal{CP}$ holds, the magnitude of the polarization of the Y and $\overline{Y}$ must be the same, with $\alpha_Y = -\alpha_{\overline{Y}}$. Consequently, one can define the parameter:

$$A_{Y\overline{Y}} = \frac{\alpha_{\overline{Y}} + \alpha_Y}{\alpha_{\overline{Y}} - \alpha_Y} \tag{1.1}$$

that should be zero if $\mathcal{CP}$ is conserved.
In the case of the $p\overline{p} \to \Lambda\overline{\Lambda}$ reaction, the average value of A is $A_{\Lambda\overline{\Lambda}} = 0.006 \pm 0.014$ [58], which is lower than the one quoted in Ref. [5] (0.012 ± 0.021).
The discovery of a $\mathcal{CP}$ violation in the hyperon decay would be the first observation in a baryonic system; the effect is expected to be smaller than 10^{-4} [58].
At $\overline{\mathrm{P}}$ANDA further studies of these topics would be possible; in addition, they could be extended also to doubly strange and charmed hyperons.
Nothing is known experimentally on the $p\overline{p} \to Y_c\overline{Y}_c$ reactions; it would be very interesting, for example, to investigate whether the creation of a $c\overline{c}$ pair in the $p\overline{p} \to \Lambda_c^+\overline{\Lambda}_c^+$ reaction will show the same features as the $s\overline{s}$ creation in the $\Lambda\overline{\Lambda}$ case.
According to the studies in Ref. [49], for the channels with only charged particles in the final state the overall reconstruction efficiency is $\sim 20\%$.
The production cross sections should be orders of magnitude greater than those from e^+e^- annihilation and a number of reconstructed events per month from 10^4 to 10^9 is expected for the production of $\Lambda_c\,\overline{\Lambda}_c$ and $\Lambda\,\overline{\Lambda}$ pairs, respectively.

1.2.5 Electromagnetic processes

1.2.5.1 Partonic picture of hard exclusive $\bar{p}p$–annihilation processes

Recently, the theoretical framework of Generalised Parton Distributions (GPDs) has been developed [59, 60, 61, 62]: it allows to treat hard exclusive processes in lepton scattering experiments on a firm QCD basis. This is possible under suitable conditions where one can factorise short and long distance contributions to the reaction mechanisms.

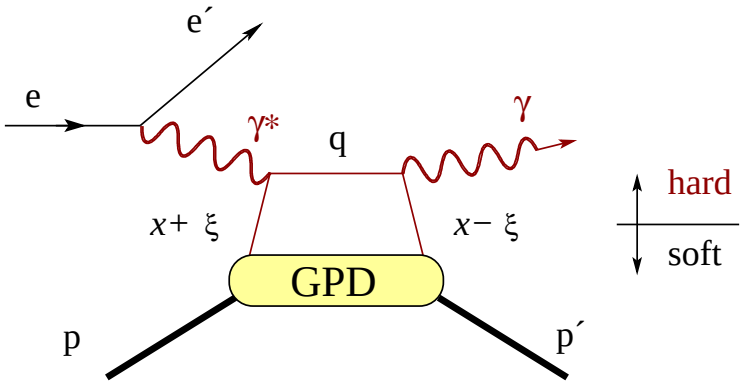

Figure 1.9: Deeply Virtual Compton Scattering (DVCS) can be described with the handbag approach, by factorising the upper "hard" part of the diagram, described by perturbative QCD and QED, and a lower "soft" part, described by GPDs. Figure taken from Ref. [4].

The importance of GPDs has been tested by studying deeply virtual Compton scattering (DVCS): it has been proved that the process can be factorised into a hard perturbative QCD process and a soft part of the diagram, which is parametrised by GPDs (see Fig. 1.9).
Another application of the handbag approach (i.e. the factorisation assumption) is, for example, the Wide Angle Compton Scattering (WACS) [63, 64, 65]: in this case, the hard scale is related to the large transverse momentum of the photons in the final state.
The important question is whether the concepts used in lepton scattering experiments can be used to describe also $\bar{p}p$ annihilation processes with crossed kinematics.
As an example, the crossed diagram of WACS can be considered: the process is $\bar{p}p \to \gamma\gamma$, with the emission of two photons in the final state at large polar angle in the centre of mass (CM) system. It has been proved that, although the handbag approach is not suitable to describe this channel neither at very small nor at very large energies, it seems that it is appropriate in the energy regime where $\overline{\text{P}}$ANDA operates.
The counterparts of GPDs that parametrise the soft part of the annihilation

process are called Generalised Distribution Amplitudes (GDAs). The experimental measurement of this process is really challenging, due to the very small cross section; nevertheless, the high luminosity and the excellent detector, especially the 4π calorimeter, should allow $\overline{\text{P}}$ANDA to discriminate the process from the large hadronic background.
In addition, the handbag diagrams can be used to describe further reactions, like $\overline{p}p \to \pi^0\gamma$, for which the E760 experiment has experimentally proved that the approach is appropriate in the range $s \sim 8.5-13.5$ GeV^2 [66], or $\overline{p}p \to M\gamma$, where M is any neutral meson.
The understanding of GPDs is just at its beginning and $\overline{\text{P}}$ANDA has the chance to contribute to an improved description of the nucleon structure by measuring the crossed–channel conterparts of these distributions in hard exclusive processes with various final states in a new kinematical region.

1.2.5.2 Transverse parton distribution functions in Drell–Yan production

The quark structure of hadrons can be described by three Parton Distribution Functions (PDFs):

- the unpolarised distribution $f_1(x)$, which is the probability of finding a quark with a fraction x of the parent hadron longitudinal momentum, whatever its spin orientation is;
- the helicity distribution $g_1(x)$, which describes the helicity of the quark in a longitudinally polarised hadron, that is the asymmetry between the density functions of the quarks with a given momentum fraction x and with spins parallel and antiparallel to that of the parent hadron spin;
- the transverse polarisation $h_1(x)$, which is like $g_1(x)$ but related to a transversely polarised hadron.

This description is valid only in the so–called collinear kinematics approach, that is if quarks are perfectly collinear: in this case, $f_1(x)$, $g_1(x)$ and $h_1(x)$ would contain all information on the internal dynamics of the nucleon.
The quark transverse momentum, however, is not always negligible and it has to be explicitly accounted for; in this case, a full set of eight Transverse–Momentum Dependent (TMD) PDFs and Fragmentation Functions (FFs) is available. The most relevant TMD PDFs for the $\overline{\text{P}}$ANDA proposed physics program are[1]:

- the Boer–Mulders (BM) function $h_1^\perp$, that is the distribution of transversely polarised partons in unpolarised hadrons;

[1]The adopted TMD's nomenclature is the following: f, g and h refer respectively to unpolarised, longitudinally and transversely polarised quarks; subscript T to transverse hadron polarisation; the subscript 1 refers to the leading twist and the apex $\perp$ to the explicit dependance on instrinsic momenta.

- the Sivers function $f_{1T}^{\perp}$, that is the distribution of unpolarised partons in a tranversely polarised nucleon;

- the transversity h_{1T}, that is the distribution of transversely polarised partons in a transversely polarised nucleon.

A complete and detailed description of these PDFs, together with a review of the experimental data available from the literature and their interpretation, can be found in [4].
The experimental information on $h_1^{\perp}$ and h_{1T} is very poor, since these distributions are not directly observable in fully inclusive deep inelastic scattering (DIS), the reaction providing the largest amount of data on structure functions.
The Drell–Yan (DY) production of muon pairs is an excellent tool to obtain information about transverse spin effects within the nucleon. A DY program in $\overline{\text{P}}$ANDA would allow to evaluate these three PDFs in a kinematic region where the valence contributions are expected to be dominant. In particular, with an unpolarised or polarised target, the Boer–Mulders distribution $h_1^{\perp}$ and the Sivers distribution $f_{1T}^{\perp}$ could be accessed very well. The polarised target needed in the latter case is not yet foreseen in the present $\overline{\text{P}}$ANDA layout but it is indicated as an almost necessary upgrade.
In addition, if a polarised antiproton beam would be available, it would be also possible to access the transversity distribution h_{1T} directly and without any convolution with other PDFs. In fact, at present h_{1T} can be obtained from semi–inclusive DIS (SIDIS) measurements, but only by extracting the data from fragmentation functions obtained from other experiments.

1.2.5.3 Electromagnetic form factors in the time–like region

The electron–nucleon interaction is described by the exchange of one photon with space–like four momentum transfer q^2.

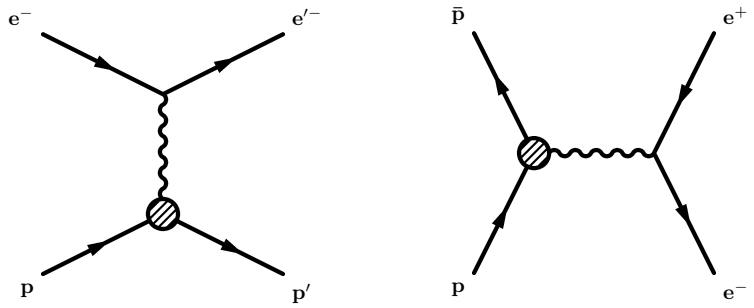

Figure 1.10: Feynman diagrams for elastic electron scattering (left) and its crossed channel $\overline{p}p \to e^+e^-$ (right) which will be measured at $\overline{\text{P}}$ANDA. Figure taken from Ref. [4].

On the nucleon vertex, which can be completely described by QED, the structure of the nucleon is parametrised by two real scalar functions depending only on the variable q^2. These functions are the Dirac form factor $F_1^{p,n}$ and the Pauli form factor $F_2^{p,n}$; alternatively, the Sachs form factors $G_E^{p,n}$ and $G_M^{p,n}$, which are linear combinations of $F_{1,2}^{p,n}$, can be used.
Usually, the matrix element for elastic electron–proton scattering in the framework of one–photon exchange is:

$$M = \frac{e^2}{q^2}\bar{u}(k_2)\gamma_\mu u(k_1)\bar{u}(p_2)[F_1(q^2)\gamma_\mu + i\frac{\sigma_{\mu\nu}q^\nu}{2m_p}F_2(q^2)]u(p_1), \qquad (1.2)$$

where k_1 (p_1) and k_2 (p_2) are the four momenta of the initial (final) electron (nucleon), represented by the spinors $\bar{u}(k)$ ($\bar{u}(p)$) and $u(k)$ ($u(p)$), m_p is the nucleon mass and $q = k_1 - k_2$, such that $q^2 < 0$.
The form factors (FFs) are analytical functions of the four momentum transfer q^2, ranging from $q^2 = -\infty$ to $q^2 = +\infty$. The unitarity condition on the matrix of Eq. (1.2) implies that the space–like form factors are real functions of q^2, whereas the time–like ones are complex functions.
While the electron scattering allows to access the form factors only in the range of negative q^2 (space–like), with the annihilation process the FFs can be accessed at positive q^2 (time–like), starting from the threshold $q^2 = 4m_p^2$. The space–like FFs are interpreted as the Fourier transforms of the spatial charge (G_E) and the magnetisation distribution of the proton (G_M): their slope at $q^2 = 0$ directly gives information about the charge and the magnetisation radius of the proton. In time–like region, the FFs reflect the frequency spectrum of the electromagnetic response of the nucleon.
In this way, two complementary aspects of the nucleon structure can be studied and a complete description of the electromagnetic form factors over the full kinematical range of q^2 can be reached.
The experimental determination of the FFs has triggered large experimental programs at all major facilities. Recently, the interest in the time–like form factors of the nucleon has been renewed by the measurements at JLAB, showing that the ratio $\mu_p G_E/G_M$ (μ_p being the magnetic moment of the proton) deviates from unity, in contrast to the results derived from Rosenbluth [67, 68, 69, 70, 71].
This surprising result has reopened the matter of the individual determination of G_E and G_M in the time–like domain, which was not obtained up to now and which will be possible with the $\overline{\text{P}}$ANDA experiment.
In fact, with an unprecendeted luminosity and high particle identification capabilities, that are necessary to discriminate against the very large background of $\bar{p}p \to \pi^+\pi^-$, $\overline{\text{P}}$ANDA offers the opportunity to determine the moduli of the complex FFs, by measuring the angular distribution of the process $\bar{p}p \to e^+e^-$ in a q^2 range from about 5 (GeV/c)^2 up to 14 (GeV/c)^2. Moreover, the ratio $R = |G_E|/|G_M|$ can be extracted with very high precision up to 14 (GeV/c)^2: a factor 10 improved experimental precision is expected with respect to present world data, as the simulation results show in Fig. 1.11.

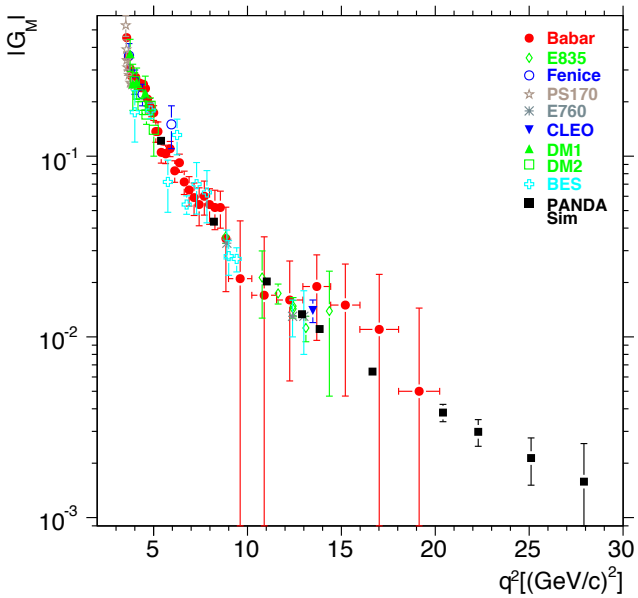

Figure 1.11: Present world data on $|G_M|$ (extracted using the hypothesis $R = |G_E|/|G_M| = 1$), together with the expected accuracy by measuring $\overline{p}p \rightarrow w^+e^-$ at FAIR with the $\overline{\text{P}}$ANDA experiment. Figure taken from Ref. [4].

1.2.6 Electroweak physics

The high intensity antiproton beam that will be available at the HESR will allow to produce a large number of D mesons, giving the chance to search for rare weak decays of these mesons, to test the predictions of the Standard Model for electroweak physics and to look for signatures of physics beyond the Standard Model.
Due to the very rare and small deviations that characterise such processes, it is necessary to have a high enough statistics, implying that measurements have to be performed at the highest possible luminosity.

1.2.6.1 $\mathcal{CP}$ violation and mixing in the charm sector

According to the Standard Model, $\mathcal{CP}$ violation is due to a single phase entering the Cabibbo–Kobayashi–Maskawa (CKM) matrix. As a result, the matrix elements V_{ub} and V_{td}, which involve the third generation of quarks, have large phases and small magnitudes.
At present, $\mathcal{CP}$ violation has been observed in neutral kaon and in neutral B meson decays [53, 54]. In the K^0 system, the $\mathcal{CP}$ violation is small and in the D^0 system it is predicted to be even smaller [55]. So a deviation from the small Standard Model effect indicating "new physics" can be more easily found out in experiments in the D meson system: for example, an enhanced mass difference of mixing D and $\overline{D}$ mesons would represent a deviation from the model.

Due to the strong correlation of the $D\overline{D}$ pairs kept in the hadronisation process, it would be advantageous to work with D mesons produced at the open charm threshold. At this energy, asymmetries are not expected in the production process and through the observation of one of the D mesons, it is possible to deduce the quantum numbers of the other one in case of production in a charge symmetric environment (flavor tagging).
As an example, the two body channels $\overline{p}p \rightarrow \Psi(3770) \rightarrow D\overline{D}$ and $\overline{p}p \rightarrow \psi(4040) \rightarrow D^*\overline{D}^*$ may be useful to investigate the $\overline{\mathrm{P}}$ANDA abilities to reconstruct open charm.
In order to measure the predicted $\alpha_{\mathcal{CP}} \sim 10^{-3}$, $\overline{\mathrm{P}}$ANDA should collect 10^9 D meson pairs running at $L = 2 \cdot 10^{32}$ cm^{-2}s^{-1}.

1.2.6.2 $\mathcal{CP}$ violation in hyperon decays

In case of two–body decays of hyperons, the decay amplitude can be a S–wave or a P–wave. Having two amplitudes, interference can occur and $\mathcal{CP}$–violating phases can enter.
Two parameters govern the decay dynamics: α denotes the asymmetry of the decay angular distribution and β the decay–baryon polarisation [56]:

$$A = \frac{\alpha\Gamma + \overline{\alpha\Gamma}}{\alpha\Gamma - \overline{\alpha\Gamma}} \sim \frac{\alpha + \overline{\alpha}}{\alpha - \overline{\alpha}} \tag{1.3}$$

$$B = \frac{\beta\Gamma + \overline{\beta\Gamma}}{\beta\Gamma - \overline{\beta\Gamma}} \sim \frac{\beta + \overline{\beta}}{\beta - \overline{\beta}}, \tag{1.4}$$

where Γ is the decay width.
The Standard Model predicts for A a value of $\sim 2 \cdot 10^{-5}$; on the other hand, some models beyond the standard one predict $\mathcal{CP}$ asymmetries of the order of several 10^{-4}.
In order to check the Standard Model limit, $\overline{\mathrm{P}}$ANDA should study the decay of $\sim 10^{10}$ hyperons: this would require an operation time of about one year under ideal conditions.

1.2.6.3 Rare decays

The study of rare decays is a test of the violation of fundamental symmetries, so it allows to open a window onto physics beyond the Standard Model.
It is possible to search for lepton flavor number violating decays, like $D^0 \rightarrow \mu e$ or $D^{\pm} \rightarrow \pi\mu e$; in addition, according to the Standard Model, flavor changing neutral currents like in the decay $D^0 \rightarrow \mu^+\mu^-$ are foreseen through box graphs or weak penguin graphs. Although the branching fractions for these events are smaller than 10^{-15}, the signatures of the decays are clean, leaving hope for their observation.

1.3 $\overline{p}$ annihilations on nuclei

In ordinary phenomena, quarks are confined in the nucleons, i.e. they cannot be extracted singularly from nucleons. Unstable non–strange or strange quark triplets and quark–antiquark doublets are produced in hadronic collisions and in antinucleon–nucleon annihilations, but also in these cases quarks appear to be confined in systems of two or three quarks.
Many theories based on QCD predict that ordinary nuclear matter, under certain conditions, could undergo transitions to excited phases, where quarks and gluons form a plasma (quark–gluon plasma, QGP). These new phases should occur when the baryon density is so high that nucleons become very close and fuse into each other, or when the baryon density is low but a hot and high enough energy density is attained. In particular, in Ref. [72] it is studied the possibility that the $\overline{p}N$ highly excited blob consisting of a gas of individual hadrons (hadronic gas, HG) could be transformed, in extreme cases, into a blob of individual quarks deconfined to form QGP.
The excited hadron phases are supposed to be generalised systems of mesons and baryons of increasing mass and volume where quarks are still confined.
Usually, the phase transitions are studied assuming that the excited blobs behave like thermodynamic systems. This means that they should consist of a large number of particles (thousands or more) which are in equilibrium for some time, that is with definite temperature, pressure, energy and entropy density [73]; also non–equilibrium conditions are considered. In this context, the transition from HG to QGP is characterised by a critical temperature T_c which, according to various authors, is expected to be in the interval 150-200 MeV. For instance, a lattice QCD calculation predicts for T_c a value of ~ 173 MeV, corresponding to an energy density $E_d \sim 700$ MeV/fm^3, which is about five times the energy density of the ordinary nuclei (0.14 nucleons/fm^3=130 MeV/fm^3) [74].
Since QGP is supposed to exist in some early stage of our Universe, its discovery is the main motivation of many experiments and theoretical investigations on relativistic heavy–ion collisions.
Despite the great amount of data that has been collected for many years looking for QGP and the many theoretical speculations that have been produced, an experimental evidence is still missing. QGP has not yet been discovered unambigously due to the mixture of processes that accompany the nuclear phase transitions and their complexity, although experimental results indicate the occurrence of new states of matter that have the characteristics of collective phenomena not reconcilable with the known physics.
Signatures of the existence of such a state are based on statistical considerations which in general predict an enhancement in the production of states with quarks heavier than the lighter couple (u, d), while some theoretical models refer to anomalies in rapidity distributions or branching ratio suppression of well known resonances. In particular, according to Refs. [75, 76, 77], an important signature of QGP formation is a high production of strange particles. A crucial

point is to define a reference with respect to which a strangeness production can be considered "high".

Since it has been suggested that the transition from ordinary hadronic matter to quark–gluon plasma could be obtained in antinucleon–nucleus annihilations, in the following the features of these annihilations are presented in detail.

1.3.1 $\overline{p}$–nucleon annihilation

When an $\overline{p}$ interacts with a proton p, the two baryons lose their identity and fuse into a highly excited blob, sometimes called "fireball", with an energy equal to twice the nucleon mass and a baryon number $B = 0$.
Then, when the blob de–excites, it materialises into a certain number of mesons directly or through intermediate states: the observed number of produced pions varies from a minimum of two to a maximum of eight, with an average of five; $K\overline{K}$ pairs are observed in about 5% of the events [78]. The variety and energy of the final products depend on the conservation laws of momentum, energy, electric charge, baryonic and leptonic numbers, strangeness, P– and G–parity.
In a QGP, q, $\overline{q}$ and g may interact with each other annihilating and/or producing additional $q\overline{q}$ pairs and gluons. So the initial $\overline{p}p$ system made of three non–strange $q\overline{q}$ pairs is replaced by a higher number of $q\overline{q}$ pairs ($s\overline{s}$ pairs included). Due to the higher mass, $s\overline{s}$ pairs are produced with lower probability than $u\overline{u}$ and $d\overline{d}$; anyway, they can be produced and absorbed via the reactions $q\overline{q} \leftrightarrow s\overline{s}$ with a 10% probability and $gg \leftrightarrow s\overline{s}$ with a 90% probability.
A QGP feature is that the strangeness density is predicted to be up to 10 times larger than in HG [75]: in a qualitative way, the energy required to produce a $K\overline{K}$ pair in a conventional hadronic collision requires at least 700 MeV, whereas only $2m_s \sim 300$ MeV are necessary to create a $s\overline{s}$ pair in QGP.

1.3.2 $\overline{p}$–nucleus annihilation

In the case of an antiproton annihilating on a nucleus, many final states are similar to those of annihilation on one free nucleon, but the panorama is wider and some states are substantially different, like the ones with only one meson in the final state (Pontecorvo reactions: $\overline{p}d \to \pi^- p$, $\overline{p}^3He \to \pi^- d$ and $\overline{p}d \to K\Lambda$ [79]). The main features of this annihilation can be found in Ref. [78].
It is worth pointing out that in the case of annihilation on a single nucleon bound in a nucleus, the emitted mesons may interact with the residual nucleons according to the known physics of meson–nucleon interactions. Since the average momentum of the mesons is of the order of 300 MeV/c, they may interact in a resonant way and be absorbed by nucleons.
This kind of annihilation mechanism is referred to as single–nucleon annihilation (SNA) followed by final state interaction (FSI).

The strangeness production could be evaluated through reactions like the following:

$$\omega N \rightarrow KY, \tag{1.5}$$
$$\omega N \rightarrow NK\overline{K}, \tag{1.6}$$
$$nK^+ \leftrightarrow pK^0, \tag{1.7}$$
$$nK^- \leftrightarrow p\overline{K}^0, \tag{1.8}$$
$$\overline{K}N \rightarrow \pi Y. \tag{1.9}$$

Since antikaons (and not kaons) are strongly absorbed by nucleons, according to the previous reactions the number of K increases due to Eq. (1.5) and (1.6) and the number of $\overline{K}$ decreases with respect to K due to Eq. (1.9), despite the positive contribution of Eq. (1.6). According to Ref. [80], the total production of $s\overline{s}$ pairs in single nucleon annihilation in a nucleus should be of the order of 1.5 with respect to SNA on free nucleons.
SNA followed by FSI is a particular case of the $B > 0$ processes, since it starts with a blob having $B = 0$ and ends with a state with $B > 0$, after involving the other nucleons of the nucleus.
In the case of annihilation of an antiproton on a nucleus, it is also possible that the $\overline{p}$ fuses with A nucleons, forming a fireball with energy $(A+1)m_p$ and baryonic number $B = A - 1 \geq 1$, consisting of HG or QGP. Such process is called multi–nucleon annihilation (MNA). Also in the case of MNA the energy blob may interact with the residual nucleons.
MNA on nuclei are expected, however, to be a minority with respect to the whole set of annihilation reactions, so they are hidden by the many background events due to SNA plus FSI; in order to disentangle them, it is necessary to select specific reaction channels.
Anyway, these two mechanisms produce similar final states; in order to evaluate experimentally their relative importance it is necessary to resort to statistical characteristics. The main difference stays in the amount of strangeness production: that has been studied through statistical models of the blob de-excitation, by extending the production observed in the case of single nucleon annihilations.
According to Ref. [81], kaon production (i.e. the total strangeness production) increases much more in MNA than in the case of SNA plus FSI, in particular more than three times from $A = 1$ to $A = 2$ and at lower pace at higher A values. On the other hand, antikaon production is almost constant and much lower than kaon production for $A \geq 2$. In addition, due to the lower energy required to create a hyperon with respect to a kaon, the occurrence of channels containing YK is higher than that of $K\overline{K}$ channels when A increases, resulting in a strangeness increase with A.
Another feature of MNA is that the ratio of the antistrange quarks to the total antiquark content of the produced particles $R = \overline{s}/\overline{q}$ increases with A up to a factor seven between $B = 0$ and $B = 4$.

Finally, it is important to point out that the strangeness production from a hadronic gas strongly depends on the nucleon density. According to Ref. [82], the total strangeness is expected to increase by a factor 10 between $A = 1$ and $A = 4$. This value can be taken as an upper limit on strangeness production: any substantial excess would be interpreted as QGP signal.
In conclusion, QGP could be the natural consequence of the quark deconfinement induced by the antiproton annihilation on the nucleus. If the antiproton annihilation on a single free nucleon is assumed as reference, the strangeness production is expected to increase going from SNA followed by FSI, to MNA without QGP formation; the occurrence of QGP is denoted by a much higher increase.

1.3.3 $\overline{p}-^4$He annihilation

According to the previous remarks, the probability of QGP occurrence is higher if the antiproton annihilates in a high density region of the nuclear matter, that is close to the centre of the nucleus. In order to reach that region, $\overline{p}$ should have a sufficiently high initial momentum, since it decreases by scattering as the $\overline{p}$ approaches the centre of the nucleus (slow $\overline{p}$ are known to have a high probability to annihilate on the nuclear surface, where the density is low [84]). In this context, the ^{4}He nucleus offers favorable conditions for the formation of $A > 1$ and $B \geq 1$ fireballs, since the nucleons are strongly bound in a small volume at the same energetic level. The ^{4}He radius (≈ 1.6 fm) is less than twice the proton radius (≈ 0.87 fm), so the four nucleons are partially overlapped, helping the formation of a blob containing the antiproton and more than one nucleon. In fact, since they are so close to each other, it is very likely that all are involved if one of them is "touched" by the antiproton.
In addition, the small number of initial nucleons and of final mesons facilitates the identification of the final particles and of single and multi–nucleon annihilations ($A = 1$ and $A = 2, 3, 4$).
The previously outlined expectations find confirmation in the analyses of the annihilation data at rest on ^{1}H, ^{2}H, ^{3}He and ^{4}He reported in Refs. [83, 84, 85, 86]. The data were collected by the Obelix spectrometer, operating at the accelerator LEAR at CERN from 1992 to 1996.
The analyses of $\overline{p}-^4$He annihilation data have unambiguously identified the existence of annihilations on more than one nucleon [87]. Moreover, it has put in evidence that the IntraNuclear Cascade models proposed in Refs. [81, 82] cannot properly describe the enhancement in strangeness production observed in some selected channels of $\overline{p}-^4$He annihilations with respect to the production in the same annihilation channels on hydrogen or deuterium [84, 85, 86]. In particular, from the analysis of the Obelix data in Ref. [86] a strangeness enhancement higher than 22 is obtained comparing the K^+ production in $\overline{p}-^4$He events into four charged mesons and one fast proton to the K^+ production in $\overline{p}p$ annihilations into four charged prong events. This value is significantly higher than six, the value assumed in Ref. [82] as an upper limit for the strangeness

enhancement in annihilations involving four nucleons in a hadronic frame.
Moreover, the same analysis shows that the strangeness enhancement production for the annihilation into $K^+2\pi^+2\pi^-$ without neutral mesons with respect to the reaction $K^+\pi^+2\pi^-$ on hydrogen reaches a value even higher, namely ~ 32.
These enhancement factors are too high to be explainable in terms of hadronic interactions: they could be interpreted as a signature of the occurrence of quark deconfinement and of QGP formation.

In the light of the presented scenario, it has to be stressed that the use of a well bound nucleus such as the ^{4}He as target could favour the transition to quark–gluon plasma. Moreover, given the relatively limited number of particles in the final state with respect to the experimental conditions of the heavy–ion collisions, the possibility to measure exclusive channels could help to clarify part of the uncertainties connected to the experimental signatures.
In this framework the use of a Helium target in the $\overline{\text{P}}$ANDA experiment could be of absolute relevance: the experiment would produce data of incomparably rich statistics with respects to the Obelix data. In addition, its capability of particle identification in a wide momenta range, together with the covered solid angle, would allow strangeness and charm production studies in exclusive annihilation channels.

Bibliography

[1] M. Kotulla et al., *Letter of Intent for $\overline{P}ANDA$ – Strong Interaction Studies with Antiprotons*, GSI-ESAC/Pbar January 8, 2004.

[2] http://www-panda.gsi.de/.

[3] http://www.gsi.de/portrait/index_e.html.

[4] W. Erni et al., *Physics Performance Report for $\overline{P}ANDA$ – Strong Interaction Studies with Antiprotons*, Mar 2009, arXiv:0903.3905v1.

[5] K. Nakamura et al. (Particle Data Group), J. Phys. G 37, 075021 (2010) http://pdg.lbl.gov.

[6] J.P. Lees et al., Phys. Rev. D81, 052010 (2010).

[7] B. Aubert at al., Phys. Rev. D78, 012006 (2008).

[8] C.–H. Wu at al.,Phys. Rev. Lett. 97, 162003 (2006).

[9] C. Edwards et al., Phys. Rev. Lett. 48, 70 (1982).

[10] S. Choi et al., Phys. Rev. Lett. 89, 102001 (2002).

[11] D. Asner at al., Phys. Rev. Lett. 92, 142001 (2004).

[12] B. Aubert et al., Phys. Rev. Lett. 92, 142002 (2004).

[13] T. Armstrong et al., Phys. Rev. Lett. 69, 2337 (1992).

[14] M. Andreotti et al., Phys. Rev. D72, 032001 (2005).

[15] J. Rosner et al., Phys. Rev. Lett. 95, 102003 (2005).

[16] N. Drenska, R. Faccini, F. Piccinini, A. Polosa, F. Renga and C. Sabelli, arXiv:1006.2741v1.

[17] N. Brambilla et al., arXiv:hep-ph/0412158 preprint (2004).

[18] M. Gell–Mann, Phys. Lett. 8 (1964) 214.

[19] R.L. Jaffe and K. Johnson, Phys. Lett. B 60, 201 (1976).

[20] A.I. Vainshtein and L.B. Okun, Yad. Fiz. 23.

[21] T. Barnes and F.E. Close, Phys. Lett. B 116, 365 (1982).

[22] T. Barnes, F.E. Close, F. De Viron, J. Weyers, Nucl. Phys. B 224, 241 (1983).

[23] P. Hasenfratz, R.R. Horgan, J. Kuti, J.M. Richard, Phys. Lett. B 95, 299 (1980).

[24] Y.S. Kalashnikova and D.S. Kuzmenko, Phys. Atom. Nucl. 66, 955 (2003).

[25] D. Horn and J. Mandula, Phys. Rev. D 17, 898 (1978).

[26] M. Tanimoto, Phys. Lett. B 116, 198 (1982).

[27] M. Tanimoto, Phys. Rev. D 27, 2648 (1983).

[28] F. Iddir et al., Phys. Lett. B 205, 564 (1988).

[29] S. Hishida, H. Sawazaki, M. Oda, K. Yamada, Phys. Rev. D 47, 179 (1993).

[30] S. Hishida, H. Sawazaki, M. Oda, K. Yamada, Prog. Theor. Phys. 82, 119 (1989).

[31] S. Perantonis and C. Michael, Nucl. Phys. B 347, 854 (1990).

[32] T. Barnes, F.E. Close and E.S. Swanson, Phys. Rev. D 52, 5242 (1995).

[33] C. Morningstar and M. Peardon, Phys. Rev. D 60, 34509 (1999).

[34] J. Sexton, A. Vaccarino, D. Weingarten, Phys. Rev. Lett. 75, 4563 (1995).

[35] P. Page, in *Proceedings of the "pbar2000 Workshop"*, edited by D. Kaplan and H. Rubin, pages 55–64, Chicago, 2001.

[36] W. Weise, in *Proc. Int. Workshop on the Structure of Hadrons*, Hischegg, Austria, 2001.

[37] F. Klingl, N. Kaiser, and W. Weise, Nucl. Phys. A624, 527 (1997).

[38] J.D. Bjorken and S.D. Drell, *Relativistic Quantum Fields*, Mc Graw Hill, New York, 1965.

[39] N.S. Demir, *Chiral Symmetry Breaking in Quantum Chromodynamics* http://www.phy.duke.edu/courses/346/section3/EssayNasserDemir.pdf.

[40] V. Koch, LBNL Report 38000, Dec 2005, arXiv:nucl-th/9512029v1.

[41] http://www-hades.gsi.de.

[42] F. Klingl, S. Kim, S. Lee, P. Morath, and W. Weise, Phys. Rev. Lett. 82, 3396 (1999).

[43] S. Lee and C. Ko, Phys. Rev. C67, 038202 (2003).

[44] S. Lee, Proceedings of Int. Workshop *HADRON 2003* in Hadron Spectroscopy, edited by H.K.E. Klempt and H. Orth, Aschaffenburg, 2004.

[45] A. Sibirtsev, K. Tsushima and A. Thomas, Eur. Phys. J. A6, 351 (1999).

[46] A. Hayashigaki et al., Phys. Lett. B 487, 96 (2000).

[47] P. Morath, PhD Thesis, TU München, 2001.

[48] B. Friman, S. Lee and T. Song, Phys. Lett. B 548, 153 (2002).

[49] M. Kotulla et al., *Technical Progress Report for $\overline{P}$ANDA - Strong Interaction Studies with Antiprotons*, Feb 2005.

[50] K. Itonaga, T. Ueda, T. Motoba, Nucl. Phys. A 691, 197c (2001).

[51] A. Parreno, A. Ramos, C. Bennhold, Nucl. Phys. A 65, 015205 (2001).

[52] K. Sasaki, T. Inoue, M. Oka, Nucl. Phys. A 726, 349 (2003).

[53] B. Aubert et al., Phys. Rev. Lett. 87, 091801 (2001).

[54] K. Abe et al., Phys. Rev. Lett. 87, 091802 (2001).

[55] G. Burdman, arXiv:hep-ph/9407378

[56] N.H. Hamann, Prepared for SUPERLEAR Workshop, Zurich, Switzerland, Oct 9-12, 1991.

[57] A. Rotondi for the $\overline{\text{P}}$ANDA Collaboration, *Prospects for Hadron Physics in $\overline{P}$ANDA* , Frascati Physics Series, Vol. XLVI (2007).

[58] T. Johansson et al., Nucl. Phys. B Proc. Suppl. A 56, 46 (1997).
K.D. Paschke et al. Phys. Rev. C 74, 015206 (2006).

[59] A.V. Belitsky and A.V. Radyushkin, Phys. Rept. 418, 1 (2005).

[60] X. Ji, Ann. Rev. Nucl. Part. Sci. 54, 413 (2004).

[61] M. Diehl, Phys. Rept. 388, 41 (2003).

[62] K. Goeke, M.V. Polyakov, M. Vanderhaeghen, Prog. Part. Nucl. Phys. 47, 401 (2001).

[63] X.–D. Ji, Phys. Rev. Lett. 78, 610 (1997).

[64] A.V. Radyushkin, Phys. Lett. B 380, 417 (1996).

[65] X.–D. Ji, Phys. Rev. D 55, 7114 (1997).

[66] P. Kroll and A. Schafer, Eur. Phys. J. A26, 89 (2005).

[67] M. Jones at al., Phys. Rev. Lett. 84, 1398 (2000).

[68] O. Gayou et al., Phys. Rev. Lett. 88, 092301 (2002).

[69] O. Gayou et al., Phys. Rev. C 71, 055202 (2005).

[70] M. Jones at al, Phys. Rev. C 74, 035201 (2006).

[71] V. Punjabi et al., Phys. Rev. C 71, 055202 (2005).

[72] J. Rafelski, Phys. Lett. 91 B (1980) 281.

[73] P. Braun–Munzinger and J. Stachel, Nature 448 (2007) 302.

[74] G. Bendiscioli, Nucl. Phys. News, Vol. 20, No. 2, 2010.

[75] J. Rafelski, B. Müller, Phys. Rev. Lett. 48 (1982) 1066;
J. Rafelski, Nucl. Phys. A 418 (1984) 215c.

[76] H.C. Eggers, J. Rafelski, in: Peniscola 1989, Proceedings, The Nuclear Equation of State, 1989, p. 187.

[77] J. Rafelski, J. Letassier, J. Phys. G: Nucl. Phys. 30 (2004) s1.

[78] G. Bendiscioli and D. Kharzeev, Riv. Nuovo Cimento 17 (1994) 1.

[79] B. Pontecorvo, JETP 3 (1956) 966.

[80] J. Cugnon, P. Deneye, J. Vandermeulen, Phys. Rev. C 41 (1990) 1701.

[81] J. Cugnon, J. Vandermeulen, Phys. Rev. C 39 (1989) 181;
J. Cugnon, J. Vandermeulen, Phys. Lett. B 146 (1984) 16.

[82] C. Derreth et al., Phys. Rev. C 31 (1985) 1360.

[83] P. Montagna et al., Nucl. Phys. A 700 (2002) 159.

[84] A. Panzarasa et al., Nucl. Phys. A 747 (2005) 448.

[85] P. Salvini et al., Nucl. Phys. A 760 (2005) 349.

[86] G. Bendiscioli et al., Nucl. Phys. A 815 (2009) 67.

[87] A. Adamo et al., Nucl. Phys. C 31 (1985) 1360.

Chapter 2

The $\overline{\text{P}}$ANDA detector

2.1 Detector overview

The rich physics program, as described in Sec. 1.2, poses significant challenges on a detector. But $\overline{\text{P}}$ANDA is in a favourable situation: it takes advantage of the experience from previous experiments in this field, like Crystal Barrel and Obelix at LEAR, E835 at Fermilab, FINUDA in Frascati. In addition, it can take into account new concepts and instruments optimised or introduced by the construction of the LHC detectors and of the B factory experiments.
So the $\overline{\text{P}}$ANDA detector will be able to combine the best ever available high–resolution high–intensity antiproton beam with a hermetic detector for charged and neutral particles, in the energy range between 10 MeV and 10 GeV.
Clearly, the design choices for the detector should represent a balance between physics needs and available resources.
Since no other detectors are foreseen for the HESR and no other similar antiproton beam will be available elsewhere, the detector has to be sufficiently robust and resistant to radiation damage to guarantee an operation over many years.
The main requirements the $\overline{\text{P}}$ANDA detector has to fulfil are the following:

- nearly 4π solid angle coverage;
- good capability of tracking charged particles with momentum between 100-200 MeV/c and 8 GeV/c;
- good vertex reconstruction for the identification of the charmonium states;
- excellent energy resolution;
- good particle identification for photons, pions, kaons, protons, electrons and muons;
- high rate compatibility, since the estimated event rate is of $2 \cdot 10^7$ antiproton annihilations per second;

- high modularity, in order to allow different and complementary measurements from nuclear to particle physics.

To achieve these goals, the detector will be composed of two magnetic spectrometers: the *Target Spectrometer* (TS) to detect particles emitted with laboratory angles greater than 5 and 10 degrees in the vertical and horizontal directions respectively, and the *Forward Spectrometer* (FS) for small angle tracks [1, 2, 3].

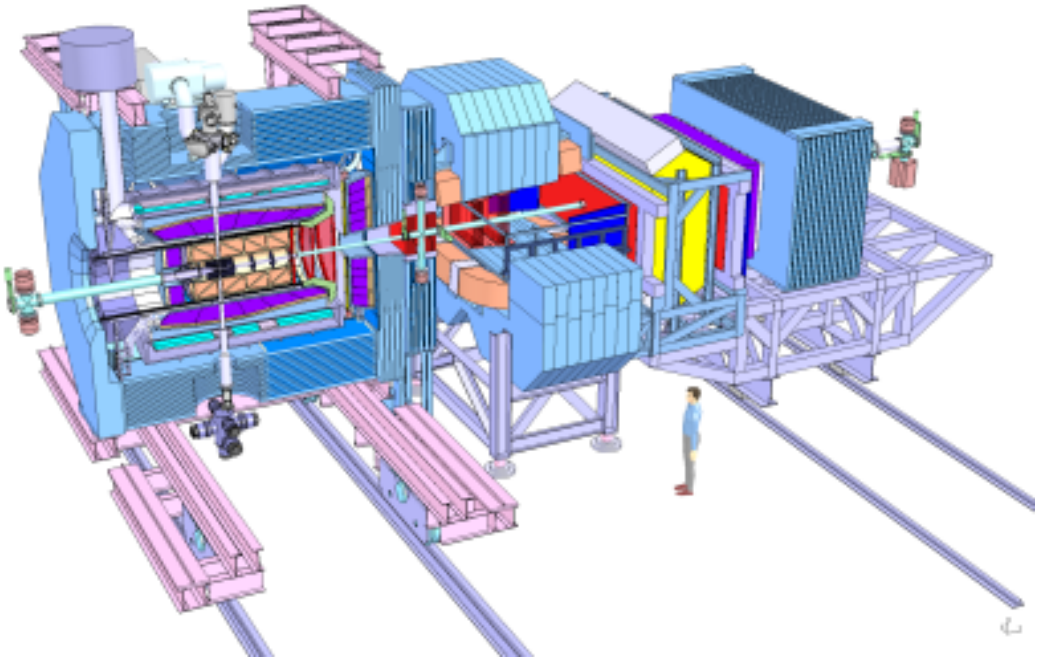

Figure 2.1: Layout of the $\overline{\text{P}}$ANDA detector. Figure taken from Ref. [4].

2.1.1 Target Spectrometer

The basic concept of the Target Spectrometer (TS) is a shell–like arrangement of various detector systems surrounding the interaction point, with the aim of measuring charged tracks in a highly homogeneous (better than $\pm$ 2%) solenoidal field of 2 T.
It will be arranged in three parts:

- the barrel, covering angles in the range from 22° to 140°;
- the forward end cap, extending the angles down to 5° and 10° in the vertical and horizontal planes respectively;
- the backward end cap region, between about 145° and 170°.

An overview is shown in Fig. 2.2.

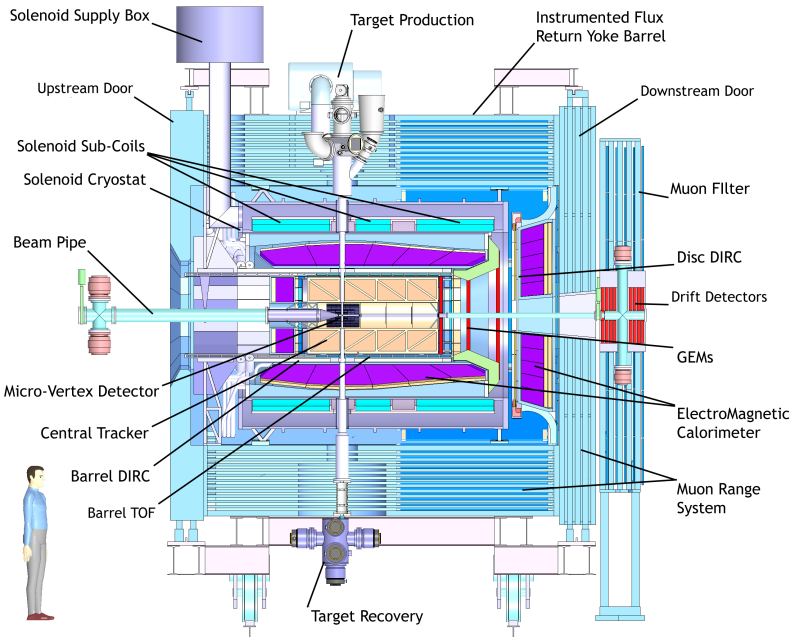

Figure 2.2: Side view of the Target Spectrometer (TS) of $\overline{\text{P}}$ANDA. To the right of this, the Forward Spectrometer (Fig. 2.6) follows. Figure taken from Ref. [4].

2.1.1.1 Target

Regarding the interaction point, two complementary techniques are taken into account: a *pellet target* and a *cluster–jet target*.

Pellet Target It consists of a stream of frozen hydrogen pellets (micro–spheres) that traverse the antiproton beam perpendicularly. At the interaction point, typical parameters are a pellet rate of 10-15 kHz, a fall speed greater than 60 m/s and a pellet size of 25 μm, leading to an average target thickness of a few 10^{15} atoms/cm^2. The pellet train has a lateral spread $\sigma \sim 1$ mm and an interspacing of pellets between 0.5 and 5 mm. The advantage of this target is the high resolution in the vertex position (50 μm) that can be reached thanks to the large number of interactions expected in every pellet and to the foreseen pellet tracking system.

Cluster–Jet Target It is a narrow supersonic jet of hydrogen clusters, each of them consisting of 10^3-10^6 hydrogen molecules. The advantage of cluster targets is the high homogeneity in density of the targets and the possibility to focus the antiproton beam at highest density in phase space. On the other hand, it cannot allow a very precise definition of the interaction point.

Other targets Targets for the hypernuclear physics are under consideration. In addition, a current R&D is studying the development of a liquid helium target and a polarised ^{3}He target. A wire target may also be employed to study antiproton–nucleus interactions.

2.1.1.2 Tracking devices

The tracking system of the Target Spectrometer will consist of a *Micro–Vertex Detector* and of a *Central Tracker*.

Micro–Vertex Detector The Micro–Vertex Detector (MVD) is the detector closest to the primary interaction vertex.
It is a tracking device for charged particles, optimised for a very precise determination of secondary decay vertices of short–lived particles such as hyperons and strange or charmed mesons.
The foreseen layout, depicted in Fig. 2.3, consists of a four layer barrel detector (inner radius of 2.5 cm, outer radius of 13 cm) surrounding the beam pipe and of eight detector wheels arranged perpendicular to the beam, in order to achieve the best acceptance for the forward part of the particle spectrum.
The two innermost barrel layers (1-2), as well as the inner four wheel layers (1-4), will be entirely made of silicon pixel detectors; the two outer barrel layers (3-4) and the last two wheels (7-8), placed further downstream to achieve a better acceptance of hyperon cascades, will be made of double–sided silicon strip detectors. The remaining wheel layers (5-6) will be a combination of strip detectors on the outer radius and pixel detectors closer to the beam pipe.

Central Tracker The Central Tracker is designed like a barrel enclosing the target and beam pipe and surrounding the MVD. It will occupy the space from 15 to 42 cm (radial distance) from the beam pipe and will extend from 40 cm upstream to 110 cm downstream of the interaction point.
This charged–particle tracking system should have an almost complete 4π coverage around the interaction point and should be able to handle the high particle fluxes (expected event rate of $2{\cdot}10^7$ s^{-1}) anticipated for a luminosity of few 10^{32} cm^{-2} s^{-1} and to resolve the complex pattern of multiple tracks (expected track multiplicity 4 - 6 tracks/event).
The momentum resolution $\delta p/p$ should be on the percent level over a momentum range of a few hundred MeV/c in the backward region, to some GeV/c in the forward region. As well, it should be able to reach a high spatial resolution $\sigma_{r\phi} = 150$ μm and $\sigma_z = 1$ mm.
The tracker should also have good detection efficiency for secondary vertices which can occur outside the inner vertex detector (i.e. K^0_S or Λ). This will be achieved by combining the Central Tracker with the MVD.
Two options are currently under study:

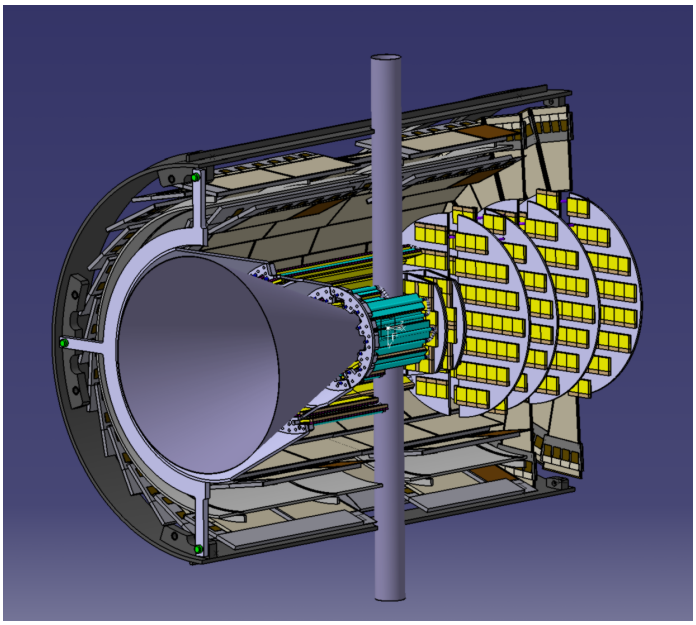

Figure 2.3: The Micro–Vertex Detector (MVD). The two outer layers have been cut out for a better visibility. Figure taken from Ref. [1].

- a *Straw Tube Tracker* (STT), that will consist of planar layers of aluminised mylar tubes (*straws*) arranged in a hexagonal layout that have to fill the cylindrical volume of the Central Tracker. This solution, sketched in Fig. 2.4 - left, will be described in detail in Sec. 2.2.

- a *Time Projection Chamber* (TPC), sketched in Fig. 2.4 - right, that will consist of two large gas–filled half–cylinders. An electrical field along the cylinder axis will separate positive gas ions from electrons created by ionising particles traversing the gas volume.

In the next months/years, the $\overline{\text{P}}$ANDA collaboration will evaluate the best solution between STT and TPC as Central Tracker. The decision will be taken on the basis of the performances resulting from Monte Carlo simulations and tests with prototypes, of the particle identification capabilities and of the detectors costs.

Gas Electron Multiplier The other detector composing the tracking system of the Target Spectrometer will consist of three sets of *Gas Electron Multiplier* (GEM) stations, placed 1.1, 1.4, 1.9 m downstream of the target, in order to be able to detect the particles emitted at angles below 22° which do not enter the STT/TPC.
For the GEM stations, gaseous micro–pattern detectors based on GEM foils as amplification stages are chosen, since they have rate capabilities three orders of magnitude higher than drift chambers.

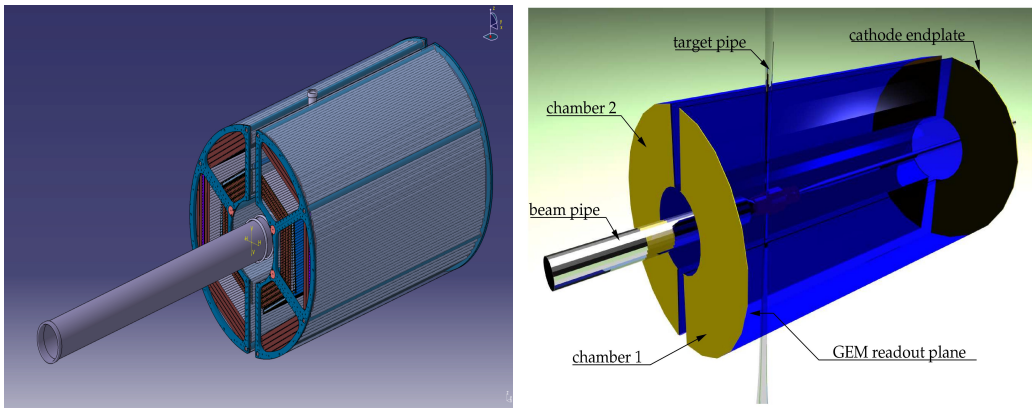

Figure 2.4: The $\overline{\text{P}}$ANDA Straw Tube Tracker (STT) (left) and Time Projection Chamber (TPC) (right), with beam and target pipes seen from upstream. Figure taken from Ref. [1].

2.1.1.3 Particle identification devices

The identification of charged particles over a large range of angles and momenta is one of the main requirement of the physics objectives of $\overline{\text{P}}$ANDA. This will be performed by different subdetectors: the main part of the momentum spectrum above 1 GeV/c will be covered by the *Cherenkov counters*; in addition, a *Time–Of–Flight* barrel will identify slow particles.

Barrel Time–Of–Flight The Barrel Time–Of–Flight (TOF) will provide particle identification for slow particles at large polar angles. In order to achieve this goal, the detector will have a time resolution between 50 and 100 ps.
The TOF system will be made of scintillator bars and strips or pads of multi–gap resistive plate chambers. It will cover angles in the range from 22° to 140° using a barrel arrangement around the Central Tracker at 42 - 45 cm radial distance.

Detectors of Internally Reflected Cherenkov light The Detectors of Internally Reflected Cherenkov light (DIRC) will be essentially used for particle identification at polar angles between 5° and 22° (Forward End–Cap DIRC) and for polar angles between 22° and 140° (Barrel DIRC).
The Barrel DIRC will consist of 1.7 cm thick fused silica slabs surrounding the beam line at a radial distance of 45 - 54 cm; the images will be then focused by lenses onto micro–channel plate photomultiplier tubes, insensitive to magnetic fields.
The Forward End–Cap DIRC will employ a similar concept of radiator but in shape of a disk: it will be 2 cm thick with a radius of 110 cm and will be placed directly upstream of the forward end cap calorimeter.

2.1.1.4 Calorimetry device

The ElectroMagnetic Calorimeter (EMC) requires fast scintillation materials, with short radiation length and Moliere radius. It is foreseen the use of lead tungsten ($PbWO_4$), which has a short decay time (< 10 ns) and shows a good radiation hardness; different crystals are also taken into consideration.
The envisaged energy resolution is $< 2\%$ at 1 GeV, the time resolution < 2 ns. With such a good resolution, the EMC will allow to reach a e/π ratio of 10^3 for momenta above 0.5 GeV/c.
The setup, as shown in Fig. 2.5, will consist of 11360 tapered crystals (approximately 22 X_0) with a length of 22 cm, mounted in a barrel shape with an inner radius of 57 cm. In addition, there will be other 3600 tapered crystals with a planar arrangement in the forward end cap and 592 crystals in the backward end cap.

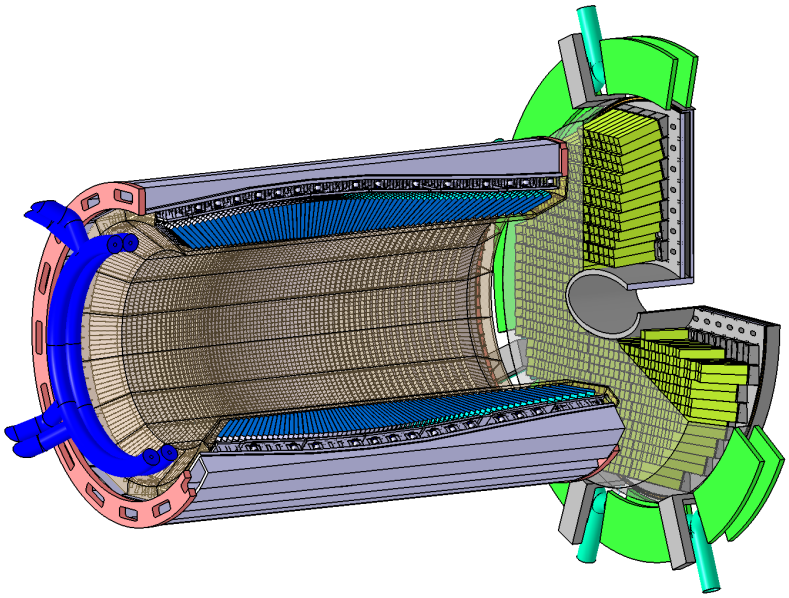

Figure 2.5: Barrel and forward end cap of the $\overline{\text{P}}$ANDA ElectroMagnetic Calorimeter (EMC) with its mounting structures and cooling pipes. Figure taken from Ref. [2].

2.1.1.5 Solenoid Magnet

A superconducting solenoid will provide the magnetic field inside the Target Spectrometer. It will produce a maximum magnetic field of 2 T, with a field homogeneity better than 2% over the volume of the Micro–Vertex Detector and Central Tracker.
The solenoid will have an inner radius of 105 cm and a length of 2.8 m.

2.1.1.6 Muon detection devices

In the yoke of the solenoid magnet a fine segmentation as absorber with interleaved tracking detectors will be implemented in order to allow a proper separation between primary muons, pions and kinks from pion decays.
In the barrel region, it is foreseen to segment the yoke in one layer of 6 cm iron, followed by 11 layers with a thickness of 3 cm and finally the last layer of 6 cm iron: this amount of material is enough to absorb pions.
Then the muon system will be split up in several layers: six detection layers will be placed around five iron layers of 6 cm thickness each within the door; in addition, a removable muon filter with five more layers of 6 cm iron will be placed in the space between the solenoid and the dipole.

2.1.1.7 Hypernuclear detector

It is foreseen that a data acquisition session will be devoted to the hypernuclei physics. In order to perform such studies, during this dedicated session the $\overline{\text{P}}$ANDA detector will be modified, providing a specific configuration. In particular, by removing the backward part of the calorimeter, it will add an hypernuclear array: it will consist of a dedicated nuclear target station for the hypernuclei production and the required additional detectors, that will be a high resolution and high efficiency germanium scintillator array for γ spectroscopy.

2.1.2 Forward Spectrometer

The Forward Spectrometer (FS) (Fig. 2.6) will detect particles emitted in the entire angular acceptance of the Target Spectrometer of $\pm 5°$ and $\pm 10°$ in the vertical and horizontal direction respectively.
In this region, a magnetic field will be provided by a dipole magnet; Cherenkov detectors, calorimeters and muon counters will guarantee the detection of particles of all types.

2.1.2.1 Dipole magnet

To analyse the momentum of charged particles in the Forward Spectrometer, a 2 T m dipole magnet with a window frame, a 1 m gap and more than 2 m aperture is foreseen.
The magnet yoke will be placed at a distance of 3.9 m downstream of the target and will occupy about 1.6 m.
The deflection of the antiproton beam due to the bending power of the dipole will be of about $2.2°$ at the maximum momentum of 15 GeV/c. This deflection will be compensated by two correcting dipole magnets, placed around the $\overline{\text{P}}$ANDA detection system.

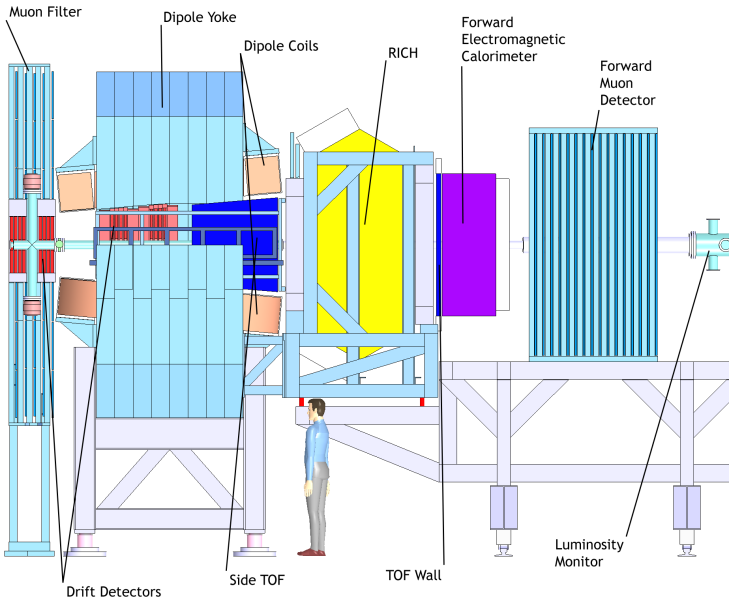

Figure 2.6: Artistic side view of the Forward Spectrometer (FS) of $\overline{\mathrm{P}}$ANDA. It is preceded on the left by the Target Spectrometer (TS), shown in Fig. 2.2. Figure taken from Ref. [4].

2.1.2.2 Tracking devices

Three pairs of tracking drift detectors (wire chambers) will be used to measure the deflection of particle trajectories in the field of the dipole magnet. The first pair will be placed in front, the second within and the third behind the dipole magnet.
Each independent detector will consist of four double layers of straw tubes (Fig. 2.7), in order to allow track reconstruction in each pair of tracking detectors separately, also in case of multi–track events. According to the foreseen layout, two double layers will have vertical wires, the other two wires inclined by a few degrees; the value of the skew angle is still under study and will be optimised by ongoing simulations.

2.1.2.3 Particle identification devices

Ring Imaging Cherenkov detector The Ring Imaging Cherenkov (RICH) detector has been proposed in order to assure a good π/K and K/p separation also at the very highest momenta: in particular, by using a dual radiator RICH detector made of silica aerogel and C_4F_{10}, like the one used at Hermes, it will be possible to separate $\pi/K/p$ in a broad momentum range from 2 to 15 GeV/c.
The Cherenkov light will be focused by a lightweight mirror on an array of phototubes placed outside the active volume.

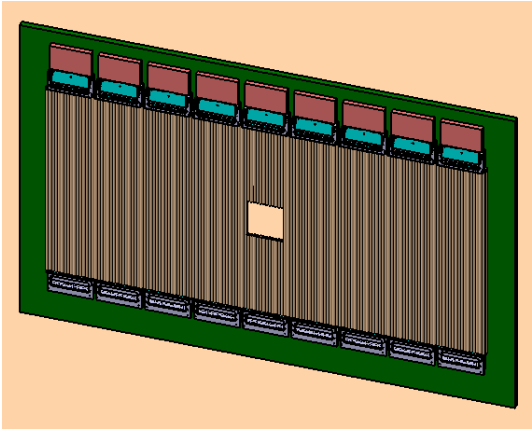

Figure 2.7: Double layer of straw tubes with preamplifier cards and gas manifolds mounted on rectangular support frame. The opening in the middle of the detector is foreseen for the beam pipe. Figure taken from Ref. [4].

Time–Of–Flight Wall The Time–Of–Flight stop counter will consist of a wall of slabs made of plastic scintillators, read out by fast phototubes on both ends and placed at about 7 m from the target. Similar detectors will be positioned inside the dipole magnet opening in order to detect low momentum particles which do not exit the dipole magnet.
With the expected time resolution $\sigma = 50$ ps, it will be possible to separate π/K and K/p on a 3σ level up to momenta of 2.8 GeV/c and 4.7 GeV/c respectively.

2.1.2.4 Calorimeter device

A Shashlyk–type calorimeter with high resolution and efficiency is predicted to be used to detect photons and electrons, thanks to lead–scintillator sandwiches read out by wavelength shifting fibers coupled to photomultipliers. This choice has been successfully used in the E865 experiment and adopted in various others.
351 Shashlyk modules (110 mm $\times$ 110 mm $\times$ 680 mm = 20 X_0) will be used to cover the forward acceptance; they will be arranged in 13 rows and 27 columns at 7.5 m from the target.

2.1.2.5 Muon detection devices

A tracking system consisting of interleaved absorber layers and rectangular aluminium drift tubes, similar to the muon system in the target spectrometer, has been designed for the very forward part of the muon spectrum. It allows the discrimination of pions from muons, the detection of pion decays and also the energy determination of neutrons and antineutrons.

2.1.3 Luminosity monitor

The determination of the time integrated luminosity L available while collecting a given data sample for reactions at the $\overline{\text{P}}$ANDA interaction point is needed to derive the cross section for physical processes.
The basic goal of the luminosity monitor is to reconstruct the angle of the scattered antiprotons in the polar angular range of 3-8 mrad with respect to the beam axis. Due to the large transverse dimensions of the interaction region when using the pellet target, there is just a weak correlation between the position of the antiproton at e.g. $z = 10$ m and the recoil angle. Therefore, it is necessary to reconstruct the angle of the antiproton at the luminosity monitor. It will consist of four planes of double–sided silicon strip detectors located as far downstream of and as close to the beam axis as possible. The planes, each consisting of four wafers (e.g. 2 cm $\times$ 5 cm $\times$ 200 μm, with 50 μm pitch), will be separated by 20 cm along the beam direction. The silicon wafers will be placed inside a vacuum chamber to minimise scattering of the antiprotons before traversing the four tracking planes.
The luminosity monitor will be located in the space between the downstream side of the forward muon system and the HESR dipole needed to redirect the antiproton beam out of the $\overline{\text{P}}$ANDA chicane back into the direction of the HESR straight stretch (e.g. between $z = 11$ m and $z = 13$ m downstream of the target).

2.2 The Straw Tube Tracker

The Straw Tube Tracker (STT) of the $\overline{\text{P}}$ANDA experiment is one of the two foreseen options for tracking charged particles inside the Target Spectrometer. It exhibits the most simple geometry of highly symmetric, cylindrical tubes and has several advantages:

- robust electrostatic configuration, thanks to the shielding tube surrounding each high voltage wire, which suppresses signal cross–talk and protects neighbouring straws in case a wire breaks;
- robust mechanical stability if the straws are arranged in close–packed multilayers and pressurised;
- high tracking efficiency ($\sim 1\%$ dead zone);
- high spatial resolution ($\sigma_{r\phi} < 150$ μm, $\sigma_z \sim 1$ mm);
- high momentum resolution ($\delta p/p \sim 1\%$);
- small radiation length ($X/X_0 \sim 0.05\%$ per tube, in the case of straws with film tubes of about 30 μm wall thickness);
- high rate capability, which can be improved by using a fast drift gas.

2.2.1 Straw tubes description

2.2.1.1 Straw materials

The straw tubes that will be used for the $\overline{\text{P}}$ANDA detector have a length varying from 1200 to 1500 mm, 10 mm inner diameter and a wall thickness of 29 μm. They are made of two layers of 12 μm aluminised mylar films glued together; the aluminisation at the inner tube wall is used as the cathode, whereas the aluminisation of the second, outer strip layer is used to prevent light incidence.
A gold–plated tungsten–rhenium wire with 20 μm diameter is used as anode. The tubes are closed at both ends by cylindrical precision end plugs made of ABS with a wall thickness of 0.5 mm. They are glued to the mylar film leaving a small film overlap (1.5 mm) on both ends. There, a gold–plated copper–beryllium spring wire is inserted in order to provide the electric cathode contacting. The end plugs have a central hole with a 3 mm thick cylindrical nose to insert and glue a crimp pin that fixes the wire. In addition, a micro PVC tube is glued to another hole of the end plugs, to provide a gas flow through the tube.
The anode wire is stretched by a weight of 50 g and crimped in the copper pins at a gas overpressure in the straw tube of 1 bar. At this tension, the calculated gravitational sag of the wire is less than 35 μm, much below the foreseen spatial resolution of 150 μm.
The total weight of a fully assembled straw is 3 g.
Tab. 2.1 lists the different components of a straw tube (Fig. 2.8) and their thickness in radiation length.

Table 2.1: Materials and their radiation lengths of a straw tube components.

Element	Material	X(cm)	X_0 (cm)	X/X_0
Film tube	Mylar, 30 μm	$6{\cdot}10^{-3}$	28.7	$2.1{\cdot}10^{-4}$
Coating	Al, 2×0.2 μm	$6{\cdot}10^{-6}$	8.9	$6.7{\cdot}10^{-7}$
Gas	$ArCO_2$ (90/10%)	1	6353	$1.6{\cdot}10^{-4}$
Wire	WRe, 20 μm diam.	$3.14{\cdot}10^{-6}$ [a]	0.35	$9{\cdot}10^{-6}$

[a] The equivalent thickness X of a wire having diameter d is calculated assuming that its material is spread uniformly on a pitch: $X = \pi(d/2)^2$ [5].

The $\overline{\text{P}}$ANDA straw tubes will be filled with a mixture of $ArCO_2$; the percentage in which the two gases will be mixed is still under investigation, but the choice is between 90/10% and 80/20%. The scheme of gas supply and electric readout are under study and will be developed in the future.
It is foreseen that the tubes will be operated at a high voltage of 1800 V and 2 bar absolute pressure.
Tests are ongoing with a laboratory setup in Jülich (described in Chap. 4) in order to investigate options for the electronics.

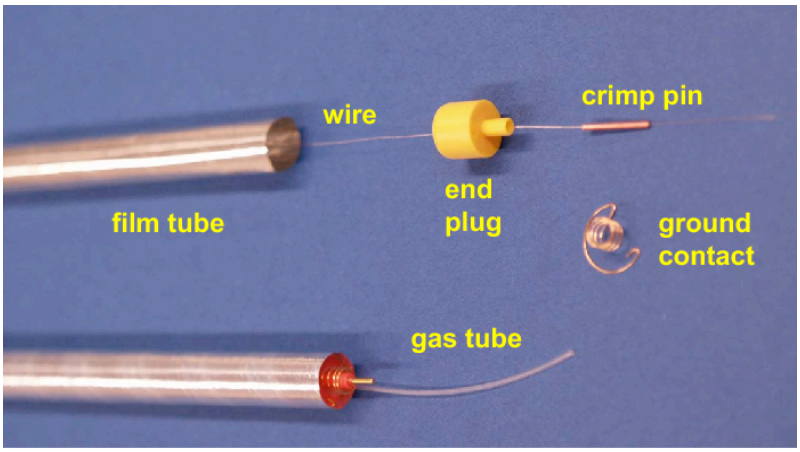

Figure 2.8: A straw tube with all its components. Design and picture by IKP–FZ, Jülich.

2.2.1.2 Pressurised straws

Both the efficiency and the resolution of a straw tube are optimal when the film tube has a perfect cylindrical shape and the anode wire is located exactly along the cylinder axis. Due to the gravitational and electrostatic forces, however, the wire and the straw centers do not coincide. The gravitational sag of the wire is given by [6]:

$$\delta = \frac{ML}{8T}, \tag{2.1}$$

where M and T are the wire mass and tension[1] in grams and L is the length of the wire.
Having a wire tension of about 50 g inside a 1.5 m long horizontal straw tube, the maximum sag due to gravitation in the tube is less than 35 μm. Furthermore, the electric field acting on an eccentric wire will induce an additional bending δ_1 depending on the actual voltage applied to the wire [6]:

$$\delta_1 = \frac{\pi\epsilon_0 \Delta L^2 V^2}{4TR^2[\ln(R/r)]^2} \tag{2.2}$$

where ϵ_0 is the permittivity of the free space, Δ is the shift of the wire from the tube centre due to the gravitational sag, L is the tube length, V is the voltage applied to the anode, T is the wire tension, R and r are the radii of the tube and of the wire.
Considering that the $\overline{\text{P}}$ANDA Straw Tube Tracker will consist of about 4200 tubes, these sags will sum up to a tension equivalent to $\sim$ 210 kg, which must be maintained. This is usually done by fixing the straw tubes to a strong and massive surrounding frame or by using additional support structures along the

[1]The wire tension is usually expressed in terms of the mass weight used to stretch the wire.

tubes to keep them straight. All these methods have the inconvenience to increase the global weight of the apparatus. This can be avoided by using a new technique developed for the COSY–TOF Straw Tube Tracker [7], consisting in self–supporting straw layers with intrinsic wire tension: the straw tubes are assembled and the wire stretched by 50 g at an overpressure of ~ 1 bar. Then they are closed–packed and glued together to planar double–layers on a reference table, that allows to precisely define the tube to tube distance to a value of 10.1 mm. At this gas overpressure the double–layers maintain the nominal wire tension of 50 g for each tube, so they become self–supporting.

2.2.2 The detector layout

The Straw Tube Tracker will consist of planar double–layers of straw tubes arranged in a hexagonal layout, that has to fill up a cylindrical volume with an inner diameter of 150 mm, an outer one of 418 mm and a length varying from 120 cm to 150 cm. Due to the presence of the target pipe, this volume will be divided in two halves in the (x, y) plane, with a gap of 42 mm in between.
A straw double–layer consists of 2 close–packed, staggered layers of tubes: the position of the straws in the second layer has an offset of half straw diameter (5.05 mm) compared to the upper one. Each layer consists of closed–packed straws glued together on a reference plate with precise positioning (50 μm); each straw is fixed to the neighbouring one along its length, through glue dots.

The proposed design will have, in radial direction, four double–layers parallel to the detector axis (z axis), four skewed double–layers with an angle of $\pm 3^\circ$ with respect to the beam axis to reconstruct the z coordinate of the tracks and further two straight double–layers. Additional single–layers will be placed in the outer region to approach the cylindrical shape (Fig. 2.9). Moving from the inner to the outer of the detector, the number of straws per layer changes from layer to layer; the total number of tubes is 4210 [8].

2.2.2.1 Mechanics

An external mechanical structure is needed to support and to precisely position the straw tube double–layers. This should be rigid enough to support the weight of the tubes and of the services (i.e. electronics, gas pipes, etc.), but on the other side it needs to be extremely light not to increase too much the material budget.
On the basis of the experience of experiments like FINUDA [9], COSY–TOF [7] and BTeV [10], the foreseen mechanical structure is the one shown in Fig. 2.10. In the hypothesis of using Aluminium for the realisation, the support will be very light and characterised by the parameters in Tab. 2.2.

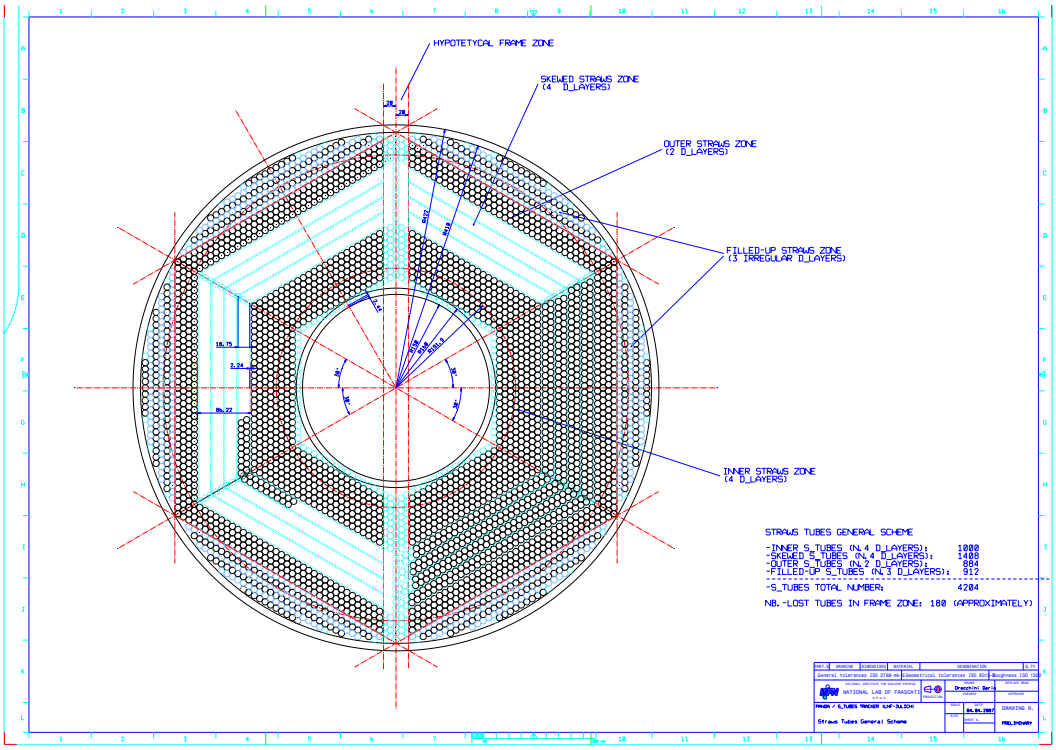

Figure 2.9: Cross section of the general layout of the Straw Tube Tracker. Not all straws are visible (blue marked region) for a better view of the details. CAD drawing by D.Orecchini (SSE–LNF, Frascati).

Figure 2.10: A full size prototype of the foreseen mechanical frame to support one half of the tracker. Design and construction by D.Orecchini (SSE–LNF, Frascati).

Table 2.2: Parameters of the mechanical frame.

Density	2.7 g/cm^3
Young modulus	70 GPa
Radiation length (X_0)	9 cm
Thermal expansion	24 ppm/°C
Weight	8.2 kg

The straw double–layers will be fixed to the support frame through side–bands (Fig. 2.11). They are light strips made of fiberglass 1 mm thick, gold–plated on the straw tube side to allow the electrical grounding and with circular holes with a diameter of 3.2 mm, except for two holes needed to give mechanical precision to the double–layer, that have a diameter of 3.0 mm (Fig. 2.12).
The tubes are fixed to the side–bands with an elastic ring placed in the groove of the end–plugs (Fig. 2.13). The double–layers are then fixed to the frame through fixing pins inserted in two additional larger holes of the side–bands.

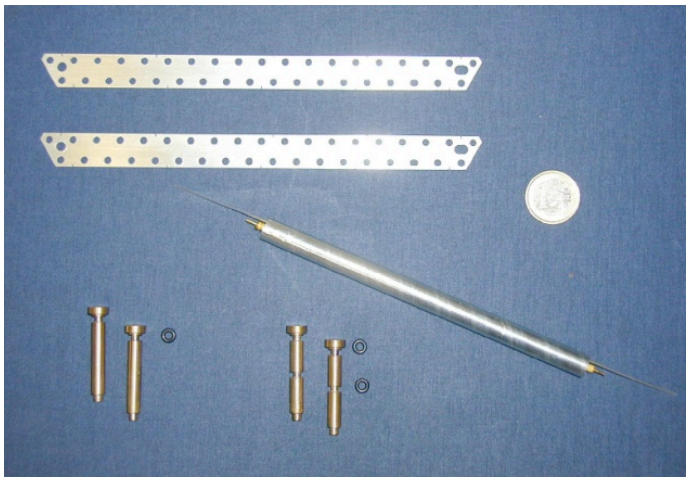

Figure 2.11: Prototype of the side–bands used to fix straw tubes double–layers to the mechanical frame. Design by D.Orecchini (SSE–LNF, Frascati).

2.2.2.2 Full scale prototype

During the year 2009 the assembly of a first full–scale prototype has started at the Jülich Research Centre (IKP–FZJ), to study the mechanical properties and assembly techniques of the hexagonal straw layer stacks.
About 2000 straw tubes with the same characteristics of the straw tubes foreseen for $\overline{\text{P}}$ANDA have been assembled and glued together to double–layers. A

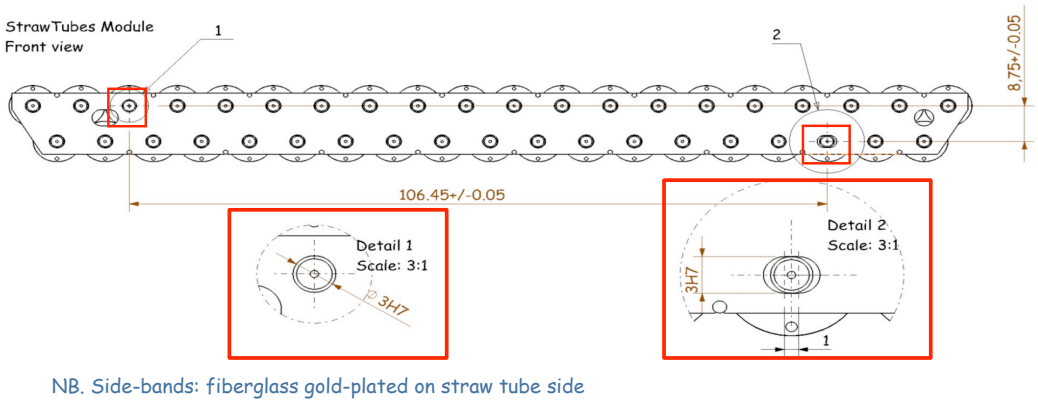

Figure 2.12: Sketch of the side–bands. The insets show in detail the more precise holes with a diameter of 3.0 mm, used to give mechanical precision to the module. Design by D.Orecchini (SSE–LNF, Frascati).

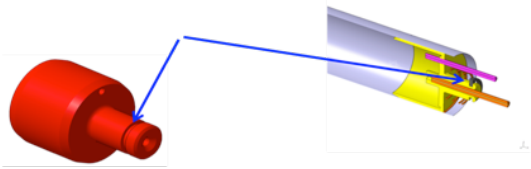

Figure 2.13: Straw Tube end–plug. A groove (indicated by the arrows) is used to fix it to the side–bands by the insertion of an elastic ring. Design by D.Orecchini (SSE–LNF, Frascati).

simple mechanical frame structure, consisting of two aluminium end flanges, is used to hold the straw layers. The individual double–layers are positioned and attached to the flanges by only two pins at both ends.
The (incomplete) setup, shown in Fig. 2.14, confirms that the pressurised straw layers are self–supporting and no or only weak support structures for the STT are needed.
The scheme of gas supply and electric readout will be developed next. Finally, the mechanical precision of the setup will be measured by reconstructed tracks of cosmic rays or proton beam at COSY [11].

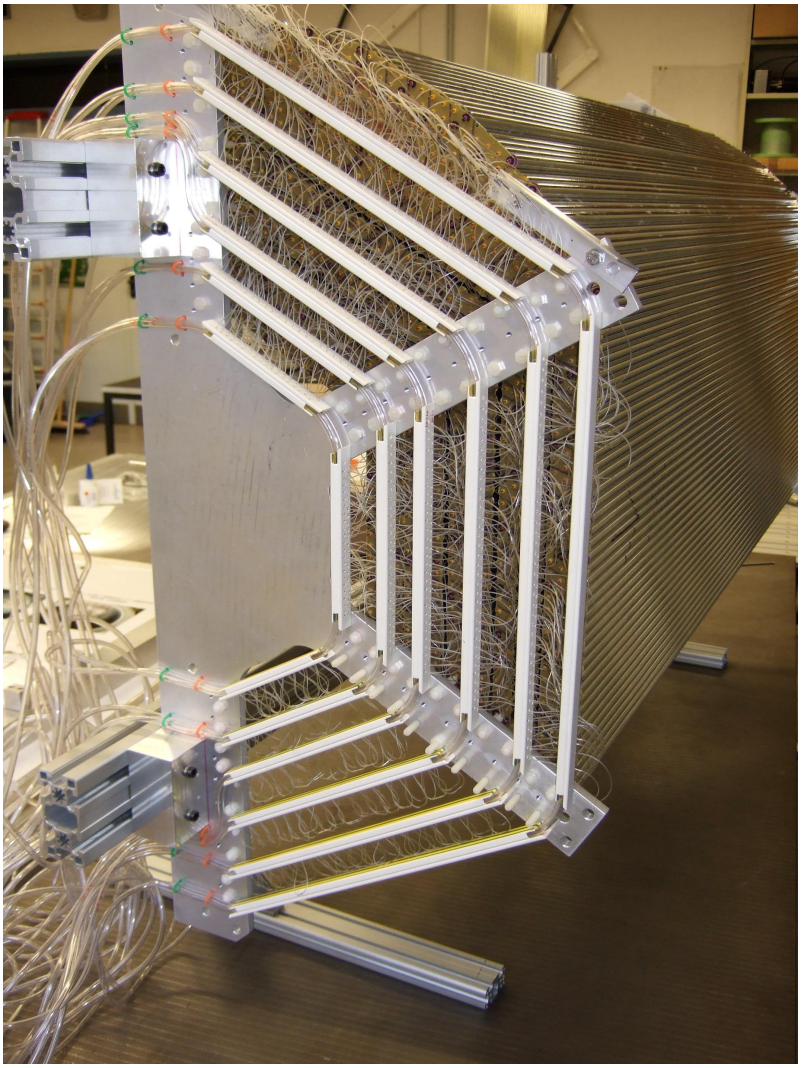

Figure 2.14: Assembly of a full–scale semi–barrel prototype. Construction by IKP–FZJ.

Bibliography

[1] M. Kotulla et al., *Technical Progress Report for $\overline{P}$ANDA - Strong Interaction Studies with Antiprotons*, Feb 2005.

[2] W. Erni et al., *Technical Design Report for $\overline{P}$ANDA Electromagnetic Calorimeter (EMC)*, Oct 2008, arXiv:0810.1216v1.

[3] W. Erni et al., *Technical Design Report for the $\overline{P}$ANDA Solenoid and Dipole Spectrometers Magnets*, Feb 2009, arXiv:0907.0169v1.

[4] http://www-panda.gsi.de/.

[5] P.W. Cattaneo, *The effect of the gas filling the detector volume on the tracking resolution*, Pavia, May 2003.

[6] A. Sokolov, *Development of proportional chamber detectors and simulations to measure charm hadrons in antiproton-proton annihilation*, PhD Thesys, Giessen (Germany), July 2005.

[7] P. Wintz, *Intersection of Particles and Nuclear Physics: 8^{th} Conference CIPANP 2003*, AIP Conf. Proc. (2004) 628 Issue 1.

[8] S. Costanza et al., Nucl. Instr. and Meth. A 617 (2010) 148-150.

[9] L. Benussi et al., Nucl. Instr. and Meth. A 419 (1998) 648-653.

[10] E. Basile at al., IEEE Trans. Nucl. Sci. 53 (2006) 1375-1379.

[11] *The $\overline{P}$ANDA experiment at FAIR*, Highlights of IKP Annual Report 2009, Jülich 2010.

Part II

Study of a single straw tube

Chapter 3

Physics performances of a single straw tube

3.1 Basic principles of a single straw tube

Straw tubes are proportional counters consisting of a gas filled tube with a conductive inner layer as cathode and an anode wire stretched along the cylinder axis.
A radial high electric field between the wire and the outer conductor separates electrons and positive ions produced by charged particles traversing the gas volume along their trajectories. The electrons of the primary ionisation drift towards the anode, which is usually at positive voltage of a few kV, while the ions drift towards the cathode.
Due to the high electric field strength near the thin anode wire, the drifting electrons gain enough energy to ionise the gas molecules. The resulting secondary electrons then produce tertiary ionisation and so on, leading to the formation of an avalanche. Thanks to this process, the electric charge collected on the anode is many orders of magnitude higher than that produced in the primary ionisation. Depending on the high voltage set and the gas characteristics, an amplification of about $10^4 - 10^5$ of the primary charge is possible, high enough to be read out by the electronics.

In this section, a short review of the main physics processes that govern the functioning of a straw tube is presented. A more detailed description of these processes and of the basic principles of such detector can be found in Refs. [1, 2, 3, 4].

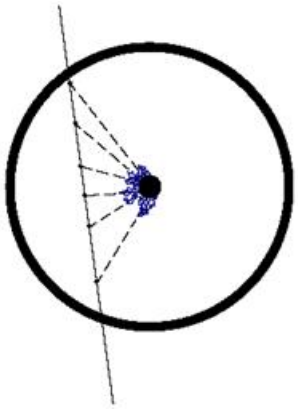

Figure 3.1: Drift of an electron cluster in a straw tube. Figure taken from Ref. [5].

3.1.1 Energy loss of charged particles

In order to understand the mechanisms that lead to the formation of electric signals inside a straw tube, it is necessary to study the passage of charged particles through matter, i.e. the basic reactions which occur when they traverse matter and the effects produced by these processes.

3.1.1.1 Heavy charged particles

Two main features characterise the passage of heavy[1] charged particles through matter: particle energy loss and deflection of the particle from its incident direction; these effects are mainly caused by inelastic collisions with the atomic electrons and elastic scattering from nuclei. Other processes are the emission of Cherenkov radiation, nuclear reaction and bremsstrahlung.
The average energy loss per unit path length $\mathrm{d}E/\mathrm{d}x$ can be described by the Bethe–Bloch formula:

$$-\frac{\mathrm{d}E}{\mathrm{d}x} = 2\pi N_A r_e^2 m_e c^2 \rho \frac{Z}{A}\frac{z^2}{\beta^2}\left[\ln\left(\frac{2m_e\gamma^2 v^2 W_{max}}{I^2}\right) - 2\beta^2 - \delta - 2\frac{C}{Z}\right] \quad (3.1)$$

where $2\pi N_A r_e^2 m_e c^2 = 0.15354$ MeVcm^2/g; ρ is the density of the absorbing material, whereas Z and A are its atomic number and weight; $\gamma = 1/\sqrt{1-\beta^2}$, where $\beta = v/c$, being v the velocity of the incident particle and z is its charge in units of e. Finally, I is the mean excitation potential and W_{max} is the maximum energy transfer in a single collision. In addition, in this formula the density effect correction δ and the shell correction C are taken into account.

[1] "Heavy" particles are particles heavier than electrons and positrons, i.e. muons with an energy less than 10 GeV, pions, protons, $\alpha-$particles and other light nuclei, for which the energy loss by radiation is negligible. Particles heavier than these, like the heavy ions, are excluded from this discussion.

3.1.1.2 Electrons and positrons

Like heavy charged particles, electrons and positrons suffer as well a collisional energy loss when passing through matter.
The ionisation is a statistic process that can be described by the Poisson law:

$$p(n) = \frac{n^k}{k!} e^{-n}, \tag{3.2}$$

where n is the mean number of ion–electron pairs per cm and k is the actual number.
Concerning collisions, they can be divided into two groups depending on the energy involved:

- soft collisions, in which only excitations result: $X + p \rightarrow X^* + p$;
- hard collisions, in which the transfer of energy is enough to cause ionisation: $X + p \rightarrow X^+ + p + e^-$. These recoil electrons are referred to as *δ-rays* or *knock-on electrons*. If their energy is sufficiently high, they can themselves transfer their energy, producing secondary ionisation.

To describe the basic mechanisms of collision loss for electrons and positrons, the Bethe-Bloch formula of Eq. (3.1) must be modified in order to take into account the small mass of the incident particle, which does not necessarily remain undeflected during the collision. In addition, it must be considered the indistinguishability of the two colliding electrons. These considerations lead to the fact that the maximum transferable energy is $W_{max} = T_e/2$, being T_e the kinetic energy of the incident electron (or positron). Therefore, the Bethe-Bloch formula becomes:

$$-\frac{\mathrm{d}E}{\mathrm{d}x} = 2\pi N_A r_e^2 m_e c^2 \rho \frac{Z}{A} \frac{1}{\beta^2} \left[\ln \frac{\tau^2(\tau+2)}{2(I/m_e c^2)^2} + F(\tau) - \delta - 2\frac{C}{Z} \right], \tag{3.3}$$

where τ is the kinetic energy of the particle in $m_e c^2$ units and

$$F(\tau) = 1 - \beta^2 + \frac{\frac{\tau^2}{8} - (2r+1)\ln 2}{(\tau+1)^2} \qquad \text{for } e^-,$$

$$F(\tau) = 2\ln 2 - \frac{\beta^2}{12}\left(23 + \frac{14}{\tau+2} + \frac{10}{(\tau+2)^2} + \frac{4}{(\tau+2)^3}\right) \qquad \text{for } e^+.$$

In addition to the collision and ionisation processes, in case of electrons and positrons another mechanism comes into play: bremsstrahlung, which is the emission of electromagnetic radiation arising from the scattering in the electric field of a nucleus.
Therefore the total energy loss of electrons and positrons is composed of two contributes:

$$\left(\frac{\mathrm{d}E}{\mathrm{d}x}\right)_{tot} = \left(\frac{\mathrm{d}E}{\mathrm{d}x}\right)_{rad} + \left(\frac{\mathrm{d}E}{\mathrm{d}x}\right)_{coll}. \tag{3.4}$$

At energies of a few MeV or less, bremsstrahlung does not contribute too much to the energy loss; as the energy increases, it takes place with higher probability until energy loss by radiation becomes comparable to energy loss by collision and ionisation (Fig. 3.2). This energy value is called critical energy:

$$\left(\frac{\mathrm{d}E}{\mathrm{d}x}\right)_{rad} = \left(\frac{\mathrm{d}E}{\mathrm{d}x}\right)_{coll}. \tag{3.5}$$

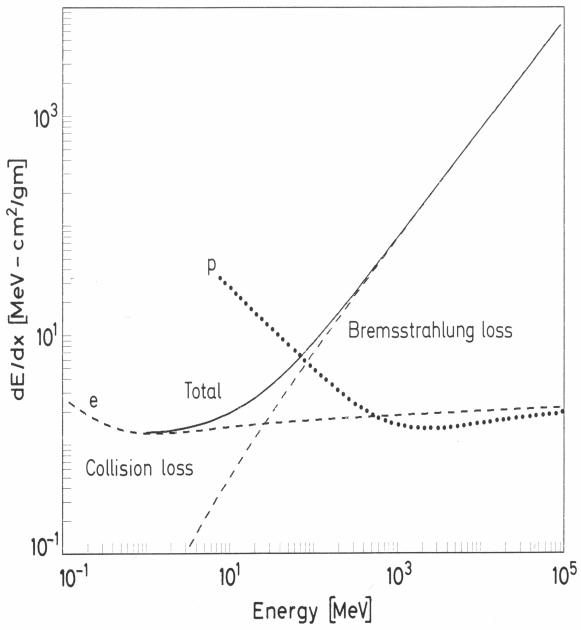

Figure 3.2: Radiation loss vs. collision loss for electrons in copper. For comparison, the $\mathrm{d}E/\mathrm{d}x$ for protons is also shown (dotted line). Figure taken from Ref. [1].

Up to now, discussions were related to the mean energy loss of charged particles traversing a thickness of absorber. This mean value is affected by statistical fluctuations which occur in the number of collisions suffered and in the energy transferred in each collision. According to Ref. [6] and references quoted therein, these fluctuations are characterised by the parameter:

$$\kappa = \frac{\xi}{E_{max}}, \tag{3.6}$$

where

$$\xi = 153.4\ \frac{z^2 Z}{\beta^2 A}\ \rho d \tag{3.7}$$

is the mean energy loss and E_{max} is the maximum energy transferred in an atomic collision:

$$E_{max} = \frac{2m_e\beta^2\gamma^2}{1 + 2\gamma m_e/m + (m_e/m)^2}. \tag{3.8}$$

κ takes into account both the projectile energy and the geometrical thickness of the absorber. Depending on the values of the parameters, the absorbers can be divided into (straggling condition):

a. heavy absorbers ($\kappa > 10$);

b. moderate absorbers ($0.01 < \kappa < 10$);

c. thin absorbers ($\kappa < 0.01$, collision number $N_{coll} > 50$);

d. very thin absorbers ($\kappa < 0.01$, $N_{coll} < 50$).

In cases (a) and (b), the energy straggling is well described by the Gauss and Vavilov distributions, which also allow to calculate the finite variance of energy and inverse momentum:

$$\sigma(E) = \frac{\xi^2}{\kappa}\left(1-\frac{\beta^2}{2}\right) = \xi E_{max}\left(1-\frac{\beta^2}{2}\right), \tag{3.9}$$

$$\sigma\left(\frac{1}{p}\right) = \left[\frac{\mathrm{d}}{\mathrm{d}p}\left(\frac{1}{p}\right)\right]^2 \sigma^2(p) = \frac{1}{p^4}\sigma^2(p) = \frac{E^2}{p^6}\sigma^2(E). \tag{3.10}$$

The cases of thin (c) and very thin (d) absorbers are treated with the Landau and sub-Landau distributions. Because of the δ-electron emission, the tail of the distribution of the energy lost by the particle is very long. This makes the energy straggling variance infinite (for the Landau distribution) or so big (sub-Landau model) that the uncertainty on the track momentum is meaningless; also the full mean of the distributions is infinite.
There is no universally accepted solution to this problem: an option is to use the truncated mean method. It consists in cutting the Landau distribution $f_L(\lambda)$ to an area α, such that:

$$\alpha = \int_{\lambda_{min}}^{\lambda_{max}} f_L(\lambda)\mathrm{d}\lambda, \tag{3.11}$$

where λ is the Landau variable

$$\lambda = \frac{E - E_{med}}{\xi} - 1 + \gamma' - \beta^2 - \ln\kappa, \tag{3.12}$$

with $\gamma' = 0.577215$ being the Euler's constant; $\lambda_{min} \simeq -3.5$. Different choices of λ_{max} correspond to different values of α and of the mean and σ of the energy distribution; for some examples, see Tab. 3.1. For the definition of the λ variable, it is possible to assume $\sigma(E) = \xi\sigma_\alpha$.
The problem of the strong fluctuation of the energy loss due to the long δ-ray tail can be treated also with the Urban distribution [7]. According to this model, the total energy loss in a certain thickness Δx can be expressed as the sum of the excitation and the ionisation energy.

Table 3.1: Results of the integration of the Landau distribution (Eq. (3.11)).

λ_{max}	α	μ	σ_α
11.1	0.90	1.61	2.83
22.4	0.95	2.40	4.23
110	0.99	4.19	10.16
200	0.995	4.82	13.88
256	0.996	5.08	15.76
339	0.997	5.37	18.19
507	0.998	5.78	22.33
1007	0.999	6.48	31.59

First off, let's introduce the excitation macroscopic cross sections Σ_1 and Σ_2 and the ionisation macroscopic cross section Σ_3.

$$\Sigma_i = C\frac{f_i}{E_i}\frac{\ln\left(2m\beta^2\gamma^2/e_i\right)-\beta^2}{\ln\left(2m\beta^2\gamma^2/I\right)-\beta^2}(1-r), \qquad i=1,2 \tag{3.13}$$

where $r = 0.4$, $I = 16Z^{0.9}$ eV and $f_1 = 1 - f_2$, with:

$$f_2 = \begin{cases} 0 & \text{if } Z \leq 2 \\ 2/Z & \text{if } Z > 2. \end{cases} \tag{3.14}$$

e_1 and e_2 are two fixed excitation energies of the model:

$$e_1 = \left(\frac{I}{e_2^{f_2}}\right)^{1/f_1}, \qquad e_2 = 10Z^2 \text{ (eV)}. \tag{3.15}$$

Finally, $C = E_{med}/\Delta x$, being $E_{med} = (\mathrm{d}E/\mathrm{d}x)\cdot\Delta x$, is the energy loss in the absorber with thickness Δx.
Concerning the ionisation macroscopic cross section, it is computed as:

$$\Sigma_3 = C\frac{E_{max}}{I(E_{max}+I)\ln\left((E_{max}+I)/I\right)}r. \tag{3.16}$$

Σ_1, Σ_2 and Σ_3 are such that it is possible to get the total number of collisions from the following relation:

$$N_c = (\Sigma_1+\Sigma_2+\Sigma_3)\cdot\Delta x = N_1+N_2+N_3 \tag{3.17}$$

By defining the excitation energy:

$$E_e = \Sigma_1 e_1 + \Sigma_2 e_2 = N_1 e_1 + N_2 e_2 \tag{3.18}$$

and the energy E_3 lost by δ-electron emission:

$$E_3 = \frac{I(E_{max}+I)}{E_{max}}\frac{1}{E^2}, \quad I < E < (E_{max}+I), \tag{3.19}$$

the total energy loss in a certain thickness Δx is:

$$E = E_e + \Sigma_3 E_3 \Delta x = N_1 e_1 + N_2 e_2 + N_3 E_3. \tag{3.20}$$

In this equation e_1 and e_2 are constants, N_1, N_2 and N_3 are sampled from the Poisson distribution and E_3 is sampled from the δ-ray ionisation energy E_i:

$$E_i = \sum_{j=1}^{N_3} \frac{I}{1 - u(E_{max}/(E_{max} + I))}. \tag{3.21}$$

Also in this case, the tail of the distribution is truncated; if δ is chosen as truncation parameter:

$$\delta = \frac{I(E_{max} + I)}{E_{max}} \int_I^{E_\delta} \frac{1}{E^2} \mathrm{d}E = \frac{(E_{max} + I)}{E_{max}} \frac{E_\delta - I}{E_\delta}, \tag{3.22}$$

representing the considered fraction of the δ-ray energy distribution, then:

$$E_\delta = \frac{I}{1 - \delta E_{max}/(E_{max} + I)}. \tag{3.23}$$

The mean and the variance of the truncated distribution can be calculated:

$$\sigma^2(E) = \langle N_1 \rangle e_1^2 + \langle N_2 \rangle e_2^2 + \langle N_3 \rangle \langle E_3 \rangle^2 + \sigma_\delta^2(E_3) \langle N_3 \rangle, \tag{3.24}$$

where:

$$\begin{aligned} \langle E_3 \rangle &= \frac{I(E_{max} + I)}{E_{max}} \int_I^{E_\delta} \frac{1}{E} \mathrm{d}E = \frac{I(E_{max} + I)}{E_{max}} \ln\left(\frac{E_\delta}{I}\right), \\ \langle E_3^2 \rangle &= \frac{I(E_{max} + I)}{E_{max}} \int_I^{E_\delta} \mathrm{d}E = \frac{I(E_{max} + I)}{E_{max}} (E_\delta - I), \\ \sigma_\delta^2(E_3) &= \langle E_3^2 \rangle - \langle E_3 \rangle^2. \end{aligned} \tag{3.25}$$

The Urban approach is the one that has been used to sample the energy loss in the fast simulation of the single straw tube (see Sec. 3.2.5).

3.1.2 Transport of electrons in gases

3.1.2.1 Thermal diffusion

In the absence of an electric field, the electrons generated in an ionisation event lose their energy very quickly by colliding with the gas molecules, until they reach the thermal equilibrium. According to the classical kinetic theory of gases, the velocity of the charges is described by the Maxwell distribution:

$$v = \sqrt{\frac{8kT}{\pi m}}, \tag{3.26}$$

where k is the Boltzmann constant, T is the absolute temperature and m is the particle mass. The mean value of the thermal energy is:

$$\epsilon_T = \frac{3}{2}kT \simeq 0.04 \text{ eV}. \tag{3.27}$$

If no other effects are present, the electrons diffuse isotropically outward from their point of creation according to a gaussian distribution.
The equation:

$$\frac{\mathrm{d}N}{\mathrm{d}x} = \frac{N_0}{\sqrt{4\pi Dt}} \exp\left(-\frac{x^2}{4Dt}\right) \tag{3.28}$$

describes the fraction of charges dN which is present in the space element dx at a distance x from the origin after a time t. N_0 is the total number of charges and D is the diffusion coefficient:

$$D = \frac{2\epsilon}{3m}\tau = \frac{\epsilon_k}{m}\tau, \tag{3.29}$$

where ϵ is the electronic energy, ϵ_k is the so called characteristic energy ($\epsilon_k = 2\epsilon/3$) and τ is the mean time between collisions. The root mean square of the distribution is given by:

$$\sigma_x = \sqrt{2Dt} \tag{3.30}$$

$$\sigma_V = \sqrt{6Dt} \tag{3.31}$$

in case of a linear or a volumetric diffusion, respectively. This means that an electronic cloud, which is point–like at $t = 0$, at time t will be distributed like a gaussian having a diffusion spread equal to σ_x or σ_V.

3.1.2.2 Drift

When an electric field is present, the electrons and ions start to diffuse anisotropically: the phenomenon can still be described by a Gauss distribution but it is necessary to introduce two different diffusion parameters D_L and D_T, describing the diffusion in the longitudinal and transverse directions, respectively (Fig. 3.3).
The anisotropic diffusion is just one of the effects of the electric field: in fact, electrons and ions start to be accelerated and drift to the anode and the cathode, respectively (Fig. 3.4).
Charge transport and thermal diffusion are now superimposed, so the movement of the charges can be represented as the superposition of the average drift movement, which has a certain velocity, and of the chaotic movement around the average position, which leads to the charge cluster diffusion.
The mean velocity that characterises the drift motion is called drift velocity ($w = x/t$); it is a linear function of the electric field and can be expressed by the Townsend formula:

$$w = \frac{e}{2m}E\tau. \tag{3.32}$$

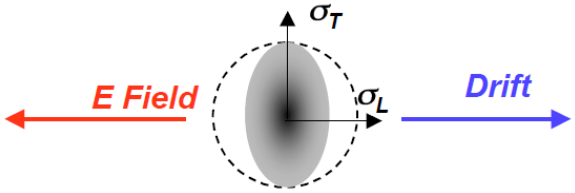

Figure 3.3: If an electric field is present, two diffusion widths are introduced, the longitudinal σ_L and the transverse σ_T ones with respect to the electric field direction. Figure taken from Ref. [4].

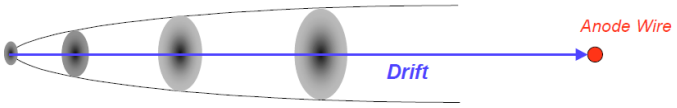

Figure 3.4: The diffusing electron cloud drifts towards the anode wire under the effect of an electric field. Figure taken from Ref. [4].

For electrons, the drift velocity w is of the order of 10^6 cm/s, whereas for ions, since their mass is bigger than the electron one, $w \sim 10^4$ cm/s. In addition, the energy distribution will be no longer described by a Maxwell function and the mean energy value will be higher then the thermal one (Eq. 3.27).
Not only the drift velocity, but also the diffusion coefficient is a function of the electric field. By introducing the mobility:

$$\mu = \frac{w}{E}, \tag{3.33}$$

which is constant for a given gas (at fixed pressure and temperature), the diffusion coefficient becomes:

$$\frac{D}{\mu} = \frac{kT}{e}. \tag{3.34}$$

It is also possible to derive an expression for the diffusion spread σ_x, from Eqs. (3.30) and (3.34):

$$\sigma_x = \sqrt{2Dt} = \sqrt{\frac{2kT}{e}\frac{x}{E}}, \tag{3.35}$$

so it is mass independent, hence it is the same for all ions.
It is interesting to separate two different situations:

- in the case of a weak electric field or a quenching gas mixture, the energy of the electrons produced in the primary ionisation does not increase too much between one collision and the other. In this case, electrons are in thermal equilibrium with the surrounding medium, their energy is comparable with the average thermal energy of $\sim 0.025 - 3$ eV and their

drift velocity is proportional to the intensity of the electric field. Gases that act like this are usually known as "cold" gases for a given electric field strength;

- on the contrary, there are gas mixtures such that the drift velocity saturates and does not depend anymore on the electric field strength and, therefore, on the distance to the straw anode. The advantage is that many sources of systematic errors are removed and the track reconstruction is easier. The disadvantage is that the spatial resolution in the so called "hot" gas mixtures is limited by the large diffusion and cannot be better than ~ 50 μm.

In the presence of a magnetic field, the drift properties change. First of all, the small segment of motion between two subsequent collisions is deflected by the Lorentz force, which is applied to each moving charge: the electrons generated by the passage of a charged particle into the gas spiralize towards the anode, as shown in Fig. 3.5. In particular, the global effect of the magnetic field is to rotate the swarm of an angle θ_B (Lorentz angle) with respect to the direction of the electric field (Fig. 3.6).

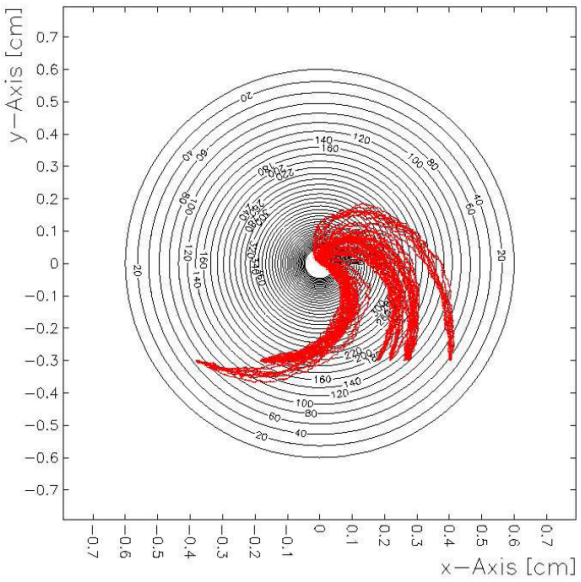

Figure 3.5: The red spots are the trajectories of the electrons inside the straw tube, when both an electric and a magnetic field are present.

By writing the differential equations of motion of an electron moving in a gas with random velocities and subject to crossed fields **E** and **B**, when a suitable averaging is done on the velocities, one finds:

$$\tan\theta_B = \omega\tau_B, \tag{3.36}$$

$$w_B = \frac{E}{B}\frac{\omega\tau_B}{\sqrt{1+\omega^2\tau_B^2}}. \tag{3.37}$$

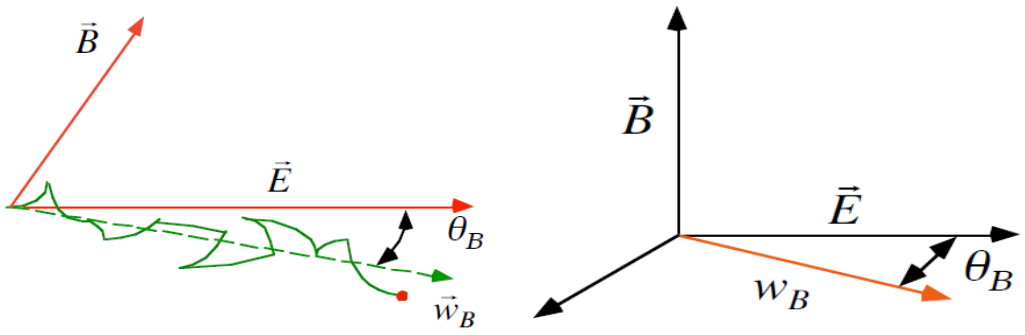

Figure 3.6: Effect of a magnetic field **B** on the drift trajectory. θ_B is the Lorentz's angle. On the right, the electric and magnetic field are orthogonal. Figures taken from [4].

In the previous forumlae, $\omega = eB/m$ is the Larmor frequency, τ_B is the time between subsequent collisions in presence of a magnetic field and w_B is the drift velocity in the case $\mathbf{B} \neq 0$.
The approximation that leads to Eqs. (3.36) and (3.37) consists essentially in assuming that electrons freely move to a time τ_B, then having fully isotropic elastic collisions. Such an averaging is not allowed whenever the electron energy or the collision cross section are strong functions of the electric field; therefore, these two equations describe properly the data only at low values of **E**.
To be precise, τ_B is a function of both the electric and the magnetic field ($\tau_B = \tau_B(\mathbf{E}, \mathbf{B})$) but in this case the approximation $\tau_B = \tau \equiv \tau(\mathbf{E}, \mathbf{B} = \mathbf{0})$ results to be enough accurate. From Eq. (3.32) and the knowledge of the drift velocity at $\mathbf{B} = 0$, τ can be derived.
With this assumption [8], Eqs. (3.36) and (3.37) reduce to:

$$\tan\theta_B = \omega\tau, \tag{3.38}$$

$$w_B = \frac{w}{\sqrt{1+\omega^2\tau^2}}. \tag{3.39}$$

From the previous equations, it is clear that the drift velocity w_B is reduced if compared to the drift velocity w in the absence of the magnetic field.
Finally, the magnetic field has an influence also on the diffusion process: in particular, it modifies the transverse diffusion coefficient, which results to be smaller than $D_T(\mathbf{B} = \mathbf{0})$:

$$\frac{D_T(\mathbf{B})}{D_T(\mathbf{B}=\mathbf{0})} = \frac{1}{1+(\omega\tau)^2}. \tag{3.40}$$

On the contrary, the longitudinal diffusion coefficient does not change:

$$D_L(\mathbf{B}) = D_L(\mathbf{B} = \mathbf{0}). \tag{3.41}$$

3.1.3 Gas amplification

In a region where the electric field is uniform, the kinetic energy of an electron from primary ionisation increases until it is high enough to ionise a gas molecule.
If n is the number of electrons in a certain position, after a distance dx the increase in the electron number is:

$$dn = n\alpha dx, \tag{3.42}$$

where α, known as first Townsend coefficient, is the inverse free mean path (λ) for ionisation, i.e. the number of electron–ion pairs produced in a unitary length. By integrating the previous equation:

$$n = n_0 e^{\alpha x}, \tag{3.43}$$

being n_0 is the number of primary electrons. Hence, the gain or multiplication factor M is given by:

$$M = \frac{n}{n_0} = e^{\alpha x}. \tag{3.44}$$

This formula is valid only if the electric field is uniform; if it is not the case, like in a drift tube, the disuniformity itself allows to reach higher values of the multiplication factor. In this case, $\alpha = \alpha(x)$ and the gain is given by [10]:

$$M = \exp\left(\int_a^x \alpha(x)\mathrm{d}x\right), \tag{3.45}$$

where a is the anode wire radius and the integral is along the whole drift path. It is possible to find a good approximation for M if we determine the region r_{cr} where the avalanche develops. Assuming that the electric field inside the straw depends on r:

$$E(r) = \frac{U_0}{\ln(b/a)r}, \tag{3.46}$$

where U_0 is the anode voltage, a and b are the anode and cathode radii respectively, the average ionisation energy[2] becomes:

$$W_i = eE(r_{cr})\lambda(r_{cr}) = \frac{eU_0}{\ln(b/a)}\frac{\lambda(r_{cr})}{r_{cr}}. \tag{3.47}$$

Hence:

$$r_{cr} = \frac{eU_0\lambda(r_{cr})}{W_i \ln(b/a)}. \tag{3.48}$$

Remembering that $\alpha = \lambda^{-1}$ and taking into account Eq. (3.48), the mean gain can be written as:

$$M = \exp\left(\int_a^{r_{cr}} \frac{\mathrm{d}r}{\lambda(r)}\right). \tag{3.49}$$

[2]The ionisation energy W_i is the energy required to produce one electron–ion pair in the gas. For a $ArCO_2$ (90/10) mixture, $W_i \sim 26.7$ eV.

3.2 Simulation of the physics processes

A detailed simulation of the charge generation and collection in a single straw tube has been implemented in C++ and will be described in detail in this section.

3.2.1 The charge released into the tube

First of all, for each incident particle it is necessary to sample from the exponential distribution the point along the particle trajectory where an electron cluster is generated.
From the sampled number of electrons per cluster and from the number of clusters/cm (Fig. 3.7.a), the number of free electrons generated from a number of clusters is obtained. This number follows the Poisson distribution, whereas the number of clusters/cm is assumed to be 25 for Ar and 35.5 for CO_2 at NTP [3].
In order to perform a reliable simulation, it is crucial to know the cluster size distribution (Fig. 3.7.b), i.e. the number of electrons per cluster: the values used in the simulation are taken from the theoretical calculations for Ar of Ref. [11] and from the experimental data on Ar and CO_2 of Ref. [12].
The comparison with some available results in gas has demonstrated that this choice reasonably agrees with the experimental data, as shown in Fig. 3.8.
The energy lost by the projectile along its whole path (Fig. 3.7.c) is calculated by taking into account the mean value of the energy spent to create an electron–ion pair; the assumed values are 27 eV for Ar and 33.5 eV for CO_2 [3].
A further check has been performed by comparing the energy loss in the tube, for a variety of projectiles and energies, with the Urban model (Sec. 3.1.1.2), which is used in GEANT3 [14] and GEANT4 [15] in the case of gaseous thin absorbers. The experimental results for 1 GeV/c pions traversing 1 cm $ArCO_2$ (90/10) at NTP, reported in Fig. 3.9, show good agreement with the simulation.

3.2.2 The drift process from GARFIELD

The single tube response is simulated in detail by the GARFIELD code [16], which needs as input the tube dimensions, wire radius, high–voltage, gas mixture and magnetic field, since they determine the gas behaviour.
By taking into account all the physics processes that take place in a straw tube when a charged particle traverses it and the properties of the gas mixture ("cold" or "hot") as explained in Sec. 3.1.2.2, GARFIELD is able to derive the drift velocity of the particle. This is shown in Fig. 3.10 as a function of the distance from the wire for different gas mixtures ($ArCO_2$ with different percentages of the CO_2): it is clear that the increase of the CO_2 percentage in Ar tends to cool the gas, with a corresponding stronger dependence of the

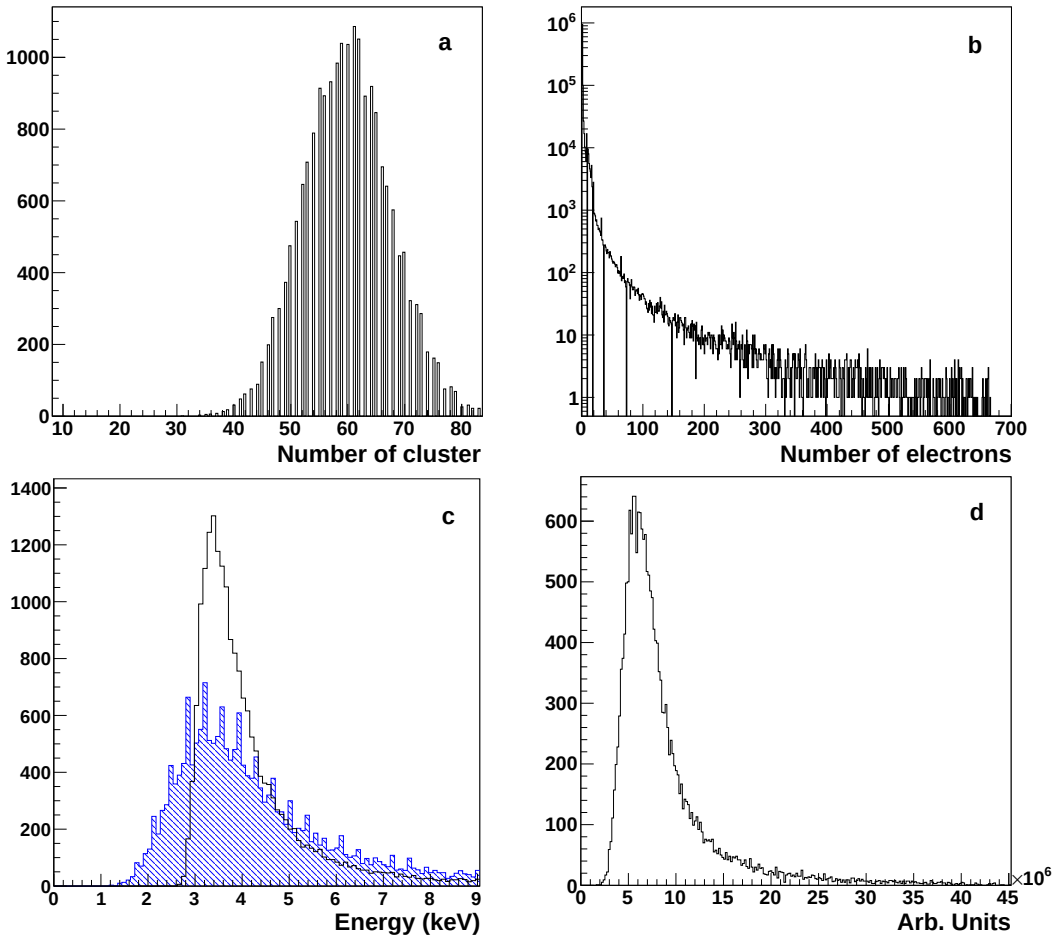

Figure 3.7: Results of the single tube simulation for a 1 GeV/c pion in a 2 atm pressure straw tube with a $ArCO_2$ (90/10) gas mixture. (a) poissonian distribution of the number of clusters; (b) cluster size distribution calculated as discussed in the text; (c) energy loss in a tube (blue dashed histogram) compared with the sharper Landau distribution (black histogram); (d) charge collected on the wire assuming a multiplication mechanism from the Polya distribution. By multiplying the number of clusters with the mean number of electrons per cluster, a number of ionised electrons (from primary and secondary ionisation) of about 200 is obtained.

velocity from the wire distance. This effect could be recovered by an accurate self–calibration (see Sec. 3.2.4); on the other hand, it requires a more precise control of temperature and pressure.
GARFIELD takes also into account the effects induced by electric/magnetic fields on the particles trajectories. Typical time vs. distance curves for the hot $ArCO_2$ (90/10) mixture, with and without magnetic field, are reported in Fig. 3.11, where the increase of the drift time due to the field is evident.
Another important input to the simulation are the transverse and longitudi-

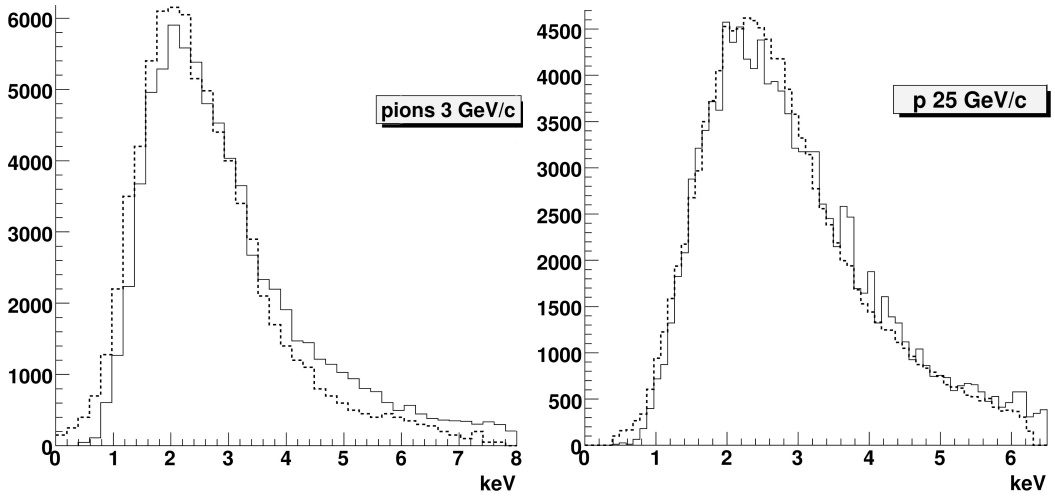

Figure 3.8: Comparison between the simulation of the energy loss in a $ArCO_2$ layer with a thickness of 1.5 cm (full line) and the experimental values reported in Ref. [13] (dotted line).

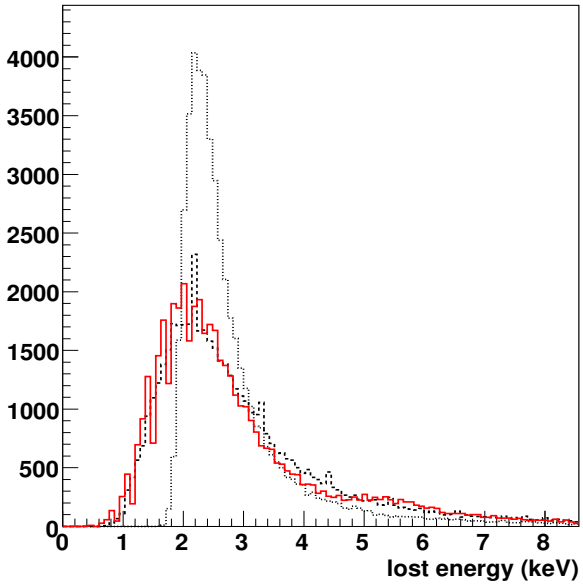

Figure 3.9: Energy loss of a 1 GeV/c pion traversing a 1 cm of $ArCO_2$ (90/10) gas mixture at NTP. Full line: Urban distribution; dashed line: specific simulation model; dotted line: Landau distribution.

nal diffusion curves, due to the thermal spread of the electron clouds during the drift. At this point, since the free electrons have been created at certain positions inside the straw tube, the GARFIELD diffusion curves are used to disperse them both transversally and longitudinally; in addition, the arrival time on the anode is computed by using the distance to time curves.

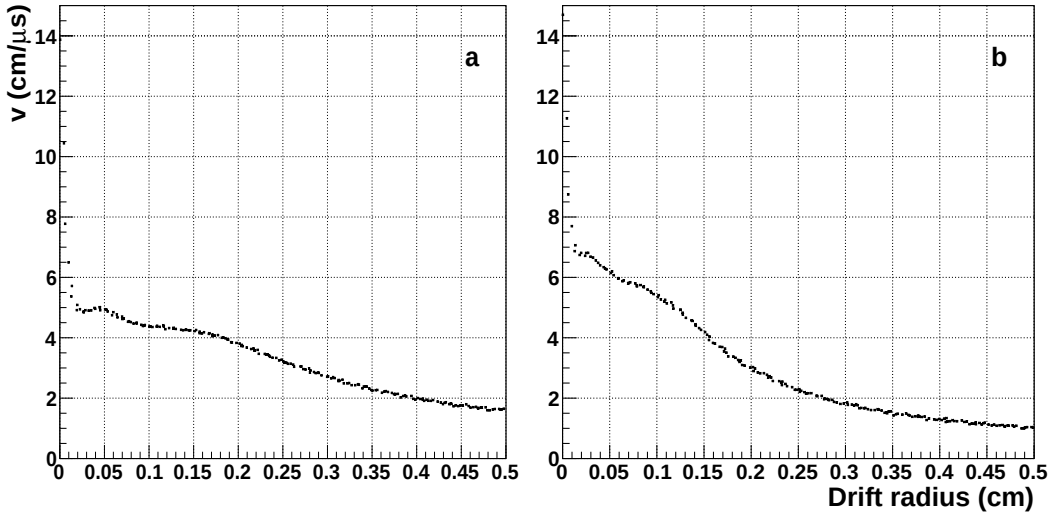

Figure 3.10: Drift velocity vs. wire distance in a straw tube of 0.5 cm radius, operated at 2150 V, 2.2 bar pressure and 2 T magnetic field for different gas mixtures: (a) $ArCO_2$ (90/10), (b) $ArCO_2$ (80/20).

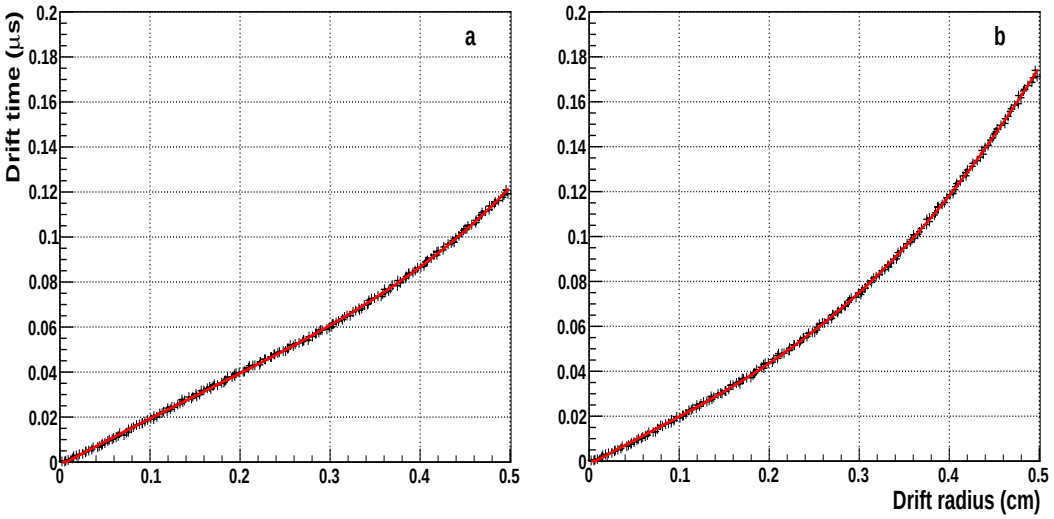

Figure 3.11: Drift time vs. wire distance in a straw tube with 0.5 cm radius filled with $ArCO_2$ (90/10) operating at 2150 V voltage and 2.2 bar pressure: (a) without magnetic field; (b) with magnetic field of 2 T.

Finally, it is also necessary for GARFIELD to know the gas amplification, that is the multiplication factor of the avalanche which is formed within a few wire radii from the wire (Sec. 3.1.3).

3.2.3 The electrical signal

The arrival of the electrons on the anode gives rise to an electric charge: in the simulation, this is obtained by sampling from a Polya distribution having the gain or multiplication factor ($\sim 10^3 - 10^4$) as mean value [10]. Then, by summing the signals generated by all electrons, the total charge is obtained, as shown in Fig. 3.7.d.
It is also possible to reproduce the signal shape by taking into account the electron arrival times and assigning a gaussian–shaped electrical response to each charge multiplication. In addition, in the signal simulation a white noise component equal to 3% of the primary signal peak value has been added.
Some examples are shown in Fig. 3.12, where two typical signals are shown. The first one (left) is generated by a track passing 1 mm far from the wire: in this case, the irregular structure of the signal is due to the dispersed cluster arriving times; in such a case, the choice of the discrimination technique is crucial for a good time resolution. The second signal in the figure (right) is produced by a track going 4 mm far from the wire: the cluster arrival is now more concentrated and the signal structure appears more regular.
These examples show the importance of the electronic treatment of the signal and of the discrimination technique to be used in order to obtain the drift time. Two discrimination techniques have been considered in the simulation: fixed (F) and constant fraction (CF) thresholds. The F threshold is set to $\sim$ 5% of the mean primary electron value, i.e. 10 primary electrons in the 2 bar case (see Fig. 3.7); this is compatible with earlier studies [17, 18]. The CF threshold is set to 5% of the peak value of the current signal.
In the following, if not explicitly specified, the displayed results are obtained with the standard F threshold.

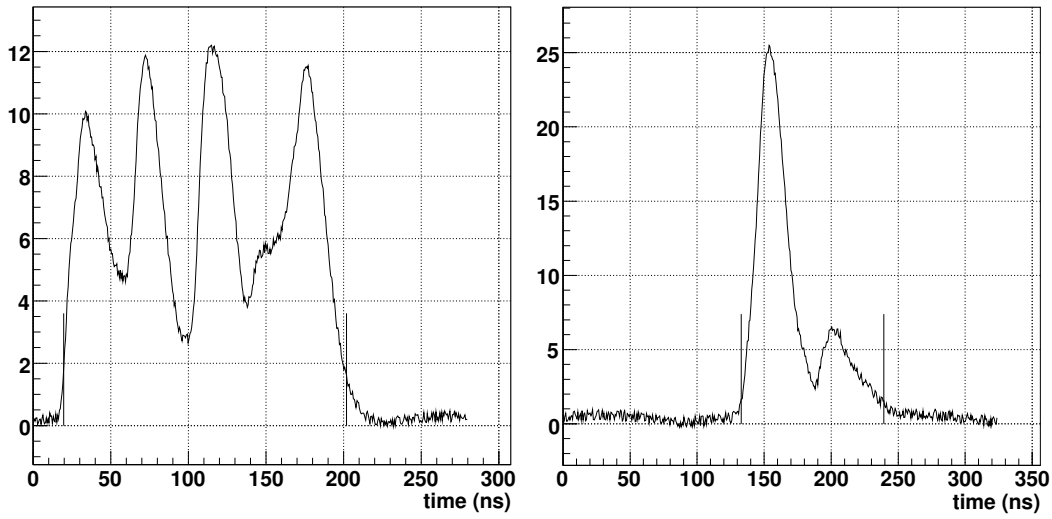

Figure 3.12: Straw tube signals simulated for a track passing near (left) and far (right) from the anode.

3.2.4 Simulation of the self–calibration procedure

The primary information from the tube is the drift time distribution of the arriving signals, that is the number of tracks dn traversing the tube within the time interval dt. A typical drift time distribution, in the case of a parallel and uniform illumination of the tube, is shown in Fig. 3.13 (left).
The self–calibration method has been simulated: it exploits the properties of this distribution.
Since the track density is constant over the tube diameter, it is possible to write:

$$\frac{\mathrm{d}n}{\mathrm{d}r} = \frac{N_{\mathrm{tot}}}{R_{\mathrm{tube}}}, \tag{3.50}$$

where n is the number of tracks, r is the wire distance, N_{tot} is the total number of tracks and R_{tube} the tube radius. The number of tracks in a time interval can be obtained directly from the above relation:

$$\frac{\mathrm{d}n}{\mathrm{d}t} = \frac{\mathrm{d}n}{\mathrm{d}r}\frac{\mathrm{d}r}{\mathrm{d}t} = \frac{N_{\mathrm{tot}}}{R_{\mathrm{tube}}}\frac{\mathrm{d}r}{\mathrm{d}t}. \tag{3.51}$$

By integrating the time spectrum up to t, the space–time relation $r(t)$, shown in Fig. 3.13 (right), is obtained:

$$r(t) = \frac{R_{\mathrm{tube}}}{N_{\mathrm{tot}}}\int_0^t \frac{\mathrm{d}n}{\mathrm{d}t'}\mathrm{d}t'. \tag{3.52}$$

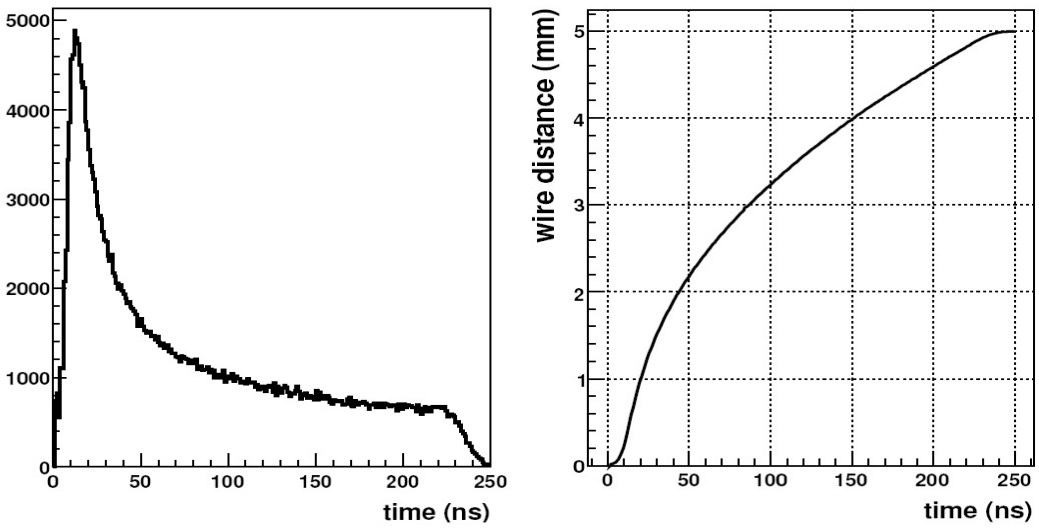

Figure 3.13: Simulation of a typical TDC spectrum of a single tube uniformly illuminated (left) and space–time relation $r(t)$ (right) obtained with the self–calibration method of Eq. (3.52).

After this step, the method requires the correction of the systematic error due to the threshold level, that appears as an offset in the histogram of the

residuals[3] of the reconstructed distance. In the simulation, a time offset t_0 has been adjusted until the mean value of this distribution approaches zero (Fig. 3.14.a).
After applying the time offset correction $(t - t_0)$ to all the measured times of the drift time spectrum, the $r(t)$ curve is corrected and it is possible to proceed with the derivation of the simulated resolution curve. This is usually intended as the standard deviation of the residual distribution as a function of the distance of the track to the wire (drift distance r), as shown in Fig. 3.14.b:

$$\sigma = \sqrt{\frac{\sum (r - \langle r \rangle)^2}{N}}. \tag{3.53}$$

The spatial resolution can also be obtained as the width of the average absolute residuals as a function of the drift distance (Fig. 3.15):

$$\sigma = \frac{\sum |r - \langle r \rangle|}{N}. \tag{3.54}$$

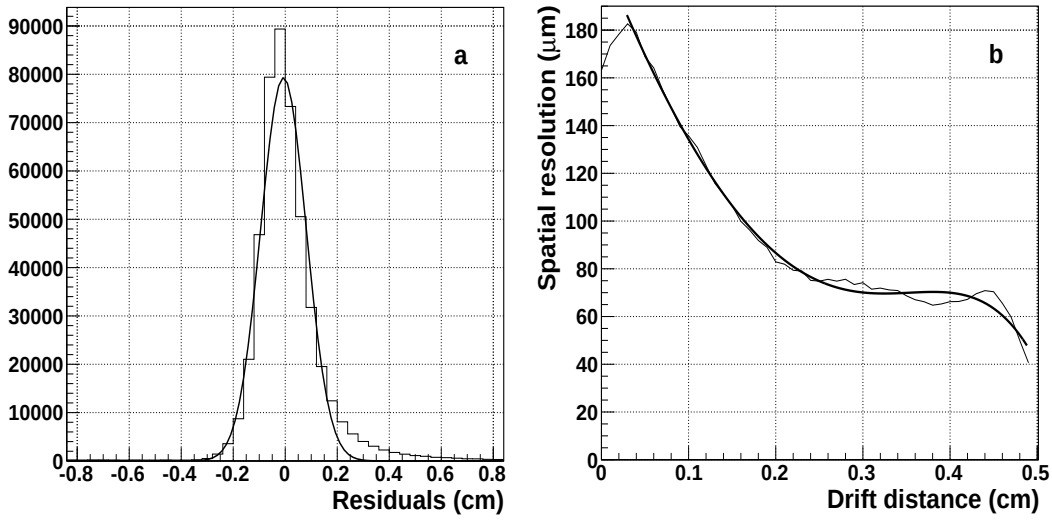

Figure 3.14: Residuals distribution (a) and spatial resolution obtained with Eq. (3.53) (b) after the time offset correction (see text). The bold line in (b) is the smoothing polynomial.

This simulated procedure corresponds, during the real calibration, to have an accurate knowledge of the relationship between the measured drift time and the minimum approach distance of the particle trajectory to the wire. The mean value of the track residuals is then used to correct the measured drift times until the residual distribution is symmetric about zero.

[3]The residuals are calculated as the difference between the reconstructed and true distance.

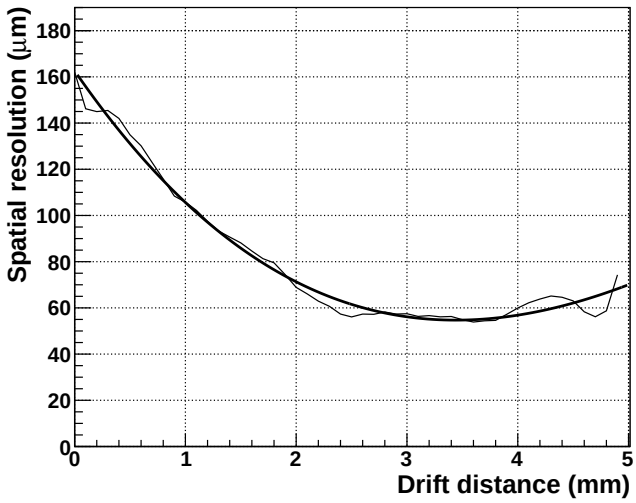

Figure 3.15: Spatial resolution obtained with Eq. (3.54) as a function of the drift distance, in presence of a magnetic field $B = 2$ T.

3.2.5 Full and fast simulation

Two kinds of simulation have been implemented. The first one is called "full" simulation, since it reproduces the time output from the drift tube and the ADC[4] response on the charge collected starting from the primary cluster formation as discussed in the sections above. The inconvenient of this option is that the time required for each event is quite long, so a faster option ("fast" simulation) has been also implemented.
In the second case, the drift radius is determined in a realistic way by sampling from a Gauss distribution having the true wire distance obtained from the MC truth as mean value. The sigma of the distribution is equal to the spatial resolution extracted from Fig. 3.14.b or 3.15 in correspondence of a drift distance equal to the true drift radius.
Concerning the charge collected on the wire, it is simulated by sampling the energy loss from the Urban distribution (see Sec. 3.1.1.2) as in Fig. 3.9, avoiding the charged cluster generation. In this way, the time spent in the tube response simulation results to be negligible when compared with the other part of the software.

[4] Analog–to–Digital Converter.

Bibliography

[1] W.R. Leo, *Techniques for Nuclear and Particle Physics Experiments*, Springer-Verlag, 1987.

[2] F. Sauli (editor), *Instrumentation in High Energy Physics*, Advanced Series on Directions in High Energy Physics – Vol. 9, World Scientific Publishing, 1992.

[3] F. Sauli, *Principles of Multiwire Proportional and Drift Chambers*, CERN 77-09.

[4] F. Sauli, *Gas–filled detectors*, Short Courses 2002 IEEE NSS/MIC, November 2002, Norfolk.

[5] A. Sokolov, *Development of proportional chamber detectors and simulations to measure charm hadrons in antiproton–proton annihilation*, PhD Thesis, Giessen (Germany), July 2005.

[6] A. Rotondi and P. Montagna, Nucl. Instr. and Meth. B 47 (1990) 215-224.

[7] K. Lassilla-Perini and L. Urban, Nucl. Instr. and Meth. A 362 (1995) 416.

[8] A. Breskin, G. Charpak and F. Sauli, Nucl. Instr. and Meth. 124 (1975) 189-214.

[9] A.R.P. Cwetansku and V. Sosnovtsev, *Studies of wire offset effect on gas gain in the ATLAS TRT straw chamber*, ATLAS Internal Note ATL-INDET-016, 2000.

[10] W. Blum, R. Rolandi, *Particle detection with drift chambers*, Springer Velag, Berlin, 1994.

[11] F. Lapique and F. Piuz, Nucl. Instr. and Meth., 175 (1980) 297.

[12] H. Fischle et al., Nucl. Instr. and Meth. A 301 (1991) 202.

[13] J. Alison et al., Nucl. Instr. and Meth., 133 (1976) 325.

[14] GEANT3 manual, CERN Program Library Long Writeup W5013 (1993).

[15] GEANT4 Collaboration, CERN/LHCC 98-44, *GEANT4: An object–oriented toolkit for simulation in HEP*, Geneva, 1998.

[16] R. Veenhof, *GARFIELD, Simulation of gaseous detectors*, Version 7.04, CERN Program library write-up W 5050.

[17] P. Branchini et al., IEEE Trans. on Nucl. Sc., 53 (2006) 317.

[18] W. Riegler et al., Nucl. Instr. and Meth. A 443 (2000) 156.

Chapter 4

Test measurements with the STT prototype in Jülich

In order to develop calibration techniques for the $\overline{\text{P}}$ANDA central Straw Tube Tracker, to understand signal formation, to optimise matching of the straws with the electronics and to investigate the straws response to β particles and the potentiality of the tracker in particle identification based on energy–loss measurements, a laboratory setup has been designed and constructed by the Institut für Kernphysik of the Jülich Research Centre.
A short description of the prototype and of the analysis performed with dedicated algorithms on the collected data, as well as the results obtained, will be presented in detail in this chapter.

4.1 Experimental setup

The setup is shown in Fig. 4.1: it consists of a dense array of 128 $\overline{\text{P}}$ANDA–type straw tubes, arranged in four double–layers of 32 straws each. The tubes, with an aluminised mylar wall 30 μm thick, are 150 cm long and have a diameter of 10 mm; in the centre of the tubes, a 20 μm anode wire is stretched. The tubes can be filled with different gas mixtures, like $ArCO_2$ or ArC_2H_6 (see the detail of the gas manifolds in Fig. 4.2), and can be operated at different conditions of high voltage and pressure.
In addition, a drift chamber with two–dimensional readout for particle tracking, a hybrid drift chamber with a GEM amplification stage for clustering investigations and a small straw tube detector (24 cm long, 4 mm diameter) are included [1]. Finally, two scintillators are placed below the double–layers and used for triggering time to select the signal events when a coincidence occurs.
Half of the channels are equipped with the amplifier–discriminator chip CMP16[1],

[1]The CMP16 board is based on an analog–to–digital converter chip with 16 channels which transforms analog signals to LVDS (Low–voltage Differential Signaling) standard. It

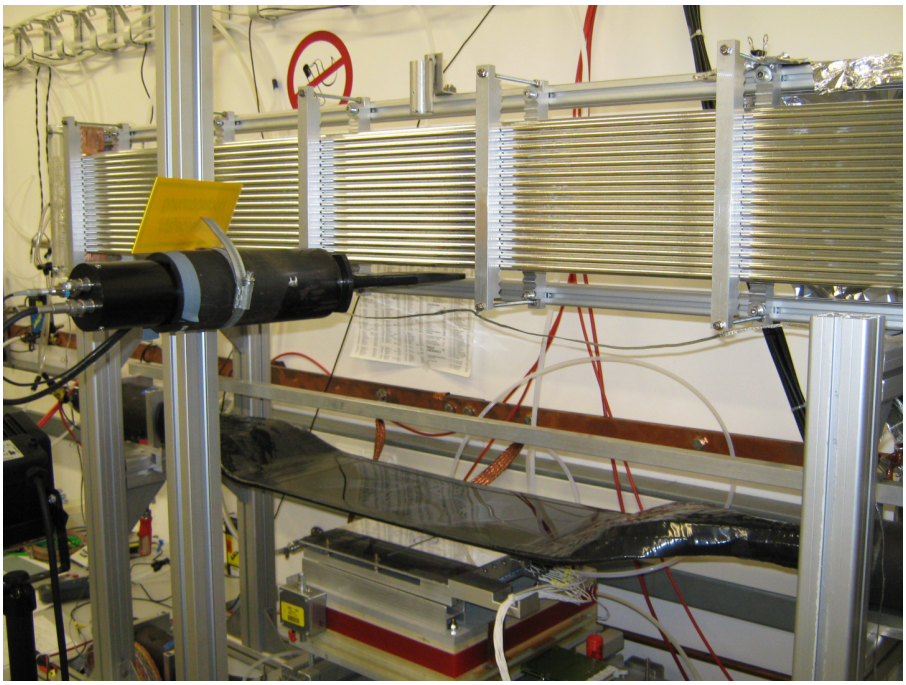

Figure 4.1: Straw tube prototype used at the Institut für Kernphysik at Forschungszentrum-Jülich. Design and construction by IKP-Jülich.

connected with the 64 channels time–to–digital converter based on the F1 TDC chip of the type used at WASA-at-COSY [3].
The anode signals of the other 64 channels are processed by modular fast current amplifiers with 8 ns rise time; thus, individual cluster or groups of few overlapping clusters created along the ionised track became visible in the signal structure.
The flash charge–to–digital converters FQDC analyse signals in terms of charge and pulse–height and disentangle signals into components originating from ionised clusters or groups of clusters in gaseous detectors.
The FPGA[2] controlling the readout of the QDC module are programmed for high flexibilty to permit also total readout in the "oscilloscope mode" and to record single spectra in a self triggering mode for calibration measurements with Fe-55 β^+ sources. In view of the limited number of oscilloscope channels several amplifiers were fed via analog OR into the oscilloscope and then the data were transferred to a computer.
The actual number of firing straws in each event can be deduced from a multiplicity signal delivered by the 8-channel discriminator [4].

can run at very high speed at reduced electromagnetic noise. The transfer characteristics of the amplification and discrimination are presented in [2].

[2]Field Programmable Gate Array.

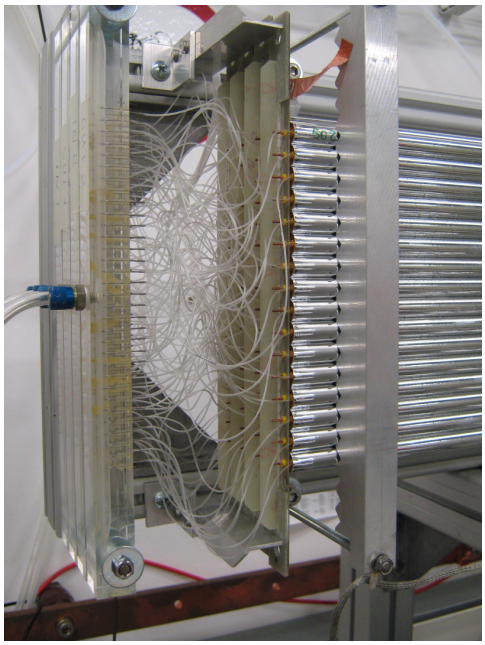

Figure 4.2: Detail of the prototype shown in Fig. 4.1.

4.2 Event samples

As already mentioned in the previous section, the prototype has been operated with $ArCO_2$ (90/10) or ArC_2H_6 (80/20), at different conditions of high voltage (from 1.5 to 1.8 kV) and absolute pressure (from 1.3 to 2 bar).
Data have been mainly recorded from cosmics events; in addition, some measurements have been performed with radioactive sources, like Sr-90 and Fe-55, in order to study the possibility to perform particle identification by dE/dx measurements.

Since the Straw Tube Tracker of the $\overline{\text{P}}$ANDA experiment will be operated with $ArCO_2$ at 1 bar overpressure, data sets from the prototype under the same conditions have been studied. In the following, detailed results will be presented for data collected at 1.7 kV; then, they will be compared with the results obtained at 1.8 kV.

4.3 Straw tube calibration

4.3.1 Fit of TDC spectra

Fig. 4.3 shows an example of the time spectrum of a uniformly illuminated tube. In this figure, time is expressed in TDC counts and runs from right to left. In order to get the time spectrum, TDC counts are converted into seconds, taking into account that one channel corresponds to 130 ps, and time

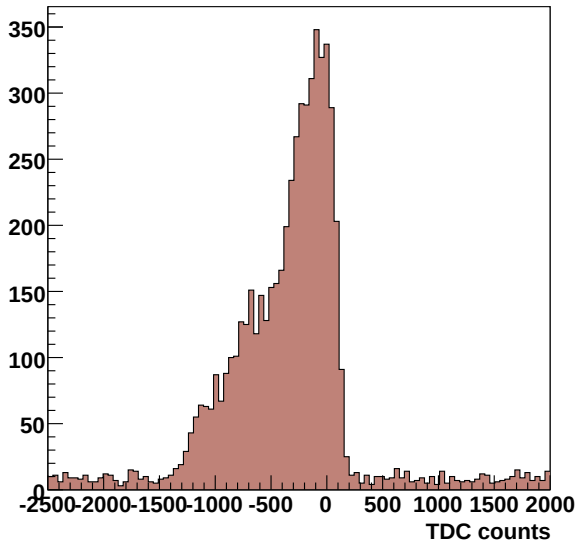

Figure 4.3: Example of a raw TDC spectrum. On the x axis, the time is expressed in TDC counts and runs from right to left.

is reversed; finally, the spectrum shown in Fig. 4.4 is obtained.
The analysis of the individual tube time distributions allows the monitoring of the data quality: the minimum and the maximum drift times, t_0 and t_{max}, correspond to a track traversing the tube close to the wire and to the cathode wall, respectively. The value of t_0 depends on delays of the signal cables and front–end electronics as well as on discriminator threshold and HV setting. Nearby tubes sharing the same front–end electronics are expected to have very similar values of t_0; on the contrary, the drift time $\Delta t = t_{max} - t_0$ depends only on the drift properties of the tubes. The number of events outside the drift time window gives an estimate of the random, constant noise level over time range (Fig. 4.3) [5].
For each tube, the parameters of the drift time distribution are derived from a fit performed with the following empirical function [5, 6, 7]:

$$\frac{\mathrm{d}n}{\mathrm{d}t} = P_1 + \frac{P_2\,[1 + P_3 \exp((P_5 - t)/P_4)]}{[1 + \exp((P_5 - t)/P_7)]\,[1 + \exp((t - P_6)/P_8)]}, \tag{4.1}$$

where P_1 is the noise level, P_2 is a normalisation factor, P_3 and P_4 are related to the shape of the distribution, P_5 and P_6 are the values of t_0 and t_{max}. P_7 and P_8 describe the slope of the leading and trailing edge of the distribution, so they are indicators of the drift tube resolution close to the wire and to the tube wall, respectively. In Fig. 4.4 the fit function is also shown (green line).
In order to do a unique calibration for all the tubes, their time spectra must have approximately the same shape and the same drift time Δt. A quality check on the uniformity of the tubes, as well as on the quality of the fit, was done by looking at the distributions of the parameters of the fits, shown in Fig. 4.5. Only the tubes satisfying the following conditions were considered:

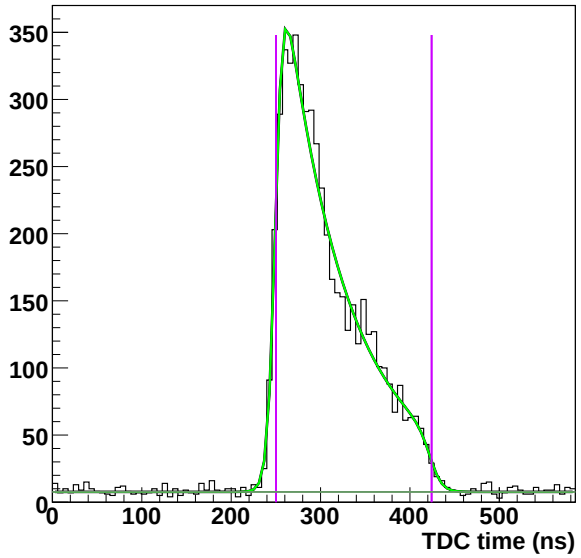

Figure 4.4: Example of a fitted TDC spectrum. The light green line is the fit of the distribution; the violet vertical lines correspond to the t_0 and t_{max} values determined by the fit. The dark green horizontal line indicates the noise level.

a. noise level $P_1 < 4$ Hz;

b. $P_3 < 15$ ns;

c. 30 ns $\leq P_4 \leq$ 120 ns;

d. 240 ns $\leq t_0(P_5) \leq$ 265 ns;

e. 380 ns $\leq t_{max}(P_6) \leq$ 440 ns;

f. 140 ns $\leq \Delta t \leq$180 ns;

g. risetime 2 ns $\leq P_7 \leq$ 6 ns;

h. χ^2/NDF < 5.

4.3.2 *r(t)* calibration curve

After this selection, all the spectra of the chosen tubes were corrected by their specific time offset t_0 and their noise level was subtracted; then, they were added into a sum spectrum, each in its Δt range.
Under the hypothesis of a uniform illumination of the tube and a constant efficiency over the tube volume, the isochrone radius – drift time relation ($r(t)$ relation in the following) already presented in Chap. 3 can be obtained

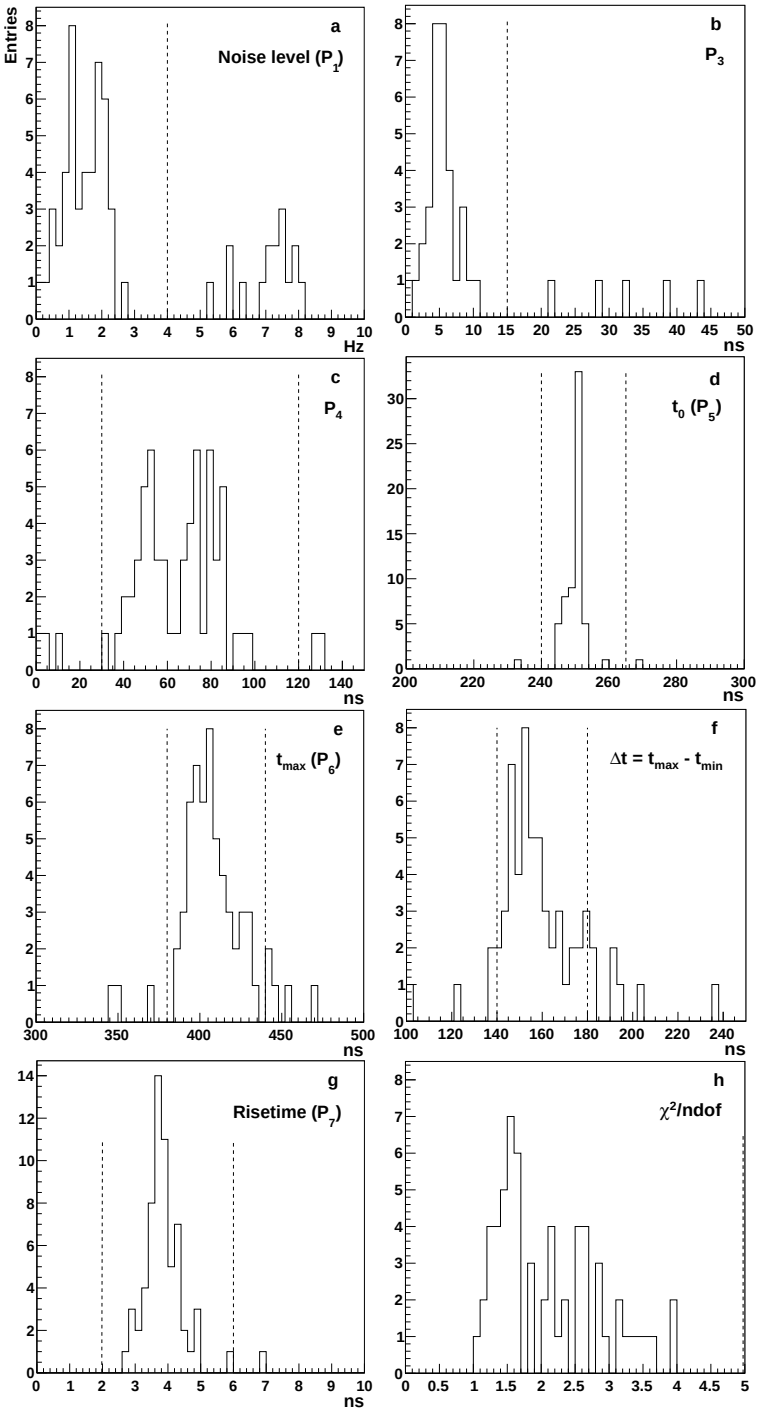

Figure 4.5: Parameters obtained from the fit of the drift time spectra: (a) noise level P_1, (b and c) the two parameters (P_3 and P_4) that describe the shape of the spectra, (d) t_0 (P_5) and (e) t_{max} (P_6), (f) $\Delta t = t_{max} - t_0$, (g) risetime of the leading edge P_7 and (h) the reduced χ^2 of the fit. The dashed lines mark the cuts applied to the parameters (see text).

(Eq. (3.52)). In particular, taking into account the finite TDC resolution (bin size) and the wire radius R_{wire}, it becomes:

$$r(t_i) = \frac{\sum_{i=1}^{i_t} N_i}{N_{tot}} \cdot (R_{tube} - R_{wire}) + R_{wire}. \tag{4.2}$$

R_{tube} and R_{wire} are the tube and wire radii, respectively; N_{tot} is the sum of all bin entries N_i.
The obtained space–time relation $r(t)$ is shown in Fig. 4.6.

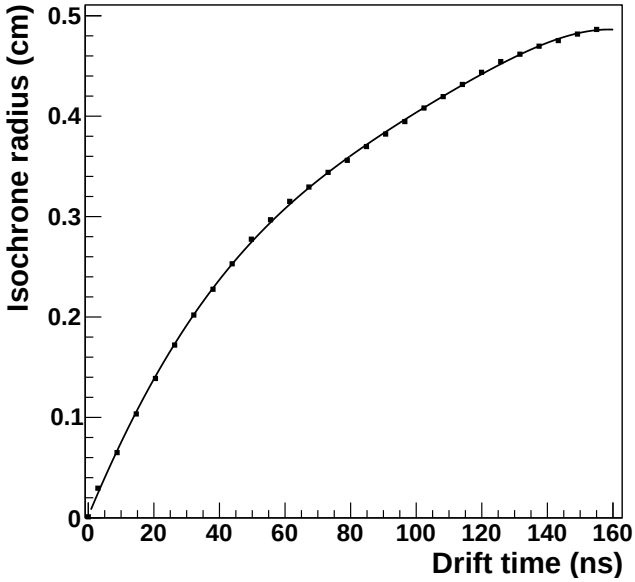

Figure 4.6: Isochrones radius – drift time relation ($r(t)$), parametrised using a combination of Chebyshev polynomials of the first kind, up to the fifth order.

It has been parameterised using a combination of Chebyshev polynomials of the first kind up to the fifth order:[3]

$$r(t) = p_0 + p_1 t + p_2(2t^2-1) + p_3(4t^3-3t) + p_4(8t^4-8t^2+1) + p_5(16t^5-20t^3+5t). \tag{4.4}$$

Once the space–time relation is known, the isochrone radius of a certain tube is computed by substituting in Eq. (4.4) the measured drift time. This is calculated by subtracting from the measured drift "raw" time the time offset t_0 of that tube, obtained from the fit of Eq. (4.1).

[3]The Chebyshev polynomials of the first kind are defined by the recurrence relation:

$$\begin{aligned} T_0(x) &= 1, \\ T_1(x) &= x, \\ T_{n+1}(x) &= 2xT_n(x) - T_{n-1}(x). \end{aligned} \tag{4.3}$$

4.4 Autocalibration

Once the calibration curve has been derived, it is possible to proceed with the track reconstruction.
In order to perform a good track fitting, it is necessary to know with high precision the relation between the measured drift time and the distance of closest approach of the particle trajectory to the wire. This implies an accurate knowledge of the $r(t)$ relation, that can be achieved with an iterative procedure called **autocalibration**, since it makes use just of the information from the tubes under investigation.
The autocalibration works as follows: at each step of the procedure, the $r(t)$ relation derived in the previous iteration is used to convert the measured drift times into drift radii, that will be used in the track fitting. At the first step, the $r(t)$ relation obtained directly from the integration of the drift time spectra (Sec. 4.3.2) is used.
Once a track candidate has been identified (Sec. 4.4.1), the track is reconstructed through the steps described in Sec. 4.4.2 and the best fit line with parameters a and b is found.
For each tube of the pattern associated with a track, the residuals $\Delta r^i = r^i_{fit}(a,b) - r^i_{raw}$ (Eq. (4.15)) are then computed and represented as a function of the N bins the drift time interval is divided into.
If the $r(t)$ relation was exact, the average residuals would be zero at all radii; deviations from zero mean miscalibrations in the $r(t)$ relation, which is then directly corrected by using the average deviations themselves.
This procedure is iterated until the corrections become less and less relevant; at this point, the $r(t)$ relation has converged to a stable and "optimal" solution.
The effects of the autocalibration procedure will be shown in Sec. 4.4.3.
In the following, the steps performed at each iteration will be analysed in detail.

4.4.1 Pattern recognition

Since the events under study were generated by cosmic rays and we were not so interested in the reconstruction efficiency but in the resolution, as a first approximation only the events with one track can be considered.
In order to identify these events, a first cut has been applied on the number of hits: since the prototype consists of layers with 16 tubes each, the maximum possible number of hits generated by a single track is 32, in case of a vertical track hitting all the tubes of two adjacent layers. Events with more than 32 hits have been rejected, since they are produced in cosmic showers or they come from electronic noise.
In this way, "good" events are selected; nevertheless, they might contain also "spurious" hits generated by secondary particles or due to the electronic noise: these hits can be eliminated by applying further cuts, as described in the following.

4.4.2 Track reconstruction

The observables measured by the straw tubes are not the (x, y) coordinates of the particle hits, but the (x, y) coordinates of the firing wires and the drift times. From these information, the (x, y) hit coordinates need to be extracted. To do this, the track fitting procedure is performed through several steps; they are:

1. a *pre-prefit*;
2. a *prefit* using Minuit [8];
3. the *Intersection Finder*;
4. a *refit*, using again a Minuit minimisation.

4.4.2.1 Pre-prefit

The **pre-prefit** step has been introduced in order to give Minuit the input parameters it requires to be initialised.
For each track, it is performed over the centers of the N firing tubes (i.e. the wires positions (x_i, y_i)). It consists in the minimisation of the perpendicular distance of these points from the best fit line $y = a + bx$ (Fig. 4.7).

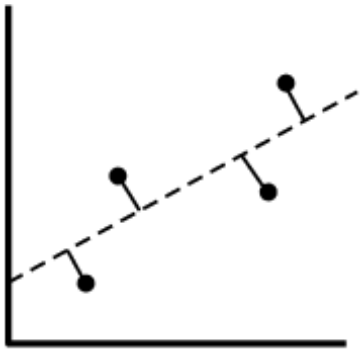

Figure 4.7: Perpendicular distances to be minimised in the pre-prefit.

The function to be minimised in the pre-prefit is:

$$R_{\perp} = \sum_{i=1}^{N} d_i \tag{4.5}$$

where d_i is the distance of the centre of the tube with coordinates (x_i, y_i) to the prefit line $y = a + bx$:

$$d_i = \frac{|y_i - (a + bx_i)|}{\sqrt{1 + b^2}}. \tag{4.6}$$

The sum is over the N hits belonging to the considered track.
Since the absolute value of the function in Eq. (4.5) does not have continuous derivatives, minimising $R_\perp$ is not amenable to an analytic solution; the square of the perpendicular distance $R_\perp^2$ is minimised instead:

$$R_\perp^2 = \sum_{i=1}^{N} d_i^2 = \sum_{i=1}^{N} \frac{[y_i - (a + bx_i)]^2}{1 + b^2}. \tag{4.7}$$

The minimisation of Eq. (4.7) can be solved in closed form [9]. $R_\perp^2$ has a minimum when:

$$\frac{\partial R_\perp^2}{\partial a} = \frac{2}{1 + b^2} \sum_{i=1}^{N} (a + bx_i - y_i) = 0 \tag{4.8}$$

and

$$\frac{\partial R_\perp^2}{\partial b} = \frac{2}{1 + b^2} \sum_{i=1}^{N} [y_i - (a + bx_i)](-x_i) + \sum_{i=1}^{N} \frac{[y_i - (a + bx_i)]^2(-1)(2b)}{(1 + b^2)^2} = 0. \tag{4.9}$$

After a bit of algebra, the result is:

$$b^2 + \frac{\sum_{i=1}^{N} y_i^2 - \sum_{i=1}^{N} x_i^2 + \frac{1}{N}\left[\left(\sum_{i=1}^{N} x_i\right)^2 - \left(\sum_{i=1}^{N} y_i\right)^2\right]}{\frac{1}{N}\sum_{i=1}^{N} x_i \sum_{i=1}^{N} y_i - \sum_{i=1}^{N} x_i y_i} b - 1 = 0. \tag{4.10}$$

By defining:

$$B = \frac{1}{2} \frac{S_{xx} - S_{yy}}{S_{xy}} \tag{4.11}$$

where

$$\begin{aligned} S_{xx} &= \sum_{i=1}^{N} x_i^2 - N\overline{x}^2, \\ S_{yy} &= \sum_{i=1}^{N} y_i^2 - N\overline{y}^2, \\ S_{xy} &= \sum_{i=1}^{N} x_i y_i - N\overline{xy}, \end{aligned}$$

the quadratic formula of Eq. (4.10) gives:

$$b = -B \pm \sqrt{B^2 + 1}. \tag{4.12}$$

a is then found by using:

$$a = \overline{y} - b\overline{x}. \tag{4.13}$$

From Eq. (4.12) we get two track hypotheses: the closest to the experimental points is chosen (Fig. 4.8).

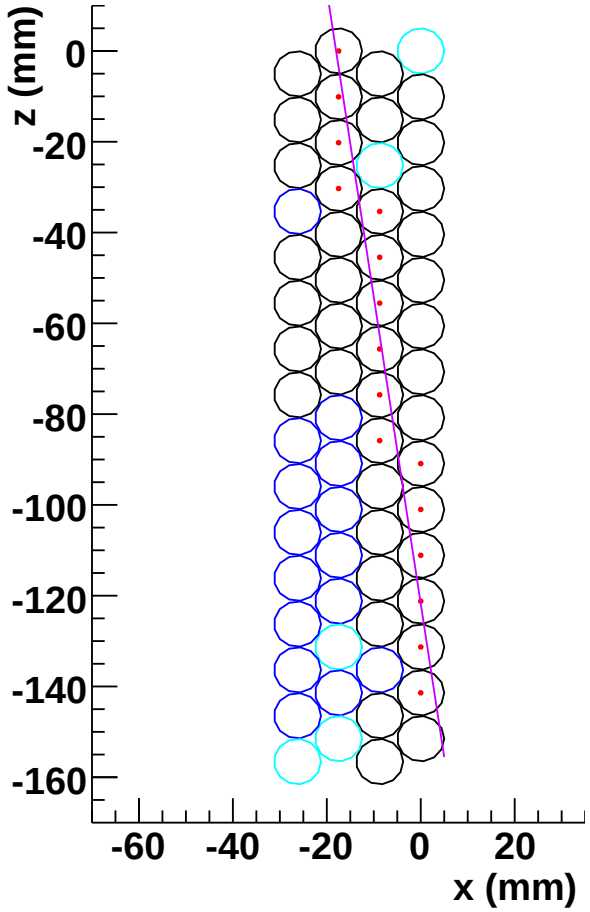

Figure 4.8: In this figure, the pre-prefit line (violet) is drawn; the red dots are the centers of the firing tubes. The cyan and the blue tubes are excluded from the calibration and the track reconstruction, because they are noisy (cyan) or their drift time spectra do not fulfill the requirements in Sec. 4.3.1.

After the pre-prefit, a first cut is applied to check the quality of the events: event by event, the distances of each hit to the pre-prefit line are computed and mediated over the number of hits of that event; if the mean distance is larger than 5 mm, the event is identified as noisy and is rejected. This cut value has been chosen in order for the cut to be very loose, so that not too many events are eliminated in this first step of the analysis: in fact, 5 mm is $\sim$ 20 times the mean distance to the pre-prefit line of the hits belonging to one event.
In addition, another cut on the single hits is applied: for each hit of an event, the distance to the pre-prefit line is computed with Eq. (4.6). If this distance is larger than 0.9 cm ($\sim$ 40 times the mean distance of the single hits to the pre-prefit line), that hit is rejected and the pre-prefit step is performed again with $N - 1$ hits.

4.4.2.2 Prefit

The parameters a and b found in the pre-prefit are then used as starting parameters for Minuit. The function to be minimised in order to find the best fit solution is [10]:

$$\chi^2 = \frac{1}{N-2}\sum_{i=1}^{N}\left(\frac{\Delta r_i(a,b)}{\sigma_{r_{i,raw}}}\right)^2, \tag{4.14}$$

where Δr_i is the residual of the i^{th} tube, defined as:

$$\Delta r_i = r_{i,fit}(a,b) - r_{i,raw} = \frac{|y_i - (a+bx_i)|}{\sqrt{1+b^2}} - r_{i,raw}. \tag{4.15}$$

In this equation, $r_{i,fit}$ is the distance of closest approach of the best fit line found in the previous step to the centre of tube i. $r_{i,raw}$ indicates the radius computed using the $r(t)$ relation with the corresponding measured drift time t^i_{drift} (Eq. (4.4)). $\sigma_{r_{i,raw}}$ is the error associated to the drift radius and is calculated with the sixth order polynomial that fits the experimental data (filled box symbols) of Fig. 4.9. This figure shows the spatial resolution of single straws of the Straw Tracker of the COSY–TOF experiment [11], and it has been used in the prefit as starting input resolution.
Notice that the Minuit minimisation in a and b is non–linear because of the term $\sqrt{1+b^2}$ in the denominator of Eq. (4.15).
If the Minuit fit is successfull, we get a new track hypothesis: the green line in Fig. 4.10.
After the prefit step, another check on the goodness of the hits is performed: for each event, the residuals of Eq. (4.15) are calculated for each hit belonging to the track. If $\Delta r_i > 0.2$ cm, the hit is rejected and the prefit is repeated without that spurious hit.
Fig. 4.11 shows an example of prefit repeated once a hit (or more than one hit) has been identified as not generated by the primary particle along its path through the straw tube. The black line in the figure is the new track hypothesis, obtained by excluding from the fit the tubes considered as not belonging to the track pattern (the ones with the red drift circles). Only the dark green circles have been used for the tracking.

4.4.2.3 Intersection Finder

After the Minuit fit, we can look for the real track points on the drift radii. This step is called **intersection finder**.
To better explain the coordinates finding procedure, let's consider only one tube: up to now, the coordinates (x_i, y_i) of its wire are known, as well as the drift radius r_{drift} (the red circles in Fig. 4.12) and a first guess of the best fit line (the green line in the figure).
The perpendicular to the prefit line passing through the wire coordinates (black dotted lines) intercepts the drift circumference in two points: the closest to the

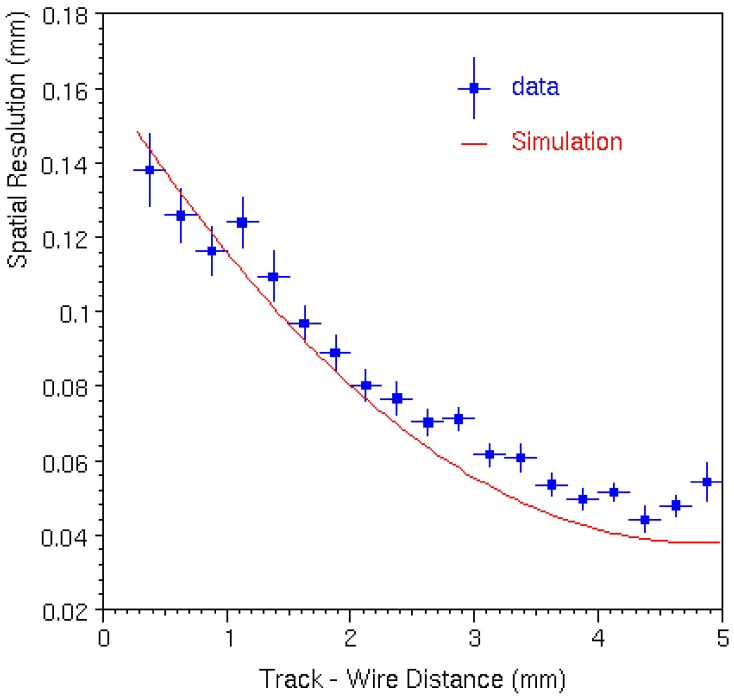

Figure 4.9: Spatial resolution σ_r of single straws obtained from the COSY–TOF experiment [10]. The data (filled box symbols) include a track reconstruction using at least 4 straws. The simulation (line) describes tracks through a single straw, based on the GARFIELD program package [12].

prefit line is chosen and set to be the (x, y) hit of the track (blue markers). The same procedure is repeated for all the track points and a refit can be performed over the new found points.

4.4.2.4 Refit

Once the "real" point coordinates where the track passed are known, they can be used to perform a **refit**. It is done again with Minuit, which has to minimise the following χ^2:

$$\chi^2 = \sum_{i=1}^{N_{hits}} \frac{d_i^2}{\sigma_{d_i,tot}^2}, \tag{4.16}$$

where

$$d_i^2 = \left[\frac{y_i - (a + bx_i)}{\sqrt{1+b^2}} \right]^2 \tag{4.17}$$

is now the distance of closest approach of the track point (x_i, y_i) to the prefit line. (x_i, y_i) are the points on the drift circles found in the intersection finder step.

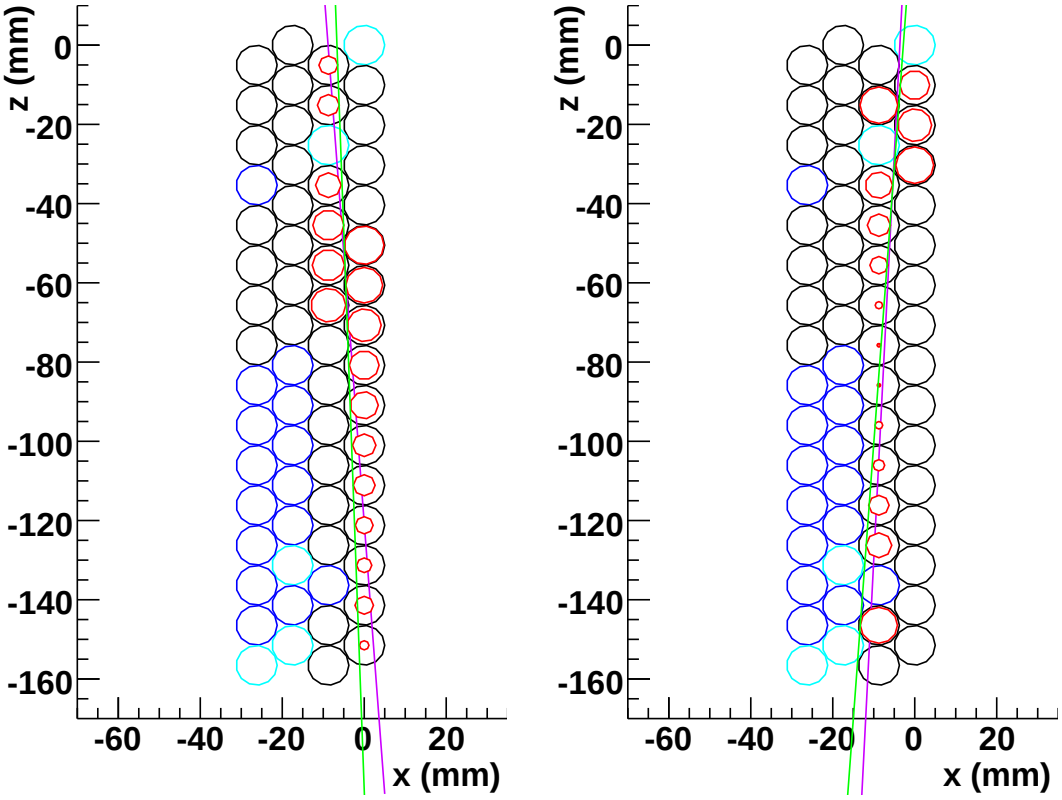

Figure 4.10: In this figure, the pre-prefit (violet) and prefit (green) lines are drawn. The red circles are the drift circles. The cyan and the blue tubes are excluded from the calibration and the track reconstruction (see Fig. 4.8).

Both x_i and y_i are affected by an error; the combination of the two gives the total error $\sigma_{d_i,tot}$ of d_i, associated to each track point:

$$\sigma^2_{d_i,tot} = \frac{\sigma^2_{i,y}}{1+b^2} + \frac{b^2\sigma^2_{i,x}}{1+b^2}. \tag{4.18}$$

$\sigma_{i,x}$ and $\sigma_{i,y}$ are the projections of the error on the drift radius σ_r onto the two axes:

$$\sigma_{i,x} = \sigma_{r,i}\cos\alpha = \frac{\sigma_{i,r}}{\sqrt{1+b^2}}, \tag{4.19}$$

$$\sigma_{i,y} = \sigma_{i,r}\sin\alpha = \frac{b\sigma_{i,r}}{\sqrt{1+b^2}}. \tag{4.20}$$

In these two equations, $\alpha = \arctan b$, being b the angular coefficient of the fitting line found in the prefit step. So:

$$\sigma^2_{d_i,tot} = \frac{2b^2\sigma^2_{i,r}}{(1+b^2)^2}. \tag{4.21}$$

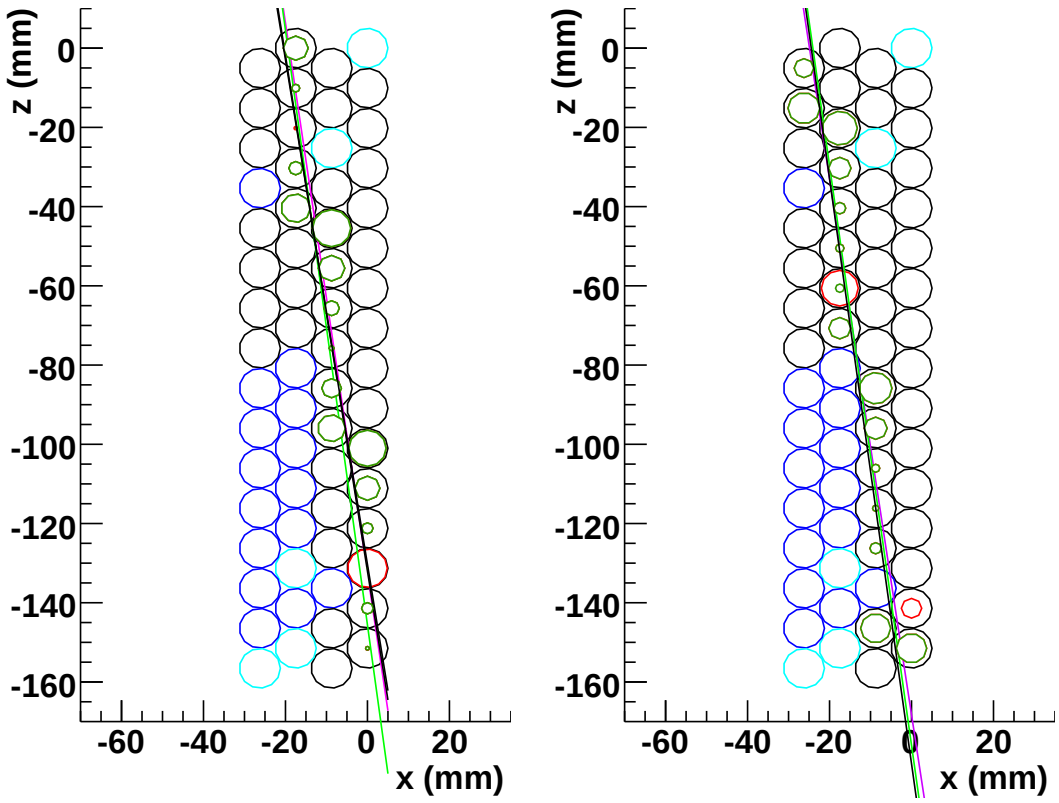

Figure 4.11: In this figure, the pre-prefit (violet) and the prefit (green) lines are drawn. The black line is the track hypothesis obtained by performing the tracking without the hits identified as spurious; for this fit, the red drift circles are excluded and only the dark green ones are considered. (For the cyan and blues tubes, the same considerations of the previous figures are valid.)

With these arrangements, the χ^2 Minuit has to minimise is the following:

$$\chi^2 = \frac{1+b^2}{2b^2} \sum_{i=1}^{N} \frac{[y_i - (a + bx_i)]^2}{\sigma_{i,r}^2}. \tag{4.22}$$

The reason for this refit is that the function in Eq. (4.14) is not the sum of standard gaussian variables, as a standard χ^2 should be:

$$\chi^2 = \sum_i \frac{(x_i - \mu)^2}{\sigma_i^2}. \tag{4.23}$$

First off, this is due to the presence of the parameter b in the denominator; then, the variable Δr_i is not a linear function of the two coordinates (x_i, y_i). On the other side, the quantity in Eq. (4.22) is closer to a standard χ^2 than the one in Eq. (4.14); nevertheless, the presence of the term $(1 + b^2)/2b^2$ requires a non linear minimisation in this case too.
The choice to perform the refit is justified by the results obtained.

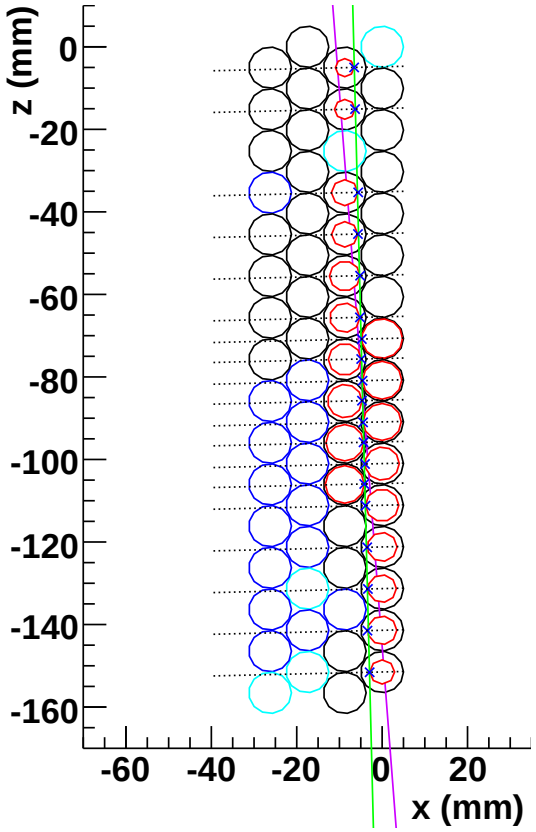

Figure 4.12: In this figure, the pre-prefit (violet) and the prefit (green) lines are drawn; the red circles are the drift circles. For each firing tube, the black dotted line goes through the centre of the tube and is perpendicular to the prefit line. The blue marker indicates the (x, y) coordinates of the intersection point closest to the prefit line and chosen as hit after the procedure.

In Fig. 4.13, the mean residual distributions obtained at the first iteration when performing the prefit (a) and the refit (b) are shown: they are very similar. In addition, no improvements from prefit to refit are evident in the parameters of the two gaussians fitting each distribution and reported in the statistic boxes of the figure (in particular: p_3, p_4, p_5 in (a) and p_0, p_1, p_2 in (b) are the parameters of the Gauss curves that fit the peaks of the distributions). Different remarks concern the resolution curves of Fig. 4.14 (they will be described in detail in Sec. 4.5.1 and 4.5.2): they are very similar in the whole drift distance except for the region close to the wire (drift distance smaller than 1 mm), where the resolution values obtained by performing both the prefit and the refit are better. Hence it has been chosen to perform both the prefit and the refit.
Once the refit is done, the final best fit line (represented by the blue line in Fig. 4.15) is obtained.
At this point, another cut on single hits is applied in order to exclude the ones

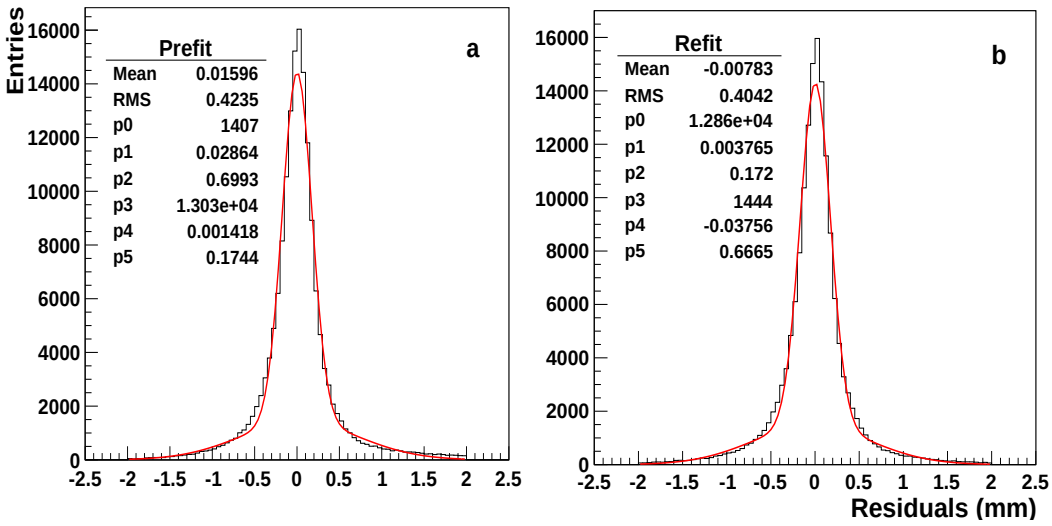

Figure 4.13: Comparison of the mean residual distributions obtained at the first iteration by performing only the prefit (a) and also the refit (b). Each distribution has been fitted with two Gauss functions; the fit parameters are reported in the statistic boxes: the parameters of the gaussian that fits the peak of the distributions are p_3, p_4, p_5 in (a) and p_0, p_1, p_2 in (b).

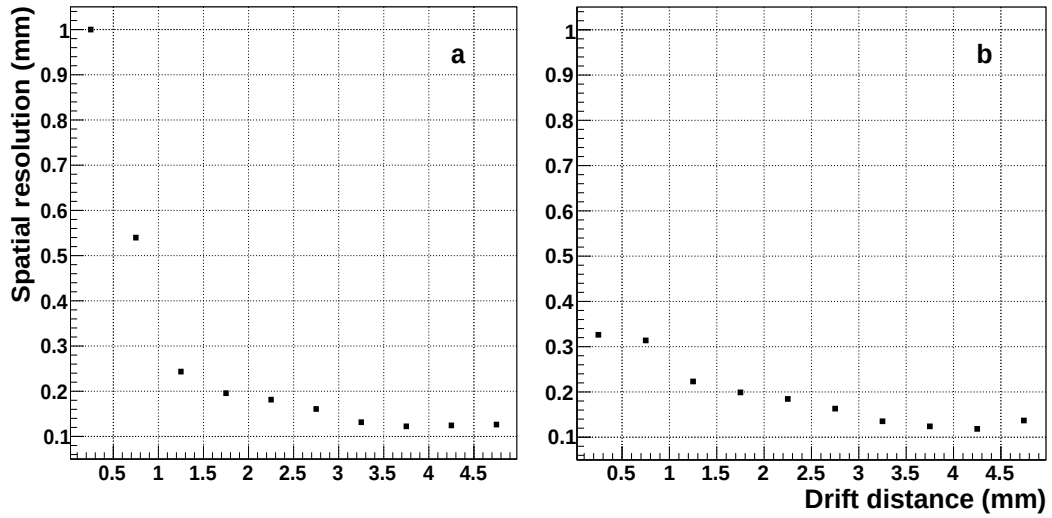

Figure 4.14: Comparison of the spatial resolution curves obtained at the sixth iteration by performing only the prefit (a) and also the refit (b).

produced by δ electrons. For each event, the residual (Eq. (4.15)) of the single hit is computed: if it is larger than 0.2 cm ($\sim$ 10 times the σ of the mean residual distribution, see Fig. 4.13), the hit is rejected.
The refit step is performed again on the remaining hits and a new track hypothesis is found.

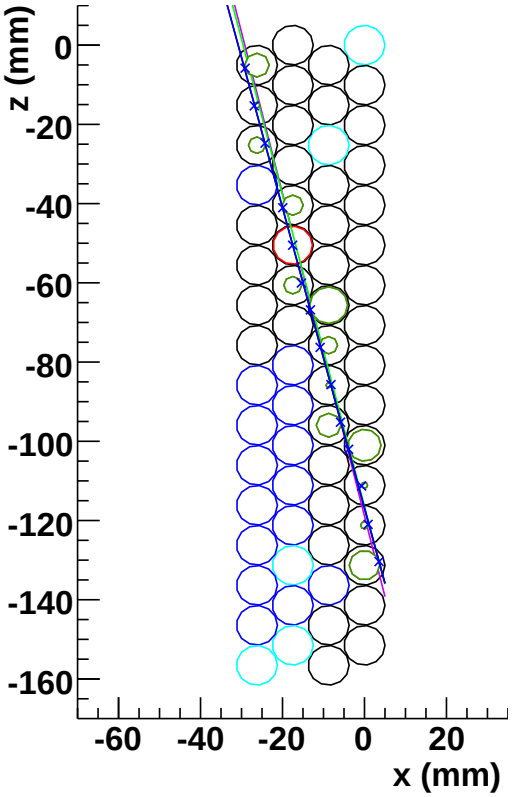

Figure 4.15: In this figure, the pre-prefit (violet), the prefit (green) and the refit (blue) lines are drawn. The dark green circles are the drift circles used for the fit; the red ones are excluded since they are identified as belonging to spurious hits. The blue markers are the space points on the drift circles.

4.4.3 $r(t)$ recalibration

Once the track has been reconstructed and the parameters a and b of the best fit line are known, it is possible to compute the residuals for each hit belonging to the track, as in Eq. (4.15).
Fig. 4.16.a shows the distribution of the residuals and Fig. 4.16.b their mean value as a function of the drift time after the first iteration. At this step, the mean values of the residuals vary from a minimum of $\sim$ -160 μm to a maximum of $\sim$ 320 μm for small radii: these deviations mean that there are miscalibrations in the *r(t)* curve. The mean values of the residuals are then used to correct the $r(t)$ relation of order 0.
The track reconstruction and the $r(t)$ recalibration by means of the residuals are then repeated until the mean values of the residuals become closer to 0, as shown in Fig. 4.17.
To study the speed and stability of the convergence of the method, the mean

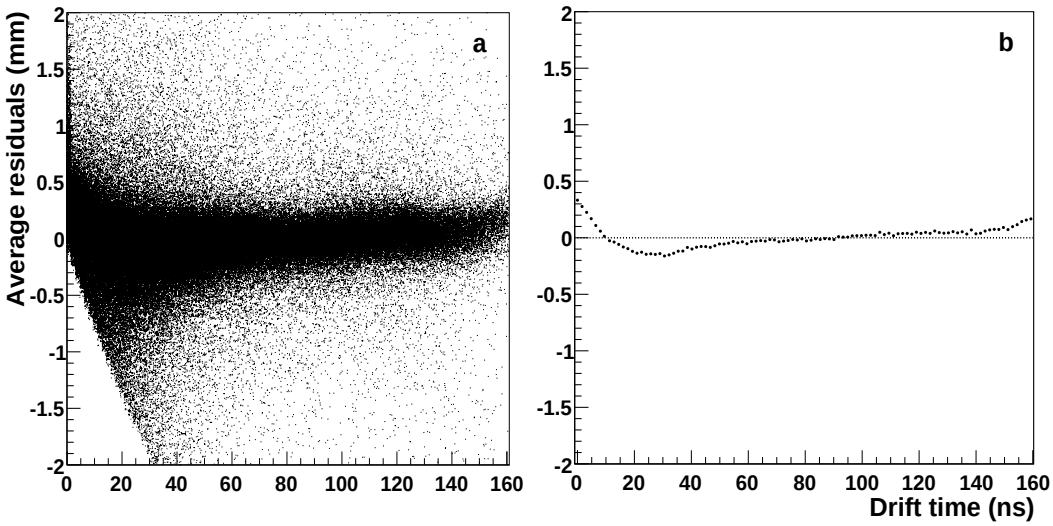

Figure 4.16: Distribution of the average residuals as a function of the drift time at the first iteration.

square correction

$$\Delta_k^2 = \frac{\sum_{i=0}^{N} \delta_{ik}^2}{N}, \tag{4.24}$$

where δ_{ik} is the mean value of the residuals in the i^{th} time bin and N is the total number of bins, is used as figure of merit.
Fig. 4.18 shows the behaviour of Δ_k as a function of the number of iterations: after 5 iterations, Δ_k has converged to a value of about 19 μm.

4.5 Results

4.5.1 Spatial resolution

Fig. 4.19 shows the distribution of the mean residuals of 162385 straw hits after the sixth iteration of the autocalibration procedure. It has been fitted with two Gauss functions, in order to better describe both the peak and the tails of the distribution. The parameters of the fits are reported in the statistics box in figure: the first three refer to the Gauss function that fits the tails of the distribution, the other three refer to the one that fits the peak.
The distribution of the residuals is highly symmetric around a mean of about 14 μm (parameter p_4 of the fit), indicating no systematic errors. The deviation σ of about 177 μm (parameter p_5 of the fit) is a measure of the mean spatial resolution of a single straw. This value is in agreement with the resolution curve of a single tube as a function of the drift distance shown in Fig. 4.20.
It has been obtained in the following way: the track to wire distance has been

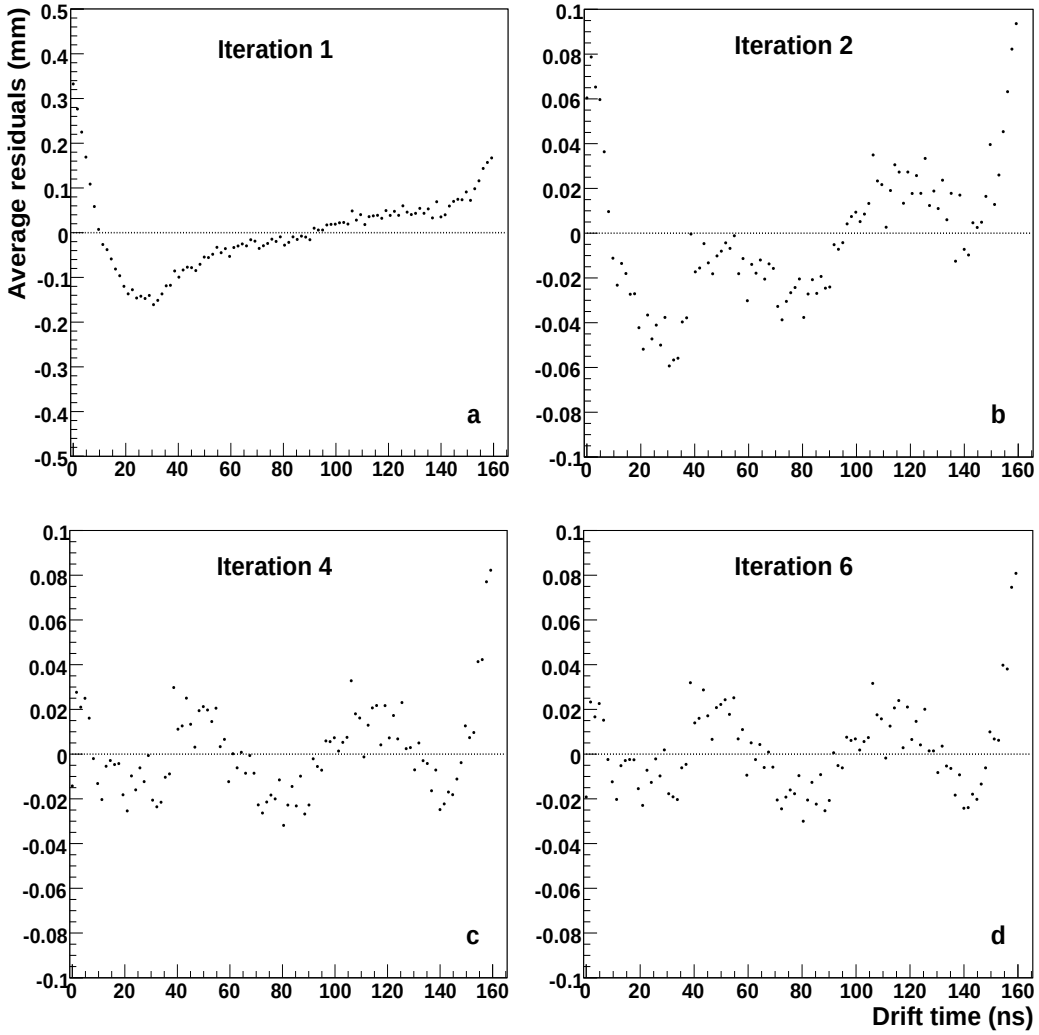

Figure 4.17: Distribution of the average residuals as a function of the drift time after one (a), two (b), four (c) and six (d) iterations of the autocalibration procedure.

divided into ten intervals of 0.5 mm each, from 0 to 5 mm. For each interval, the residual distribution has been obtained and fitted with two functions: a Gauss function for the peak and a third order polynomial for the tails for the first four intervals of distance; the fit has been performed with two Gauss functions for the remaining distance intervals. An example of residual distribution for one interval is shown in Fig. 4.21.
The values of σ of each Gauss function that fits the peaks of the residual distributions has been then used to derive the single tube resolution shown in Fig. 4.20.
This resolution curve is a factor 2 worse than the resolution curve for a single tube obtained by the COSY–TOF experiment (Fig. 4.9). This is mainly due to

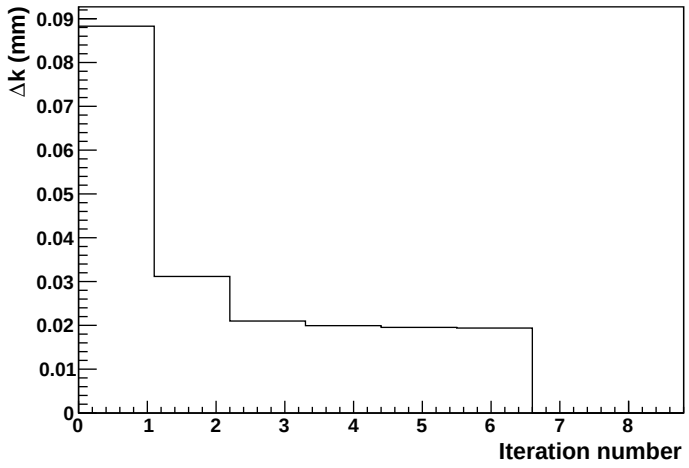

Figure 4.18: Root mean square correction from the autocalibration procedure.

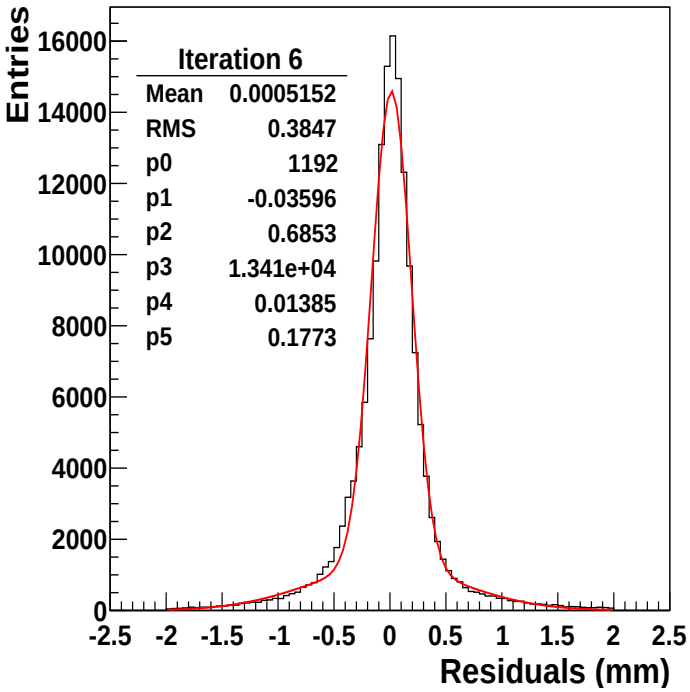

Figure 4.19: Distribution of the mean residuals after the sixth iteration of the autocalibration procedure. The parameters of the fit (red curve) are in the box: p_0, p_1 and p_2 are referred to the fit of the distribution tails; p_3, p_4 and p_5 are the parameters of the Gauss function that fits the peak.

the fact that the electronics of the prototype was a standard readout which did not have the best time resolution. Therefore, by using a dedicated electronics a better single tube resolution could be achieved.

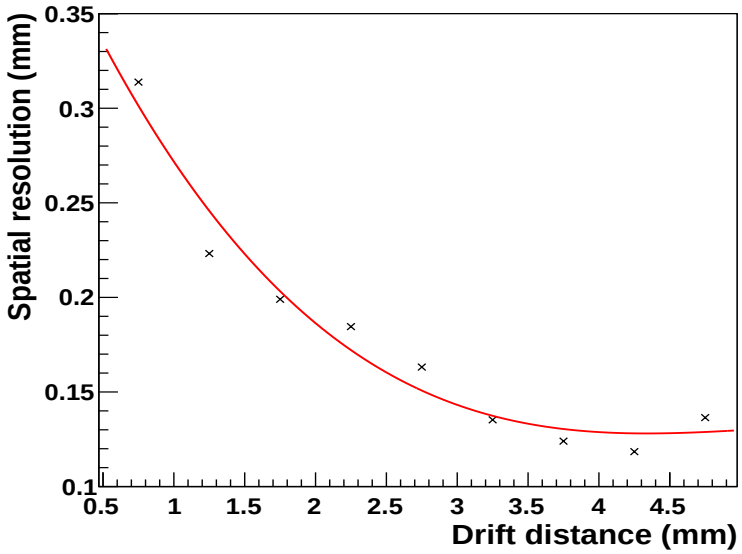

Figure 4.20: Mean spatial resolution σ for single tubes, obtained as explained in the text. The red line is the fit with a third order polynomial. (Picture analogous to Fig. 4.14, with different scales on the x and y axis.)

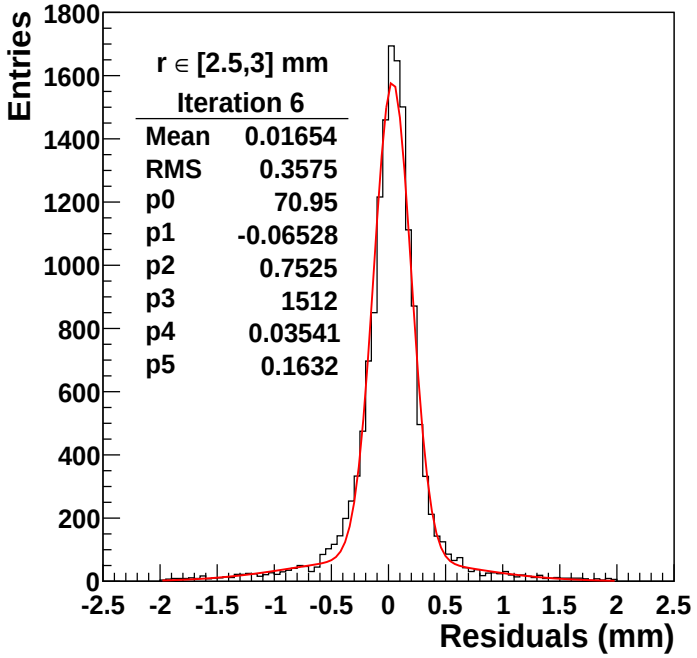

Figure 4.21: Distribution of the residuals for r in the range [2.5, 3] mm at the last step of the autocalibration. The distribution has been fitted with two Gauss functions; the parameters of the fit are in the box (p_3, p_4 and p_5 are the ones of the Gauss function that fits the peak).

4.5.2 Single tube resolution

The single tube resolution as a function of the drift distance obtained in the way previously described is "biased", since the tube whose resolution we are studying has not been excluded from the tracking. In addition, the errors on the parameters of the best fit line have not been subtracted.
In order to calculate the "unbiased" spatial resolution σ of a single tube, another method has been implemented and used. First off, tracks with $N \geq 16$ hits have been selected and fitted using $N-1$ space points. Then, the distribution of the residuals for the tube excluded from the fit has been computed as a function of the drift distance (see Fig. 4.22).

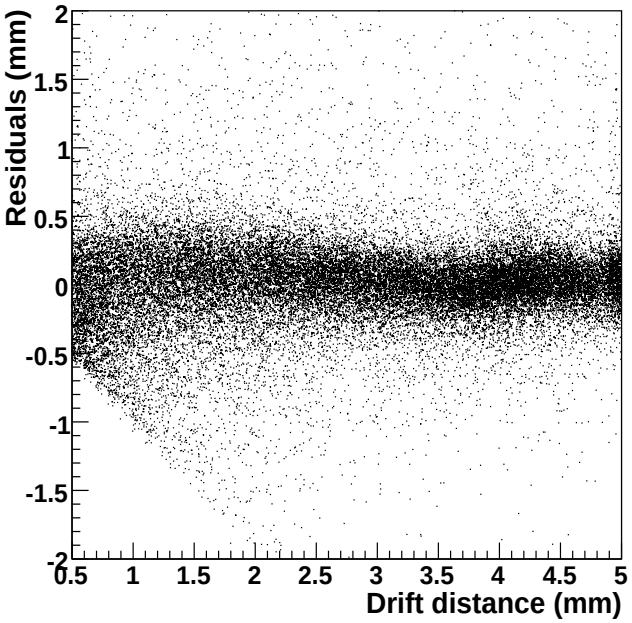

Figure 4.22: Residuals vs. drift distance.

This distribution is the convolution of the resolution of the tube and the track extrapolation errors, due to the fit. In fact, both the intercept a and the slope b of the best fit line are affected by an error σ_a and σ_b, respectively given by the covariance matrix of the Minuit fit in the refit step:

$$\begin{pmatrix} \sigma_a^2 & \sigma_{ab}^2 \\ \sigma_{ba}^2 & \sigma_b^2 \end{pmatrix}.$$

The element $\rho \doteq \sigma_{ab}^2$ is the correlation term between the parameters a and b of the fit.
So the error on the distance of each point (x, y) to the best fit line (Eq. (4.6)) can be computed as follows:

$$\sigma_d^2 = \left(\frac{\partial d}{\partial a}\right)^2 \sigma_a^2 + \left(\frac{\partial d}{\partial b}\right)^2 \sigma_b^2 + 2\rho \frac{\partial d}{\partial a}\frac{\partial d}{\partial b} \tag{4.25}$$

where

$$\frac{\partial d}{\partial a} = -\frac{1}{\sqrt{1+b^2}}, \tag{4.26}$$

$$\frac{\partial d}{\partial b} = -\frac{x+by-ab}{(1+b^2)^{3/2}}. \tag{4.27}$$

In order to disentangle the intrinsic resolution of the tube from the other contribution, we have proceeded in the following way.
First off, the distribution of Fig. 4.22 has been sliced in ten intervals of 0.5 mm each. For each of them, the residual distributions have been fitted with two Gauss functions, as in Fig. 4.23, and the mean value of σ_d has been calculated with Eq. (4.25), using all the space points belonging to that interval. Then, interval by interval, the obtained mean value of the error on the distance σ_d has been quadratically subtracted to the σ of the Gauss functions that fit the residual distribution of that interval.
The obtained values of σ are the ones used for the single tube spatial resolution, shown in Fig. 4.24.

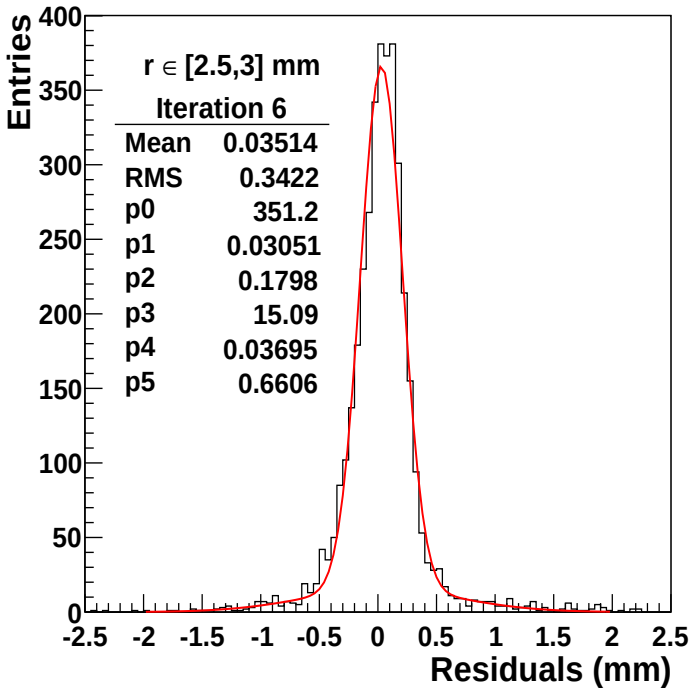

Figure 4.23: Distribution of the residuals for r in the range [2.5, 3] mm after the sixth iteration of the autocalibration, in case the hit tube is taken out from the track reconstruction (it is the analogous of Fig. 4.21). The distribution has been fitted with two gaussians; the parameters of the fit are in the box (p_0, p_1 and p_2 are the ones of the gaussian that fits the peak).

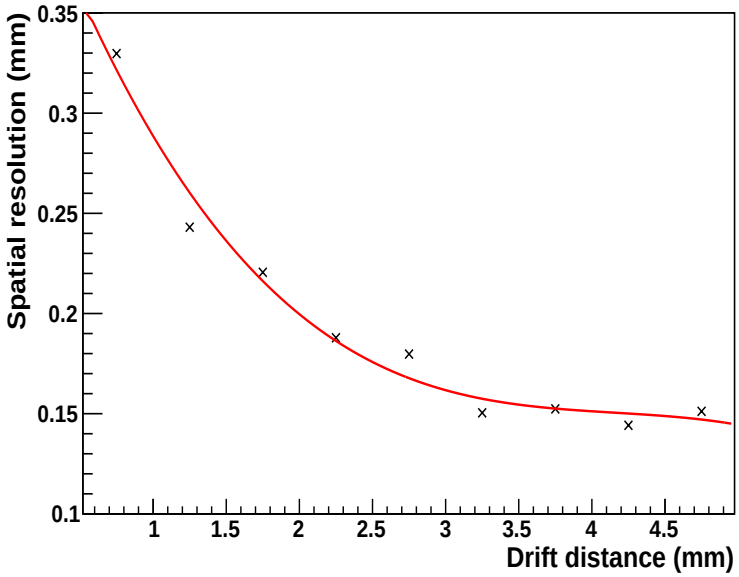

Figure 4.24: Single tube spatial resolution σ as a function of the drift distance.

4.5.3 Contribution of tubes mispositioning to spatial resolution

The resolution shown in the previous paragraph is the sum of two contributions:

$$\sigma^2_{overall} = \sigma^2_{cal} + \sigma^2_{pos}, \tag{4.28}$$

where σ_{cal} contains the contribution of the calibration but also of the electronic time measurements, primary ionisation cluster effect and gas diffusion effect and σ_{pos} is due to the wire mispositioning ($\simeq$ 50 μm). In the following, it is explained how the last contribution has been estimated.
For each track, all the tubes have been taken out from the track reconstruction one by one and the distribution of the residuals (Eq. (4.15)) of the single tubes has been computed. Fig. 4.25 shows two examples of residual distributions for two tubes: (a) tube 3 in layer 0 and (b) tube 7 in layer 2. The mean value of each histogram is a measure of the mispositioning of the single straws: if the wire positions were correct, the distributions should be centered around 0. As it is clear from Fig. 4.25.a, it does not always happen: in particular, in this case, the mispositioning ranges from few micrometers to more than 150 μm. The displacements from 0 are taken into account with their sign, meaning that the wires are shifted to the right and to the left with respect to their nominal positions.
To have an idea of the mean position error, the distributions of the residuals for each tube have been fitted with two Gauss functions and the mean values of the one that fits the peak have been reported in Fig. 4.26.a: the mean wire deviation is about 14 μm, which is negligible. This is in agreement with the

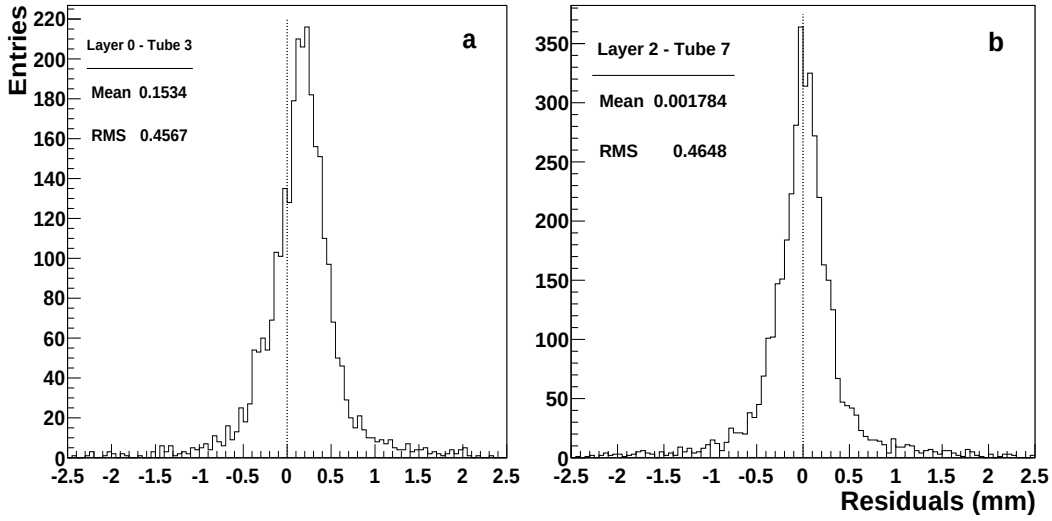

Figure 4.25: Examples of residual distributions for single tubes, which have been taken out from track reconstruction: (a) tube 3 in layer 0 and (b) tube 7 in layer 2. The distributions should be centered around 0 (dotted line).

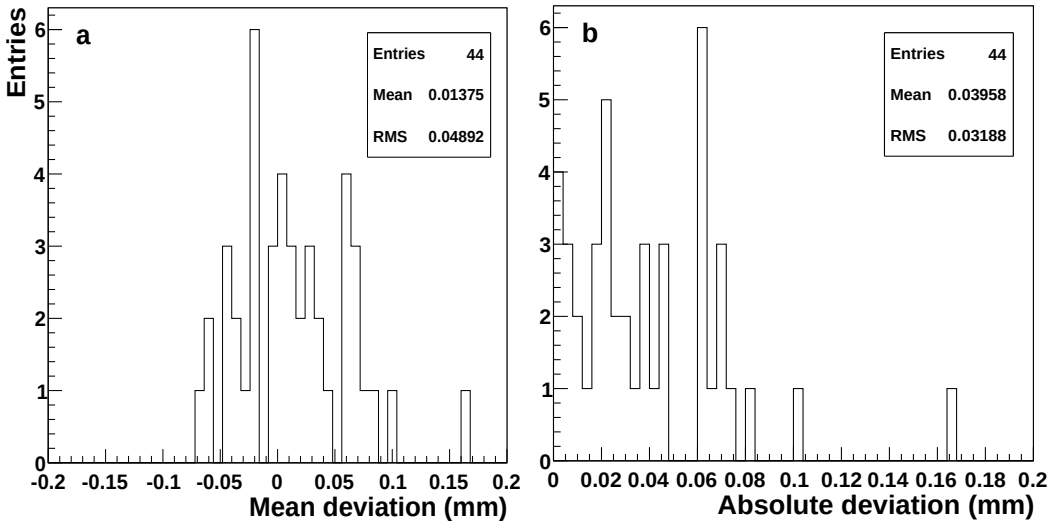

Figure 4.26: (a) Distribution of the mean deviations (with sign) of the wire positions from their nominal ones: this is a measure of the systematic shift of the wires. (b) Distribution of the absolute values of the deviations plotted in (a).

mean value of the residuals shown in Fig. 4.19 (13.85 μm). These deviations are within 50 μm, as indicated by the RMS of the figure; this value is comparable with the mean of Fig. 4.26.b, where the absolute values of the wire deviations are reported.
With $\sigma_{pos} \sim 50$ μm and $\sigma_{overall} \sim 177$ μm (see σ of the distribution in

Fig. 4.19), it results:

$$\sigma_{cal} = \sqrt{\sigma^2_{overall} - \sigma^2_{pos}} \simeq 170\ \mu m. \tag{4.29}$$

So the main contribution to the overall resolution comes from the calibration and the position error has a very small influence on the global one. Hence, it is not necessary to iteratively correct the wire position of the individual straws.

4.5.4 Drift velocity

Once the best $r(t)$ curve has been found after the last iteration of the autocalibration procedure, it is possible to produce a plot of the drift velocity $v_d(t)$: it is calculated as the integral of the linear combination of Chebyshev polynomials that fits the $r(t)$ curve (Eq. (4.4)).

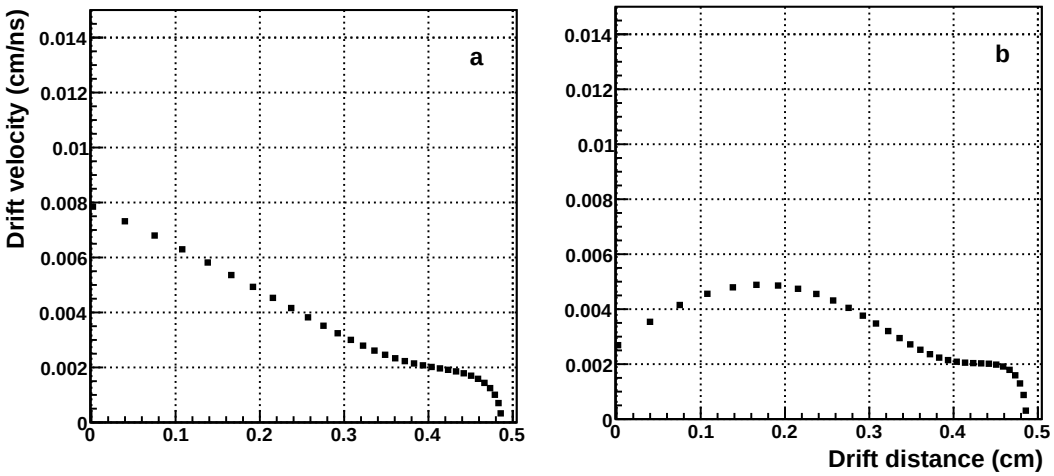

Figure 4.27: Drift velocity as a function of the drift distance, (a) at the first and (b) at the last step of the autocalibration.

Fig. 4.27 shows the drift velocity as a function of the drift distance, obtained by integrating the $r(t)$ curve at the first step of the autocalibration procedure and at the last one.
The effect of the iterations is evident, in particular by looking at the region close to the wire up to a drift distance of about 0.15 cm. In addition, the behaviour of the drift velocity is slightly different also for $r > 0.4$ cm: at the last iteration (b), it is a little bit more flat and then sharper with respect to the behaviour of the velocity at the first iteration (a). It is interesting to compare the reconstructed velocity with the simulated one, shown in Fig. 4.28.
It has been obtained from a GARFIELD simulation for tubes with 1 cm diameter filled with $ArCO_2$ (90/10) operating at a high voltage of 1700 V with 1 bar overpressure and in the absence of a magnetic field.
For $r \in [0.075, 0.475]$ cm, the simulated and the experimental drift velocities

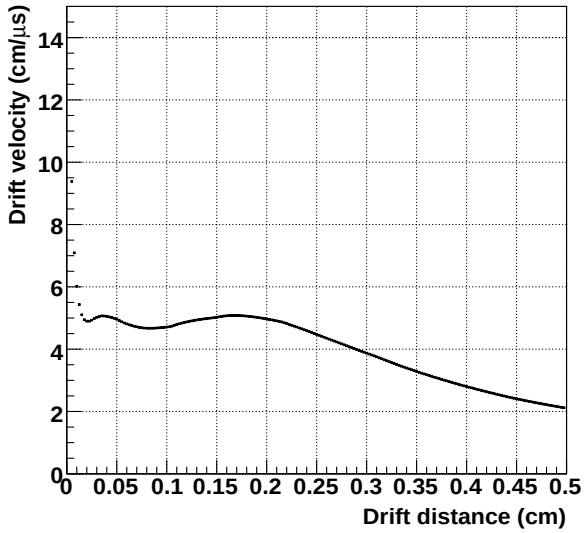

Figure 4.28: Drift velocity from GARFIELD simulation for 1 cm diameter straw tubes filled with $ArCO_2$ (90/10) operating at 1700 V, 1 bar overpressure and no magnetic field.

are very similar, with values ranging from a maximum of 5 to a minimum of 2 cm/μs. The shapes are different for $r < 0.075$ and $r > 0.475$ cm: concerning the region close to the wire, the simulated velocity grows up very rapidly due to ionisation effects. The different shape of the experimental velocity can be explained by the worse resolution usually expected in that region (Fig. 4.24). Concerning the drift distances close to the tube wall, the drop of the reconstructed velocity might be explained by the almost flat shape of the Chebyshev polynomials that fit the $r(t)$ curve in that region and also by the statistical fluctuations at the end of the TDC spectra.

4.6 Comparison with results for $ArCO_2$ (90/10) at 1800 V

All the steps of the data analysis presented in the previous sections have been repeated also for the data sample collected when the prototype was operated at 1800 V.
The results obtained are very similar to the ones shown for 1700 V. As an example, let's compare the single tube spatial resolutions, shown in Fig. 4.24 for 1700 V and in Fig. 4.29 for 1800 V.
In the case of 1800 V, all points are slightly lower than the ones in the resolution curve at 1700 V, but the effect is just of the order of 10-20 μm. So the results at 1700 and 1800 V are very similar and increasing the high voltage leads to a $\sim 10\%$ improvement in the spatial resolution.

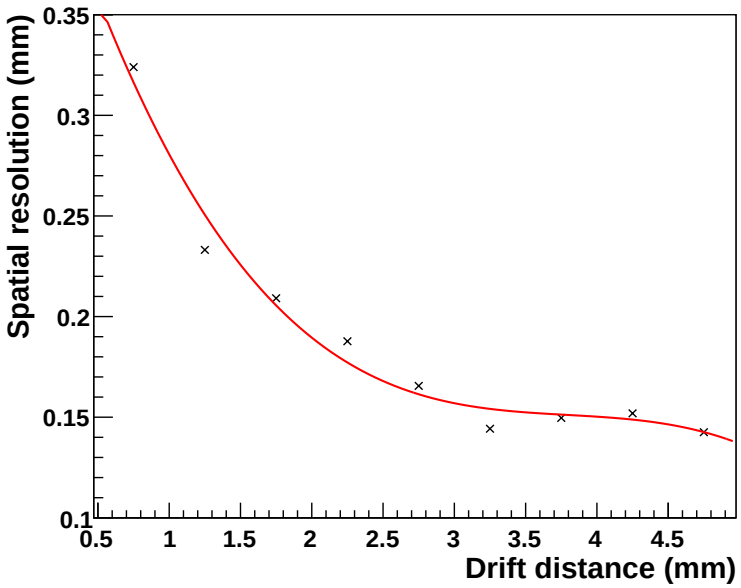

Figure 4.29: Single tube spatial resolution σ as a function of the drift distance, for data at 1800 V (spatial resolution for data at 1700 V in Fig. 4.24). The data (crosses) have been fitted with a third order polynomial (red curve).

In addition, the drift velocity has been derived as described in Sec. 4.5.4 also for the data set at 1800 V. Fig. 4.30 shows the results obtained after the first (a) and the last iteration (b) of the autocalibration procedure.
The effect of the iterations on the reconstructed velocity is the same as for the data taken with the prototype operated at 1700 V. The velocity dependences at the two voltages are very similar; the only difference is the less steep slope for drift distances close to the cathode at 1800 V.

The experimental drift velocity can be compared to the one simulated by GARFIELD, shown in Fig. 4.31. As for the data at 1700 V, the shapes of the simulated and reconstructed drift velocities are very similar, apart from the regions close to the wire and to the cathode. The reasons should be the same explained in the previous section.

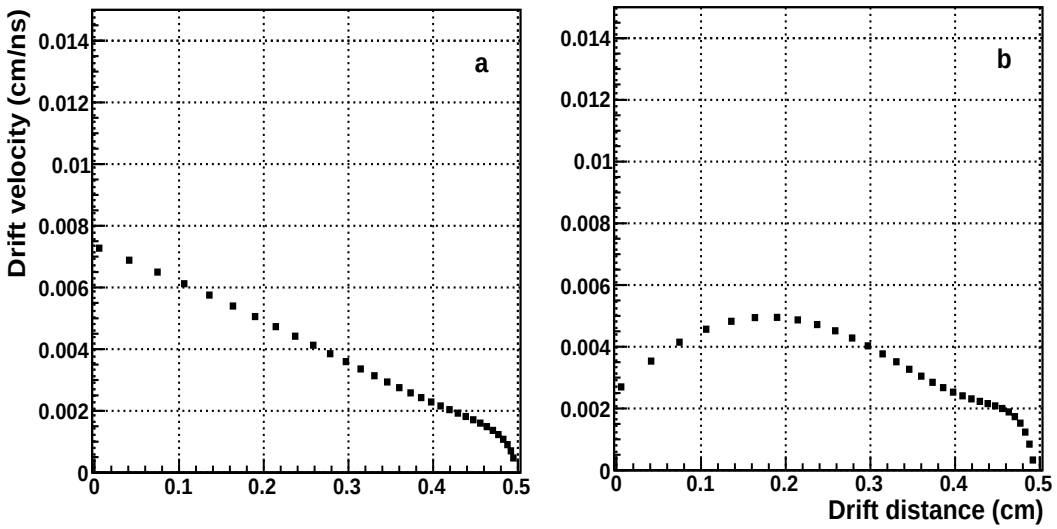

Figure 4.30: Drift velocity as a function of the drift distance, (a) at the first and (b) at the last step of the autocalibration, for data taken at 1800 V (for a comparison with data at 1700 V, see Fig. 4.27).

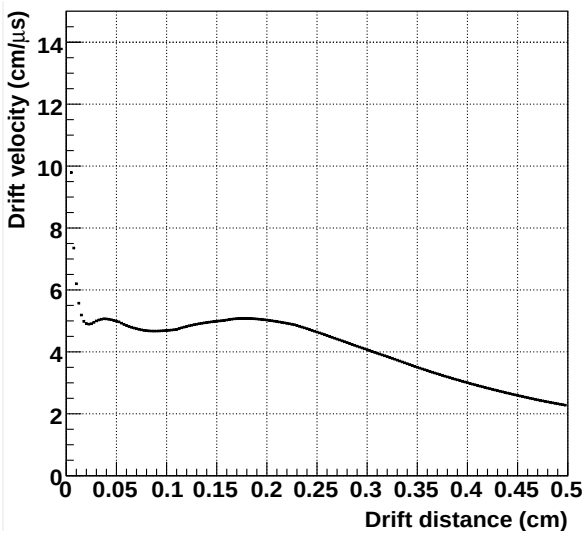

Figure 4.31: Drift velocity from GARFIELD simulation for 1 cm diameter straw tubes filled with $ArCO_2$ (90/10) operating at 1800 V, 1 bar overpressure and no magnetic field (for a comparison with data at 1700 V, see Fig. 4.28).

Bibliography

[1] K. Pysz, *Report on activities performed in the frame of external Research and development Program (FFE) of the Forschungszentrum Jülich*, Jülich, December 11, 2007.

[2] http://www-hep.phys.cmu.edu/cms/DOCUMENTATION/.

[3] K. Pysz, V. Serdyuk, P. Kulessa, H. Ohm, P. Wintz, *First measurements of energy-loss using $\overline{P}$ANDA–type straw tubes*, IKP Annual Report 2009, Jülich 2010.

[4] V. Serdyuk, K. Pysz, P. Kulessa, P. Wüstner, W. Erven, H. Ohm, P. Wintz, *A new setup for measuring the energy loss of particles in the $\overline{P}$ANDA STT*, IKP Annual Report 2009, Jülich 2010.

[5] G. Avolio et al., Nucl. Instr. and Meth. A 523 (2004) 309-322.

[6] A. Biscossa et al., Nucl. Instr. and Meth. A 419 (1998) 331-335.

[7] M. Bellomo et al., Nucl. Instr. and Meth. A 573 (2007) 340-360.

[8] F. James, *MINUIT, Function Minimization and Error Analysis, Reference Manual*, Version 94.1, CERN Program Library Long Writeup D506, CERN Geneva, Switzerland, 1994.

[9] http://mathworld.wolfram.com/LeastSquaresFittingPerpendicularOffsets.html.

[10] W. Erven, K. Kilian, V. Kozlov, I. Mohos, R. Nellen, S. Orfanitski, T. Sefzick, A. Ucar, P. Wüstner, K. Zwoll, P. Wintz, *Resolution and Efficiency of the Straw Tracker for COSY–TOF*, IKP Annual Report 2004, Jülich 2005.

[11] http://www.fz-juelich.de/ikp/COSY-TOF/index_e.html.

[12] R. Veenhof, *GARFIELD, Simulation of gaseous detectors*, Version 7.04, CERN Program library write-up W 5050.

Part III

Study of a single track

Chapter 5

Resolution studies with the $\overline{\text{P}}$ANDA Straw Tube Tracker

5.1 The simulation environment

In preparation for the $\overline{\text{P}}$ANDA experiment, large–scale simulations need to be performed in the upcoming years for the detector design, to determine analysis strategies and to be able to interpret the physics results.
In order to do this, the $\overline{\text{P}}$ANDA collaboration has developed a computing framework called PandaROOT [1, 2, 3, 4] as an extension of the FairRoot framework, a GSI project providing a common computing structure for all the experiments at the FAIR facility, such as $\overline{\text{P}}$ANDA, CBM [5], the HADES upgrade [6, 7] and R^{3}B [8].
PandaROOT is a framework for both simulation and analysis; it is mainly based on the object oriented data analysis framework ROOT [9] and on Virtual Monte Carlo (VMC) [10, 11], which allows to run different transport models such as Geant3 [12], Geant4 [13] and Fluka [14].
The PandaROOT computation is divided into three main parts.
In order to perform full simulations, the first step consists in generating the physics events of interest. In PandaROOT, several event generators are implemented, in order to fulfil to the many physics goals of the experiment: some examples of generators which are inside the code are the box generator, EvtGen [15], the Dual Parton Model (DPM) [16] and the Ultra–relativistic Quantum Molecular Dynamic model (UrQMD) [17, 18]. They are provided as external packages because they have been developed and are maintained outside the collaboration. The event output files are converted by *ad hoc* interpreters developed in PandaROOT to the standard output that can be read by the transport model part.
The generated particles are then propagated inside the detectors and their interactions with the spectrometer are computed by one of the transport models between which the user can switch via the VMC. In this way, it is also possible

to compare the results obtained with different models, to tune the cuts and to validate the physics implemented with a cross–check even with experimental data.
At this stage, the detector geometries and materials are defined: the $\overline{\text{P}}$ANDA spectrometer is now almost fully implemented in PandaROOT. Also a realistic map of the magnetic field has been implemented, with values taken from TOSCA [19] calculations. It consists of a solenoidal field in the Target Spectrometer and a dipole field in the Forward Spectrometer; the region in between presents inhomogeneities that make tracking a real challenge there.
Then, the simulation files are used as input for the digitization and reconstruction steps. The aim is to perform a real high resolution global tracking by joining the pieces of information from all the tracking detectors, such as MVD, STT (or TPC) and GEM chambers.
The procedure that allows the STT to provide the global tracking with the reconstructed hits will be described in detail in Sec. 5.2; the global fit will be briefly treated in Sec. 5.3.
In order to improve the results provided by the global fit, a Kalman filter (Sec. 5.4) is then applied on the reconstructed tracks, making use of the GEANE track follower (Sec. 5.5). Finally, the reconstructed data are used to perform the physics analysis [4].

5.2 The STT fitting algorithm

Since the STT, unlike the MVD and the GEM chambers, does not provide the (x, y, z) coordinates where the particle passed but the drift radius of the firing wires (i.e. the shortest distance to the wire of the particle traversing the tube), it is mandatory to have a procedure to find them, in order to supply the global tracking with the reconstructed points for the global pattern recognition and fitting.
At the end of this local fit, a reconstructed helix trajectory and reconstructed hits (so called helix hits) are available from STT.

The STT local fitting algorithm has been developed [20, 21] using the helix model, assuming in this preliminary step that the magnetic field is constant and ignoring all the material effects[1].
Each track is described by the following five parameters (see Fig. 5.1):

- R is the curvature radius of the track in the xy plane, whose centre has coordinates (x_C, y_C);

[1] These two assumptions can be made with no problems for the STT: in the region of the Straw Tube Tracker, the magnetic field is homogeneous and the helix model can be used for track fitting. In addition, the material effects can be ignored as a first approximation, since they will be taken into account be the track follower GEANE (Sec. 5.5) in the following steps of the track reconstruction.

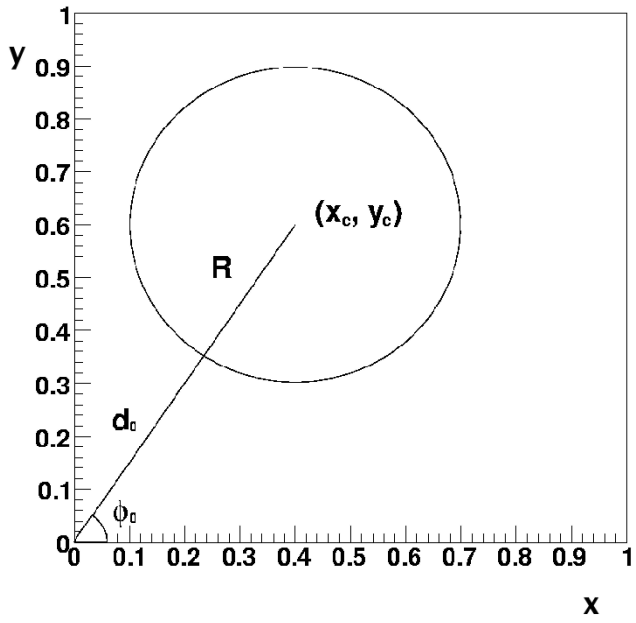

Figure 5.1: Track parameters in the xy plane. Figure taken from Ref. [20].

- d_0 is the distance of closest approach of the track to the origin;
- ϕ_0 is the azimuthal angle of the point of closest approach ($\phi_0 = \arctan \frac{y_C}{x_C}$);
- z_0 is the z coordinate of the point of closest approach calculated in the xy plane;
- $\tan\lambda$ is the tangent of the dip angle λ, i.e. the slope of the straight line in the $z-$track length ($s\cos\lambda$) plane.

The first three parameters are linked by the following relation:

$$d_0 = \frac{(x_C + y_C) - R(\cos\phi_0 + \sin\phi_0)}{\cos\phi_0 + \sin\phi_0}. \tag{5.1}$$

The fitting procedure is performed in the two planes separately:

- xy plane, perpendicular to the magnetic field direction, with a circle fit;
- $z-$track length plane with a straight line fit.

5.2.1 The xy plane algorithm

As already mentioned, the STT does not give the (x, y) coordinates of the particle hit, but gives the wire which has fired (and then its (x, y) coordinates) and the drift radius r_d.
In order to extract the hit coordinates from the straw output, a procedure performed through several steps and similar to the one described in Sec. 4.4.2 has been developed; the steps are:

1. a *pre-prefit* using the conformal mapping technique [22];
2. a *prefit* using Minuit [23];
3. the *Intersection Finder*;
4. an iterative *refit*.

5.2.1.1 pre-prefit and prefit

The **pre-prefit** has been introduced as input to Minuit, since it requires the parameters to be initialised. It is performed on the wire coordinates (x, y) by using the conformal mapping technique, which transforms the problem of fitting with a circle in a parabola fit, thanks to an appropriate change of coordinates.
The **prefit** step is performed as well on the centre of the tubes, the primary information given by the STT.
The parameters chosen for Minuit to define the track are x_C, y_C, R. The function to be minimised is:

$$\chi^2 = \left(\frac{\sqrt{(x - x_C)^2 + (y - y_C)^2} - R}{\sigma_{r_d}} \right)^2 , \tag{5.2}$$

with $\sigma_{r_d} = 1/\sqrt{12}$ if $r_d = 0$ and $\sigma_{r_d} = r_d/\sqrt{12}$ if $r_d \neq 0$, assuming a uniform distribution for r_d.

5.2.1.2 Intersection Finder

After the Minuit fit, if it succeeded, the **intersection finder** is performed. It is a procedure that works in a way similar to that described in Sec. 4.4.2.3: it allows to find the "real" coordinates of the hits, i.e. the points where the particles actually passed (the point of closest approach to the wire).
Up to now, the (x, y) coordinates of the wires, the drift distance r_d of each tube and a track hypothesis (x_C, y_C, R) are known. Each straight line (blue dotted lines in Fig. 5.2) joining the centre of curvature of the track (x_C, y_C) with the centers of each tube intercepts each drift circle (black circles in figure) in two points: the closest ones to the prefit (green line in figure) are chosen and set to be the (x, y) coordinates of the track hits.

5.2.1.3 Refit

The "real" point coordinates, the new ones found in the intersection finder step, are then used to perform a **refit** using the conformal mapping technique, followed by the intersection finder and Minuit fit (twice). In this last fit also the drift radii of the different tubes (so the whole information coming from the tracker) are taken into account.
In this step, the two errors σ_x and σ_y on the (x, y) hits coordinates and their

covariances are obtained by projecting the error on the drift radius onto the two axes. In particular, if $r_d \neq 0$:

$$\begin{aligned} \sigma_x &= \sigma_r \cdot \cos(\alpha) \\ \sigma_y &= \sigma_r \cdot \sin(\alpha) \\ \sigma_{xy} &= \sigma_r \cdot \sqrt{\cos(\alpha) \cdot \sin(\alpha)}, \end{aligned}$$

where σ_r is the estimated resolution and $\alpha = \arctan(m)$, m being the slope of the line joining the centre of curvature of the track to the centre of each tube, found in the intersection finder step. In case of $r_d = 0$, the errors are the same as in the pre-prefit step.
From this fit the parameters d_0, ϕ_0 and R in xy plane are found.
Fig. 5.2 shows an example of the local fit results.

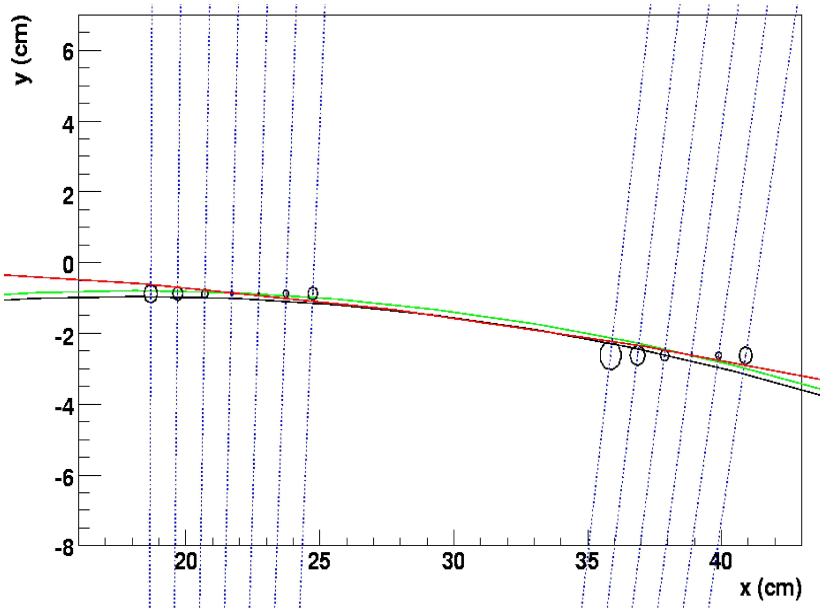

Figure 5.2: In this figure the pre-prefit (black), prefit (green) and refit (red) curves are drawn. The black circles are the drift circles; the blue dotted lines are the ones joining the centre of curvature of the track to the centers of each tube, allowing to find the tracks hits. Figure taken from Ref. [20].

5.2.2 The z coordinate

The z coordinate is reconstructed by making use of tilted tubes (see Fig. 5.3 for a better graphical explanation): from the intersection of these tubes the z coordinate can be extracted.
The procedure to find the z coordinate is divided in two steps:

1. z finder step;
2. z fit step in the $z - s\cos\lambda$ plane.

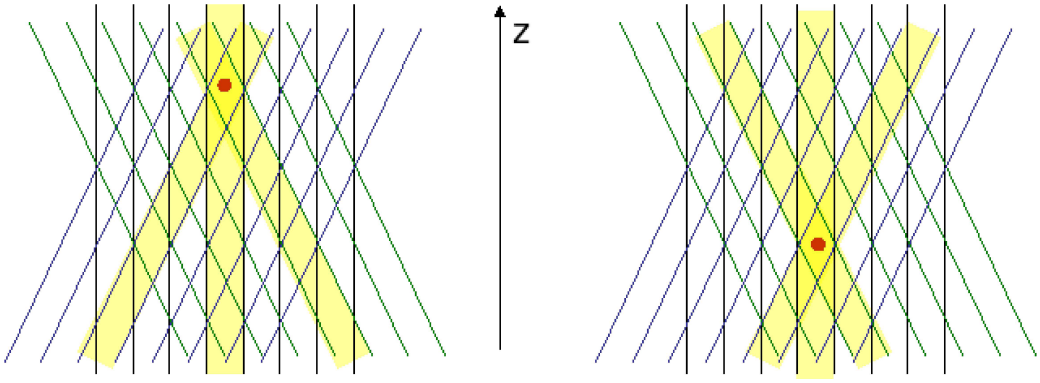

Figure 5.3: One straw tube layer parallel to the beam axis and two skewed layers tilted in opposite directions are shown. If the particle hit is denoted by the red point, it is clear that different couples of skewed firing tubes imply different z coordinate. Figure taken from Ref. [20].

5.2.2.1 z finder

As already pointed out, the z coordinate determination uses the skewed tubes. In the xy projection, the drift circles of these tubes are not tangent to the fitted trajectory; hence, they are shifted till they become tangent (Fig. 5.4). Two possible positions of the drift circle centre are found, (x_c^0, y_c^0) and (x_c^1, y_c^1). Both are kept in a first step. From them, the z_c^0 coordinate (and z_c^1 one) is inferred.
To select between the two hypotheses, the Hough transform technique[2] [24] is used to identify the points lying on a straight line and ignore the fake ones.

5.2.2.2 z fitting

The z fitting step consists in performing a fit in the plane $z -$ track length. The track length is calculated via the formula:

$$s\cos\lambda = h \cdot R \cdot \arctan\left(\frac{(y-y_0)\cos\Phi_0 - (x-x_0)\sin\Phi_0}{R + (x-x_0)\cos\Phi_0 + (y-y_0)\sin\Phi_0}\right). \tag{5.3}$$

From this fit the parameters z_0 and $\tan\lambda$ are found.

[2]The Hough transform is a method used to find patterns in an ensemble of points (e.g. to do pattern recognition in a digital image). It consists in parametrising the line we are searching for and mapping it in the parameter space, in such a way that lines in the real space are transformed to points (a, b) in the parameter space, while points (x, y) in the real space are transformed to lines in the parameter one. Thus, to find a line on which several points lie, these points are transformed in the parameters plane in several lines (all the lines which pass through them) and the point in which these lines cross provides the parameters of the straight line we are looking for.

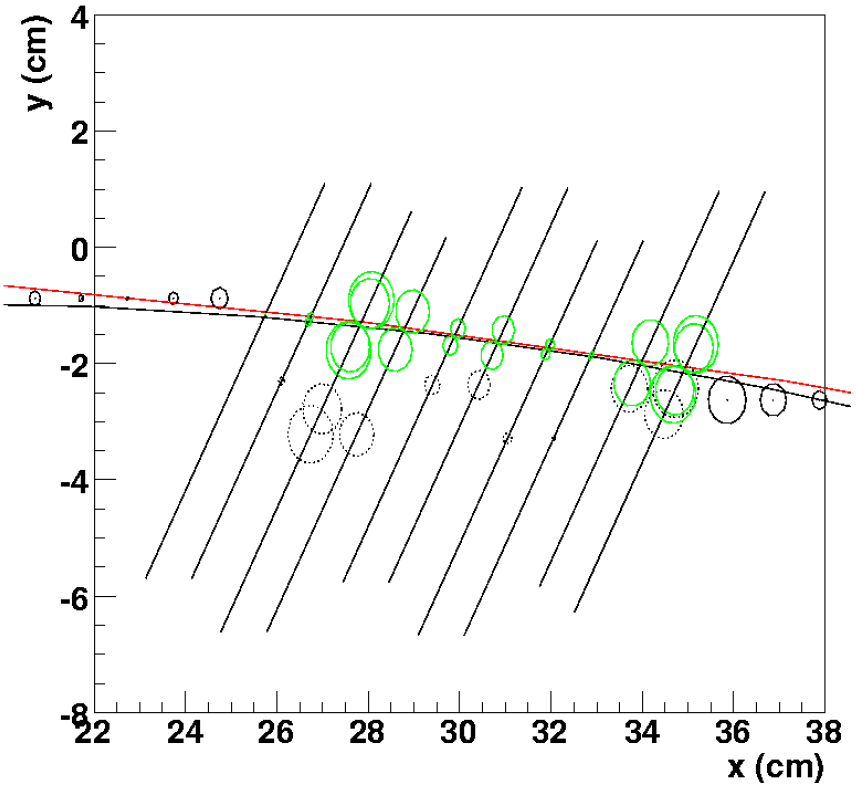

Figure 5.4: xy plane projection: the red curve is the fitted one. The circles which are not tangent to this curve are the skewed tube ones. The projection of the wires of these tubes in the plane is drawn (black segments). The green circles are the skewed tube drift circles "moved" to become tangent. This movement is actually a change in the z coordinate. Figure taken from Ref. [20].

5.3 The global tracking

Once the reconstructed hits are available for all the tracking subdetectors, the global track finding and fitting is performed by the devoted package [4]; the details of its implementation will not be treated here.
In order to construct the global track, a global pattern recognition is first performed, so that one or more track candidates are found out. Two pattern recognitions are available: the ideal one, which makes use of the Monte Carlo truth to assign the hits to the track candidate, and the real one, merging the reconstructed information from the tracking subdetectors.
Then, a helix fit[3] is performed over all the reconstructed hits: the global track and its parameters are found and can be given as input to the Kalman filter.
As already mentioned, the fitting task is not straightforward due to the presence of dense media and to the field inhomogeneities between the two spec-

[3]In the following, the fit performed by the global tracking package is referred to as helix fit.

trometers where the GEM chambers are placed. As previously explained in Sec. 5.2, the helix model assumes that the magnetic field is homogeneous, so the usage of the helix fit of the global tracking package in the GEM region introduces systematic errors in the track parameters that come out from the fit; it results, for example, in a shift of the reconstructed momentum distributions, as will be shown in Sec. 6.1.1.4.
In addition, the performances of the global tracking package are not the best when used with the STT option as Central Tracker. In fact in this case two fits are performed: the local one on the STT hits and the global one on the hits from all tracking subdetectors. Since each tracking step has its own efficiency, the global one is equal to the product of the two efficiencies, resulting in a lower one, as evident from the results that will be presented in Sec. 5.7.
Despite these problems, up to now this is the only package devoted to the global tracking implemented in PandaROOT; a new one, performing both a pattern recognition and a global fit in one step, without the need of the STT local one, is in preparation.

5.4 The Kalman Filter

Once a track candidate has been obtained from the global fit, a Kalman filter is used to improve the resolution of the track parameters.

In this section a short summary of the Kalman fit procedure is reported. A more detailed description of this topic can be found in Refs. [25] to [29], in Ref. [20] and references quoted therein.

The Kalman fit is an iterative procedure which, unlike global methods such as the helix fit, takes into account the dE/dx, the magnetic field inhomogeneities and the multiple scattering.
The aim of the Kalman filter is to find the best estimation of the true track point $\boldsymbol{f}_i$ at the i-th detector plane by minimising the χ^2:

$$\begin{aligned}\chi^2(\boldsymbol{f}) &= \sum_i [(\boldsymbol{e}_i[\boldsymbol{f}_{i-1}] - \boldsymbol{f}_i)\boldsymbol{W}_{i-1}(\boldsymbol{e}_i[\boldsymbol{f}_{i-1}] - \boldsymbol{f}_i)] \\ &\quad +(\boldsymbol{x}_i - \boldsymbol{f}_i)\boldsymbol{V}_i(\boldsymbol{x}_i - \boldsymbol{f}_i) \end{aligned} \tag{5.4}$$

where $\boldsymbol{x}_i$ are the measured points and $\boldsymbol{e}_i = \boldsymbol{e}_i[f_{i-1}]$ are the extrapolated ones (i.e. the predicted position of the track on the i-th detector plane starting from the $i-1$-th one), written as a function of the true track points $\boldsymbol{f}_{i-1}$; $\boldsymbol{W}$ and $\boldsymbol{V}$ are the weight matrices containing respectively the tracking and the measurement errors.
The minimisation of Eq. (5.4) gives an equation that depends both on $\boldsymbol{f}_i$ and

$\boldsymbol{f}_{i-1}$:

$$\begin{aligned}\frac{\partial \chi^2}{\partial \boldsymbol{f}_i} &= \boldsymbol{W}_{i-1,i}(\boldsymbol{e}_i[\boldsymbol{f}_{i-1}] - \boldsymbol{f}_i) + \boldsymbol{V}(\boldsymbol{x}_i - \boldsymbol{f}_i) \\ &\quad -\boldsymbol{T}(l_{i+1}, l_i)\, \boldsymbol{W}_{i,i+1}(\boldsymbol{e}_{i+1}[\boldsymbol{f}_i] - \boldsymbol{f}_{i+1}) = 0\ ,\end{aligned} \tag{5.5}$$

where $\boldsymbol{T}(l_{i+1}, l_i)$ is the transport or Jacobian matrix that transports the errors from a track point l_i to a track point l_{i+1} [20].
The Kalman filter is a method to solve Eq. (5.5). Usually this is done through three steps [30, 31]:

1. the first step is the *extrapolation* of the previous Kalman value $\boldsymbol{k}_{i-1}$ to the i-th plane:

$$\boldsymbol{e}_i \equiv \boldsymbol{e}_i[\boldsymbol{k}_{i-1}] = \boldsymbol{G}(\boldsymbol{k}_{i-1}) \tag{5.6}$$

$$\begin{aligned}\boldsymbol{\sigma}^2[\boldsymbol{e}_i] &= \boldsymbol{T}(l_i, l_{i-1})\, \boldsymbol{\sigma}^2[\boldsymbol{k}_{i-1}]\, \boldsymbol{T}^T(l_i, l_{i-1}) \\ &\quad +\boldsymbol{R}^{-1}_{i-1,i},\end{aligned} \tag{5.7}$$

   where $\boldsymbol{R}^{-1}$ is the error matrix relative to random effects;

2. the second step is the calculation of the *Kalman filter value* at the i-th detector plane. This is a preliminary evaluation of the track parameters $\boldsymbol{k}_i$, making a "weighted mean" between the measured value and the predicted value on plane i:

$$\begin{aligned}\boldsymbol{k}_i &= \boldsymbol{\sigma}^2[\boldsymbol{k}_i](\boldsymbol{\sigma}^{-2}[\boldsymbol{e}_i]\, \boldsymbol{e}_i \\ &\quad +\boldsymbol{V}_i \boldsymbol{x}_i)\end{aligned} \tag{5.8}$$

$$\boldsymbol{\sigma}^{-2}[\boldsymbol{k}_i] = \boldsymbol{\sigma}^{-2}[\boldsymbol{e}_i] + \boldsymbol{V}_i. \tag{5.9}$$

   These equations are simply the weighted average in the 5-fold track space;

3. the third step is the *backward smoothing* of the Kalman point solution of the second step to get the final estimate of the value $\boldsymbol{f}_i$

$$\boldsymbol{f}_i = \boldsymbol{k}_i + \boldsymbol{A}_i\, (\boldsymbol{f}_{i+1} - \boldsymbol{e}_{i+1}) \tag{5.10}$$

$$\begin{aligned}\boldsymbol{\sigma}^2[\boldsymbol{f}_i] &= \boldsymbol{\sigma}^2[\boldsymbol{k}_i] + \\ &\quad +\boldsymbol{A}_i \left(\boldsymbol{\sigma}^2[f_{i+1}] - \boldsymbol{\sigma}^2[\boldsymbol{e}_{i+1}]\right) \boldsymbol{A}_i^T\end{aligned} \tag{5.11}$$

$$\boldsymbol{A}_i = \boldsymbol{\sigma}^2[\boldsymbol{k}_i]\, \boldsymbol{T}^T(l_{i+1}, l_i)\, \boldsymbol{\sigma}^{-2}[\boldsymbol{e}_{i+1}]. \tag{5.12}$$

   This last step is often substituted by an alternative option: the so–called "backtracking", i.e. steps 1 and 2 followed by the extrapolation in the backward direction, from the last point of the track to the first one.

If the track follower and all the measured points are *not* expressed with the same set of track variables, the so called *measurement matrix* **H** is used, to make the two representations comparable, setting:

$$\boldsymbol{x}_i = \boldsymbol{H}_i \boldsymbol{e}_i + \epsilon_i \ , \tag{5.13}$$

where ϵ is the random part introduced by the measurement.

The PandaROOT framework makes use of a software package in which the Kalman filter is implemented: this is called GENFIT [32]. It is completely written in C++ and makes extensive use of object oriented design. It uses the C++ standard template library and the ROOT data analysis framework. A detailed description of the package features can be found in Ref. [33].

5.5 The track follower: GEANE

The ability to extrapolate a track described by a set of parameters[4] and their covariances to different positions in the spectrometer, taking into account the effects of materials, is mandatory for track fitting.
In order to do this, GENFIT provides an interface for the invocation of external programs or libraries that perform track extrapolations. The track follower used in PandaROOT is GEANE [31].
The task of the track follower is to provide the extrapolated points $\boldsymbol{e}[\boldsymbol{f}_i]$, $\boldsymbol{e}[\boldsymbol{f}_{i+1}]$ and $\boldsymbol{e}[\boldsymbol{f}_{i-1}]$ of Eqs. (5.4)–(5.13) of the Kalman fitting algorithm. To do this, it is necessary:

- to transport the track parameters (particle momentum, position and direction) from one point to another in the apparatus, forward and backward. The forward extrapolation (deterministic propagation) can be obtained by simply using any MC code by launching one particle only and switching off the multiple scattering and the random effects of discrete energy loss due to ionisation and delta ray production ("Landau" fluctuations, bremsstrahlung, etc.). Concerning the backward tracking (with increasing momentum), only minor modification of the MC codes are usually required;

- to propagate the errors on the track parameters together with the mean values. This is usually obtained by calculating, step by step, the 5×5 covariance matrix. This mathematical part is analytically rather complicated: some general ideas are given in the current literature [30] and some correct approaches can be found in Refs. [29, 34, 35].

[4] Usually, tracks of charged particles in magnetic fields are described by five parameters and the corresponding covariance matrix.

GEANE is a FORTRAN package which originated from the interface between the GEANT3 tracking programs, used to determine the track parameter mean values, and the routines developed by the CERN EMC collaboration [34] to calculate and transport the error matrices. Hence the name:

GEANE = GEANT3 tracking + EMC error propagation routines.

The great advantage of this structure is that the track following is automatically obtained with the same geometry banks of the Monte Carlo, without the necessity to write *ad hoc* codes.
In addition to track fitting with recursive methods like the Kalman filter, the most common applications of GEANE, as well as of the other track following codes, are:

- trajectory calculation in terms of mean values and errors:
  when the measured track value $\boldsymbol{x}$ or an estimate of the true track values $\boldsymbol{f}$ at a track length l_0 is known, the track following code determines the value at a new track length l, in the forward or backward direction. This extrapolation, which gives the parameter mean value, is denoted as an operator $\mathbf{G}(\cdot)$ (remembering GEANE):

  $$\boldsymbol{e}(l) = \mathbf{G}(l_0), \tag{5.14}$$

  where $\boldsymbol{e}$ are the quantities in Eqs. (5.4)-(5.13) and the starting point at l_0 can be chosen as $\mathbf{G}(\mathbf{f}(l_0))$ or $\mathbf{G}(\mathbf{x}(l_0))$ or in other manners. Explicit formulae for the operator $\mathbf{G}$ can be found in Ref. [35].
  During the tracking, three processes are taken into account:

  - energy loss, which affects both averages (Bethe Bloch formula) and errors (Landau fluctuations);
  - Coulomb multiple scattering, that influences the error calculation only (Molière theory or gaussian approximation);
  - magnetic field, that influences the average trajectory only;

- joining track elements:
  to find the best estimate of the intersection $\mathbf{x}$ of a particle track in a plane, starting from the measured points (Fig. 5.5.a), the following χ^2 can be minimised with respect to $\mathbf{x}$:

  $$\chi^2(\mathbf{x}) = (\mathbf{x}-\mathbf{G}(l_1))\mathbf{W}_1(\mathbf{x}-\mathbf{G}(l_1))^T+(\mathbf{x}-\mathbf{G}(l_2))\mathbf{W}_2(\mathbf{x}-\mathbf{G}(l_2))^T, \tag{5.15}$$

  obtaining the $\mathbf{x}$ estimation as the weighted mean with error:

  $$\mathbf{x} = \frac{\mathbf{W}_1\mathbf{G}(l_1)+\mathbf{W}_2\mathbf{G}(l_2)}{\mathbf{W}_1+\mathbf{W}_2} \tag{5.16}$$

  $$\sigma(\mathbf{x}) = (\mathbf{W}_1+\mathbf{W}_2)^{-1/2}; \tag{5.17}$$

- track point (vertex) optimization:
  in this case, one starts from a track point $\mathbf{x}_0$ and finds the best $\mathbf{x}_0$ that minimises the χ^2 up to a track length l_0 (Fig. 5.5.b):

$$\begin{aligned} \chi^2(\mathbf{x}_0) &= \sum_i [(\mathbf{x}_i - \mathbf{G}(l_i))[\sigma_{iT}^2]^{-1}(\mathbf{x}_i - \mathbf{G}(l_i))^T], \\ \sigma_T &= \sigma^2 + \sigma_m^2, \end{aligned} \tag{5.18}$$

  where σ and σ_m are the extrapolation and measurement covariance matrices respectively, $\mathbf{x}_i$ are the track measured points and l_i the track lengths up to $\mathbf{x}_i$. The minimisation can be done also on a subset of the 5 track parameters [31].

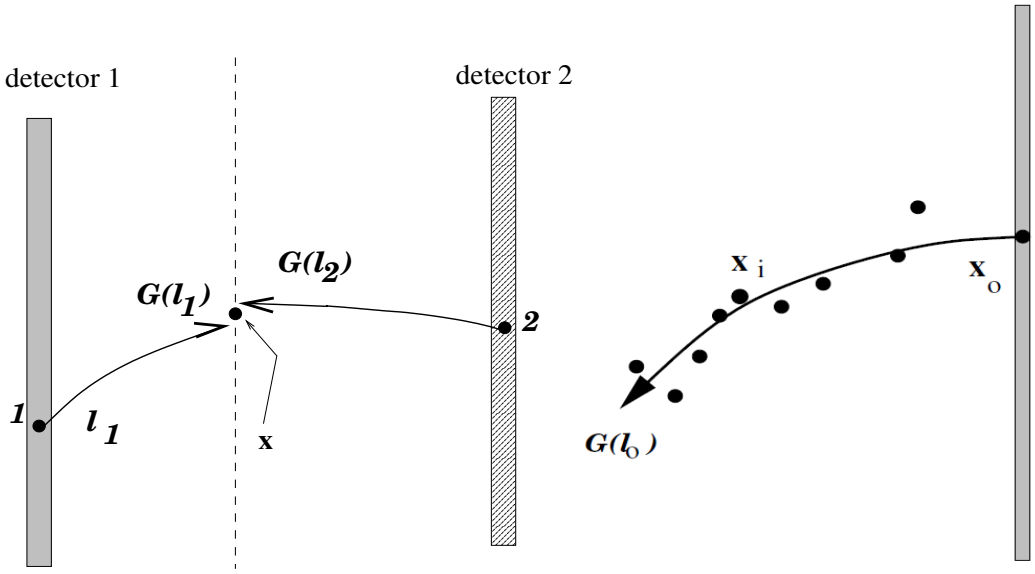

Figure 5.5: Joining track elements (left) and track point optimization (right) using a track follower $\mathbf{G}(\cdot)$. Figure taken from Ref. [29].

The GEANE package allows the user to choose between different kinds of tracking: it is possible to track a particle to a desired track–length, to a volume or to a plane.
In the case of non–planar detectors, like wire–based drift chambers or time–projection chambers, for which physical detector planes are not defined, the concept of "virtual" detector planes is used.
Since, in order to construct these planes, it is necessary to know the point of closest approach (PCA) of a track to a point or to a line (wire) positioned in space, a dedicated method has been implemented in GEANE.
Concerning space–point detectors (like TPCs), the track fit should be such

that the distances of the track to the hits are minima. Hence, the virtual detector plane associated to each hit must contain the hit position as well as the PCA of the track to the hit point. In such a way, the residual vector (i.e. the vector pointing from the hit point to the PCA) is orthogonal to the track. The orientation of the $\vec{u}$ and $\vec{v}$ vectors spanning the virtual detector plane is chosen arbitrarily in the plane (Fig. 5.6 (left)).
For wire–based drift detectors, like the $\overline{\text{P}}$ANDA STT, the virtual detector plane contains the PCA of the track to the wire and it is constructed to contain the whole wire. The $\vec{u}$ vector is perpendicular to the wire, directed from the PCA on the wire to the PCA on the track; the $\vec{v}$ vector is chosen along the wire direction (Fig. 5.6 (right)). By choosing the PCA on the wire as origin of the virtual detector plane, the v coordinate of both the extrapolated and the measured points id 0 (apart from skewed straws); concerning the u coordinate, it is a measure of the drift radius and of the wire position.

A more detailed treatment of the techniques and formulae of the track following, independently of any language or framework, can be found in Refs. [20] and [29].

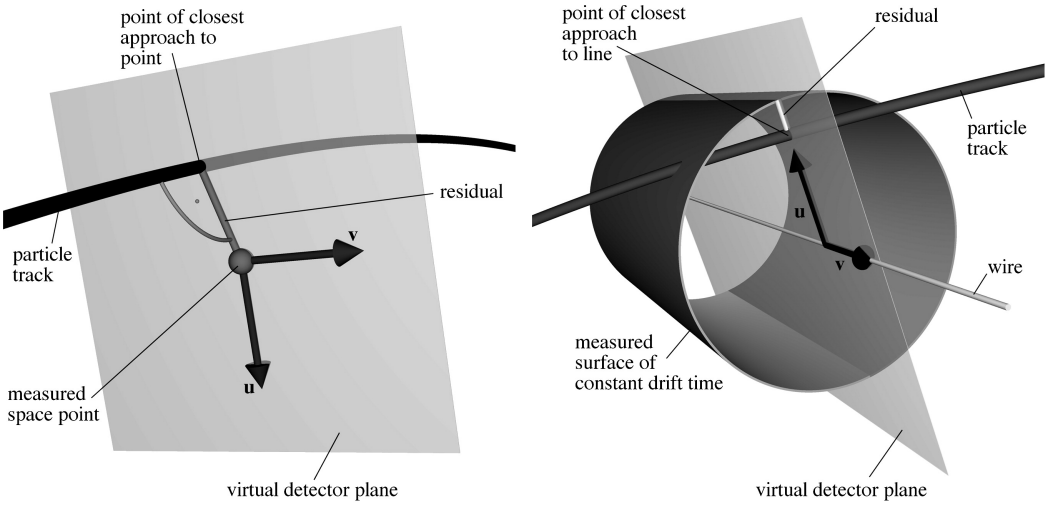

Figure 5.6: Virtual detector plane (spanning vectors $\vec{u}$ and $\vec{v}$) in the case of a space–point detector (left) and a wire–based drift detector (right). Figure taken from Ref. [33].

5.6 The general fit procedure

For the sake of clarity, the steps of the fit procedure described in detail in the previous paragraphs can be summarised as follows:

- local STT fit (Sec. 5.2), which proceeds through three steps:

  - pattern recognition: the user can choose between an ideal (i.e. based on the Monte Carlo truth) or a real (i.e. based on the information from the reconstruction) pattern recognition, depending on the purposes of the analyses to be performed;
  - fit developed using the helix model;
  - construction of the (x, y, z) reconstructed hits;

- global track finding, consisting in:
  - merging of the hits of all subdetectors;
  - global pattern recognition (again, both the ideal and the real pattern recognitions are implemented), which provides the list of track candidates;

- global track fitting (Sec. 5.3) using the conformal mapping technique. The user can choose which detector should be included in the fit and which kind of information (Monte Carlo or reconstructed) should be used for each of them;

- Kalman filter recursive method (Sec. 5.4) with the use of the GEANE track follower (Sec. 5.5), in order to improve the resolution of the reconstructed track parameters;

- backpropagation (propagation in the backward direction) with GEANE of the track parameters to the origin.

At the end of this fit procedure, the track parameters are available for further analyses like, for example, momentum resolution, efficiency and invariant mass studies, depending on which kind of events have been simulated.

5.7 Results

In order to study the performances of the designed $\overline{\text{P}}$ANDA Straw Tube Tracker in terms of geometrical acceptance of the layout, momentum resolution and reconstruction efficiency, systematic studies have been performed with single track events.
The complete simulation – digitization – reconstruction chain has been run. The simulated subdetector setup consists of MVD, STT, GEM, EMC, TOF, MDT and DRC, with the addition of the passive elements (the solenoid and the dipole magnets and the target and beam pipes).
The digitization step has been performed only for MVD, STT and GEM in order to save computation time, since the studies would have been dedicated only to the Central Tracker. The pattern recognitions, both the local STT one and the global one performed by the global tracking package, are real (Sec. 5.6).
The results are presented in the following sections.

5.7.1 Studies on the number of hits per track

In order to check the geometrical acceptance of the layout, the distributions of the number of hits coming from axial, skewed and short straws have been studied for particles generated at fixed values of the polar angle θ and as function of the azimuthal ϕ angle.
10^4 μ^+ and 10^4 μ^- single track events at 1 GeV/c, random ϕ ($\phi \in [-90°, +90°]$) and $\theta = 20°,\ 90°,\ 140°$ ($\pm 5°$) have been simulated.
Fig. 5.7 shows the distributions of the number of hits vs. ϕ for $\theta = 90° \pm 5°$.

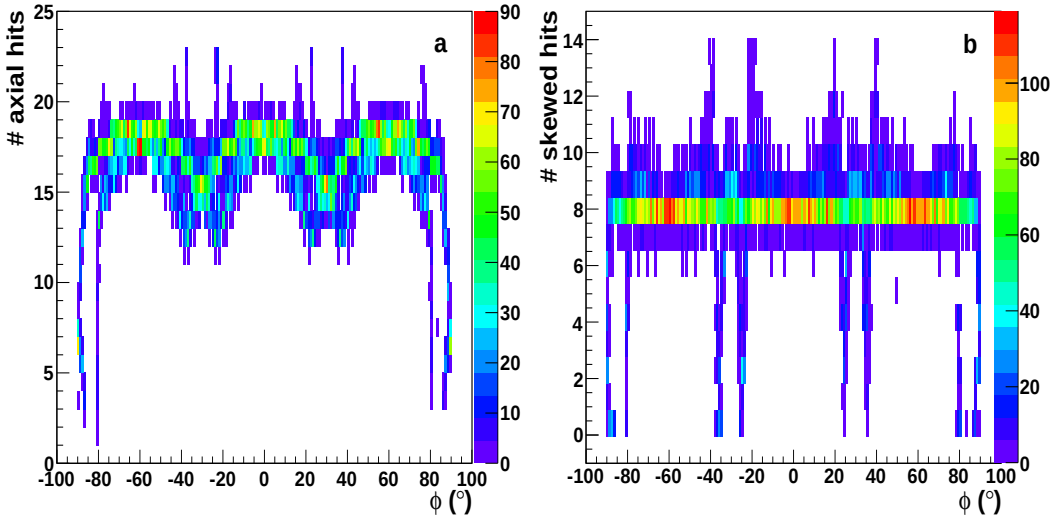

Figure 5.7: Distribution of the number of axial (a) and skewed (b) hit straws as a function of the ϕ angle for 20000 μ generated with a momentum of 1 GeV/c at $\theta = 90° \pm 5°$.

The plots show that the minimum number of hit straws is $12 - 13$ for the axial straws and $7 - 8$ for the skewed ones. These numbers correspond to the minimum number of layers (axial and skewed, respectively) that a particle flying at $\phi = \pm 30°$ can traverse. For ϕ values corresponding to regions of the detector where there are additional single–layers parallel to the beam axis, the number of axial hit straws increases up to $18 - 20$.
The low number of hit straws at $\phi = \pm 90°$ is due to the gap for the target pipe. Concerning $\phi = \pm 30°$, the losses are caused by the fact that in the corners of the hexagonal STT layout there are short tubes, which do not fill completely the volume, leaving empty spaces. As shown in Fig. 5.8.b, these losses are negligible: only $\sim 4.4\%$ of the total number of events hits less than 5 skewed straws. Nevertheless, there is a gain in efficiency when including in the z reconstruction also the hits from the MVD.
So this study demonstrates that the minimum number of hit straws obtained with such a layout is enough to perform a robust track reconstruction.

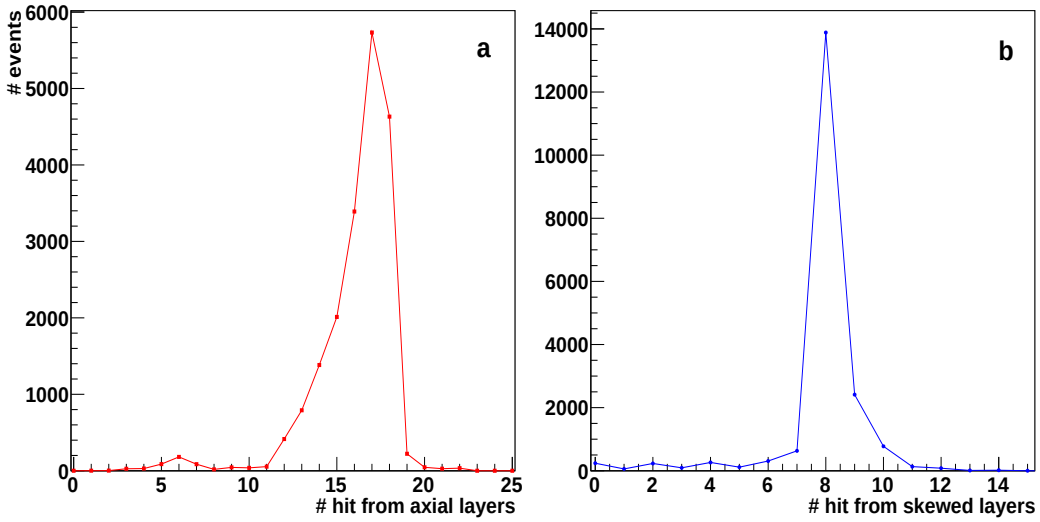

Figure 5.8: Distribution of the mean number of axial (a) and skewed (b) hit straws per event.

5.7.2 Studies on momentum resolution

5.7.2.1 Dependence on straw tubes length

As already mentioned in Chap. 2, for the Central Tracker with STT two possible layouts are under consideration: one consists in a Straw Tube Tracker with 150 cm long tubes and three GEM stations placed downstream of the STT; the other option foresees a shorter STT with 120 cm long tubes plus four GEM chambers, resulting in a lower acceptance of the STT in the forward direction. In order to understand the effects of the tube length reduction in terms of loss in acceptance, let's consider the θ angular range $[0, 180°]$, that can be divided into five regions. They are shown in Fig. 5.9, which presents a sketch of the short Straw Tube Tracker in the plane (z, r): the regions are delimited by the full and dashed lines, corresponding to the angles α, α', β and β', computed with respect to the z axis. The GEM chambers, not drawn in the picture, will be placed downstream of the STT.
The very forward region ($\theta \in [0°, \alpha]$) is the region where the tracks do not go through the straw tracker at all but hit just the Micro–Vertex Detector and the GEM layers. For $\theta \in [\alpha, \alpha']$, some of the skewed layers may not be hit; hence, the z coordinate may not be well reconstructed. For $\theta \in [\alpha', \beta']$, the GEM chambers do not have hits but, on the other side, this is the region where tracks with enough energy traverse all the straw tube layers, both the parallel to z and the skewed ones. Concerning the backward direction, for the ranges $[\beta', \beta]$ and $[\beta, 180°]$ the remarks are the same as for the ranges $[\alpha, \alpha']$ and $[0°, \alpha]$, respectively, except for the fact that the GEM chambers are not present; this means that when the straw tubes are not hit, the tracks only go through the MVD.

The angle values for the two layouts are reported in Tab. 5.1; they are obtained in the following way:

$$\alpha = \arctan\frac{r_{in}}{l_2}, \qquad \alpha' = \arctan\frac{r_{out}}{l_2},$$
$$\beta' = \arctan\frac{r_{out}}{l_1}, \qquad \beta = \arctan\frac{r_{in}}{l_1},$$

where $r_{in} = 15$ cm is the straw tracker inner radius, $r_{out} = 42$ cm is the outer radius, $l_1 = 40$ cm is the distance of the backward STT side to the interaction point and l_2 is the same for the side in the forward direction. Since, in both layouts, the tracker will be placed in such a way that l_1 will be the same, l_2 will be equal to 80 and 110 cm in the case of the shorter and longer tracker, respectively. So the only angles which differ in the two layouts are the ones in the forward region (α, α').
It is clear that shortening the Straw Tube Tracker implies a reduced number of tracks entering it with respect to the longer tracker. Nevertheless, the reduced acceptance of the shorthened tracker will be compensated by the additional (with respect to the longer STT option) GEM tracking station.
In order to compare the performances of the two proposed layouts, two sets of simulations have been performed: first, single track events with fixed total momentum and uniform $\cos\theta$, with $\theta \in [8°, 140°]$; then, again single track events with fixed total momentum but at different fixed θ values.

Table 5.1: Values of the angles α, α', β and β' (see Fig. 5.9).

Geometry layout	α	α'	β'	β
STT 120 cm + 4 GEMs	10.6°	27.7°	133.6°	159.5°
STT 150 cm + 3 GEMs	7.8°	20.9°	133.6°	159.5°

Studies with uniform $\cos\theta$

10^4 μ^- single track events have been generated in the interaction point I.P. ($x = y = z = 0$), with uniform azimuthal angle $\phi \in [0°, 360°]$ and uniform $\cos\theta$ ($\theta \in [8°, 140°]$) with fixed values of total momentum (0.3, 1, 5 GeV/c). The two layouts for the Central Tracker have been used.
Fig. 5.10 shows the reconstructed momentum distributions for particles at (a) 0.3, (b) 1 and (c) 5 GeV/c in case of 150 cm long tubes plus three GEM stations. The red dashed histograms show the prefit results (the helix fit performed by the global tracking package), while the blue histograms reproduce the Kalman fit result.
Each histogram has been fitted with a Gauss function in the range $[\mu - 3\sigma, \mu + 3\sigma]$, where μ is the mean value of the momentum distribution and σ has been calculated by dividing the FWHM of the histogram by 2.35.
Tabs. 5.2 and 5.3 summarise the values of momentum resolution and efficiency

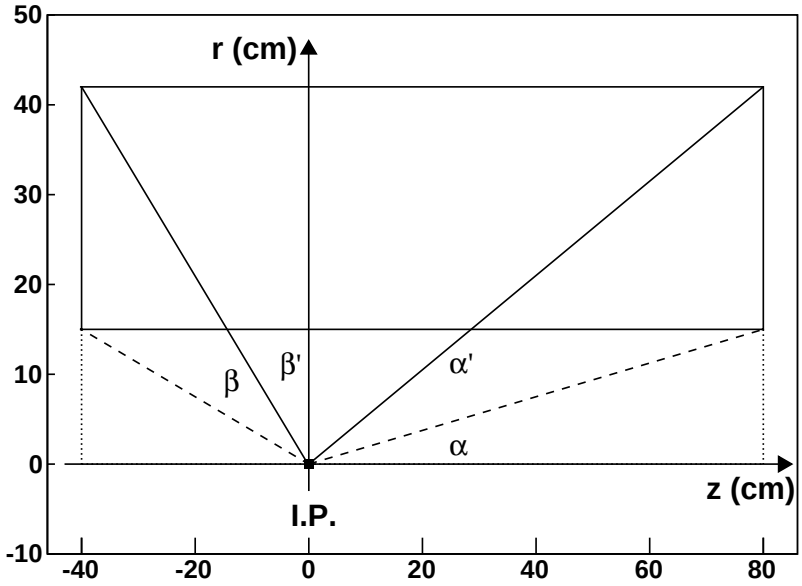

Figure 5.9: Sketch of a section of the Straw Tube Tracker in the plane (z, r), in the case of 120 cm long tubes. The black square in $(0, 0)$ corresponds to the interaction point (I.P.). The full and dashed lines, corresponding to the angles α, α', β and β' (see Tab. 5.1 for their values), divide the plane into the five regions described in the text.

obtained with the two geometries. The resolution is calculated as σ/μ, using the μ and σ values from the gaussian fit; it is then reported in percentage. The efficiency is defined by the integral below the histogram fitted region, divided by the number of generated tracks. In addition, the efficiency "in peak" is reported: it is the number of tracks in the fitted range $(\mu \pm 3\sigma)$ with respect to the total number of tracks.

Table 5.2: Momentum resolution and efficiency for 10^4 μ^- in case of the geometry layout STT 120 cm long + four GEMs.

Momentum	Resolution (%)		Efficiency (%)		Eff. in peak (%)	
(GeV/c)	Prefit	Kalman	Prefit	Kalman	Prefit	Kalman
0.3	2.71	0.72	45.67	45.03	42.25	32.60
1.0	2.80	1.71	91.34	90.12	73.16	72.31
5.0	4.37	3.64	86.33	83.95	68.90	72.04

In all cases the Kalman fit results are better than the prefit ones (as expected), both in terms of mean value and sigma of the distributions. In fact the Kalman fit improves the helix fit results both reducing the width of the distribution

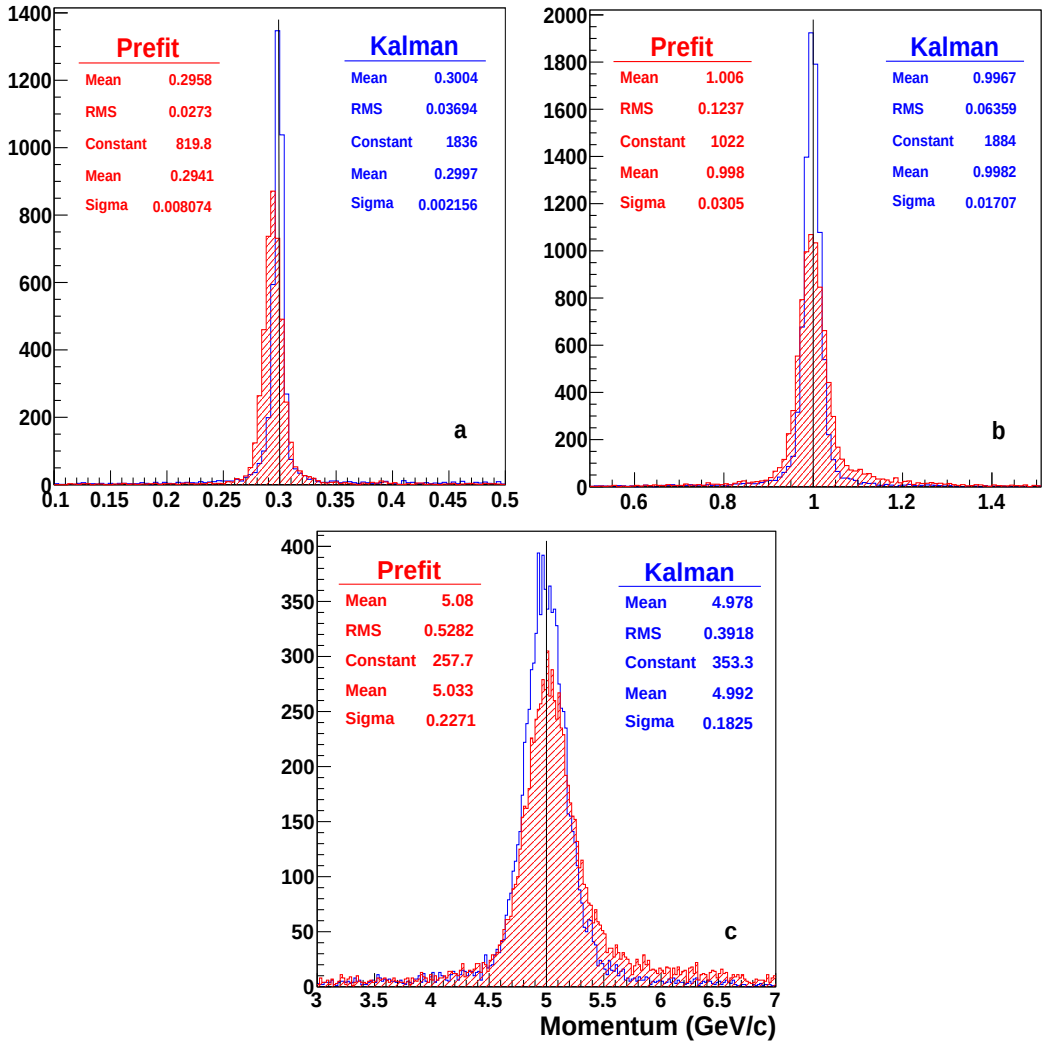

Figure 5.10: Momentum distributions for (a) 0.3, (b) 1 and (c) 5 GeV/c μ^-, reconstructed with helix (red dashed) and Kalman (blue) fits, in case of 150 cm long tubes plus three GEM stations. The statistic boxes report the mean values and RMS of the non fitted histograms, as well as mean and sigma values of the gaussian fits, before and after the Kalman fit.

Table 5.3: Momentum resolution and efficiency for 10^4 μ^- in case of the geometry layout STT 150 cm long + three GEMs (Fig. 5.10).

Momentum	Resolution (%)		Efficiency (%)		Eff. in peak (%)	
(GeV/c)	Prefit	Kalman	Prefit	Kalman	Prefit	Kalman
0.3	2.75	0.72	45.82	43.83	41.79	31.78
1.0	3.06	1.71	92.66	92.52	77.90	78.51
5.0	4.51	3.66	89.28	91.13	73.86	80.10

(i.e. improving the resolution) and shifting the distribution mean value towards a more correct value. On the other hand, the helix fit introduces a systematic offset in the momentum determination giving an underestimated value.
For a better comparison, the Kalman resolutions and efficiencies for the two options are reported in Tab. 5.4.
From the momentum resolution point of view, there are no differences between the two layouts: from the table it is clear that the values are compatible within the errors, when they are not equal. On the other hand, the "STT 150 cm + three GEMs" option seems to be better from the efficiency point of view: it is higher at 1 and 5 GeV/c with respect to the efficiency obtained with the other layout, even if slightly lower at 0.3 GeV/c.

Table 5.4: Comparison of the Kalman fit values of momentum resolution and efficiency for the two foreseen geometries (from Tabs. 5.2 and 5.3): a denotes the STT 120 cm long + four GEMs option; b the STT 150 cm long + three GEMs one.

Momentum (GeV/c)	Resolution (%)		Efficiency (%)		Eff. in peak (%)	
	a	b	a	b	a	b
0.3	0.72	0.72	45.03	43.83	32.60	31.78
1.0	1.71	1.71	90.12	92.52	72.31	78.51
5.0	3.64	3.66	83.95	91.13	72.01	80.10

Studies at fixed θ values
A systematic scan of the momentum resolutions and efficiencies has been performed with fixed angle generated particles, in order to compare the performances of the two geometry layouts with a particular attention to the forward region.
For each layout, 10^4 μ^- single track events have been generated at the interaction point with fixed total momentum (1 GeV/c) and random ϕ ($\phi \in [0°, 360°]$). The θ angular range has been scanned as follows:

i. $\theta = 8°,\ 9°, \ldots, 21°$ in steps of $1°$ ($\pm 0.5°$);

ii. $\theta = 25°,\ 30°,\ 35°,\ 40°$ in steps of $5°$ ($\pm$ 2.5°);

iii. $\theta =\ 50°,\ 80°,\ 110°$ and $140°$ in steps of $10°$ ($\pm$ 5°).

Finally, the events have been reconstructed and the Kalman fit has been performed.
The values of momentum resolution and efficiency in peak (see previous paragraph for the meaning) are summarised in Tab. 5.5 for the option STT 120 cm long plus four GEMs and Tab. 5.6 for the option STT 150 cm long plus three GEMs.

Table 5.5: Comparison of prefit and Kalman fit values of momentum resolution and efficiency for 10^4 μ^- single track events generated at 1 GeV/c and fixed θ angle with the geometry layout STT 120 cm long + four GEMs.

θ angle (°)	Resolution (%)		Efficiency in peak (%)	
	Prefit	Kalman	Prefit	Kalman
8	8.58	2.74	43.26	41.38
9	8.98	2.44	43.86	40.11
10	7.34	2.29	40.41	39.73
11	7.79	2.98	48.14	43.18
12	12.51	4.20	57.78	46.01
13	9.45	3.52	55.10	47.00
14	8.05	3.26	53.62	51.15
15	5.64	2.59	46.61	48.89
16	10.02	2.46	61.71	48.50
17	9.77	2.42	64.93	51.26
18	8.29	2.34	62.36	52.31
19	9.34	1.99	70.83	51.89
20	7.16	1.85	82.43	62.96
21	7.29	1.69	84.32	62.96
25	4.37	2.07	85.11	86.05
30	3.29	1.62	89.86	82.36
35	3.57	1.65	89.70	79.48
40	3.20	1.58	82.58	76.76
50	2.96	1.62	83.57	82.30
80	2.51	1.64	82.15	81.71
110	2.58	1.67	83.85	85.65
140	4.73	2.45	51.56	53.21

The momentum resolution and efficiency plots as function of the θ angle are shown in Figs. 5.11 and 5.12 for $\theta \in [8°, 21°]$ and in Figs. 5.13 and 5.14 for $\theta \in [25°, 140°]$: it has been decided to separate the results as a function of the θ range in order to have a closer look at the forward region, since it is the one

Table 5.6: Comparison of prefit and Kalman fit values of momentum resolution and efficiency for 10^4 μ^- single track events generated at 1 GeV/c and fixed θ angle with the geometry layout STT 150 cm long + three GEMs.

θ angle (°)	Resolution (%)		Efficiency in peak (%)	
	Prefit	Kalman	Prefit	Kalman
8	8.78	3.98	31.01	29.06
9	11.55	6.58	34.99	34.34
10	11.52	6.22	37.48	34.31
11	10.35	5.45	42.52	39.92
12	15.36	5.82	49.94	43.13
13	10.55	4.19	50.04	43.88
14	8.41	2.76	59.02	46.75
15	6.87	2.57	64.62	56.36
16	8.43	2.35	79.33	63.61
17	7.81	2.32	82.57	66.81
18	7.56	2.15	84.87	72.86
19	8.63	1.89	97.74	72.06
20	6.91	1.69	99.81	84.32
21	6.61	1.58	99.15	80.11
25	3.52	1.73	91.08	87.08
30	3.38	1.58	90.47	82.30
35	3.49	1.61	88.97	79.70
40	3.21	1.65	82.03	82.80
50	2.85	1.59	82.44	82.86
80	2.59	1.65	83.02	82.04
110	2.69	1.64	86.11	85.86
140	4.94	2.42	51.39	52.07

affected by the straw tubes shortening.
From the plots, a general improvement due to the Kalman filter (blue squares in the figures) is evident.
Concerning the region where the fine scan has been performed, it is evident from Fig. 5.11 that the momentum resolution is better in the case of STT 120 cm long + four GEMs up to $\theta = 14°$. This can be explained as follows: when the STT 120 cm + four GEMs option is considered, tracks with $\theta < 15°$ do not hit at all ($\theta < 10.6°$) or hit just few axial layers of straw tubes. So the tracking is performed mainly with the hits produced in the MVD and the GEMs; hence the global resolution is dominated by the one of these two detectors, which are very precise. With the other layout, tracks with these θ values do not necessarily hit all the GEM stations, so the available number of very precise points may be less than in the previous case. For sure, there will be more hits in the straw tubes, but in the tracker region where only ($\theta < 11.6°$) or mainly axial

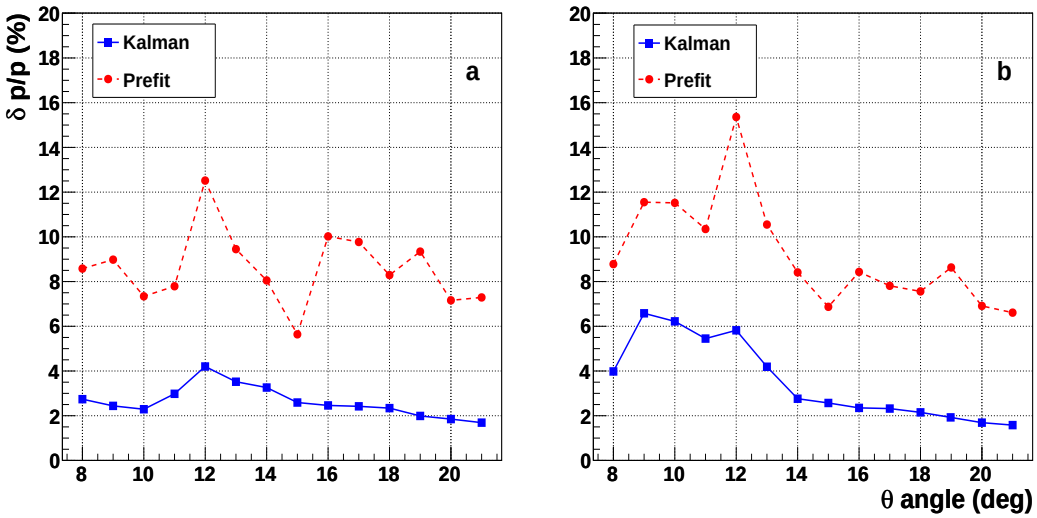

Figure 5.11: Momentum resolution vs. θ starting angle for 1 GeV/c μ^- single track events, in the range $\theta \in [8°, 21°]$: (a) STT 120 cm long + four GEMs, (b) STT 150 cm long + three GEMs. The red circles and dashed line are the prefit results, the blue squares and full line are the Kalman ones (see Tab. 5.5 and Tab. 5.6).

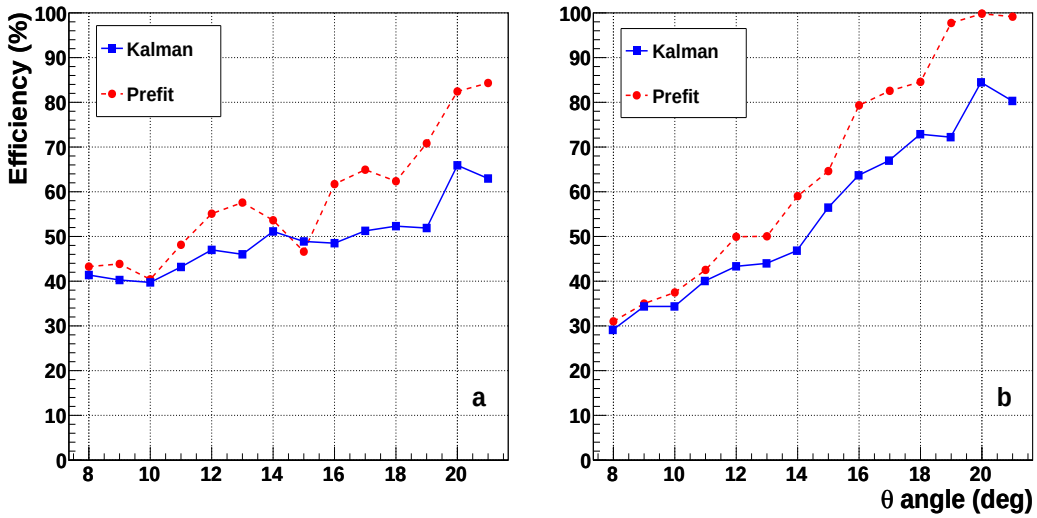

Figure 5.12: Reconstruction efficiency vs. θ starting angle for 1 GeV/c μ^- single track events, in the range $\theta \in [8°, 21°]$: (a) STT 120 cm long + four GEMs, (b) STT 150 cm long + three GEMs. The red circles and dashed line are the prefit results, the blue squares and full line are the Kalman ones (see Tab. 5.5 and Tab. 5.6).

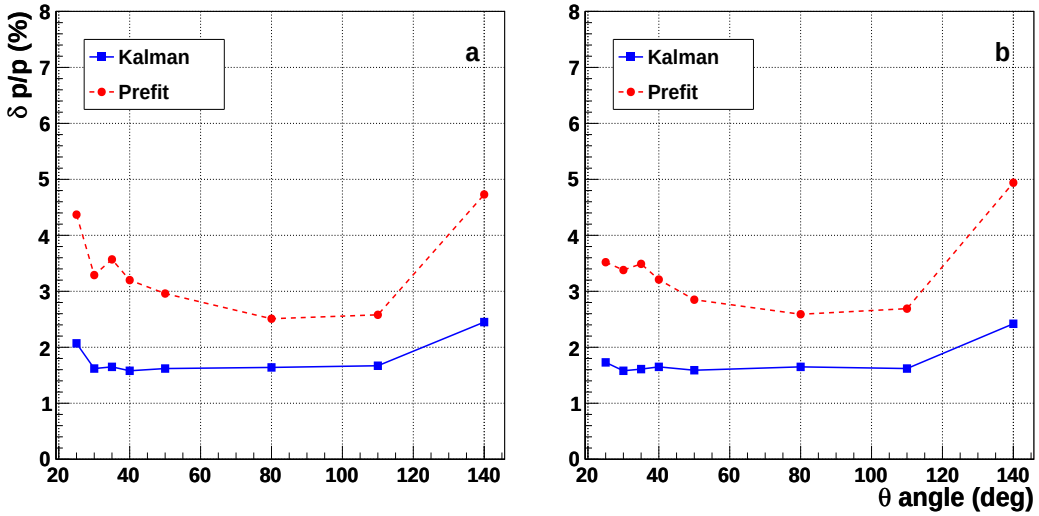

Figure 5.13: Momentum resolution vs. θ starting angle for 1 GeV/c μ^- single track events, in the range $\theta \in [25°, 140°]$: (a) STT 120 cm long + four GEMs; (b), STT 150 cm long + three GEMs. The red circles and dashed line are the prefit results, the blue squares and full line are the Kalman ones (see Tab. 5.5 and Tab. 5.6).

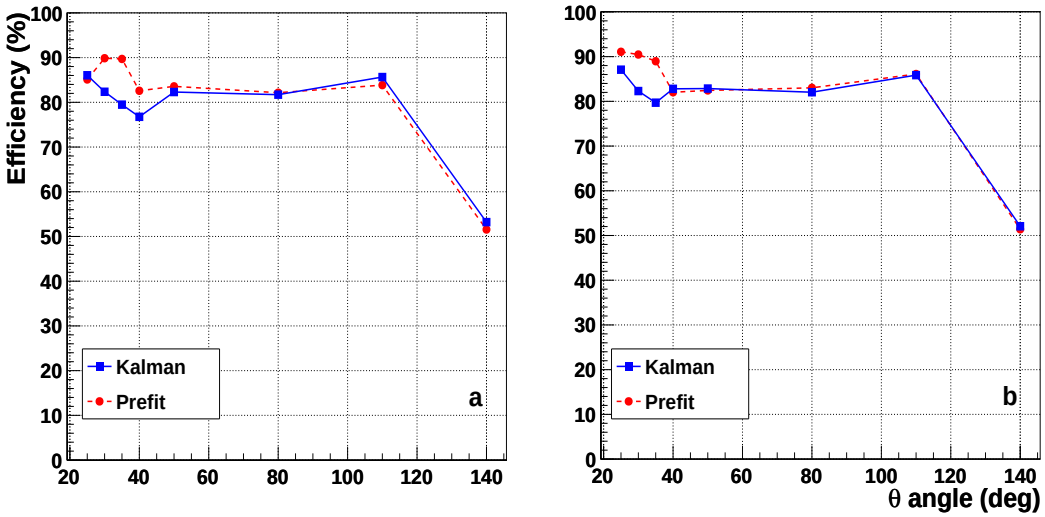

Figure 5.14: Reconstruction efficiency vs. θ starting angle for 1 GeV/c μ^- single track events, in the range $\theta \in [25°, 140°]$: (a) STT 120 cm long + four GEMs; (b) STT 150 cm long + three GEMs. The red circles and dashed line are the prefit results, the blue squares and full line are the Kalman ones (see Tab. 5.5 and Tab. 5.6).

layers are present. This would prevent from reconstructing the z coordinate of the track in the STT, resulting in a worse global resolution and in a tracking efficiency lower than that of the short STT layout in the same angular region (see also Fig. 5.12).
Then, for tracks with $\theta \in [15°, 25°]$, the performances of the two layouts in terms of momentum resolution are comparable within the errors.
Finally, concerning the angular region $\theta > 25°$, Figs. 5.13 and 5.14 show that both the momentum resolution and the efficiency of the two layouts are comparable within the errors, as expected: in fact, this is the angular range where, according to Tab. 5.1, the particles traverse only MVD and STT in the case of both layouts and there are no reasons, apart from statistics, why they should be different.

5.7.2.2 Dependence on the skew angle

Other tests have been implemented in order to study the dependence of the z residuals and of the momentum resolution on the skew angle of the tilted tubes.
10^4 μ^- single track events were generated in the interaction point with a total momentum of 1 GeV/c, uniformly in ϕ ($\phi \in [0°, 360°]$) and in $cos\theta$ ($\theta \in [28°, 133°]$[5]).
Four different geometry layouts, corresponding respectively to a skew angle of 3°, 4°, 5° and 10°, have been used.
In Fig. 5.15 the distributions of the z residuals are shown and in Tab. 5.7 the mean and sigma values of the same distributions are summarised.

Table 5.7: Mean values μ and σ of the gaussian fits of the z residual distributions shown in Fig. 5.15 as a function of the skew angles.

Skew angle	μ (cm)	σ (cm)
3°	−0.00199	0.366
4°	−0.00047	0.285
5°	0.00079	0.229
10°	−0.00066	0.133

As expected, it is clear that for bigger values of the skew angle the mean value of the z residuals distributions is shifted towards 0, the width of the distributions is reduced (see σ values in Tab. 5.7), and there is an enhancement of the peak of the distribution.

[5]Tracks generated in this θ range traverse for sure the straw tracker, both in the case of the 120 cm long tracker and in the case of the 150 cm long tubes (see Tab. 5.1).

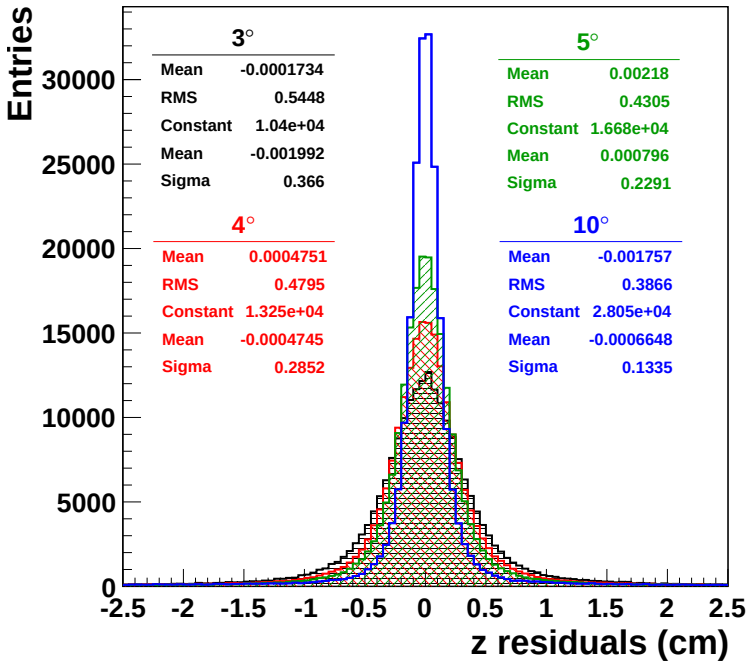

Figure 5.15: Distributions of the z residuals for 10^4 μ^- single track events at 1 GeV/c: black histogram with horizontal lines, 3°; red left dashed histogram, 4°; green right dashed histogram, 5°; blue empty histogram, 10°.

Concerning the dependence of the momentum resolution and reconstruction efficiency on the skew angle, the values of the momentum resolutions are summarised in Tab. 5.8. They do not seem to be too much affected by the increasing value of the skew angle (compatible within the errors): this is due to the fact that these values are obtained after the Kalman filter has been applied on the global reconstructed tracks, so taking also into account the MVD points. Since they are very precise, the overall resolution is dominated by the MVD one. Concerning the efficiency, it increases with the skew angle.

Table 5.8: Momentum resolution and efficiency values for 1 GeV/c μ^- as a function of the skew angles.

Skew angle	Resolution (%)	Efficiency (%)	Eff. in peak (%)
3°	1.63	92.98	82.65
4°	1.68	93.85	83.20
5°	1.60	94.72	84.87
10°	1.60	94.59	84.28

5.7.2.3 Dependence on the single tube resolution

Further tests have been implemented in order to study the dependence of the momentum resolution on the single tube resolution curves.
10^4 μ^- single track events were simulated at different momenta (0.3, 1., 5. GeV/c) using the geometry layout with STT 150 cm long. They were generated at the interaction point, uniformly in ϕ ($\phi \in [0°, 360°]$) and in $cos\theta$, with the azimuthal angle $\theta \in [28°, 133°]$.
Five sets of simulations in correspondence of each value of momentum, using different single tube resolutions, have been performed. In particular:

- the simulated curve with magnetic field (Fig. 3.15), obtained from the GARFIELD [36] simulations on the single tube response [37];
- the curve experimentally obtained in Jülich at COSY–TOF without magnetic field (Fig. 4.9);
- the curve experimentally obtained in Jülich from the prototype without magnetic field (Fig. 4.24);
- a flat resolution curve with $\sigma_{xy} = 100$ μm;
- a flat resolution curve with $\sigma_{xy} = 150$ μm;
- a flat resolution curve with $\sigma_{xy} = 300$ μm.

The values of resolution and efficiency are summarised in Tab. 5.9. The summary plots in Fig. 5.16 show the behaviour of momentum resolution and efficiency at different momentum values as functions of the different single tube resolution curves.
The results obtained with the experimental and simulated resolution curves, as well as with the flat curve at 100 μm, are very similar and compatible within the errors. In addition, both momentum resolutions and efficiencies become lower while worsening the single tube resolution, as expected.

5.7.2.4 Summary of the results

The performances of the Central Tracker have been investigated through the simulation of different sets of single track (muon) events, generated at the interaction point at different momentum values, polar angle θ and uniform azimuthal angle ϕ.
The tracks have been fitted by applying the procedure summarised in Sec. 5.6.
The attention has then been focused on the momentum resolution of the generated particles and on the tracking efficiency.
In all the sets of simulations, the improvements due to the Kalman filter is evident, in particular in terms of momentum resolution: the mean values of the momentum distributions after the Kalman fit are more centered around

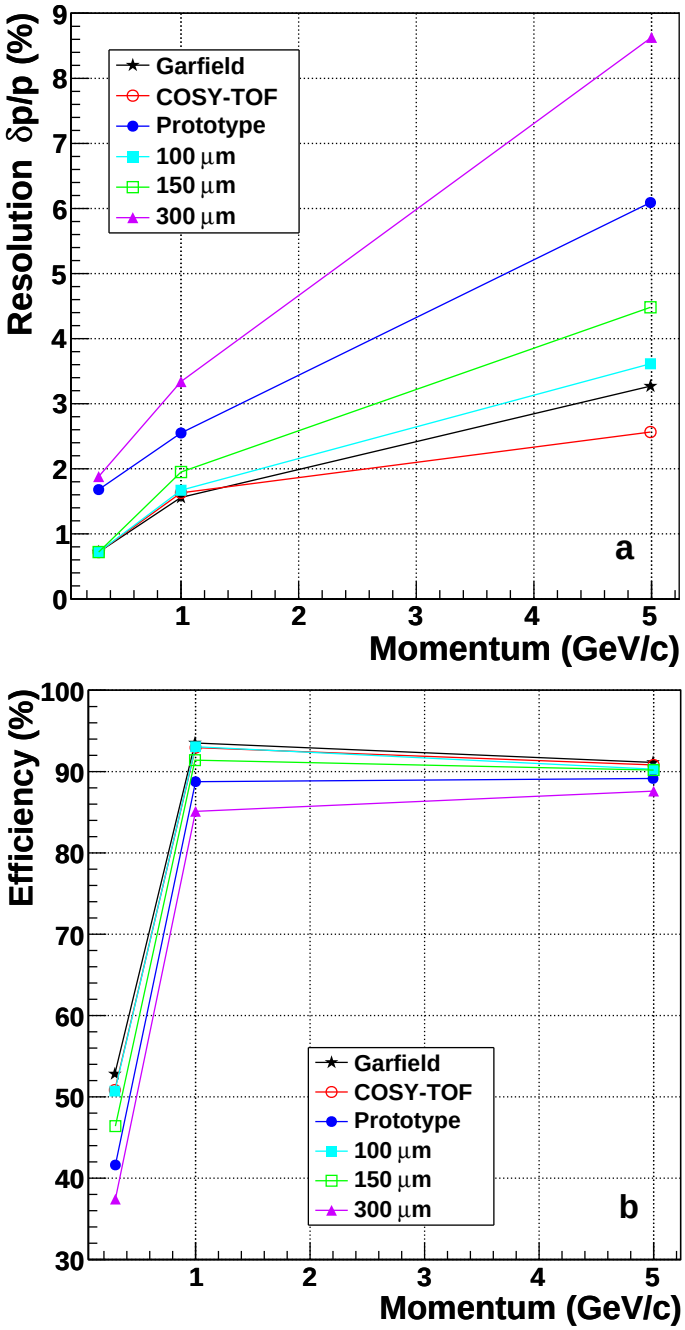

Figure 5.16: Momentum resolution (a) and efficiency (b) vs. particle momentum, as a function of the different single tube resolution: GARFIELD simulated curve (black stars), COSY–TOF experimental curve (red empty circles), Jülich prototype experimental curve (blue full circles), 100 μm flat (cyan full squares), 150 μm flat (green empty squares) and 300 μm flat (violet triangles).

Table 5.9: Momentum resolution, efficiency and efficiency in peak from Kalman fit for $10^4\mu^-$ single track events at 0.3, 1 and 5 GeV/c, obtained by varying the single tube resolution curve.

Momentum (GeV/c)	Single tube resolution curve	Resolution (%)	Efficiency (%)	Efficiency in peak (%)
0.3	Simulated	0.72	52.78	41.34
	COSY–TOF	0.72	50.74	39.56
	Prototype	1.68	41.62	41.34
	100 μm flat	0.72	50.63	39.70
	150 μm flat	0.72	46.40	35.42
	300 μm flat	1.88	37.42	28.94
1	Simulated	1.56	93.46	83.92
	COSY–TOF	1.63	92.95	82.65
	Prototype	2.55	88.76	83.92
	100 μm flat	1.67	93.06	82.48
	150 μm flat	1.95	91.36	78.52
	300 μm flat	3.34	85.11	75.99
5	Simulated	3.26	91.04	81.10
	COSY–TOF	3.67	90.82	82.69
	Prototype	6.09	89.03	79.14
	100 μm flat	3.61	90.30	81.23
	150 μm flat	4.47	90.19	82.61
	300 μm flat	8.63	87.60	81.59

the correct value than the ones obtained after the global helix fit. In addition, the Kalman distributions are narrower than the helix ones, resulting in better resolution values.

Two design options for the layout of the Central Tracker with STT have been studied: one consisting in 120 cm long straw tubes plus four GEM chambers and the other one made of 150 cm long straw tubes plus three GEMs.
Tests with tracks generated with random θ and ϕ show that the momentum resolution obtained with the two layouts are compatible within the errors, ranging from $\sim$ 0.7% in case of 0.3 GeV/c tracks, to $\sim$ 3.65% for 5 GeV/c tracks (Tab. 5.4).
From a more detailed investigation through the simulation of tracks scanning the forward angular region in steps of $\pm 0.5°$, a difference in the performances of the two layouts emerges. The results (Figs. 5.11–5.12) show that a better momentum resolution is attained in the case of 120 cm long tubes plus four

GEMs: in fact, with this layout and in such a forward region there are not so many hits in the STT; hence the global resolution is dominated by that of the MVD and of the GEMs, which are very precise.
Concerning the central and backward angular region ($\theta > 25°$), where the two layouts are geometrically equivalent, the same results have been obtained in correspondence of the two options (Fig. 5.13–5.14).

The dependence of the performances on the skew angle of the tilted straw layers has been studied too. Although the choice of a higher value for the skew angle could facilitate the mechanical construction of the tracker, the performances are not too much affected: the momentum resolution does not improve significantly when going from 3° to 10° (Tab. 5.8).

Finally, it has been studied the effect that the spatial resolution of the single straw tubes has on the tracker performances (Tabs. 5.9, Fig. 5.16).
The results obtained with the experimental curve without magnetic field from COSY–TOF, the GARFIELD curve with magnetic field and the 100 μm flat resolution are compatible within the errors. Concerning the other resolutions used in the tests, the results show that the worse the single tube resolution, the worse the tracker performances, as expected.

Bibliography

[1] $\overline{\text{P}}$ANDA Computing Group, *A data analysis and simulation framework for the $\overline{P}$ANDA collaboration*, Scientific Report GSI, 2006.

[2] $\overline{\text{P}}$ANDA Computing Group, *Status of the PandaROOT simulation and analysis framework*, Scientific Report GSI, 2007.

[3] A. Wronska for the $\overline{\text{P}}$ANDA Collaboration, *Simulation of the $\overline{P}$ANDA experiment with PandaROOT*, eConf C070910(2007)307, Proceedings of MENU2007.

[4] S. Spataro , Jour. Phys. Conf. Ser. 119, 032035 (2008), doi:10.1088/1742-6596/119/3/032035.

[5] CBM Collaboration, *CBM Technical Status Report* GSI, Darmstadt, 2005.

[6] The HADES Collaboration, *Proposal for a High Acceptance Spectrometer* GSI, Darmstadt, 1994.

[7] R. Schicker et al., Nucl. Instr. and Meth. A 380 (1996) 586-596.

[8] http://www-land.gsi.de/R3B.

[9] http://root.cern.ch.

[10] http://root.cern.ch/root/vmc.

[11] I. Hrivnacova, D. Adamova, V. Berejnoi, R. Brun, F. Carminati, A. Fasso, E. Futo, A. Gheata, I. Gonzalez Caballero, A. Morsch for the ALICE Collaboration, *The Virtual Monte Carlo*, ArXiv Computer Science e-prints, cs/0306005.

[12] GEANT3 manual, CERN Program Library Long Writeup W5013 (1993).

[13] GEANT4 Collaboration, CERN/LHCC 98-44, Geneva, 1998.

[14] A. Fassò, A. Ferrari, J. Ranft, P.R. Sala, CERN-2005-10, INFN/TC 05/11, SLAC-R-773 (2005).

[15] http://www.slac.stanford.edu/~lange/EvtGen.

[16] A. Capella, U. Sukhatme, C.-I. Tan, J. Tran Thanh Van, Phys.'Rep. 236 (1994) 225-329.

[17] M. Bleicher et al., J. Phys. G 25 (1999) 1859-1896.

[18] S.A. Bass et al., Prog. Part. Nucl. Phys. 41 (1998) 225-369.

[19] Vector Fields Ltd. Oxford, U.K., TOSCA/OPERA–3d Software, http://www.vectorfields.com.

[20] L. Lavezzi, *The fit of nuclear tracks in high precision spectroscopy experiments*, PhD Thesis, Pavia University (Italy), November 2007, http://bamboo.pv.infn.it/doc/L_Lavezzi.pdf.

[21] S. Costanza and L. Lavezzi, *Study of the Kalman filter performances with STT + MVD*, $\overline{\text{P}}$ANDA Report PV/01-09, http://panda-wiki.gsi.de/pub/Computing/PandaRootPapers/tracking.pdf.

[22] M. Hansroul et al., Nucl. Instr. and Meth. A 270 (1988), 498-501.

[23] F. James, *MINUIT, Function Minimization and Error Analysis, Reference Manual*, Version 94.1, CERN Program Library Long Writeup D506, CERN Geneva, Switzerland, 1994.

[24] P. Hough, *Methods and Means for Recognizing Complex Patterns*, U.S.Patent 3069645 (1962).

[25] R.E. Kalman, Transaction of the ASME – Journal of Basic Engineering Series D 82 (1960) 35.

[26] R. Frühwirth, Nucl. Instr. and Meth. A 262 (1987) 444.

[27] G. Kitagawa, Annals of the Institute of Statistical Mathematics 46 (4) (1994) 605.

[28] R. Frühwirth, A. Strandlie, Computer Physics Communications 120 (1999) 197.

[29] A. Fontana, P. Genova, L. Lavezzi and A. Rotondi, *Track following in dense media and inhomogeneous magnetic fields*, $\overline{\text{P}}$ANDA Report PV/01-07.

[30] R. Frühwirth et al., *Data Analysis Techniques For High Energy Physics*, 2^{nd} edition, Cambridge University Press, Cambridge, 2000.

[31] V. Innocente and E. Nagy, Nucl. Instr. and Meth. A 324 (1993) 297.

[32] http://sourceforge.net/projects/genfit.

[33] C. Höppner et al., Nucl. Instr. and Meth. A(2010), doi:10.1016/j.nima.2010.03.136.

[34] W. Wittek, EMC internal reports: EMC/80/15, EMC/CSQ/80/39, 81/13 and 81/18.

[35] B.B. Niczyporuk, M. Maire and E. Nagy, *Track fitting in a Inhomogeneous Magnetic Field*, Report CEBAF-PR-91-004, 1991.

[36] R. Veenhof, *GARFIELD, Simulation of gaseous detectors, Version 7.04*, CERN Program library write-up W 5050, CERN, Geneva, Switzerland.

[37] S. Costanza et al., Nucl. Instr. and Meth. A 617 (2010) 148-150.

Part IV

Results

Chapter 6

Study of physics channels

Two benchmark channels covering relevant topics for the $\overline{\mathrm{P}}$ANDA physics and allowing a comparison with well known results from other experiments have been chosen to be studied in this thesis:

$$\overline{p}p \rightarrow \Psi(3770) \rightarrow D^+D^- \rightarrow (K^-2\pi^+) + (K^+2\pi^-)$$

and

$$\overline{p}p \rightarrow \eta_c(2979) \rightarrow K^0_S K^+\pi^-.$$

The main purpose is to demonstrate that the proposed detector setup can fulfil the physics case and to study the invariant mass resolutions, on which the attention will be focused.

The analysis procedure and the results obtained will be presented in the following sections; in addition, the open points and the software–related problems (i.e. the low reconstruction efficiency) will be pointed out.
It is important to keep in mind that the software used for these analyses is rather complicated and not finished yet. For example, since the routines for particle identification are not ready for all individual subdetectors, both benchmark results are based on studies without background production. The same consideration is true also for the kinematic fitting routines, which require a precise knowledge from individual subdetectors or detector combinations about spatial and energy resolution of all reconstructed particles: these routines have been used just in the study of the $\Psi(3770)$ decay.
Since there is still a lot of space for improvements of tracking reconstruction, fitting and particle identification, better results could be certainly achieved in the future, once the software will be ready in all its parts.

6.1 Analysis of $\overline{p}p \rightarrow \Psi(3770) \rightarrow D^+D^-$

The study of the charmonium spectrum above the $D\overline{D}$ breakup threshold at 3.73 GeV/c^2 is one important part of the $\overline{\text{P}}$ANDA physics program (Sec. 1.2.1.1); it is relevant not only for the open charm spectroscopy, but also for the search for charmed hybrids decaying into $D\overline{D}$ and the investigation of rare decays and CP violation in the D meson sector.
In order to study the tracking capabilities and performances of the $\overline{\text{P}}$ANDA Central Tracker in the detection of charmonium states above the open charm threshold, the following channel has been chosen:

$$\overline{p}p \rightarrow \Psi(3770) \rightarrow D^+D^-.$$

The dominant channel for the $\Psi(3770)$ decay is a s–wave 2–body decay into a $D\overline{D}$ pair [1].
Many decay modes are possible for D mesons; for this analysis, the channel $D^\pm \rightarrow K^\mp\pi^\pm\pi^\pm$ has been chosen, since it can be completely reconstructed by using the Central Tracker thanks, to the absence of neutral particles in the final state.
The channel has been simulated at an energy in the centre of mass corresponding to $\sqrt{s} = m_{\Psi(3770)}$. The production has been done directly into the $D\overline{D}$ pair, which corresponds to ≈ 40 MeV above the open charm threshold.
In order to estimate the $D\overline{D}$ cross section, a Breit–Wigner approach can be used [2]:

$$\sigma_R(s) \equiv \frac{4\pi(\hbar c)^2}{(s - 4m_p^2c^4)} \frac{B_{in}B_{out}}{1 + [2(\sqrt{s} - M_Rc^2)/\Gamma_R]^2} \tag{6.1}$$

where M_R and Γ_R are the mass and the full width of the resonance (the $\Psi(3770)$ for this channel) and m_p is the proton mass. B_{in} and B_{out} are the branching ratios $B_{in} \equiv B(\Psi(3770) \rightarrow \overline{p}p)$ and $B_{out} \equiv B(\Psi(3770) \rightarrow D^+D^-)$.
Since the charm production cross sections close to the open charm threshold in $\overline{p}p$ annihilations are unknown, B_{in} can be estimated by scaling the known branching ratio $J/\psi \rightarrow \overline{p}p$ [3]:

$$\begin{aligned} B_{in} \equiv B(\Psi(3770) \rightarrow \overline{p}p) &= B(J/\psi \rightarrow \overline{p}p) \cdot \Gamma_{J/\psi}/\Gamma_{\Psi(3770)} = \\ &= 2.17 \cdot 10^{-3} \times \frac{93.2 \text{ keV}}{27.3 \text{ MeV}} = 7.4 \cdot 10^{-6}. \\ B_{out} &\equiv B(\Psi(3770) \rightarrow D^+D^-) \simeq 36\%. \end{aligned} \tag{6.2}$$

For the condition $\sqrt{s} = M_Rc^2$, the cross section results in:

$$\sigma(\overline{p}p \rightarrow \Psi(3770) \rightarrow D^+D^-) \simeq 1.22 \text{ nb}.$$

This value can be considered as a lower limit for the cross section; other considerations [4] yield a much higher value of the cross section(~ 150 nb). The lower value has been used in the following calculations.

Since the branching ratio of this decay is $B(D^\pm \to K^\mp\pi^\pm\pi^\pm) \simeq (9.29 \pm 0.25)\%$ [1], the total cross section for the chosen channel is:

$$\sigma(\overline{p}p \to D^+D^- \to K^-\pi^+\pi^+ + \ c.c.) \simeq 10.6 \text{ pb}.$$

Finally, assuming 45 mb for the $\overline{p}p$ inelastic cross section and a 100% suppression of elastic events, the signal to background ratio is:

$$R \equiv \frac{\sigma(\text{signal})}{\sigma(\overline{p}p \to X)} = \frac{1.06 \cdot 10^{-11}}{4.5 \cdot 10^{-2}} = 2.4 \cdot 10^{-10}.$$

Since the particle identification (PID) in PandaROOT is not yet ready for all subdetectors, the simulation of background events in order to evaluate the ability to suppress the background to a sufficient level was not performed. As soon as the PID code will be ready, a detailed study of specific background reaction is foreseen. For example, it could be possible to simulate inelastic collisions coming from $\overline{p}p$ annihilations and including six prong events, which could be kinematically interpreted as signal events, such as $\overline{p}p \to K^+K^-2\pi^+2\pi^-$, $\overline{p}p \to 3\pi^+3\pi^-$ and $\overline{p}p \to 3\pi^+3\pi^-\pi^0$.
Such background studies have been already performed in the framework that has preceded PandaROOT; the results are reported in Ref. [5].

6.1.1 Event simulation

6.1.1.1 Generation

10^5 events have been generated with the EvtGen [6] generator. This is one of the event generators used for the simulation of particle decays in high energy experiments, such as Belle, BaBar, CDF and many others. It is written in C++ and it allows to handle complex sequential decay channels, like the decays of bottomonium and charmonium states. There are about 60 models in it but many others describing new decays can be implemented by the users; it is even possible to set angular distributions according to the experimental results [7]. The user can set the desired decay chain by himself; the following is an example of the decay file used for the generation of the $\Psi(3770)$ events:

```
Decay psi(3770)
1.00 D+ D- PHSP;
Enddecay
Decay D+
1.00 K- pi+ pi+ PHSP;
Enddecay
Decay D-
1.00 K+ pi- pi- PHSP;
Enddecay
End
```

As it can be seen, the decay of the $\Psi(3770)$ resonance has been set to D^+D^- with branching ratio 1; the same consideration for the decays of the two D mesons. The model used is PHSP: it generates a generic n–bodies phase space, mediated on the spin of the initial and final states.
The output of EvtGen is an ASCII file like the one shown in Tab. 6.1.

Table 6.1: EvtGen output. See the text for a detailed explanation.

N	Id	Ist	DF	DL	px	py	pz
0	40443	2	1	2	0.00000000	-0.00000000	6.56864758
1	411	2	3	5	-0.10155585	-0.10117576	2.89165554
2	-411	2	6	8	0.10155585	0.10117576	3.67699204
3	-321	1	-1	-1	-0.40708232	-0.47942717	1.50353817
4	211	1	-1	-1	0.43376330	0.22751339	1.41096498
5	211	1	-1	-1	-0.12823683	0.15073802	-0.02284760
6	321	1	-1	-1	-0.46110391	-0.00055324	0.76275362
7	-211	1	-1	-1	0.09292556	-0.07710118	2.27918418
8	-211	1	-1	-1	0.46973420	0.17883018	0.63505423

E	t	x	y	z
7.57359076	0.00000000	0.00000000	0.00000000	0.00000000
3.44623046	0.00000000	0.00000000	0.00000000	0.00000000
4.12736030	0.00000000	0.00000000	-0.00000000	0.00000000
1.70291321	0.00833487	-0.00024562	-0.00024470	0.00699360
1.50007163	0.00833487	-0.00024562	-0.00024470	0.00699360
0.24324562	0.00833487	-0.00024562	-0.00024470	0.00699360
1.01888672	0.71252716	0.01753210	0.01746648	0.63477780
2.28664385	0.71252716	0.01753210	0.01746648	0.63477780
0.82182973	0.71252716	0.01753210	0.01746648	0.63477780

In the first column there is an increasing number N associated with particles ordering (the number 0 refers to the mother particle); Id is the identification number associated to each particle ($\Psi(3770) = 40443$, $D^{\pm} = \pm 411$, $K^{\pm} = \pm 321$, $\pi^{\pm} = \pm 211$). Ist is a number equal to 1 or 2, depending on the fact that the particle is stable or not. DF (Daughter First) and DL (Daughter Last) indicate the N values of the first and last daughter particles produced in the decay; in the case of a non decaying particle, DF and DL are set to -1. Finally, the momentum components (GeV/c), the energy (GeV) and the space–time coordinates follow (mm).
The events have been generated at the interaction point $(0, 0, 0)$ with an antiproton beam momentum of ~ 6.57 GeV/c along the z direction, in order to have an energy in the CMS equal to the $\Psi(3770)$ mass. The input $D^{\pm}$ masses to the simulation are 1.8693 GeV/c^2, while for the Ψ the mass is 3.7699 GeV/c^2 and the width is 0.0236 GeV/c^2.

6.1.1.2 Simulation

The EvtGen output file, through a suited interpreter, has been used as input for the simulation. All the sensitive detectors have been included in the simulation, in order to take into account the whole material budget. Concerning the Central Tracker, the option with 120 cm long straw tubes together with four GEM tracking stations has been chosen.
Fig. 6.1 shows the total momentum of the generated kaons and pions as a function of the θ angle: from these plots, it is possible to have an idea of the flight direction and momentum of the daughter particles.

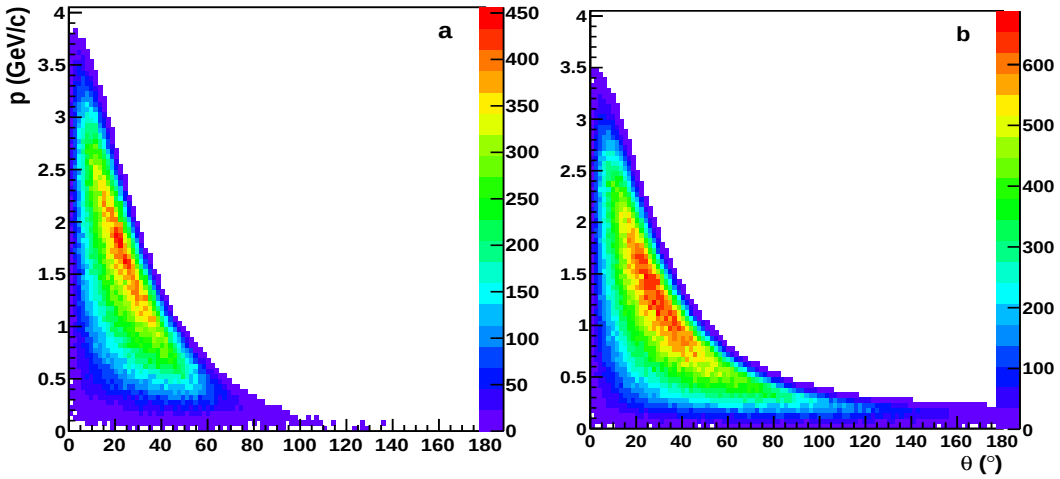

Figure 6.1: Momentum distributions of the generated kaons (a) and pions (b).

By looking at the red spots in the plots, it is possible to estimate the mean values of θ and p (θ, p) of the tracks: in particular, they are $(23.69°, 1.477$ GeV/c) and $(34.77°, 1.088$ GeV/c) for kaons and pions, respectively. From these numbers, it is clear that most of the particles are flying in the forward direction, and this is more evident from the angular distributions of Fig. 6.2.
In particular, for the $\Psi(3770)$ simulated events, Tab. 6.2 reports the percentages related to the different angular regions for kaons and pions.
The high number of tracks having not so many hits in the straw tracker may affect the reconstruction efficiency and the quality of the fit.

6.1.1.3 Digitization

In the digitization step, all the detectors have been included.
Concerning the straw tubes, the reconstructed radii have been obtained by sampling both from the COSY–TOF resolution curve (Fig. 4.9) and the resolution curve obtained by the analysis of the data from the Jülich prototype (Fig. 4.24). Since these two curves represent the lower and upper limits for the single straw resolution (see Sec. 4.5.2), the idea was to check their effect on the final resolution.

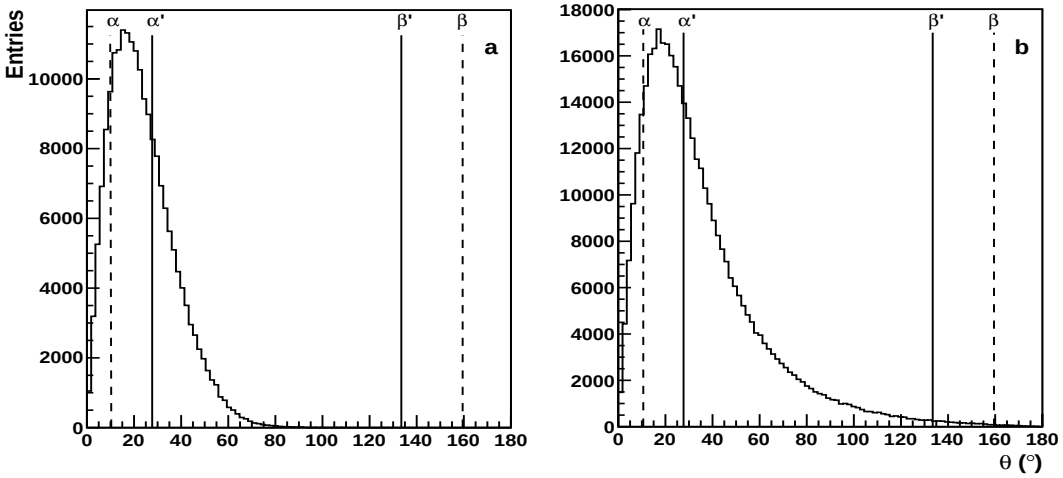

Figure 6.2: Angular distributions of the generated kaons (a) and pions (b). $\alpha = 10.6°$, $\alpha' = 27.7°$, $\beta' = 133.6°$ and $\beta = 159.5°$ (see Sec. 5.7.2.1 for a detailed explanation of the five regions the θ angular range has been divided into).

Table 6.2: Angular distribution of the simulated kaons and pions for the $\Psi(3770)$ decay channel.

Angular range (°)	Kaons (%)	Pions (%)
0 - 10.6	15.88	11.22
10.6 - 27.7	51.73	39.97
27.7 - 133.6	32.39	48.11
133.6 - 159.5	∼0	0.58
159.5 - 180	0	0.12

6.1.1.4 Reconstruction

The reconstruction has been performed using only the tracking detectors belonging to the Target Spectrometer: Micro–Vertex Detector, Straw Tube Tracker and GEM chambers.

The track fitting has been performed by using the global tracking package described in Sec. 5.3.
Since some problems concerning the efficiency came up (see in the following Tabs. 6.4 and 6.5), in order to increase the number of tracks passing all the cuts it has been decided to use the ideal pattern recognition: the Monte Carlo truth has been used to assign hits to the tracks.
By looking at the invariant masses (as an example) of the D mesons after the global fit, it has been noticed that the distributions were not peaked around

the right value ($m_{D^\pm} = 1869.3$ MeV/c^2), as shown in Fig. 6.3.a. This shows that the helix fit performed by the global tracking package is not suitable in the GEM region. In fact, the particle trajectory can be assumed to be a helix (which is the hypothesis used by the global tracking package) only in case of a constant magnetic field. Instead, in the region between the solenoid and the forward spectrometer, where the GEM layers are placed, the field inhomogeneities must be taken into account and a helix fit is not the best choice to describe the track trajectories.
Nevertheless, by completely excluding the GEM points both from the prefit and from the Kalman fit, it is evident from Fig. 6.3.b that the prefit results are not improved by the Kalman fit. This is probably due to the fact that the momenta of the tracks going in the forward direction are so badly reconstructed without GEM chambers that the Kalman filter is not able to improve the prefit results.

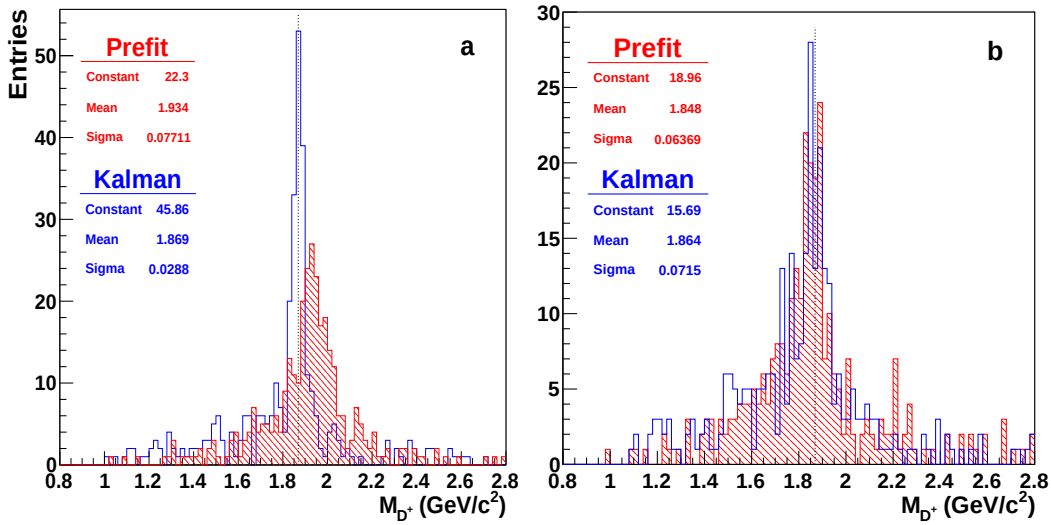

Figure 6.3: D^+ invariant mass obtained when GEM chambers are included both in the prefit and in the Kalman fit (a) and when GEM chambers are excluded both from the prefit and from the Kalman fit (b). Red dashed histogram: prefit; blue empty histogram: Kalman fit. The black dotted line indicates the input value for the D^+ mass ($m_D = 1869.3$ MeV/c^2). The values in the statistics boxes are the gaussian fit parameters of the distributions.

Therefore, in order to give to the Kalman filter a better starting momentum, it has been decided to include the GEM hits to perform the global pattern recognition, to exclude them from the prefit and to include them in the Kalman filter. The result is shown in Fig. 6.4: the peak of the prefit distribution (red histogram in the plot) is now centered around the right value and the results are improved by the Kalman fit (higher peak, smaller width).

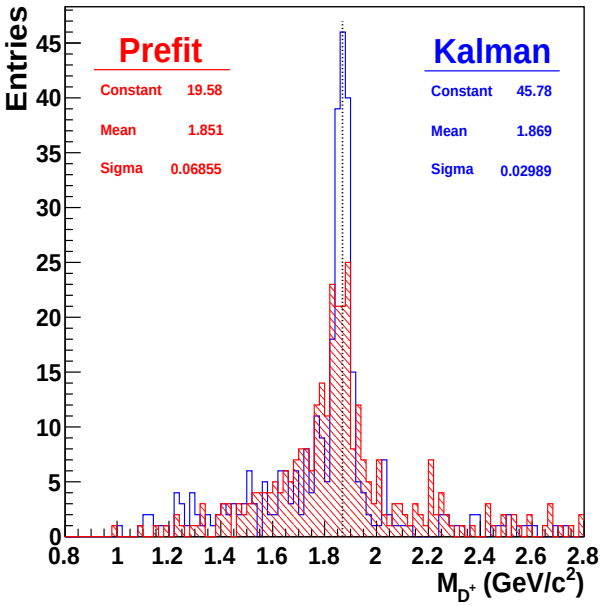

Figure 6.4: D^+ invariant mass in the case of GEM chambers excluded from the prefit and included in the Kalman fit. Red dashed histogram: prefit; blue empty histogram: Kalman fit. The dotted line indicates the input value for the D^+ mass ($m_D = 1869.3$ MeV/c^2). The values in the statistics boxes are the gaussian fit parameters of the distributions.

6.1.1.5 Backpropagation to the vertex

Since the output of the Kalman fit is an object in which the track parameters at the first hit are stored, it is necessary to propagate each track back to its vertex in order to have more precise momentum values to be used in the calculation of the invariant masses.
In order to do this, since a vertex fitter is still in preparation in PandaROOT, the tracks have been backpropagated by Geane to their vertices, which are known *a priori* from the Monte Carlo truth. In particular, kaons and pions have been propagated to the D meson decay vertices; similarly, the Ds have been propagated to $(0, 0, 0)$, where the $\Psi(3770)$ was set to decay.

6.1.1.6 Particle identification

The next step in the reconstruction chain concerns the particle identification. Its implementation is ongoing and not yet finished for all $\overline{\text{P}}$ANDA detectors, so at the moment it is not possible to use a realistic PID. Therefore, for the analysis of this physics channel, as well as for the decay channel described in Sec. 6.2, an ideal particle identification has been used: the Monte Carlo truth has been used to assign the mass and the charge to each track.

6.1.1.7 Covariance matrix calculation

After the particle identification step, the 7×7 covariance matrix has been calculated for each track: it contains the 6×6 covariances of momentum and position components given by Geane after the backpropagation of the tracks to their vertex.
Concerning the seventh row (and column) of the matrix, it contains the covariances of energy, computed in the following way:

$$\mathrm{Cov}(i, E) = \mathrm{Cov}(E, i) = \frac{1}{E}\left[p_x \,\mathrm{Cov}(i, p_x) + p_y \,\mathrm{Cov}(i, p_y) + p_z \,\mathrm{Cov}(i, p_z)\right] \tag{6.3}$$

with $i = x, y, z, p_x, p_y, p_z$. The variance of E is computed as:

$$\mathrm{Var}(E) = \frac{1}{E^2}\left[\sum_i^{x,y,z} p_i^2 \,\mathrm{Var}(p_i) + \sum_{\substack{i,j \\ i \neq j}}^{x,y,z} 2\, p_i\, p_j \,\mathrm{Cov}(p_i, p_j)\right]. \tag{6.4}$$

6.1.2 Analysis results

6.1.2.1 D candidates selection

The output of the PID is a list of charged and neutral[1] candidates. For this specific channel, the charged candidates have been then classified as kaons and pions by using the Monte Carlo truth.
Since the $D^\pm$ mesons have been set to decay into $K^\mp\pi^\pm\pi^\pm$ with branching ratio 100%, the requirement for the selection of D candidates is the presence of one reconstructed kaon and two reconstructed pions with a common vertex. First of all, only events with at least three charged "well" reconstructed tracks were selected. In order to a have an idea of the quality of the reconstruction, a cut has been applied on a Kalman flag, that indicates if the fit has been done (positive flag) or has failed (negative flag). In spite of this, a positive flag (fit done) does not necessarily mean that the fit result is good when compared with the expected value from simulation. Nevertheless, this check is useful at least to reject tracks for which the fit has completely failed.
Once the events with at least three fitted tracks have been selected, a check on the (Monte Carlo) vertices is performed.
At this point, the D meson candidates have been identified and the square of the invariant mass $M^2_{D^\pm}$ has been calculated:

$$M^2_{D^\pm} = (p_{D^\pm})^2 = (p_{K^\mp} + p_{\pi^\pm} + p_{\pi^\pm})^2 = \left(\sum_i E_i\right)^2 - \left|\sum_i \boldsymbol{p_i}\right|^2 \tag{6.5}$$

where $p_{K^\mp}$ and $p_{\pi^\pm}$ are the four–momenta of the kaons and pions respectively. Fig. 6.5 shows the invariant mass distributions of the selected $D^\pm$ mesons.

[1] In this thesis, we are not interested in neutral candidates, since the chosen decay channels are such that only charged particles are present in the final states.

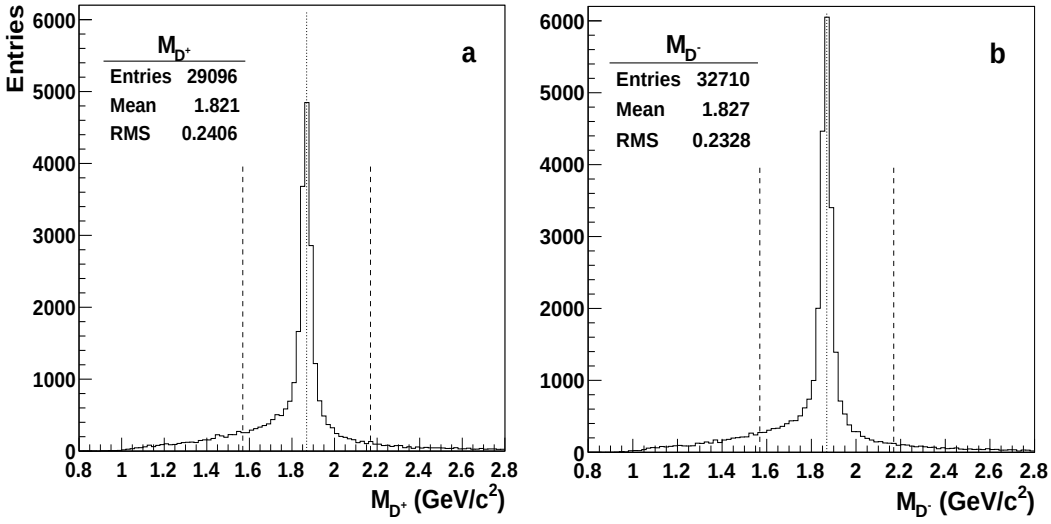

Figure 6.5: Invariant mass of the D^+ (a) and D^- (b) candidates. The dotted line indicates the input mass value $m_D = 1869.3$ MeV/c^2. The dashed lines define the mass window at $m_D \pm 0.3$ GeV/c^2 for the selection of D^+D^- pairs.

6.1.2.2 $\Psi(3770)$ candidates selection

The next step of the analysis consisted in the identification of the Ψ candidates: first of all, the events with at least one D^+ and one D^- candidates have been selected.
After that, a mass cut has been applied to the D candidates: only the ones included in the mass windows identified by the dashed line of Fig. 6.5 are considered. Mathematically, the candidates have to satisfy the condition:

$$|M_{K\pi\pi} - m_D| \leq 0.3 \text{ GeV/c}^2, \tag{6.6}$$

where $M_{K\pi\pi}$ is the invariant mass of the system $(K\pi\pi)$ and m_D is the mass of the D mesons.
With the selected D^+D^- pairs, the invariant mass is computed:

$$M^2_\Psi = (p_{D^+} + p_{D^-})^2 \tag{6.7}$$

where p_{D^+} and p_{D^-} are the four–momenta of the D mesons, obtained as in Eq. 6.5.
The resulting invariant mass of the selected Ψ candidates is shown in Fig. 6.6. On the selected events, a kinematic fit has been then applied.

6.1.2.3 Kinematic fit: general theory

A kinematic fit is a mathematical procedure in which the "external knowledge" of physical laws describing a particle interaction or decay is used as constraint.

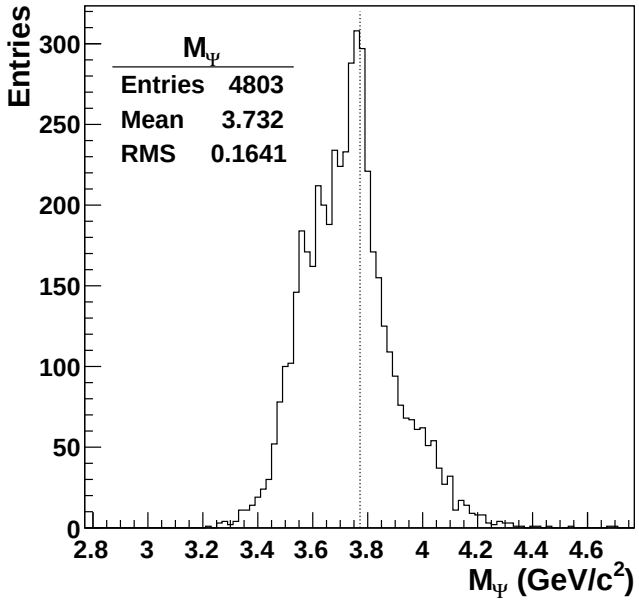

Figure 6.6: Invariant mass of the $\Psi(3770)$ candidates. The dotted line indicates the input mass value $m_\Psi = 3769.9$ MeV/c^2.

The aim is to govern the behaviour of the fit, forcing it to conform to physical conditions which are unknown by the internal variables of the fit itself, thus improving the results that describe the process.
For example, forcing two tracks to come from a common vertex or to be back–to–back are commonly used constraints. In the first case, the external knowledge is the fact that the tracks had to emerge from a single space–time point. In the second one, the knowledge of the kinematics of two body decay constraints the behaviour of the fit.
The kinematic fitting procedure is essentially a least squares fitting method which incorporates the constraints among the variables by the use of the Lagrange multipliers. In particular, the procedure consists in imposing the constraints by adding a new term in the χ^2 equation [8].
The χ^2 minimisation enables us to find the best kinematic configuration reproduced by the fit among the infinite possible configurations for the fit variables that satisfy the given constraints.
It is worth noting that the minimisation does not always have a solution. In particular, by denoting with i the number of measured variables, with k the number of the unknowns and with r the number of constraints, in order to be able to determine the k unknowns, it must be $r \geq k$. Let's analyse in detail the possible situations:

- $r = k$: the unknowns can in general be calculated without modifying the i measured quantities. Thus the final solution implies $\chi^2 = 0$ but the number of degrees of freedom is $r - k = 0$, so this is not a fitting problem;

- $r > k$: this case is more interesting:
  - $r > i + k$: in general, it will be impossible to choose values of the $i + k$ variables satisfying all r constraint equations simultaneously;
  - $r = i+k$: the variables can be calculated exactly from the constraint equations and the χ^2 is calculated directly;
  - $r < i + k$: in this case, the (measured and unmeasured) variable values are "adjusted" in order to satisfy the constraints. After the minimisation, the χ^2 value indicates if the measured variables, in order to satisfy the kinematic equations, have been changed too much with respect to the measured errors.

So the χ^2 value is interpreted as the probability that our hypothesis about the reaction is incorrect, enabling us to decide whether or not to accept it (χ^2 test).
In conclusion, from the fit improved estimates of the track variables are obtained: the extra information given by the constraints allows us to obtain the values of the variables with an accuracy better than that from the measurements alone. Furthermore, the fitted variables are physically consistent since they satisfy the conservation equations [9].

For a detailed description of the mathematics of the kinematic fit, see Appendix A.1 [10].

6.1.2.4 Kinematic fitter in PandaROOT

In PandaROOT a kinematic fit is implemented inside Rho, the package devoted to the event analysis [11].
For the study of the $\Psi(3770)$ decay channel, a four constraints fit (4C) with mass conservation for the daughter particles has been used. The set of constraints can be written as:

$$\sum_{i}^{n_d} p_i^{\mu} - p_C^{\mu} = 0, \qquad \mu = x, y, z, E \tag{6.8}$$

where the sum is over the n_d daughters (six for this channel) and p_C is the constrained four–momentum, set to be equal to the invariant mass of $\Psi(3770)$. The condition on the mass of the daughters implies that their masses cannot be modified by the fit, but only their momenta and energy, accordingly (see Appendix A.2 for the mathematical derivation of the formula used in the fit).

Before applying the 4C fit to the selected D^+D^- pairs, the fitter has been tested with the 10^5 smeared simulated events of the Ψ decay used as input: each position component has been sampled from a Gauss distribution with the mean value equal to the component itself and $\sigma_{\mathbf{x}} = 0.5$ cm. The same

has been done for the momentum, with $\sigma_{\mathbf{p}} = 0.01$ GeV/c^2. Concerning the 7×7 covariance matrix, it has been set diagonal and its elements have been computed as follows:

$$\begin{aligned} \sigma^2_{ii} &= \sigma^2_{\mathbf{x}} = 0.5^2 \text{ cm}^2 \\ \sigma^2_{jj} &= \sigma^2_{\mathbf{p}} = 0.01^2 \text{ GeV/c}^2 \\ \sigma^2_{EE} &= \frac{p_x \cdot \sigma^2_{p_x} + p_y \cdot \sigma^2_{p_y} + p_z \cdot \sigma^2_{p_z}}{E} \end{aligned}$$

where the index ii corresponds to xx, yy and zz, whereas jj means p_xp_x, p_yp_y and p_zp_z.
Under these hypotheses, the plots of the D meson invariant mass have been produced. They are shown in Fig. 6.7: the red distributions are the invariant masses before the kinematic fit, the blue ones have been obtained after the kinematic fit. Since the starting points were the smeared true values, the peaks of the invariant mass distributions were already centered around the right value. So in this very "clean" case, the effect of the kinematic fit was not on the mean value of the distribution but on its width and on its height, which are smaller and higher with respect to those of the distributions before the kinematic fit.

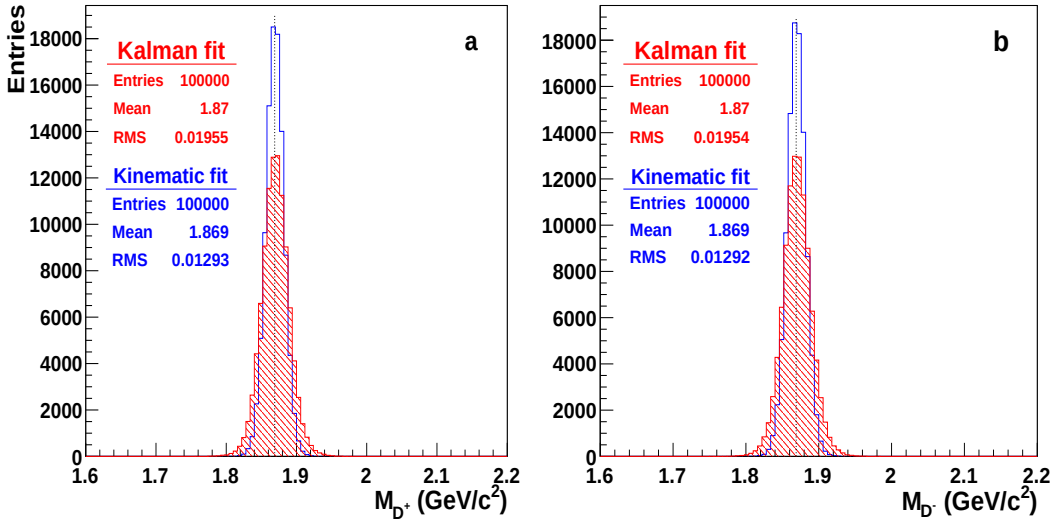

Figure 6.7: D^+ (a) and D^- (b) invariant mass distributions before (red dashed histogram) and after (blue empty histogram) the kinematic fit. The dotted line indicates the input mass value $m_D = 1869.3$ MeV/c^2.

What is more interesting is the χ^2 distribution, shown in Fig. 6.8.
By denoting with Q a random variable having a χ^2 distribution and by χ^2 its values, it is true that $Q(\nu) \sim \chi^2(\nu)$ and the density of the variable Q with ν degrees of freedom is:

$$p_\nu(\chi^2)\mathrm{d}\chi^2 \equiv p(\chi^2;\nu)\mathrm{d}\chi^2 = \frac{1}{2^{\frac{\nu}{2}}\Gamma(\frac{\nu}{2})}(\chi^2)^{\frac{\nu}{2}-1}e^{-\frac{\chi^2}{2}}\mathrm{d}\chi^2. \qquad (6.9)$$

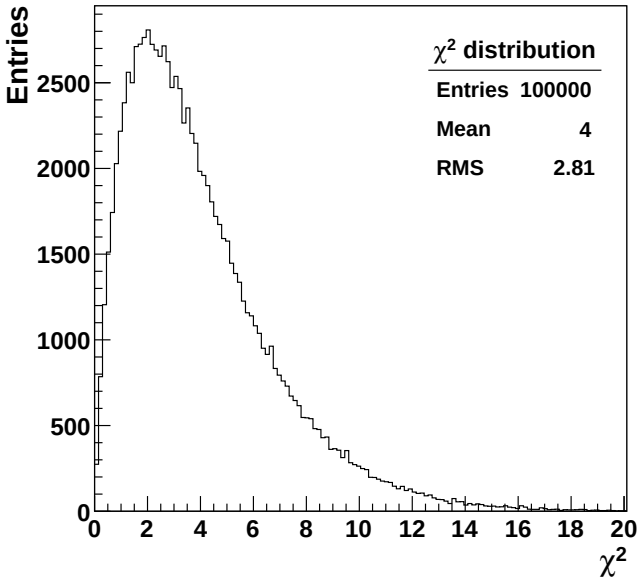

Figure 6.8: χ^2 density distribution obtained with the Monte Carlo events.

It is easy to demonstrate [12] that the mean and variance are:

$$\langle Q \rangle = \frac{1}{2^{\frac{\nu}{2}}\Gamma(\frac{\nu}{2})} \int_0^\infty x(x)^{\frac{\nu}{2}-1} e^{-\frac{x}{2}} \mathrm{d}x = \nu \tag{6.10}$$

$$Var[Q] = \frac{1}{2^{\frac{\nu}{2}}\Gamma(\frac{\nu}{2})} \int_0^\infty (x-\mu)^2 (x)^{\frac{\nu}{2}-1} e^{-\frac{x}{2}} \mathrm{d}x = 2\nu. \tag{6.11}$$

So for $\nu = 4$, the mean and the standard deviation of the distribution should be 4 and $\sqrt{8}$ respectively. This is exactly the case of the distribution of Fig. 6.8 (see statistics box in the plot): it means that the kinematic fit implemented into PandaROOT works fine.

6.1.2.5 Results

The kinematic fitter previously described has been applied to the selected events.
In order to reject bad events, a cut has been applied in the χ^2 density distribution.
Since, according to the statistics theorem about random cumulative variables[2], C is always uniform, the quantile value of χ^2 has been chosen such that the

[2]Having a random variable X with a continuous probability density $p(x)$, the cumulative variable:

$$C(X) = \int_{-\infty}^{X} p(x)\,\mathrm{d}x \tag{6.12}$$

is always uniform in [0,1] ($C \sim U(0,1)$), whatever the starting distribution $p(x)$ may be [12].

probability distribution is almost flat. As shown in Fig. 6.9.b, it is more or less uniform up to a value of 0.95 (dashed region); in the case of $\nu = 4$, $P = 0.95$ corresponds exactly to a quantile value of 9.49. So the rejected events are the ones with $\chi^2 > 9.49$, corresponding to the white region of Fig. 6.9.a and to the right peak of Fig. 6.9.b.
As shown by the dashed line in Fig. 6.9.a, the chosen cut value is 9.49: this is the quantile value of χ^2 such that the probability that $Q \in [0, \chi^2]$ is:

$$P = P\{0 \leq Q(\nu) \leq \chi^2\} = \int_0^{\chi^2} p_\nu(\chi^2) \mathrm{d}\,\chi^2 = 0.95, \tag{6.13}$$

where p_ν is the probability density of Eq. (6.9).
The probability of Eq. (6.13) is equal to the probability that the cumulative variable C belongs to the interval $[c_1 \equiv c(0), c_2 \equiv c(\chi^2)]$.

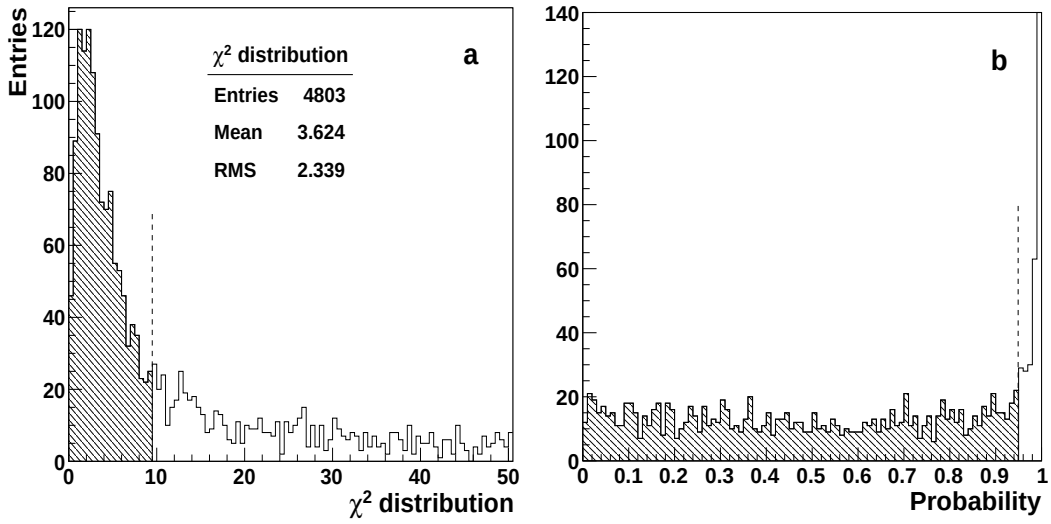

Figure 6.9: a: χ^2 distribution for the selected Ψ candidates. The dashed line indicates the χ^2 value (9.49) up to which the candidates are accepted (dashed region). The statistics box is referred to the dashed distribution. b: Probability associated with the χ^2.

The kinematic fit has been applied to the events passing the χ^2 cut.
Fig. 6.10 and Fig. 6.11 show the invariant mass distributions of the $\Psi(3770)$ and $D^\pm$ candidates before (red histogram) and after (blue histogram) the fit.
Concerning the first plot, since the invariant mass of the system of the daughter particles was forced to m_Ψ by the kinematic constraint of Eq. (6.8), it is obvious that almost all the events fall in the histogram bin corresponding to the input mass value 3769.9 MeV/c^2. So it is meaningless to say anything about the mass resolution of the $\Psi(3770)$ meson.
Concerning the $D^\pm$ mesons, Fig. 6.11 shows the effects of the kinematic fit, in particular on the width and on the height of the distributions: the momenta of

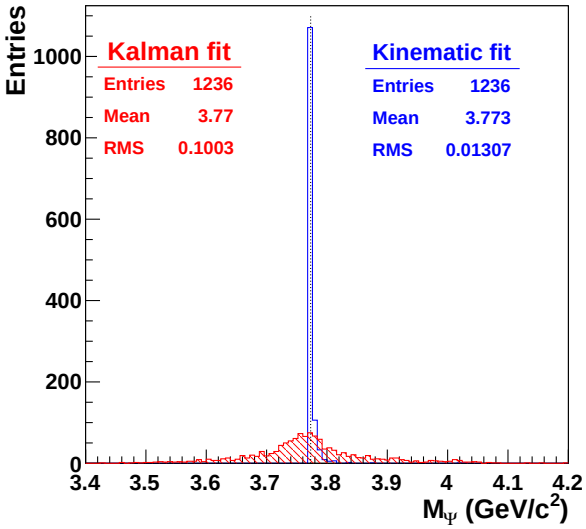

Figure 6.10: $\Psi(3770)$ invariant mass distribution before (red dashed histogram) and after (blue empty histogram) the kinematic fit applied to the events selected by the χ^2 cut.

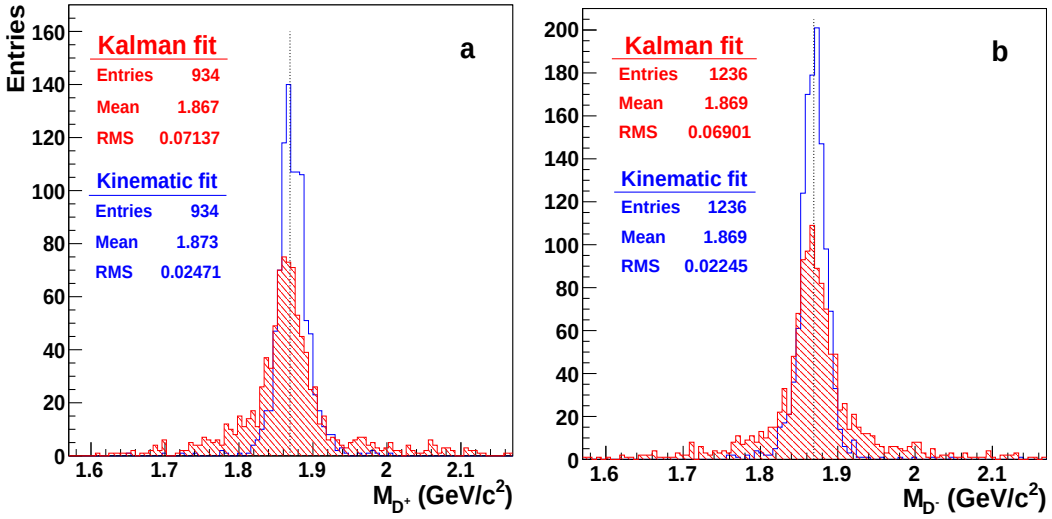

Figure 6.11: D^+ (a) and D^- (b) invariant mass distributions before (red dashed histogram) and after (blue empty histogram) the kinematic fit. The dotted line indicates the input mass value $m_D = 1869.3$ MeV/c^2.

the daughter particles (kaons and pions) have been adjusted in order to satisfy the constraint equation (Eq. (6.8)), resulting in a better mass distribution also for the D candidates.
Since the spread of the antiproton beam momentum was assumed to be zero, the width of the $D^{\pm}$ invariant mass distributions should give directly the de-

tector invariant mass **resolution**.
In Fig. 6.12 the invariant mass distributions obtained after the kinematic fit (the blue distributions of Fig. 6.11) are reported and fitted with a Gauss function in the range $m_{D^\pm} \pm 0.03$ GeV/c^2, in order to get information about the resolution. The mean and σ values of the $D^\pm$ masses after the gaussian fit and the corresponding mass resolutions are reported in Tab. 6.3.

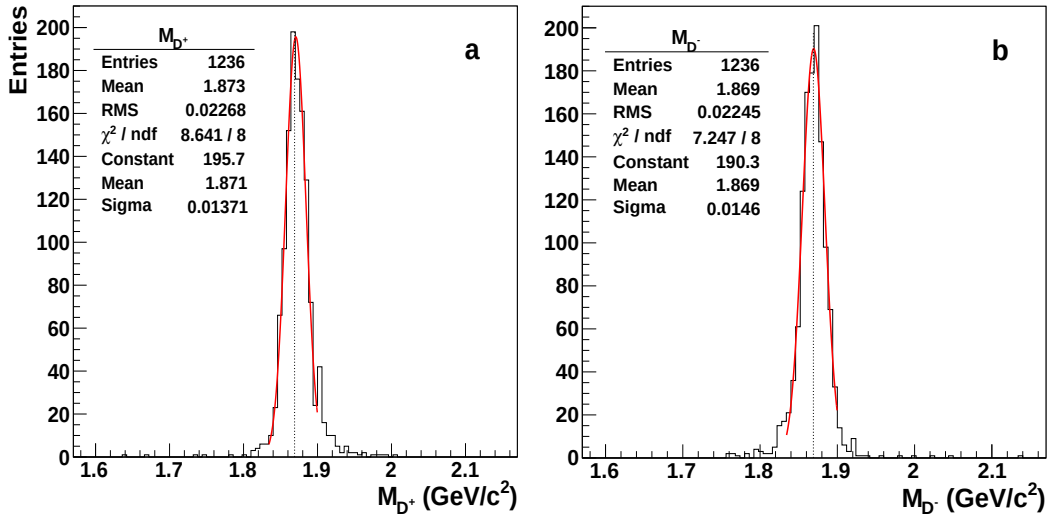

Figure 6.12: Gaussian fit (red curves) of the D^+ (a) and D^- (b) invariant mass distributions after the kinematic fit (Fig. 6.11) in the mass range 1.8693 ± 0.03 GeV/c^2. In the statistics boxes, the mean and σ values of the fitted distributions are also reported.

Table 6.3: $D^\pm$ mass resolutions (see Fig. 6.12). The errors on μ and σ are the ones of the gaussian fit; the error on the resolution is the squared sum of the relative errors on μ and σ ($\sigma_R = R \cdot \sqrt{(\sigma_\mu/\mu)^2 + (\sigma_\sigma/\sigma)^2}$).

	D^+	D^-
μ (GeV/c^2)	1.871 ± 0.0001	1.869 ± 0.0001
σ (GeV/c^2)	0.0137 ± 0.0004	0.0146 ± 0.0004
resolution (%)	$\mathbf{0.73 \pm 0.02}$	$\mathbf{0.78 \pm 0.02}$

Concerning the reconstruction **efficiency**, it has been noticed that it is quite low. In order to have a closer look at the values, the efficiencies at each step of the analysis chain are reported in Tab. 6.4 and Tab. 6.5 for single tracks and events, respectively.
Starting with the single track efficiencies (Tab. 6.4), it can be noticed that only $\sim$84% of the single generated tracks survive the global reconstruction made by

Table 6.4: Reconstruction efficiency related to single tracks.

	n° of tracks	% of tracks
Simulated tracks	600000	
Output tracks from prefit	503293	83.88 (w.r.t. simul.)
Good tracks from Kalman fit	418186	83.09 (w.r.t. prefit)
Good tracks from backpropagation	407428	80.95 (w.r.t. prefit)

the devoted package. Of the ∼16% of the lost tracks, just ∼0.34% are the ones with total momentum smaller than 50 MeV/c, which have been excluded from the reconstruction due to the presence of software problems in dealing with very low momentum tracks.
Apart from these tracks, the main reason for the low prefit efficiency is the fact that the global tracking package used at present is not the best package to perform a global tracking with the STT, because of the way the global fit is implemented in it. In fact, as previously explained in Chap. 5, a local fit with the straw tubes is first performed, giving as output the reconstructed coordinates (the z coordinate only when skewed straws have been hit). Then, the global merging of the hits from the different detectors is performed, as well as another global fit, to derive the track parameters which are then given to the Kalman filter. So the efficiency value that comes out from the global tracking is the product of the efficiency of the local STT fit and of that of the global fit, thus resulting in a value lower than the individual ones.
At the moment, a new algorithm which does not make use of the present global tracking package is in preparation, in order to avoid the inconvenient of having a double fit, so that the efficiency is expected to be improved.
Let's consider now the 83.88% of prefit reconstructed tracks as the input tracks (100%): for ∼83.1% of them, the Kalman fit has been performed without failing. Of the remaining percentage, some tracks may have been rejected because of a wrong reconstructed charge; concerning the others, the fit may have failed because the prefit starting point and momentum were so wrong that the Kalman fit was not able to improve them in the right direction.
Finally, another ∼2% of the tracks are lost in the backpropagation step: this may be due to Geane failures, mostly in the case of events for which the Kalman filter has been performed but the results were not good; so the starting point and momentum for the backpropagation were so different from the real ones that Geane could not find the point of closest approach to the track vertex.
Concerning the event reconstruction (Tab. 6.5), the efficiencies are worse with respect to the ones for single tracks. This is obvious, since an event is counted only if all its six tracks have been reconstructed: in particular, the event efficiency is of the order of the sixth power of the track efficiency. So in this case, just ∼34% of the simulated events pass the prefit cuts. Regarding the Kalman and backpropagation, it can be assumed (and checked) that the behaviour of

the event efficiency is the same.
At this point, the ∼26% of the events from the prefit which have been propagated to their vertex should all be events with a Ψ candidate. Just ∼14% of these events are considered good candidates: the rejected ones are the events for which at least one of the D candidates is not included in the chosen mass window. Finally, after applying also the χ^2 cut at the kinematic fit step, just ∼3.6% of the events are selected. This percentage is really low: when simulating also background events, it would be hardly possible to see a clean signal over the background if the reconstruction efficiency is so low.
Since the low efficiency, however, seems to be connected with software–related problems, the new global fit in preparation which will avoid the use of the present global tracking package should improve the results.

Table 6.5: Reconstruction efficiency related to six track events.

	n° of events	% of events
Simulated events	100000	
Output eventss from prefit	34010	34.01 (w.r.t. simul.)
Good events from Kalman fit	10858	31.93 (w.r.t. prefit)
Good events from backpropagation	8889	26.14 (w.r.t. prefit)
Ψ(3770) candidates found	4803	14.1 (w.r.t. prefit)
Ψ(3770) candidates after kinematic fit	1236	3.6 (w.r.t. prefit)

6.1.2.6 Results with the resolution curve measured with the Jülich prototype

The results shown up to now have been obtained by using the COSY–TOF resolution curve (Fig. 4.9) as input in the digitization step to sample the reconstructed isochrone radii, as explained in the related paragraph of the previous section. All the steps of the analysis chain have been repeated from digitization to the kinematic fit on the same simulated events with the $\sigma_r(r)$ curve obtained from the data analysis of the Jülich prototype (see Fig. 4.24 and Sec. 4.5.2). The aim of this is to check how the different sampling of the reconstructed drift radii in the digitization and the different isochrone errors influence the invariant mass resolution. The results are presented in the following.
Fig. 6.13 shows the $D^{\pm}$ invariant mass distributions before (red histogram) and after (blue histogram) the kinematic fit, to be compared with the corresponding ones in Fig. 6.11.
The first comment that can be made concerns the number of Ψ candidates identified in the two cases: with the COSY–TOF resolution curve, there are 1236 Ψ, whereas in this case only 934 candidates are found.
The shapes of the distributions are very similar but the RMS values of the histograms are not compatible within the statistical errors, which are of the

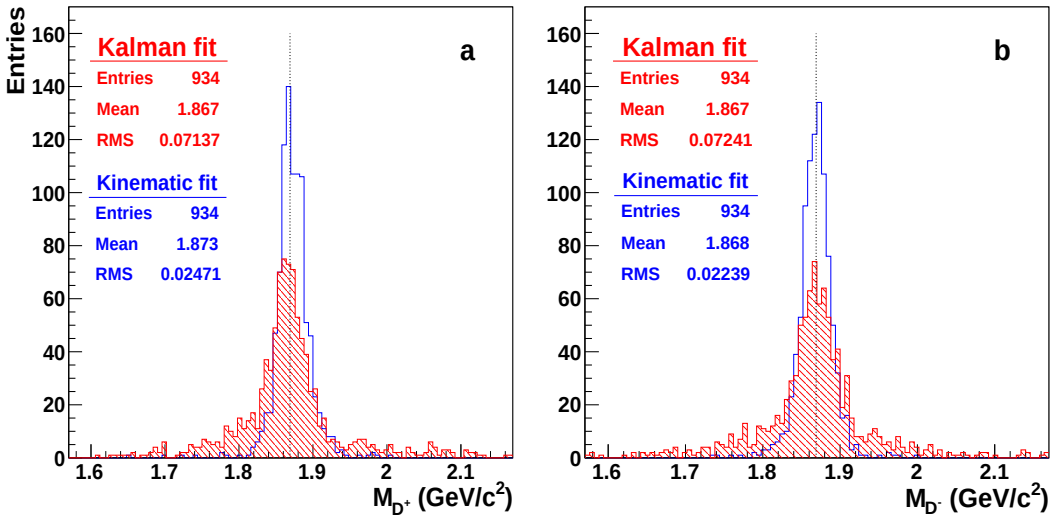

Figure 6.13: D^+ (a) and D^- (b) invariant mass distributions before (red dashed histogram) and after (blue empty histogram) the kinematic fit, as in Fig. 6.11, obtained with the $\sigma_r(r)$ curve measured with the Jülich prototype. The dotted line indicates the input mass value $m_D = 1869.3$ MeV/c^2.

order of some hundreds of keV/c^2. Nevertheless, the improvements due to the kinematic fit are evident also in this case: the peaks of the blue histograms are higher and the distribution widths are smaller with respect to the corresponding ones of the red histograms.
Fig. 6.14 shows the invariant mass distributions after the kinematic fit (blue histograms in Fig. 6.13), fitted with a Gauss function in the range $m_{D^\pm} \pm 0.03$ GeV/c^2.
Tab. 6.6 reports the comparison of the fit parameters of the invariant mass distributions obtained with the two resolution curves. The fit mean values are compatible within the errors, but it is not the same for the σ of the distributions, since the errors on this variable are of the order of hundreds of keV/c^2. Concerning the resolution values, they are not compatible within the errors, neither for D^- nor for D^+. This shows that the use of the resolution curve obtained with the Jülich prototype, which is about a factor 2 worse than the COSY–TOF resolution curve (see Sec. 4.5.1), turns out into a loss in resolution of about 10%.

6.2 Analysis of $\bar{p}p \to \eta_c(2979) \to K^0_S K^+ \pi^-$

The $\eta_c(1^1S_0)$ state of charmonium occupies a special place in the study of heavy quarkonia. It is the only ground state of a heavy quarkonium system which has been experimentally identified and it is the only confirmed heavy

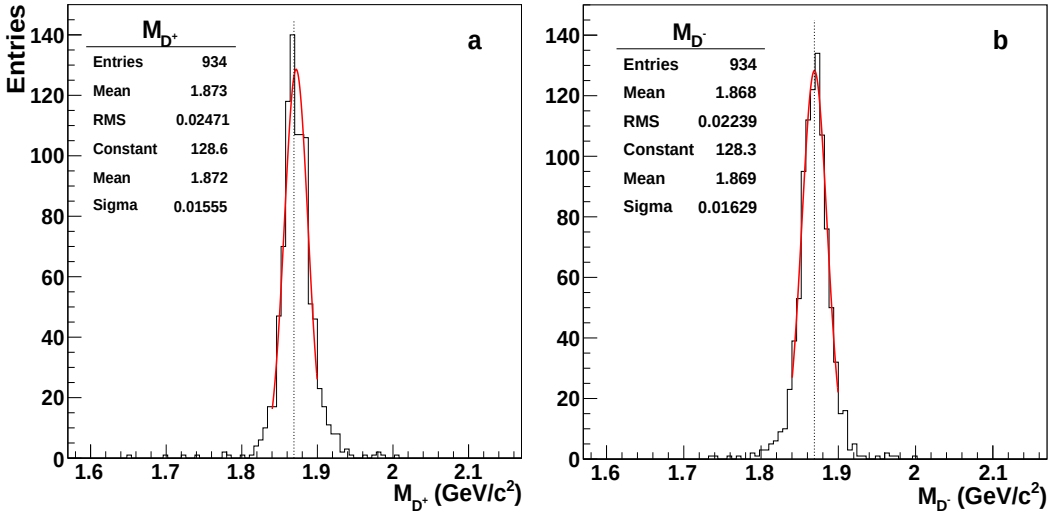

Figure 6.14: Gaussian fit (red curves) of the D^+ (a) and D^- (b) invariant mass distributions after the kinematic fit (Fig. 6.13) in the mass range 1.869 ± 0.03 GeV/c^2, as in Fig. 6.12. In the statistics boxes, the mean and σ values of the fitted distributions are also reported.

Table 6.6: Comparison of the fit parameters of the $D^\pm$ invariant masses obtained with the COSY–TOF and Jülich prototype resolution curves (see Fig. 6.12 and 6.14).

D^+	COSY–TOF	Jülich prototype
μ (GeV/c^2)	1.871 ± 0.0001	1.871 ± 0.001
σ (GeV/c^2)	0.0137 ± 0.0004	0.0155 ± 0.0006
resolution (%)	$\mathbf{0.73 \pm 0.03}$	$\mathbf{0.83 \pm 0.03}$

D^-	COSY–TOF	Jülich prototype
μ (GeV/c^2)	1.869 ± 0.0001	1.869 ± 0.001
σ (GeV/c^2)	0.0146 ± 0.0004	0.0163 ± 0.0007
resolution (%)	$\mathbf{0.78 \pm 0.02}$	$\mathbf{0.87 \pm 0.04}$

quarkonium singlet state. Therefore, an accurate knowledge of the parameters of the η_c is important to understand and test QCD models.
The η_c, however, represents a challenge to experiment. In fact, it cannot be formed directly at e^+e^- colliders since its quantum numbers ($J^{PC} = 0^{-+}$) are different from 1^{--} of the γ and its indirect production via M1 radiative decay of J/ψ and ψ' leads to small branching ratios. The η_c can be produced exclusively in photon–photon fusion reactions ($e^+e^- \to e^+e^-\eta_c$) [13] and inclusively as decay products of B mesons produced in B–factories [14]. The uncertainties in η_c resonance parameters, however, remain large; even with improved

statistics, the above techniques depend critically on a detailed understanding of the detector calibration and resolution [2].
On the contrary, in experiments like $\overline{\text{P}}$ANDA, the formation of the η_c in a reaction as $\bar{p}p \rightarrow \eta_c$ is not forbidden by quantum number conservation and it can be used advantageously to measure $M(\eta_c)$, $\Gamma_{tot}(\eta_c)$ and other partial widths, as long as the large hadronic background can be controlled.
In the past, E760 [15] and E835 [2] detected the decay channel $\bar{p}p \rightarrow \eta_c \rightarrow \gamma\gamma$: the 2γ signature helps cleaning the hadronic background besides allowing the calculation of $\Gamma(\eta_c \rightarrow \gamma\gamma)$, that has a high theoretical relevance. The η_c mass and width can be determined from the excitation curve with a scan obtained by varying the antiproton beam energy and measuring the resonant cross section at the different CMS energies.
With this technique, the systematic uncertainties are greatly reduced compared with the e^+e^- production experiments, since they depend only on the error on the antiproton beam momentum. Since this error for the $\overline{\text{P}}$ANDA experiment is expected to be $\delta p/p < 7 \cdot 10^{-6}$, that would ensure a resolution in the η_c parameters far superior than the previous experiments. In addition, it would be possible to study η_c decaying also into $K\overline{K}\pi\pi$, $K\overline{K}\pi$, $4K$, 4π and $\eta\pi\pi$, which have a relative BR higher than the $\gamma\gamma$ channel, thus allowing to collect a much higher statistics than in the past and to improve the statistical errors on the measurements of the η_c mass and total width.

The η_c decay channel that has been chosen for this thesis is:

$$\bar{p}p \rightarrow \eta_c(2979) \rightarrow K^0_S K^+ \pi^-,$$

having only charged particles in the final state.
Since the cross section of the $\bar{p}p \rightarrow \eta_c \rightarrow \gamma\gamma$ channel around 3-5 GeV is about 200-300 pb ([2, 15]) and the branching ratio $BR(\eta_c \rightarrow \gamma\gamma) = (2.8 \pm 0.9) \cdot 10^{-4}$ [1], it results[3] that:

$$\sigma(\bar{p}p \rightarrow \eta_c) \simeq 800 \text{ nb}. \tag{6.14}$$

Using the branching ratio $\eta_c \rightarrow K\overline{K}\pi = 7.0 \pm 1.2 \cdot 10^{-2}$ [1], from Eq. (6.14) we obtain:

$$\sigma(\bar{p}p \rightarrow \eta_c \rightarrow K^0_S K^{\pm}\pi^{\mp}) \simeq 19 \pm 3 \text{ nb}. \tag{6.15}$$

Knowing the annihilation branching ratios around 3.6 GeV/c of antiproton beam momentum, it is possible to evaluate the contamination due to the competing annihilation channels. The results are shown in Tab. 6.7; in particular, it is worth noting the rather high value of the direct production $\bar{p}p \rightarrow K^0_S K^{\pm}\pi^{\mp}$ [18]:

$$\sigma(\bar{p}p \rightarrow K^0_S K^{\pm}\pi^{\mp}) = 11 \pm 6 \ \mu\text{b}. \tag{6.16}$$

[3] This cross section has been obtained from experimental data measured with a beam spread of 0.3 MeV/c. It is orders of magnitude larger than the η_c indirect production in e^+e^- annihilation, which is of the order of few pb at 3-5 GeV [16, 23].

By applying appropriate kinematical cuts on total energy and momentum, geometrical cuts on both primary and secondary vertices and the kinematical fit, it should be possible to select the η_c signal with a low contamination probability by the background reactions $K^+K^-\pi^+\pi^-$ and $2\pi^+2\pi^-$, as shown in Ref. [3] (see Sec. 13.5.4.3, Tab. 13.13): with the cuts used in the analysis presented there, no background events survived, apart from the non resonant $K^0_S K^\pm\pi^\mp$ channel.

Table 6.7: Comparison between the $\overline{p}p \to \eta_c(2979) \to K^0_S K^\pm\pi^\mp$ channel to other background final states.

Reaction	Cross section	Ratio S/N	$\mathbf{p}_{\overline{p}}$ (GeV/c)	Ref.
$\eta_c \to K^0_S K^\pm\pi^\mp$	19 ± 3 nb	-	$\simeq 3.6$	-
$\overline{p}p \to K^0_S K^\pm\pi^\mp$	11 ± 6 μb	1/1100	3.66	[18]
$\overline{p}p \to 2\pi^+2\pi^-$	430 ± 30 μb	1/40000	3.59	[19]
$\overline{p}p \to K^+K^-\pi^+\pi^-$	240 ± 30 μb	1/24000	2.90	[20]

6.2.1 Event simulation

6.2.1.1 Generation

As for the $\Psi(3770)$ decay, 10^5 $\overline{p}p \to \eta_c$ events have been generated with the EvtGen generator at the vertex position $(0, 0, 0)$. The decay file used to generate the events is the following:

```
Decay etac
1.00 K0S K+ pi- PHSP;
Enddecay
Decay K0S
1.00 pi+ pi- PHSP;
Enddecay
End
```

This means that the decay of the η_c has been set to $K^0_S K^+\pi^-$ with branching ratio 1 and that the K^0_S meson decays into $\pi^+\pi^-$ with 100% probability in order to have only charged particles in the final state; the decay model used is the PHSP model.
In order to have an energy in the CMS equal to the η_c mass, the antiproton beam momentum has been set to 3.676 GeV/c^2 along the z direction.
The input K^0_S mass to the simulation is 0.49767 GeV/c^2, while for the η_c the mass is 2.9798 GeV/c^2 and the width is 0.0270 GeV/c^2.

6.2.1.2 Simulation

The EvtGen ASCII output file has been given as input to the simulation – digitization – reconstruction chain. Each of these steps has been performed exactly in the same conditions described in Sec. 6.1.1.

One comment can be related to the angular distribution of the decay products: also in this channel, they are emitted mostly in the forward direction, as shown in Fig. 6.15 and 6.16. The first picture represents the momentum distributions of K^+ (a) and $\pi^\pm$ (b) as a function of the θ angle; the second plot shows the angular distributions of those particles.

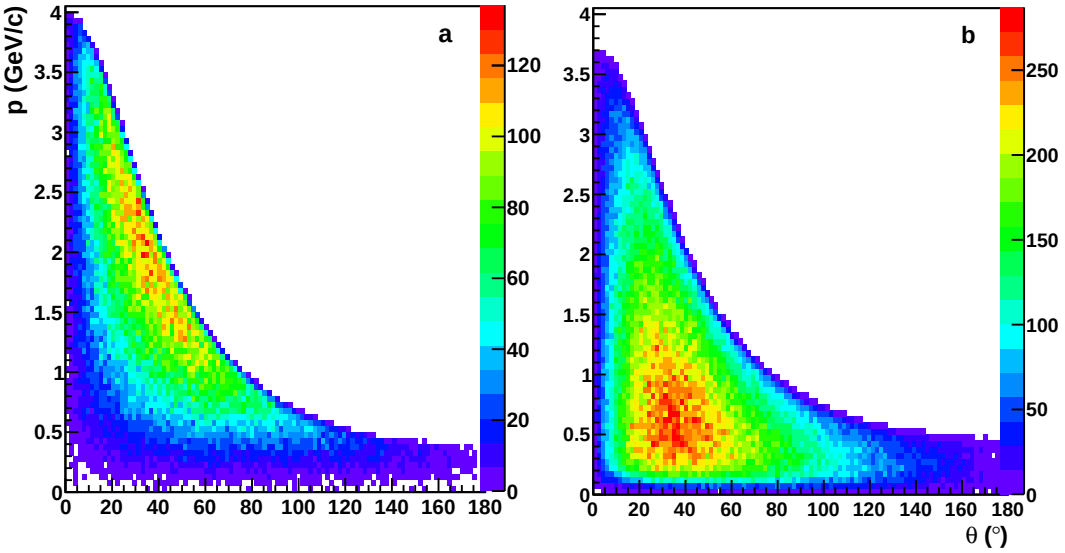

Figure 6.15: Momentum distributions of the generated kaons (a) and pions (b).

Tab. 6.8 reports the percentages of tracks traversing the different regions of the Central Tracker, as illustrated in Fig. 5.9.

Table 6.8: Angular distribution of the simulated kaons and pions for the η_c decay channel.

Angular range (°)	Kaons (%)	Pions (%)
0 - 10.6	7.67	7.04
10.6 - 27.7	33.57	30.87
27.7 - 133.6	57.99	60.52
133.6 - 159.5	0.62	1.28
159.5 - 180	0.15	0.29

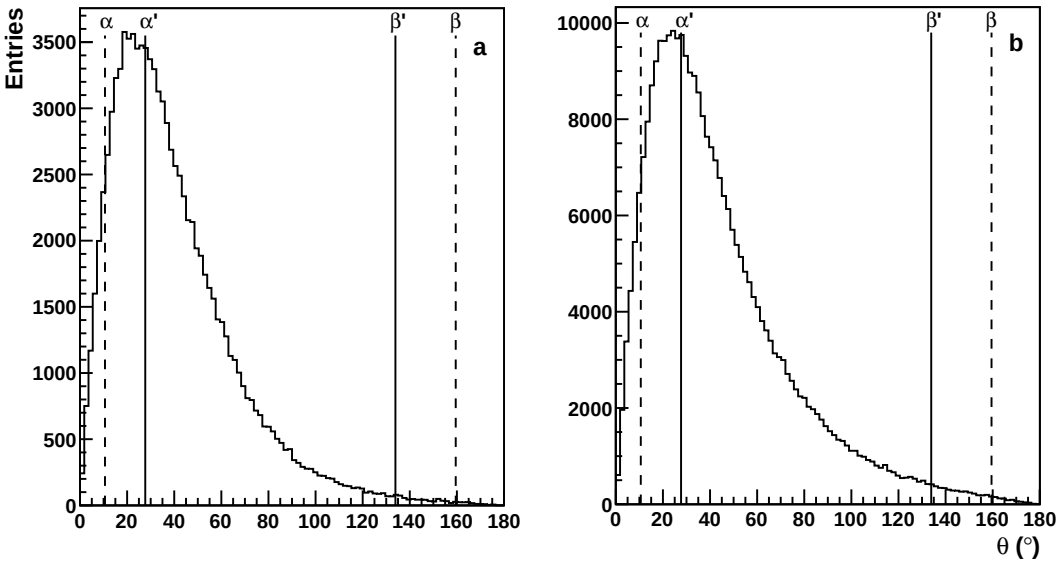

Figure 6.16: Angular distributions of the generated kaons (a) and pions (b). $\alpha = 10.6°$, $\alpha' = 27.7°$, $\beta' = 133.6°$ and $\beta = 159.5°$ (see Sec. 5.7.2.1 for a detailed explanation of the five regions the θ angular range has been divided into).

These numbers show that, since many tracks are emitted in the forward direction, they do not have so many hits in the Straw Tube Tracker and this may have an effect on the reconstruction efficiency and also on the quality of the track fitting.
In addition to this, it should be pointed out that the K^0_S decay is not at $(0, 0, 0)$ because the K^0_S travels through the apparatus before decaying ($c\tau = 2.684$ cm assuming $\mathcal{CPT}$ [1]). So not all the tracks have the maximum possible number of hits in the STT and this may affect the efficiency as well.

6.2.2 Analysis results

6.2.2.1 K^0_S candidates selection

The first step after the reconstruction and particle identification has been the selection of tracks for which the Kalman fit was successful[4].
The next step was the candidate selection: since the K^0_S decay has been set to $\pi^+\pi^-$ with branching ratio 1, the requirement for the selection of K^0_S candidates is the presence of two reconstructed pions with a common vertex.
Unfortunately, the preparation of a vertex fitter is still ongoing: hence, again, the position of the secondary decay vertex is known *a priori* from the Monte

[4]Successful Kalman fit for a track means that the fit has been performed, no matter how good the reconstructed momentum and position are compared with the Monte Carlo truth (see Sec. 6.1.2.1).

Carlo truth.
Once the K^0_S candidates have been identified, the invariant mass is computed as follows:

$$M^2_{K^0_S} = (p_{\pi^+} + p_{\pi^-})^2 = 2 \cdot [m^2_\pi + (E_{\pi^+} E_{\pi^-} - \mathbf{p}_{\pi^+} \cdot \mathbf{p}_{\pi^-})], \tag{6.17}$$

where $\mathbf{p}_\pi$ are the reconstructed momenta at vertex and the energy is calculated via $E_\pi = \sqrt{m^2_\pi + |\mathbf{p}_\pi|^2}$.
Fig. 6.17 shows the invariant mass distribution for the selected $\pi^+\pi^-$ pairs. The blue dotted line indicates the input K^0_S mass value to the simulation; the red dashed lines define a mass window[5] ($m_{K^0_S} \pm 0.015$ GeV/c^2) in which a gaussian fit of the distribution has been performed (red curve in the plot). From this peak fit, it results:

$$\begin{aligned} \mu &= 0.4972 \pm 0.0001 \text{ GeV/c}^2 \\ \sigma &= 0.0065 \pm 0.0001 \text{ GeV/c}^2. \end{aligned}$$

Hence, the K^0_S mass **resolution** results to be $1.31 \pm 0.02\%$.

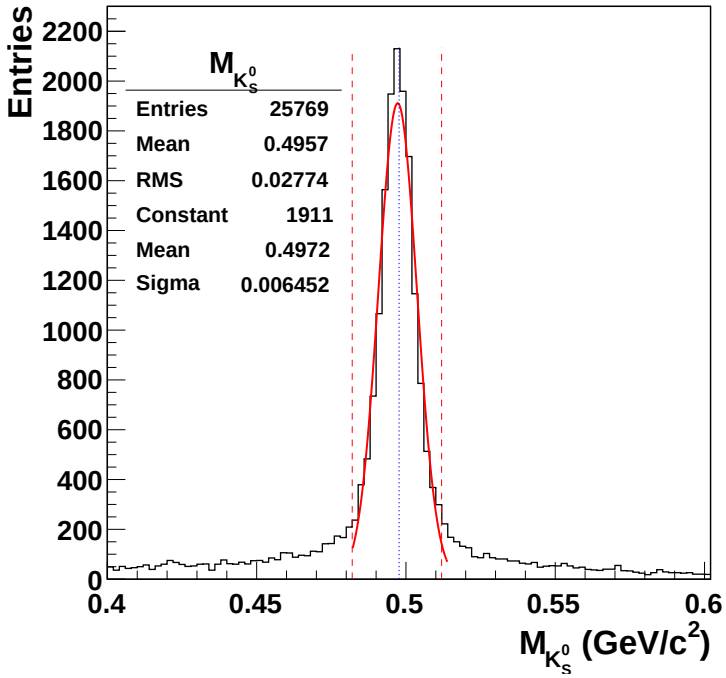

Figure 6.17: K^0_S invariant mass distribution. The blue dotted line indicates the input value of the K^0_S mass to the simulation ($m_{K^0_S} = 497.67$ MeV/c^2). The red dotted lines set the mass window ($m_{K^0_S} \pm 15$ MeV/c^2). The red full curve is the gaussian fit of the distribution in the mass window; the parameters obtained from the fit are reported in the statistics box.

[5]The width of the mass window has been chosen as in Ref. [21].

6.2.2.2 η_c candidates selection

In order to select the η_c candidates, only the $\pi^+\pi^-$ pairs whose invariant mass is included in the mass window defined above have been considered. The η_c invariant mass has been calculated with:

$$M^2_{\eta_c} = (p_{\pi^-} + p_{K^+} + p_{\pi^+(K^0_S)} + p_{\pi^-(K^0_S)})^2. \tag{6.18}$$

The invariant mass distribution is shown in Fig. 6.18.

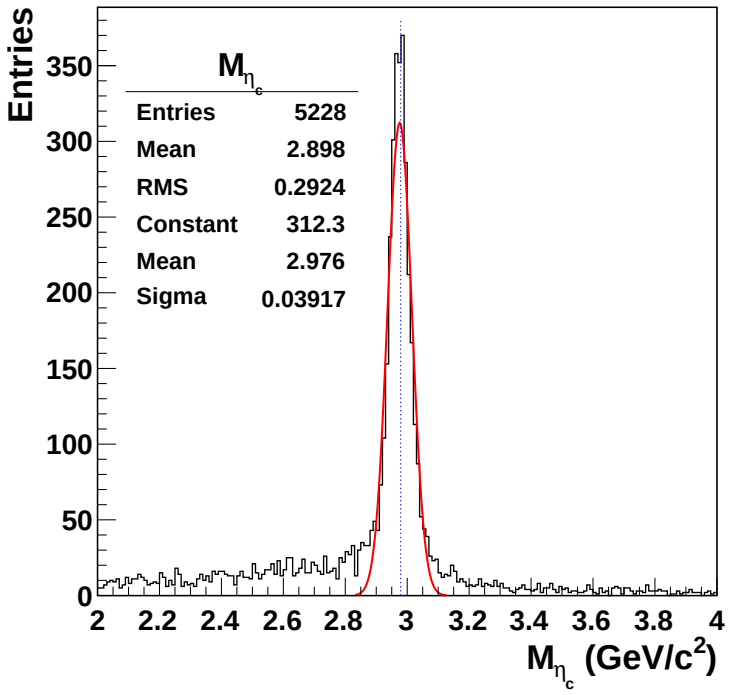

Figure 6.18: η_c invariant mass distribution. The blue dotted line indicates the input value for the η_c mass ($m_{\eta_c} = 2979.8$ MeV/c^2). The red full curve is the gaussian fit of the distribution in the interval $[m_{\eta_c} - 150, m_{\eta_c} + 150]$ MeV/c^2; the parameters obtained from the fit are reported in the statistics box.

From the fit peak in the interval $m_{\eta_c} \pm 0.150$ GeV/c^2, it results:

$$\begin{aligned} \mu &= 2.976 \pm 0.001 \text{ GeV/c}^2 \\ \sigma &= 0.0392 \pm 0.0009 \text{ GeV/c}^2. \end{aligned} \tag{6.19}$$

Since the η_c has an intrinsic width, it is necessary to take it into account in order to calculate the mass **resolution** due to the detector. This can be done as follows:

$$\sigma^2_{res} = \sigma^2_{reco} - \sigma^2_{intr} \simeq 37.5 \text{ MeV/c}^2, \tag{6.20}$$

where $\sigma_{intr} = \Gamma_{sim}/2.35 = 11.5$ MeV/c^2, Γ_{sim} being the intrisic width value assumed in the simulation (27 MeV/c^2). σ_{reco} is the value obtained from the fit

of the distribution in Fig. 6.18 ($\sigma_{reco} = 39$ MeV/c^2). This leads to an invariant mass resolution of $1.26 \pm 0.03\%$.
The obtained resolution can be compared, as an example, to the resolution of 0.5% declared in Ref. [22] for the η_c invariant mass reconstruction in the channel $B \to KK^0_S K^-\pi^+$. Our result is 2.5 times worse than the resolution in Ref. [22], but it must be stressed that in the present analysis the kinematic fit has not been used. Further improvements are expected once the vertex fit will be ready and could be applied.

6.2.2.3 Results

Concerning the reconstruction **efficiency**, the results are similar to the ones obtained for the Ψ decay channel. The percentages are shown in Tab. 6.9 for single tracks and in Tab. 6.10 for the events.

Table 6.9: Reconstruction efficiency related to single tracks.

	n° of tracks	% of tracks
Simulated tracks	400000	
Output tracks from prefit	343989	85.99 (w.r.t. simul.)
Good tracks from Kalman fit	255511	74.28 (w.r.t. prefit)
Good tracks from backpropagation	235528	68.47 (w.r.t. prefit)

Table 6.10: Reconstruction efficiency related to four track events.

	n° of events	% of events
Simulated events	100000	
Output events from prefit	56086	56.09 (w.r.t. simul.)
Good events from Kalman fit	14882	26.53 (w.r.t. prefit)
Good events from backpropagation	10126	18.05 (w.r.t. prefit)
K^0_S candidates found	25769	
K^0_S candidates in the mass window	15530	
η_c candidates found	5228	9.32 (w.r.t. prefit)

By looking at the values in the tables, the same remarks as for the Ψ channel can be made.
The difference between the two decay channels is that in the η_c decay only four tracks instead of six are needed to be reconstructed in order not to reject the event. As a consequence, the event efficiencies are equal to the fourth power (instead of sixth power) of the single track efficiency; hence, they are obviously higher with respect to the corresponding efficiencies in the Ψ case.
In addition, the only cut applied in the analysis step is the one on the mass

window for the K^0_S candidates; any kinematic fit has been applied, so the events do not have been selected by a χ^2 cut. The consequences of this is that the final percentage of η_c candidates is higher (9.32%) with respect to the percentage of $\Psi(3770)$ candidates (3.6%). On the other hand, the resolution both of the η_c and K^0_S invariant masses (∼1.25 and 1.31%, respectively) are a little worse than the $D^{\pm}$ resolution (∼0.73 - 0.78%).
When a vertex fitting will be ready, the resolution is expected to improve.

6.2.2.4 Results with the resolution curve measured with the Jülich prototype

The results presented in the previous paragraph have been obtained by using the COSY–TOF resolution curve (Fig. 4.9) in the sampling of the reconstructed isochrone radii during the digitization.
As for the $\Psi(3770)$ decay channel (Sec. 6.1.2.6), the simulated data have been digitized also with the resolution curve measured from the prototype (Fig. 4.24). The analysis has then been performed as previously described and the results are shown here.

The K^0_S and η_c invariant mass distributions in Fig. 6.17 and 6.18 have to be compared with the ones in Fig. 6.19 and 6.20 respectively.
First off, it is worth noting that in this case the efficiency values obtained with the COSY–TOF and the prototype resolution curves are compatible within 1σ.
Concerning the mass resolutions, Tab. 6.11 reports the values of the parameters of the fitted data, going from 1.31 to 1.40% for K^0_S and from 1.26 to 1.48% in the case of η_c. So the use of the resolution curve obtained with the Jülich prototype, which is about a factor 2 worse than the COSY–TOF resolution curve, turns out into a loss in mass resolution of about 9% and 17% in the case of K^0_S and η_c, respectively.

6.3 $\overline{p}-^4$He annihilations

As already mentioned in Sec. 1.3.3, antiproton annihilations on light nuclei (such as ^{4}He) could favour the transition to exotic states and quark–gluon plasma. In addition, it could allow strangeness and charm production studies in exclusive annihilation channels.
In the light of these interesting perspectives, it has been decided to perform studies of $\overline{p}-^4$He annihilations to test the $\overline{\text{P}}$ANDA detector performances applied to these specific events.
The study is of interest despite the fact the $\overline{\text{P}}$ANDA at present does not plan to have a ^{4}He target, since similar effects are expected on other light nuclei. Moreover, in the future a ^{4}He target could be designed for the experiment.

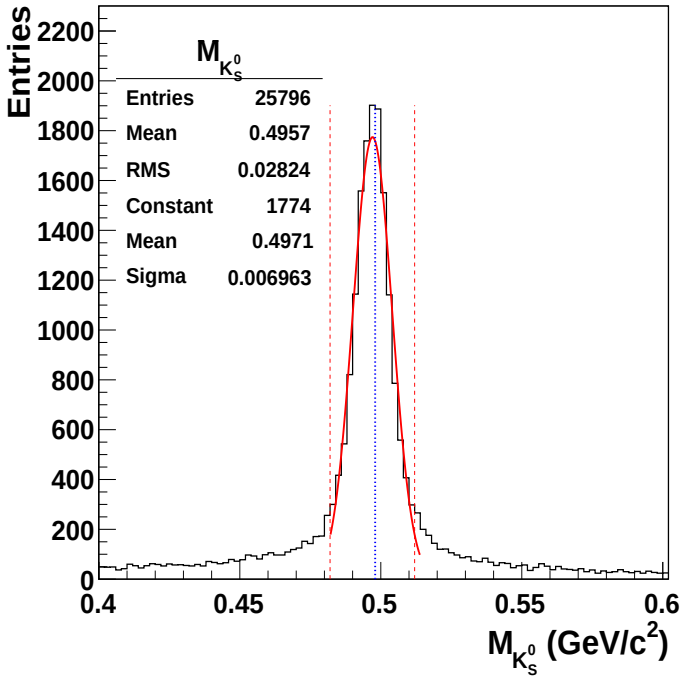

Figure 6.19: K^0_S invariant mass distribution as in Fig. 6.17, obtained with the resolution curve measured with the Jülich prototype. The parameters reported in the statistics box are referred to the Gauss function that fits the distribution in the mass window ($m_{K^0_S} \pm 15$ MeV/c^2) indicated by the red dashed lines in figure.

Table 6.11: Comparison of the fit parameters of the K^0_S and η_c invariant masses obtained with the COSY–TOF and Jülich prototype resolution curves (see Fig. 6.17–6.20).

K^0_S	COSY–TOF	Jülich prototype
μ (GeV/c^2)	0.4972 ± 0.0001	0.4971 ± 0.0001
σ (GeV/c^2)	0.0065 ± 0.0001	0.0070 ± 0.0006
resolution (%)	**1.31 ± 0.02**	**1.40 ± 0.01**

η_c	COSY–TOF	Jülich prototype
μ (GeV/c^2)	2.976 ± 0.001	2.974 ± 0.001
σ_{reco} (GeV/c^2)	0.0392 ± 0.0009	0.0455 ± 0.0009
σ_{res} (GeV/c^2)	0.0375 ± 0.0009[a]	0.0440 ± 0.0009
resolution (%)	**1.26 ± 0.03**	**1.48 ± 0.03**

[a]Recalling that σ_{res} is calculated with Eq. (6.20), the error on σ_{res} is the same of σ_{reco} because the error on $\sigma_{int} = 0$ since the intrinsic meson width Γ_{sim} assumed in the simulation is given without error.

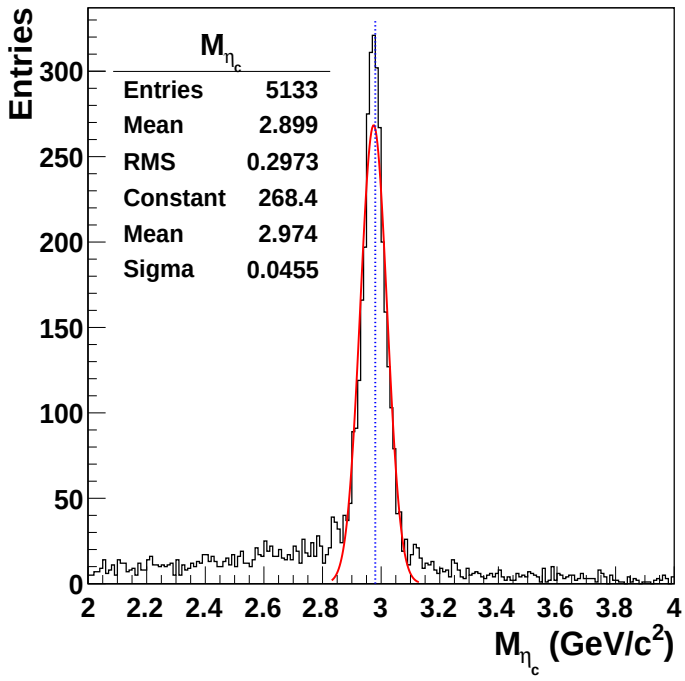

Figure 6.20: η_c invariant mass distribution as in Fig. 6.18, obtained with the resolution curve measured with the Jülich prototype. The parameters reported in the statistics box are referred to the Gauss function that fits the distribution in the mass window $m_{\eta_c} \pm 150$ MeV/c^2.

6.3.1 Event simulation

6.3.1.1 Generation

10^4 antiprotons at 1.5 GeV/c momentum annihilating on ^{4}He have been generated with the Ultrarelativistic Quantum Molecular Dynamic (UrQMD) generator. A detailed description of the UrQMD generator can be found in Refs. [23, 24, 25].
At present, there is no unique theoretical description of nucleus–nucleus interactions, but the UrQMD model is the most appropriate one for the energy range of the $\overline{\text{P}}$ANDA experiment.
It is a microscopic model based on a phase space description of nuclear reactions. The phenomenology of hadronic interactions at low and intermediate energies ($\sqrt{s} < 5$ GeV) is described in terms of interactions between known hadrons and their resonances. At higher energies ($\sqrt{s} > 5$ GeV), the excitation of colour strings and their subsequent fragmentation into hadrons are taken into account.
According to the standard UrQMD generator, only direct annihilations on a single nucleon are possible. In addition, the residual nucleons may interact with the annihilation products; this rescattering is usually called final state interaction (FSI).

6.3.1.2 Simulation chain

The output of the UrQMD generator is a ROOT file that has been used as input for the simulation – digitization – reconstruction chain. Each of these steps has been performed exactly under the same conditions described in Sec. 6.1.1. Just to briefly review, all the sensitive detectors have been included both in the simulation and in the digitization, in order to take into account the whole material budget; on the contrary, the global tracking has been performed in the reconstruction step by using only the information from the tracking detectors of the Target Spectrometer (MVD, STT, GEM). As a consequence, only charged particles have been reconstructed and not the neutral ones. The Kalman filter has been applied to the reconstructed tracks. Concerning the particle identification, the Monte Carlo truth has been used to assign the mass and the charge to each track.

6.3.2 Analysis results

6.3.2.1 Proton spectra

The momentum distributions of the particles produced in the $\overline{p}-^4$He annihilations have been studied. Most interesting is the protons distribution, reported in Fig. 6.21 for the simulated (a) and reconstructed (b) tracks.

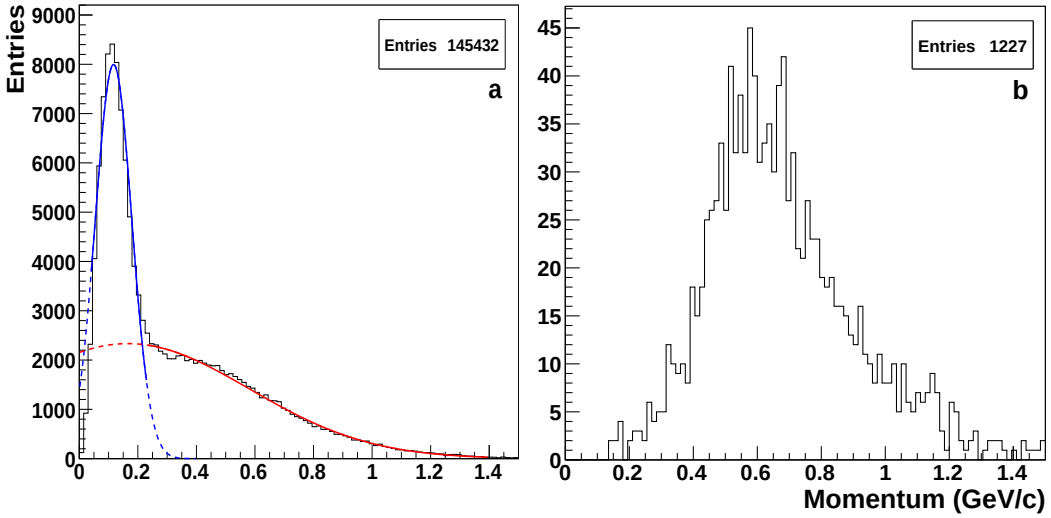

Figure 6.21: Simulated (a) and reconstructed (b) proton momentum distributions. In plot (a), the blue curve fits the contribution of the spectator protons; the red curve fits the contribution of the "fast" protons involved in the final state interactions.

In the simulated spectrum it is easy to identify two different contributions: the first contribution at low momentum values, around 0.15 GeV/c (blue gaussian fit in the figure), is associated with the spectator protons ($\sim$ 58%), the ones

not directly involved in the annihilation, having a momentum equal to the Fermi momentum. The gaussian fit of the peak suggests it can be estimated to vary within the range $[0, 0.3]$ GeV/c. The contribution at higher momenta (red gaussian fit in the figure) is due to the "fast" protons, the ones involved in the interaction of the final states.
Unfortunately, it is no longer possible to recognize these two peaks in the reconstructed plot; in fact, after the reconstruction procedure, less than 1% of the protons survive, as shown in Fig. 6.21.b. This is partially due to a cut implemented in the algorithm that performs the global tracking: protons having a momentum smaller than 50 MeV ($\sim 5\%$) are not tracked. Concerning the other missing protons, their absence may be connected with failures in the global reconstruction, especially for tracks with low momentum, due to instabilities in the global tracking code. In addition, a certain number of reconstructed tracks may have been rejected after the Kalman fit in case it is failed (negative Kalman flag).

6.3.2.2 $p - E$ plots

In $\overline{p}$–nucleus annihilations the use of kinematic fitting is usually impossible due to the presence of many unmeasured particles. However, useful pieces of information can be derived from the analysis of the $p - E$ plots that will be presented in this section [26].

The $\overline{p}-^4$ He annihilation reactions can be summarised by the following scheme, according to the role of the initial and final particles:

$$\overline{p}^4\text{He} \rightarrow A + S \rightarrow (M + U) + S, \tag{6.21}$$

where A indicates the system composed of the antiproton plus the interacting nucleons; S stands for the spectator nucleons, the ones with low momentum, not directly involved in the annihilation process; M are the measured particles, usually charged mesons and fast protons and U are the unmeasured particles, mainly π^0, K^0, n, p_s (slow protons) but also missed charged particles.
If the total measured energy and momentum are denoted by E and $\mathbf{p}$, respectively, and the total unmeasured energy and momentum by E_u and $\mathbf{p}_u$, the conservation laws can be written as follows:

$$E_0 = E_{\bar{p}} + m_{^4\text{He}} = E + E_u + m_s, \tag{6.22}$$

$$\mathbf{p}_{\bar{p}} = \mathbf{p} + \mathbf{p}_u, \tag{6.23}$$

being m_s the mass of the spectator nucleons ($\sim hm_p$, $h = 1, 2, 3$) and $|\mathbf{p}_{\bar{p}}| = 1.5$ GeV/c. By introducing the invariant mass M_u of the unmeasured particles,

$$M_u^2 = E_u^2 - |\mathbf{p}_u|^2, \tag{6.24}$$

from the previous equations it is easy to obtain

$$p_u \equiv |\mathbf{p}_u| = \sqrt{E_u^2 - M_u^2} = \sqrt{(E_0 - m_s - E)^2 - M_u^2}. \tag{6.25}$$

So for fixed values of M_u and m_s, $\mathbf{p}_u$ is a decreasing function of E and becomes zero when $E = E_{max} = E_0 - m_s - M_u$.
If all the tracks of each event were reconstructed, the events would accumulate in a blob around the point ($p_u = 0, E = E_{max}$); if not, they would be spread in the (p_u, E) plane; in particular, they would be placed in the area of the (p_u, E) plot on the left of the line identified by M_u = minimum.
Two physical effects may contribute to the spreading of the events in the (p_u, E) plane far from the sites described by Eq. (6.25): in case the fast unseen nucleons have an invariant mass higher than the sum of their masses, the measured energy is smaller than expected and the events are shifted to the left–side of the lines with $B = 1, 2, 3$. If the annihilating nucleons have some initial momentum due to the binding in the nucleus (Fermi momentum), instead of a null momentum, the events are shifted above the point ($p_u = 0$, $E = E_{max}$).

Fig. 6.22 shows the event distribution in the (p_u, E) plane after the application of the Kalman filter to the reconstructed tracks: events with only mesons (and protons, if present) in the final state have been selected, regardless of the number of nucleons involved in the annihilation. The spectator nucleons are not included in the plot.
The coloured lines drawn on the distribution are described by Eq. (6.25), in correspondence of different values of m_s and M_u. In particular, the green curve refers to the antiproton annihilation on one proton ($B = 0$) with three spectators and without unseen particles:

$$\begin{aligned} E_0 &= E_{\overline{p}} + m_{^4\mathrm{He}} \\ m_s &= m_p + 2m_n \\ M_u &= 0. \end{aligned}$$

The maximum energy available in this case is $E_0 - m_s = E_{1\,nucl} \simeq 2.68$ GeV.
If the annihilations were all of such kind, the events would be distributed in the left side of the plot and the right side delimited by the green curve (unphysical region) would be empty. This is not the case since the model used to generate the $\overline{p}$–^{4}He annihilation reactions foresees annihilations on one nucleon plus final state interactions (SNA + FSI).
The other curves are referred to the antiproton annihilation on two protons ($B = 1$) with two spectator neutrons and with various unseen particles: none (black), one pion (orange), one kaon (violet), one proton (yellow) or one Λ^0 (red); in this case:

$$\begin{aligned} E_0 &= E_{\overline{p}} + m_{^4\mathrm{He}} \\ m_s &= 2m_n \\ M_u &= 0,\ m_\pi,\ m_K,\ m_p,\ m_{\Lambda^0}. \end{aligned}$$

For these events, the maximum available energy is $E_0 - m_s = E_{2\,nucl} \simeq 3.62$ GeV.

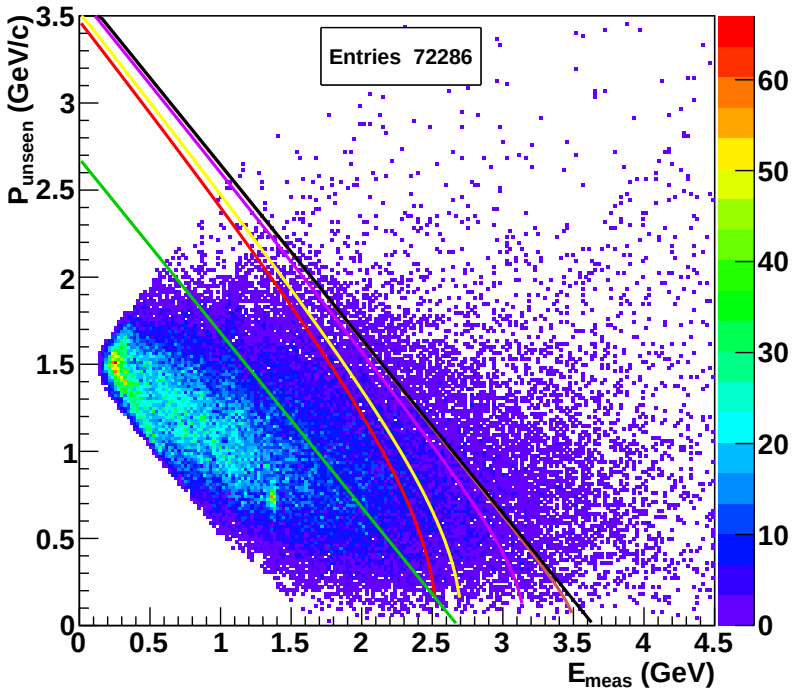

Figure 6.22: p_{unseen} vs. $E_{measured}$ for antiproton annihilations on ^{4}He. Events with only mesons (and protons) in the final state have been selected. The green curve identifies the $B = 0$ annihilations without unseen particles; the other curves are referred to the $B = 1$ annihilations, without unseen particles (black curve), with one unmeasured pion (orange), kaon (violet), proton (yellow) or Λ^0 (red).

As before, the region on the right side of the black curve is the unphysical one. The points located in that region are associated with tracks with not well reconstructed momentum (and energy).

The possibility to use the (p_u, E) plots to distinguish between annihilations on a different number ($h = 1, 2, 3, 4$) of nucleons has been studied.
According to the physical model used to generate these events, only in case of annihilation on a single nucleon (SNA) the annihilation is direct; when more than one nucleon is involved in the annihilation, the process comes out from the interaction of the final state (FSI).
According to the shape of the Monte Carlo momentum distribution of the protons shown in Fig. 6.21.a (the one for neutrons is similar), nucleons having a momentum smaller than 0.3 GeV/c can be considered to be spectators in the annihilation process. So by checking the Monte Carlo momentum of the nucleons, the number of spectators is deduced; this allows to classify the events in different groups, depending on how many nucleons are involved in the annihilation, being it SNA or FSI.

The event distributions in the (p_u, E) plane are reported in Fig. 6.23 as a function of the number of involved nucleons: the figures show the unseen momentum vs. the measured energy for antiproton annihilations into charged and/or neutral mesons ($\pi^{\pm}$, π^0, $K^{\pm}$, K^0) in case the annihilation is on one (a), two (b), three (c) or four (d) nucleons. Fast nucleons (when present), as well as the spectator ones, have not been included in the plot.

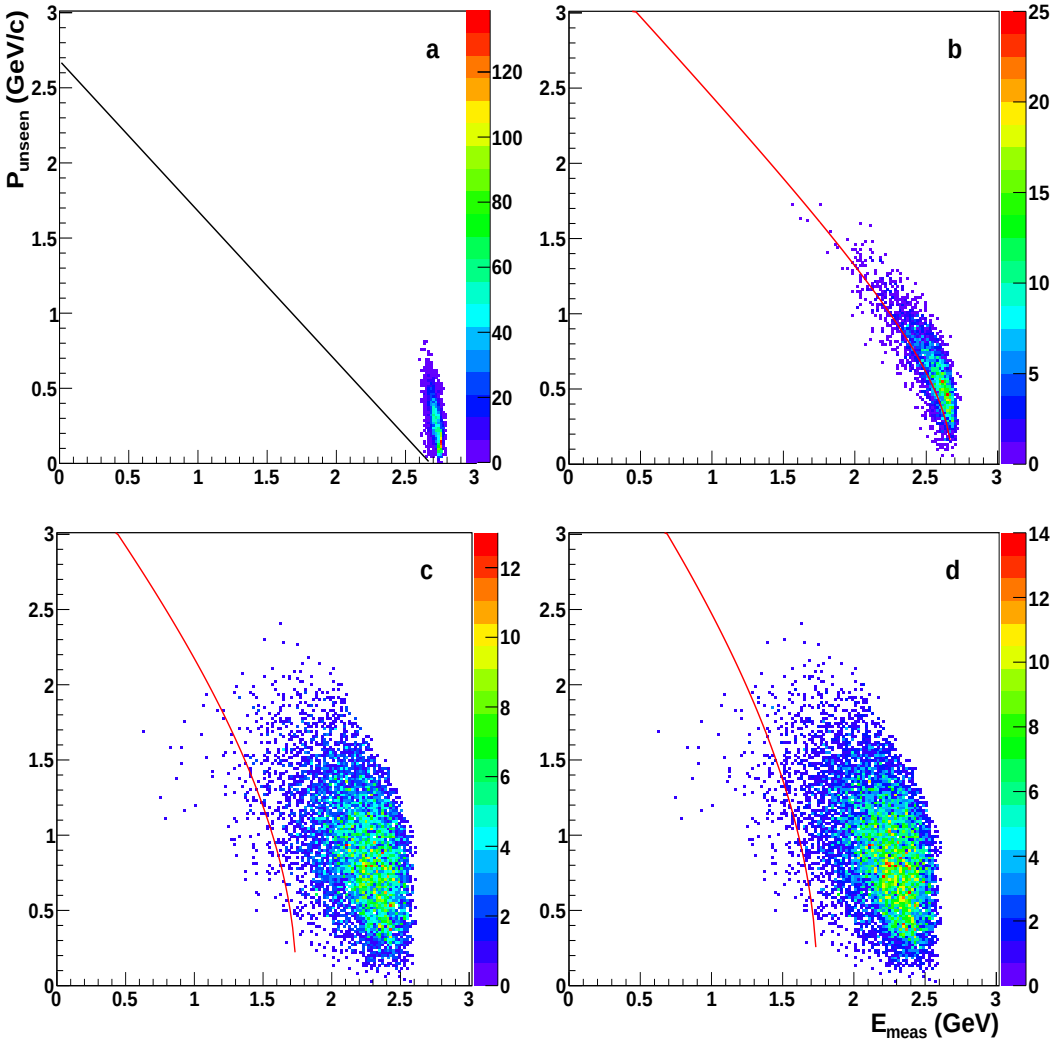

Figure 6.23: Monte Carlo p_{unseen} vs. $E_{measured}$ for $\overline{p}-{}^4$He annihilations on one proton (a), two protons (b), three (c) and four (d) nucleons into mesons. Fast nucleons, when present, have not been included in the plot, as well as the spectator nucleons. The black curve in (a) is the $p_u(E)$ line in the case $B = 0$ without unseen particles; the curves in the other plots are the $p_u(E)$ functions for $B = 1, 2, 3$ annihilations with one, two and three unseen nucleons, respectively.

From the figure it is clear that the four groups of events populate different regions in the (p_u, E) plane: in particular, in the case of single nucleon annihilations (Fig. 6.23.a) the events are accumulated in a blob at $p_u \simeq 0$ and $E \simeq E_{max} = E_{1\,nucl} \simeq 2.68$ GeV. Due to the Fermi motion of the nucleons inside the ^{4}He nucleus, which cannot be neglected, the contours of the blob are not well–defined and the spot is positioned at energies slightly higher than the maximum allowed.
In the case of annihilations on two protons (Fig. 6.23.b), the events are distributed at higher values of unseen momentum with respect to the previous case and lie on the $p_u(E)$ function for $B = 1$ and $M_u = m_p$.
Concerning the other two plots (Figs. 6.23.c–6.23.d), the events are more spread in the (p_u, E) plane than in the previous two cases; most of these events are characterised by unseen momentum values in the range $[0.3, 1.2]$ GeV/c and energy values in the interval $[2.1, 2.5]$ GeV.
Thanks to the features of these distributions, associated with specific regions of the (p_u, E) plane, it would be possible to identify which kind of annihilation characterise a certain set of experimental data.
All the plots shown up to now have been produced with Monte Carlo data. In principle, if the $\overline{\text{P}}$ANDA detector allowed to perform a good track reconstruction, not only for the charged particles but also for the neutral ones, and in the hypothesis that no tracks are lost during the global tracking procedure due to reconstruction failures, the analogous plots filled with the reconstructed data would be very similar to the simulated ones.
This is not the case if only MVD, STT and GEMs are used to perform the global tracking: since these subdetectors can track only charged particles, all the neutral ones are unseen. This results in a spread of the events in the (p_u, E) plot.
To check if it is possible to distinguish between the different kinds of annihilations by looking at the (p_u, E) plots and to have a qualitative idea of the change in the distributions, the events shown in Fig. 6.23 have been reported in Fig. 6.24 excluding all the neutral particles: not only fast neutrons possibly present, which were already excluded from the plot, but also neutral mesons in the final state.
Events with only charged mesons in the final state still occupy the same position in the (p_u, E) plane; the other events are spread in the plane, depending on the number of the unseen particles, their masses and momentum values.
Qualitatively, the events with annihilation on a single nucleon (SNA) tend to form a "cloud" that lies along the $B = 0$ curve (Fig. 6.24.a); in addition, a small group of events (the ones with only charged particles in the final state) still form a spot in correspondence of $(p_u \simeq 0, E_m \simeq E_{max} = E_{1\,nucl} = 2.68$ GeV/c).
Figs. 6.24.c and 6.24.d related to annihilations on more than one nucleon show that the points are accumulated in a more central region of the plane.
So in this case it is still quite easy to distinguish between SNA and FSI, but

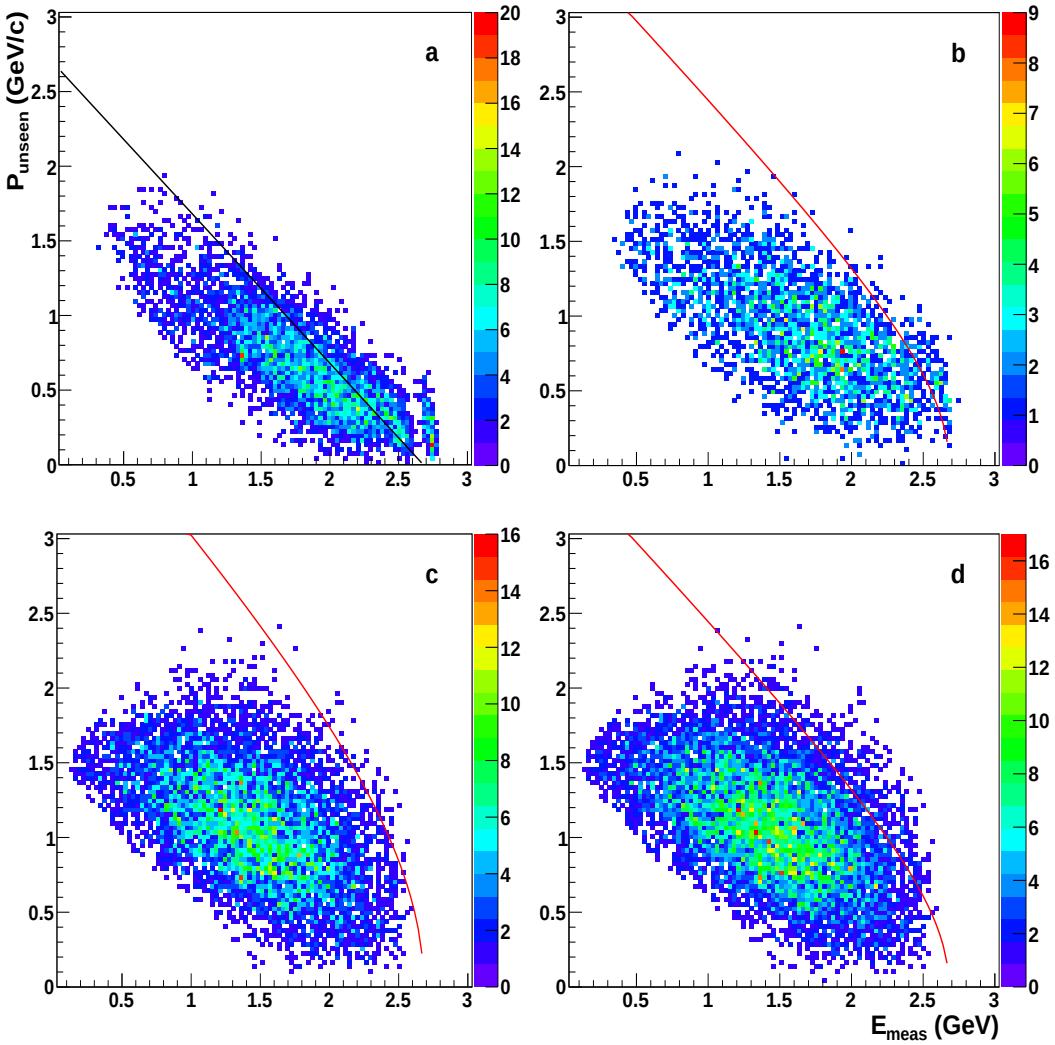

Figure 6.24: Monte Carlo p_{unseen} vs. $E_{measured}$ for $\overline{p}-^4$He annihilations on one (a), two (b), three (c) or four (d) nucleons into mesons. The events are the same as in Fig. 6.23, but in these plots neutral particles are considered as unseen particles (hence, not included). Fast nucleons, when present, have not been included in the plot, as well as the spectator nucleons. The meaning of the lines is defined in Fig. 6.23.

it is no longer possible to discriminate between annihilations on two, three or four nucleons.
It is even more difficult to identify the various annihilation processes from the (p_u, E) plots when the reconstructed data are used. The distributions for the reconstructed events are reported in Fig. 6.25.
The shapes of all distributions are different with respect to the corresponding ones of Fig. 6.24: in particular, the events tend to accumulate in the region where the momentum approaches 1.5 GeV/c and the energy approaches 140

GeV[6]. This means that there are many events in which a very small number of particles has been reconstructed. The low efficiency is mainly due to the software–related problems already pointed out in the previous sections.
From Fig. 6.25 it is clear that at present it is not possible to distinguish between SNA and the various cases of FSI only from the analysis of the (p_u, E) plots.

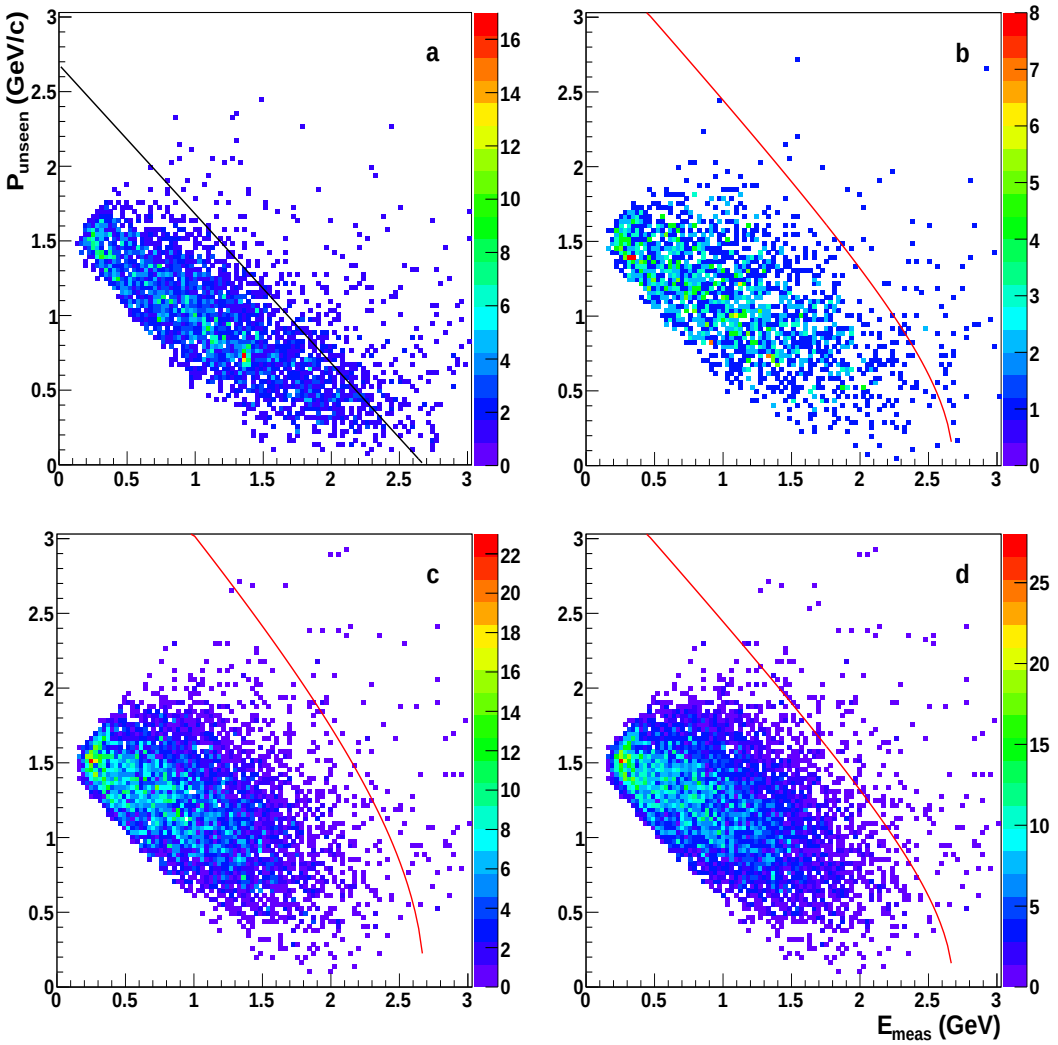

Figure 6.25: Reconstructed p_{unseen} vs. $E_{measured}$ for $\overline{p}-^4$He annihilations on one (a), two (b), three (c) or four (d) nucleons into mesons. Fast nucleons, when present, have not been included in the plot, as well as the spectator nucleons. The meaning of the lines is defined in Fig. 6.23.

[6]For the events included in the plot, at least one meson has to be reconstructed; so the minimum measured energy corresponds to the mass of one pion.

6.3.3 Exotic channel

Another aim of this study is to estimate the ability of the $\overline{\text{P}}$ANDA detector to extract "exotic" channels from the background.
In order to perform this test, the following channel has been chosen:

$$\overline{p}\ (pp) \rightarrow \pi^+\pi^- K^+\Lambda^0 \rightarrow \pi^+\pi^- K^+(\pi^- p). \tag{6.26}$$

This reaction is "exotic" with respect to the antiproton annihilations on hydrogen at rest, since in this case it is impossible to produce Λ^0 mesons.
The Monte Carlo data presented in Sec. 6.3.2 are used as background, since they have been generated according to a model that foresees annihilations on a single nucleon plus interaction of the final states.
The signal events have been generated with the EvtGen generator, by setting the antiproton annihilations directly on two protons, in order to emulate a multinucleon annihilation in the case $\overline{p}-{}^4$He. The output file of the generation has then been given as input to the simulation – digitization – reconstruction chain, with the same procedure described in Sec. 6.1.1. The (p_u, E) plot for the reconstructed events, filled with the momentum values obtained after the Kalman filter, is shown in Fig. 6.26.

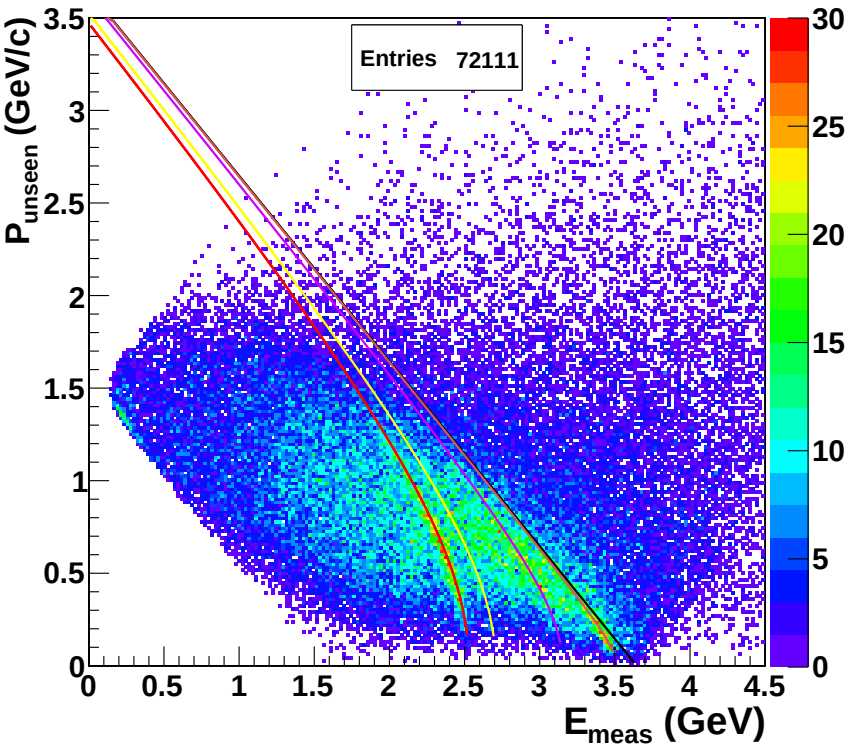

Figure 6.26: p_{unseen} vs. E_{meas} for the reconstructed events of the annihilation channel $\overline{p}\ (pp) \rightarrow \pi^+\pi^- K^+\Lambda^0 \rightarrow \pi^+\pi^- K^+(\pi^- p)$. The meaning of the lines is defined in Fig. 6.23.

The event distribution is particularly interesting and can be easily explained, since the particles that should be present in the final state are known.
First off, it is evident that the reconstruction efficiency is not 100%: if it was the case, all the events would accumulate in a spot around the point ($P_u \simeq 0, E = E_{max} = E_{2\,nucl} \simeq 3.62$ GeV).
The effect of the reconstruction is the spreading of the events in the plane. The area between the orange and the red curves, corresponding to $B = 1$ annihilation events with one unmeasured pion and Λ^0, respectively, are characterised by a higher population. In particular, the Λ^0 missing band is populated by the events in which both the proton and the pion produced in the Λ^0 decay (thus having an invariant mass of $\sim$1.12 GeV/c^2) have not been meausered.
In order to estimate the capabilities of the detector to extract this specific signal from the background, the (p_u, E) plots for the signal and the background (Figs. 6.22 and 6.26) have been compared.
For sure, the probability to be able to identify the signal is low if a momentum/energy region where many background events are accumulated is chosen, like the region at energy values smaller than 1.5 GeV (see Fig. 6.22): with such a choice, the signal would be merged into the noise represented by the other channels. On the contrary, it is easier to look for it in a less populated region, in order to have a higher signal to noise ratio. For this reason, it has been decided to investigate the region defined by the black lines in Fig. 6.27, where a large number of events is accumulated in the plot related to the channel (Fig. 6.26) but there are not so many entries in the background plot.

Fig. 6.28 shows the event distribution in the chosen band for the background (a) and for the signal (b).
The projections of these plots on the energy axis give the energy profile of the two distributions: they are reported in Fig. 6.29 for the background (a) and the signal (b). The different shapes and mean values of the two energy distributions could be useful for the signal detection.

Suppose now to observe experimentally a distribution such that 10% of the events are signal events and the remaining 90% are background events. Since there are no real data from $\overline{\text{P}}$ANDA at present, the "experimental" distribution has been obtained as described in the following.
First off, it is worth noting that the background and the signal distributions have almost the same number of reconstructed events (72286 vs. 72111): hence, taking 10% of the background events corresponds to take 10% of the signal events. In addition, sampling a certain percentage of events from the original distribution and looking for the subset of this percentage lying in the selected band is equivalent to sample the same percentage of events directly from the original ones that fill the band region.
That being so, the "experimental" distribution has been obtained by adding two distributions: one obtained by sampling 90% of the events from the background

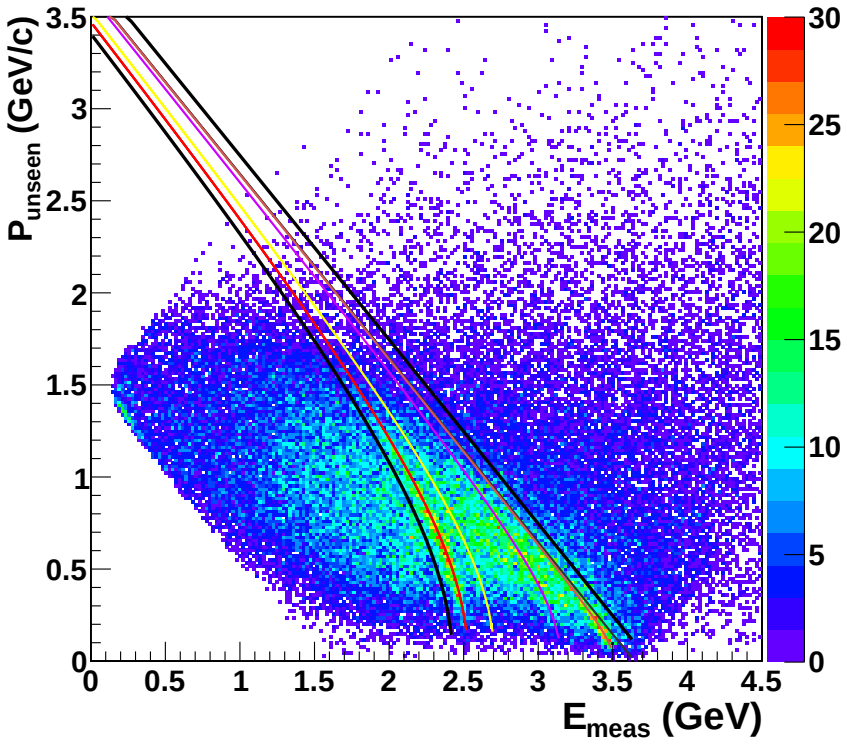

Figure 6.27: Same as in Fig. 6.26; in addition, the two black lines define the region where exotic signals are looked for in the background.

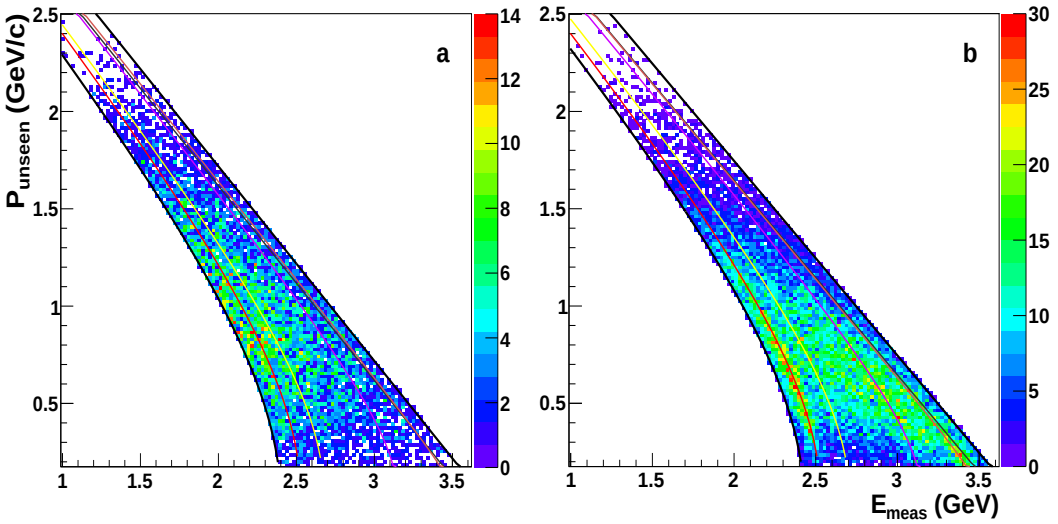

Figure 6.28: Event distribution for the background (a) and signal (b) events in the band defined by the black lines (see also Fig. 6.27).

distribution in the band (Fig. 6.29.a) and the other one by sampling 10% of the signal events lying in the band (Fig. 6.29.b).

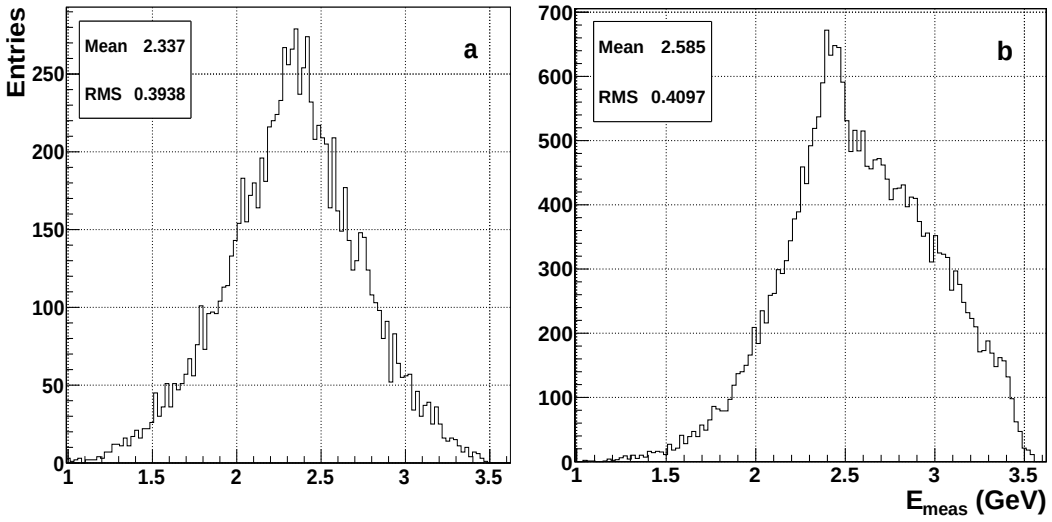

Figure 6.29: Energy distributions for the background (a) and signal (b) events contained in the bands reported in Fig. 6.28.

The "experimental" distribution is the black empty one in Fig. 6.30; the red dashed histogram represents the background distribution (from Fig. 6.29.a). The difference between these two histogram is the blue filled distribution, which represents the signal.

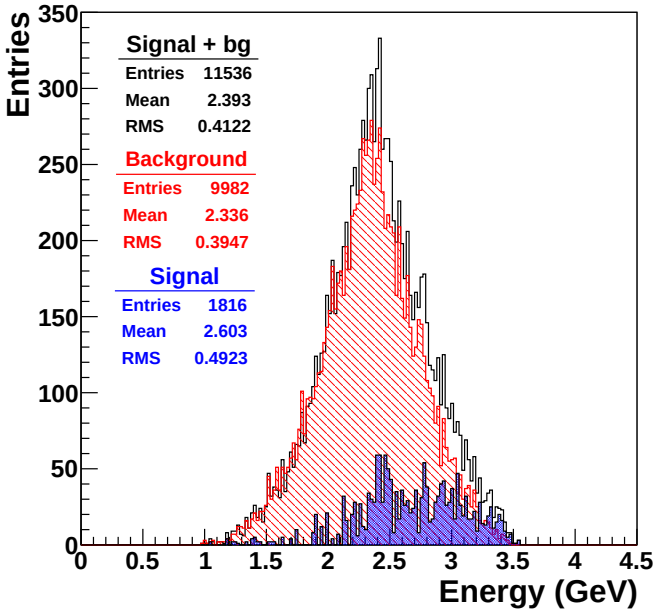

Figure 6.30: Energy distributions obtained as described in the text. Black empty histogram: "experimental" distribution; red dashed histogram: background events; blue full histogram: signal events.

In order to check the statistical significance of the signal over the background, the following formula has been used:

$$n = \frac{N_s}{\sqrt{2N_b + N_s}}, \tag{6.27}$$

where N_s and N_b are the number of signal and background events, respectively, and n indicates the significance level. In this case, $N_s = 1816$ and $N_b = 9982$; hence the value obtained for the significance is $n = 12.3$. It means that the signal can be extracted from the background with statistical significance, being 5 the minimum required.
The same analysis has been repeated by choosing other two bands in the (p_u, E) plot, to check whether there is a region that allows to better identify the signal from the background. A wider and a narrower bands have been defined: they are delimited by the black lines in Fig. 6.31.

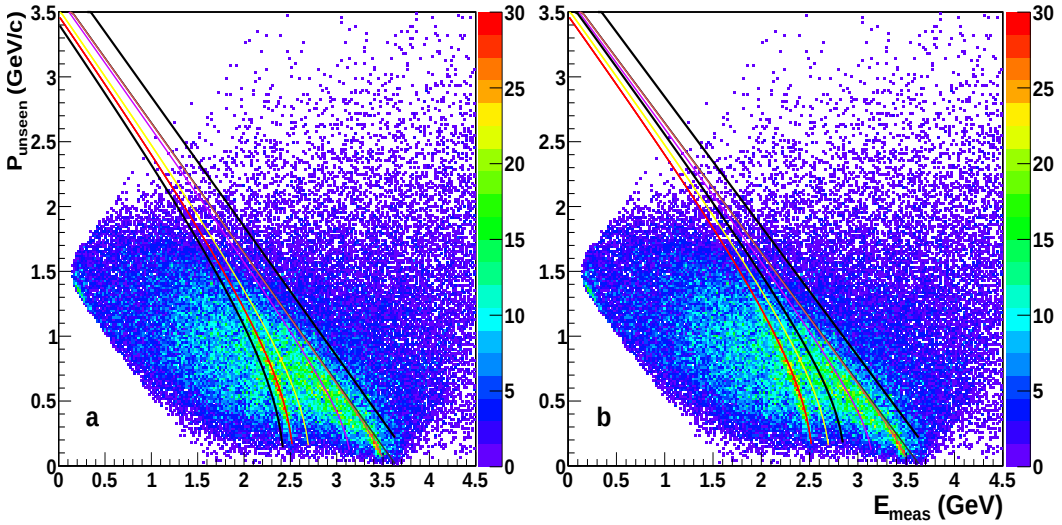

Figure 6.31: Same as in Fig. 6.27, with a different choice of the bands (defined by the black lines) in which the signal is search for in the background.

The "experimental" energy distributions have been obtained as previously described and subsequently compared with the background distributions; the signals obtained are the blue filled distributions in Fig. 6.32.

In these two cases, Eq. (6.27) gives the following results:

a. in the case of the wider band (Fig. 6.31.a):

$$n = \frac{N_s}{\sqrt{2N_b + N_s}} = \frac{1600}{\sqrt{2 \cdot 10695 + 1600}} = 10.6; \tag{6.28}$$

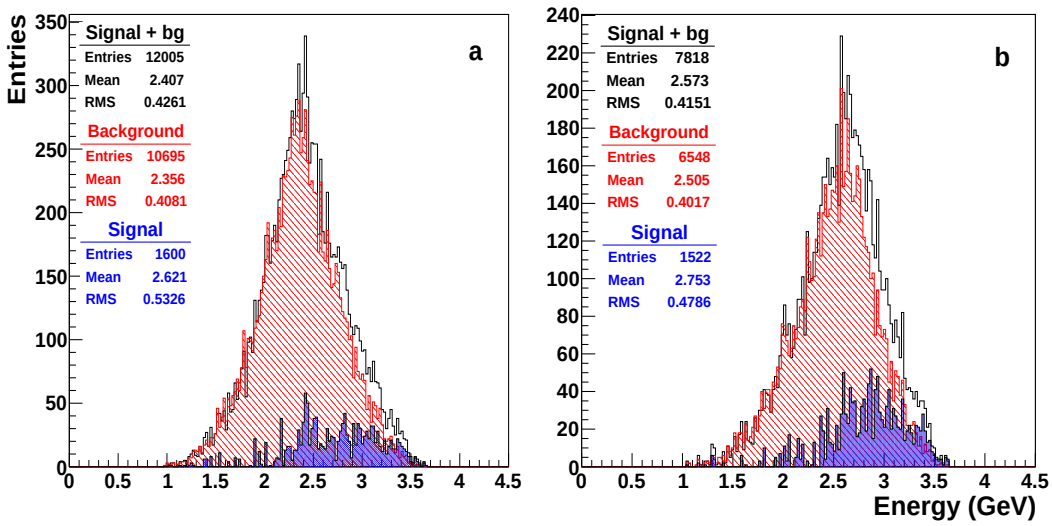

Figure 6.32: Same as in Fig. 6.30 for the bands defined in Fig. 6.31.

b. in the case of the narrower band (Fig. 6.31.b):

$$n = \frac{N_s}{\sqrt{2N_b + N_s}} = \frac{1522}{\sqrt{2 \cdot 6548 + 1522}} = 12.6. \tag{6.29}$$

In both cases, the statistical significance is high.

The significance values obtained when the signal is 10% of the "experimental" distribution allows to state that, having as a reference a Monte Carlo code including single nucleon annihilations (SNA) plus final state interactions (FSI), it would be possible to extract the signal from the background with a statistical significance greater than 5σ even if the signal is 4–5% of the "experimental" distribution.

Bibliography

[1] K. Nakamura et al. (Particle Data Group), J. Phys. G 37, 075021 (2010).

[2] M. Ambrogiani et at.(E835 Collaboration) , Phys. Lett. B566, 45 (2003).

[3] M. Kotulla et al. ($\overline{\text{P}}$ANDA Collaboration), *Technical Progress Report for $\overline{P}$ANDA - Strong Interaction Studies with Antiprotons*, Feb 2005 http://www-panda.gsi.de/framework/documents.php

[4] L.K.W. Cassing, Ye.S. Golubeva, Eur. Phys. J. A7, 279 (2000).

[5] W. Erni et al. ($\overline{\text{P}}$ANDA Collaboration), *Physics Performance Report for $\overline{P}$ANDA – Strong Interaction Studies with Antiprotons*, Mar 2009 arXiv:0903.3905v1

[6] D. Lange, Nucl. Instrum. and Meth. A 462, 152 (2001) http://www.slac.stanford.edu/~lange/EvtGen

[7] S. Spataro , Jour. Phys.: Conf. Ser. 119, 032035 (2008), doi:10.1088/1742-6596/119/3/032035

[8] P. Avery, *Applied Fitting Theory I - General Least Squares Theory*, CBX 91-72, October 18, 1991 http://www.phys.ufl/edu/~avery/fitting/fitting1.pdf

[9] L. Lyons, *Statistics for nuclear and particle physicists*, Cambridge University Press, 1986.

[10] P. Avery, *Applied Fitting Theory VI - Formulas for Kinematic Fitting*, CBX 98-37, June 9, 1998 http://www.phys.ufl/edu/~avery/fitting/kinematic.pdf

[11] http://savannah.fzk.de/websites/hep/rho

[12] A. Rotondi, P. Pedroni, A. Pievatolo, *Probabilità Statistica e Simulazione*, Springer (2001).

[13] Branden et al. (CLEO COllaboration), Phys. Rev. Lett. 85, 3095 (2000).

[14] Edwards et al. (CLEO COllaboration), Phys. Rev. Lett. 86, 30 (2001).

[15] T. Armstrong et al. (E760 Collaboration), Phys. Rev. D52, 4839 (1995).

[16] B. Aubert et al. (BaBar Collaboration), Phys. Rev. Lett. 87, 162002 (2001).

[17] G. Brandenburg et al., Phys. Rev. Lett. 85, 3095 (2000).

[18] C. Baltay et al., Phys. Rev. 142, 932 (1966).

[19] J. Debray et al., Nucl. Phys. B62, 13 (1973).

[20] P. Eastman et al., Nucl. Phys. B51, 29 (1973).

[21] B. Aubert (BaBar Collaboration), Phys. Rev. Lett. 92, 142002 (2004).

[22] S.-K. Choi (Belle Collaboration), Phys. Rev. Lett. 89, 10 (2002).

[23] M. Kotulla et al. ($\overline{\text{P}}$ANDA Collaboration), *Technical Progress Report for $\overline{P}ANDA$ - Strong Interaction Studies with Antiprotons*, Feb 2005.

[24] M. Bleicher et al., J. Phys. G 25 (1999) 1859-1896.

[25] S.A. Bass et al., Prog. Part. Nucl. Phys. 41 (1998) 225-369.

[26] P. Montagna et al., Nucl. Phys. A 700 (2002) 159.

Conclusions

The $\overline{\text{P}}$ANDA detector is a state–of–the–art internal target detector that will be built at the FAIR facility in order to study fundamental questions of hadron and nuclear physics by means of interactions of antiprotons with nucleons and nuclei. Thanks to the high–intensity cooled antiproton beams that will be provided by the High Energy Storage Ring (HESR), gluonic excitations, the physics of strange and charm quarks and studies of the nucleon structure will be performed with very high accuracy, allowing tests of the strong interaction. For this reason it is fundamental that the detector is designed to achieve results with an unprecedented precision.
This thesis is mainly dedicated to the design of the Straw Tube Tracker (STT), one of the two proposed configurations of the $\overline{\text{P}}$ANDA Central Tracker, used for the determination of charged particles position, momentum and energy loss. The performances of all the tracking systems of the $\overline{\text{P}}$ANDA Target Spectrometer, consisting in the Micro–Vertex Detector (MVD), the STT and the external Gas Electron Multiplier (GEM) stations placed downstream of the STT, have been studied too.

After a review of the $\overline{\text{P}}$ANDA physics program (Chap. 1) and of the proposed layout of the detector (Chap. 2), the attention has been focused on the STT and its components.
First of all, the time and charge responses of the single straw tube have been described in detail; a description of the simulation of all these processes, from the electron drift, to the charge multiplication and collection, to the signal formation, is reported (Chap. 3).

The simulation results have been compared with the experimental ones obtained from the analysis of the data collected with a small prototype available at the Institut für Kernphysik at the Jülich Forschungszentrum.
Although it is not a complete full–scale prototype of the $\overline{\text{P}}$ANDA STT and it is equipped with non–dedicated electronics, it consists of four double–layers of straw tubes similar to the $\overline{\text{P}}$ANDA ones: the tubes have the same geometrical properties (radius, length, wall thickness), are filled with the same gas mixture

and are operated at the same high voltage and pressure. So tests with this small prototype can provide useful hints for the design and construction of the $\overline{\text{P}}$ANDA STT, as well as for the data analysis.
The experimental data collected with the prototype (cosmic ray events) have been analysed with software tools implemented *ad hoc*. A great effort has been devoted to develop a dedicated method based on an autocalibration technique, to obtain an accurate knowledge of the space–time information ($r(t)$ relation), necessary to perform a good track fitting. In addition, a dedicated track reconstruction algorithm has been implemented too.
The results obtained have been discussed in detail (Chap. 4). The attention has been mainly focused to the spatial resolution of a single tube, which has resulted to be of about 175 μm. This value is very close to the design goal of 150 μm, which could be certainly reached by using a dedicated electronics with a better time resolution.
A plot of the electron drift velocity has been obtained too, showing a good agreement with the corresponding simulated plot.

Then, systematic studies have been performed with Monte Carlo simulations with the aim of determine the optimal design parameters for the Central Tracker, thus allowing to reach the best performances in terms of geometrical acceptance of the proposed layout, momentum resolution and reconstruction efficiency (Chap. 5).
The tracker performances as a function of different geometric parameters have been investigated by using single track events generated with fixed total momentum and uniformly distributed in the polar and azimuthal angular ranges, or with fixed total momentum and fixed polar angle θ. In particular, two options have been compared: one with 120 cm long straw tubes plus four GEM chambers placed upstream the STT and another one with 150 cm long tubes plus three GEM chambers. A fine scan of the forward angular region, where the momentum resolution and efficiency may be mostly affected by the shortening of the tubes, has been performed too.
The simulated data have been analised with the software tools implemented in the $\overline{\text{P}}$ANDA code structure. Their purpose is to reconstruct the particles path, assuming a large range of approximations at a first step (global track fitting with helix) and, in a later stage, taking into account the widest range of path distorsions (Kalman filter recursive method) in order to improve the momentum resolution. To do this, a track follower is also used (GEANE): it transports the track parameters and the covariance matrix from one point of the path to another one.
The results have been extensively discussed. They demonstrate that the performances of the two options for the Central Tracker are substantially equivalent and that the proposed layout allows to reach a resolution close to the design goal of $\sim 1 - 2\%$, ranging from 0.72% to 3.6% in case of tracks generated at the interaction point with fixed total momentum (from 0.3 GeV/c to 5 GeV/c)

and randomly distributed in θ and ϕ.

The performances of the Central Tracker have been tested also by studying two benchmark channels covering relevant topics of the $\overline{\text{P}}$ANDA physics program (Chap. 6). The aim is to demonstrate that the proposed detector setup can fulfil the physics case and that the invariant mass resolution values obtained from the simulations are comparable with the well known results from other experiments.
The channels that have been simulated realistically are $\overline{p}p \rightarrow \Psi(3770) \rightarrow D^+D^-$ and $\overline{p}p \rightarrow \eta_c(2979) \rightarrow K^0_S K^+\pi^-$, such that only charged tracks (the only ones the Central Tracker is able to reconstruct) are present in the final states.
The events have been analised by using the tracking tools mentioned above; in addition, for the $\Psi(3770)$ channel, a kinematic fit has been tested and applied, in order to further improve the results.
The attention has been focused on the invariant mass resolutions: for the $\Psi(3770)$ decay channel, the $D^{\pm}$ mesons have been reconstructed by the $\overline{\text{P}}$ANDA Central Tracker with a resolution of 0.73% and 0.78%, respectively, after the kinematic fit. In the case of the other decay channel, the η_c and K^0_S mass resolutions are $\sim 1.25\%$ and 1.31%, respectively.
Some tests have been also performed to evaluate the dependence of the invariant mass resolution on the spatial resolution of the single straw tubes.
It has been shown that a factor two in the spatial resolution of the single tube turns out into a loss in invariant mass resolution. In particular, this loss amounts to $\sim 10\%$ for the $D^{\pm}$ mesons in the case of the $\overline{p}p \rightarrow \Psi(3770) \rightarrow D^+D^-$ channel and of $\sim 9\%$ and $\sim 17\%$ for the K^0_S and the η_c, respectively, in the case of the other decay channel.

Finally, starting from recent results on $\overline{p}-^4$He annihilations, it has been presented a proposal for a study of the antiproton annihilations on light nuclei, since they could allow strangeness and charm production studies in exclusive annihilation channels and could be a powerful tool to discover possible exotic signals, like the quark–gluon plasma (QGP) formation.
The $\overline{p}-^4$He simulated annihilations have been analised with the tracking algorithms already presented and through the study of the $p_{unseen} - E_{measured}$ plots: the results obtained show that they could be used to distinguish between annihilation on a single nucleon (SNA) and SNA combined with the final state interaction (FSI).
In addition, it has been proved that $\overline{\text{P}}$ANDA would be able to disentangle an "exotic" signal from the background with a statistical significance of 5σ if the signal amount is down to 4-5% of the background.

All the results discussed in this thesis have been systematically presented at the collaboration meetings within the last three years and have converged into

various technical reports, articles and internal notes.
The work is still ongoing, both from the experimental and the simulation point of view. In fact, due to the postponed start of the experiment, the software development has been delayed too, so not all the tools needed for the presented analyses were available. Once all the software instruments will be ready, the results will certainly improve.
Despite this, they already demonstrate the feasibility of the $\overline{\mathrm{P}}$ANDA Straw Tube Tracker and make a decisive step towards its realisation. Globally, as emerges from this thesis, the proposed layout allows to reach a resolution close to the required one.

Part V

Appendices

Appendix A

Mathematics of Kinematic Fitting

A.1 General algorithm

Let's denote with $\boldsymbol{\alpha}$ the column vector which represents the n_p parameters for each track of a set of n tracks, for a total of $N = n_p \times n$ parameters:

$$\boldsymbol{\alpha} = \begin{pmatrix} \alpha_1 \\ \alpha_2 \\ \vdots \\ \alpha_N \end{pmatrix}. \tag{A.1}$$

$\boldsymbol{\alpha}_0$ is the vector of the unconstrained values of the track parameters, for example the ones obtained from the track fit.
The r functions describing the constraints can be written as $\mathbf{H}(\boldsymbol{\alpha}) = \mathbf{0}$, $\mathbf{H}(\boldsymbol{\alpha})$ being a vector $\mathbf{H} \equiv (H_1, H_2, \cdots, H_r)$. Expanding about a convenient point $\boldsymbol{\alpha}_\mathrm{A}$, we obtain the linearized equations:

$$\mathbf{H}(\boldsymbol{\alpha}) = \mathbf{H}(\boldsymbol{\alpha}_\mathrm{A}) + \left.\frac{\partial \boldsymbol{H}}{\partial \boldsymbol{\alpha}}\right|_{\boldsymbol{\alpha}_\mathrm{A}} (\boldsymbol{\alpha} - \boldsymbol{\alpha}_\mathrm{A}) = \mathbf{0}. \tag{A.2}$$

By introducing the $r \times N$ matrix $\mathbf{D}$:

$$\mathbf{D} = \begin{pmatrix} \frac{\partial H_1(\boldsymbol{\alpha}_\mathrm{A})}{\partial \alpha_1} & \frac{\partial H_1(\boldsymbol{\alpha}_\mathrm{A})}{\partial \alpha_2} & \cdots & \frac{\partial H_1(\boldsymbol{\alpha}_\mathrm{A})}{\partial \alpha_N} \\ \frac{\partial H_2(\boldsymbol{\alpha}_\mathrm{A})}{\partial \alpha_1} & \frac{\partial H_2(\boldsymbol{\alpha}_\mathrm{A})}{\partial \alpha_2} & \cdots & \frac{\partial H_2(\boldsymbol{\alpha}_\mathrm{A})}{\partial \alpha_N} \\ \vdots & \vdots & \ddots & \vdots \\ \frac{\partial H_r(\boldsymbol{\alpha}_\mathrm{A})}{\partial \alpha_1} & \frac{\partial H_r(\boldsymbol{\alpha}_\mathrm{A})}{\partial \alpha_2} & \cdots & \frac{\partial H_r(\boldsymbol{\alpha}_\mathrm{A})}{\partial \alpha_N} \end{pmatrix} \tag{A.3}$$

and the $r \times 1$ column vector $\mathbf{d}$:

$$\mathbf{d} = \begin{pmatrix} H_1(\boldsymbol{\alpha}_\mathrm{A}) \\ H_2(\boldsymbol{\alpha}_\mathrm{A}) \\ \vdots \\ H_r(\boldsymbol{\alpha}_\mathrm{A}) \end{pmatrix}, \tag{A.4}$$

Eq. (A.2) can be written as:

$$\mathbf{H}(\boldsymbol{\alpha}) \equiv \mathbf{D}\delta\boldsymbol{\alpha} + \mathbf{d} = \mathbf{0}, \tag{A.5}$$

where $\delta\boldsymbol{\alpha} = \boldsymbol{\alpha} - \boldsymbol{\alpha}_\mathrm{A}$.
The χ^2 without constraints is:

$$\chi^2 = (\boldsymbol{\alpha} - \boldsymbol{\alpha}_0)^\mathrm{T}\mathbf{V}_{\boldsymbol{\alpha}_0}^{-1}(\boldsymbol{\alpha} - \boldsymbol{\alpha}_0) \tag{A.6}$$

where $\mathbf{V}_{\boldsymbol{\alpha}_0}$ is the block diagonal covariance matrix obtained from the track fitting.
The constraints can be imposed by adding a new term to the χ^2 equation; it is at this stage that the Lagrange multipliers enter the problem:

$$\chi^2 = (\boldsymbol{\alpha} - \boldsymbol{\alpha}_0)^\mathrm{T}\mathbf{V}_{\boldsymbol{\alpha}_0}^{-1}(\boldsymbol{\alpha} - \boldsymbol{\alpha}_0) + 2\boldsymbol{\lambda}^\mathrm{T}(\mathbf{D}\delta\boldsymbol{\alpha} + \mathbf{d}) \tag{A.7}$$

where $\boldsymbol{\lambda}$ is the vector of the r Lagrange multipliers.
The solution for $\boldsymbol{\alpha}$ is obtained by minimising the χ^2 of Eq. (A.7) with respect to $\boldsymbol{\alpha}$ and $\boldsymbol{\lambda}$. The minimisation conditions $\frac{\partial\chi^2}{\partial\boldsymbol{\alpha}} = 0$ and $\frac{\partial\chi^2}{\partial\boldsymbol{\lambda}} = 0$ yield the following equations:

$$\begin{aligned} \mathbf{V}_{\boldsymbol{\alpha}_0}^{-1}(\boldsymbol{\alpha} - \boldsymbol{\alpha}_0) + \mathbf{D}^\mathrm{T}\boldsymbol{\lambda} &= \mathbf{0}, & \text{(A.8)} \\ \mathbf{D}\delta\boldsymbol{\alpha} + \mathbf{d} &= \mathbf{0}. & \text{(A.9)} \end{aligned}$$

The $\frac{\partial}{\partial\boldsymbol{\lambda}}$ equation (A.9) generates the constraint conditions.
The solution of Eq. (A.8) is:

$$\boldsymbol{\alpha} = \boldsymbol{\alpha}_0 - \mathbf{V}_{\boldsymbol{\alpha}_0}\mathbf{D}^\mathrm{T}\boldsymbol{\lambda} \tag{A.10}$$

and shows that $\boldsymbol{\alpha}$ is equal to $\boldsymbol{\alpha}_0$ plus a term proportional to $\boldsymbol{\lambda}$, i.e. the constraints "pull" the parameters $\boldsymbol{\alpha}$ away from their unconstrained values.
Then, by substituing Eq. (A.10) in Eq. (A.9), we obtain:

$$\begin{aligned} \mathbf{0} &= \mathbf{D}(\boldsymbol{\alpha}_0 - \mathbf{V}_{\boldsymbol{\alpha}_0}\mathbf{D}^\mathrm{T}\boldsymbol{\lambda} - \boldsymbol{\alpha}_\mathrm{A}) + \mathbf{d} \\ &= \mathbf{D}\delta\boldsymbol{\alpha}_0 - \mathbf{D}\mathbf{V}_{\boldsymbol{\alpha}_0}\mathbf{D}^\mathrm{T}\boldsymbol{\lambda} + \mathbf{d} \end{aligned} \tag{A.11}$$

with $\delta\boldsymbol{\alpha}_0 = \boldsymbol{\alpha}_0 - \boldsymbol{\alpha}_\mathrm{A}$. Hence:

$$\begin{aligned} \boldsymbol{\lambda} &= (\mathbf{D}\mathbf{V}_{\boldsymbol{\alpha}_0}\mathbf{D}^\mathrm{T})^{-1}(\mathbf{D}\delta\boldsymbol{\alpha}_0 + \mathbf{d}) \\ &= \mathbf{V}_\mathrm{D}(\mathbf{D}\delta\boldsymbol{\alpha}_0 + \mathbf{d}) \end{aligned} \tag{A.12}$$

where the matrix $\mathbf{V}_{\mathrm{D}} = (\mathbf{D}\mathbf{V}_{\boldsymbol{\alpha}_0}\mathbf{D}^{\mathrm{T}})^{-1}$ has been introduced.
The full covariance matrix of the new parameters can be computed as:

$$\mathbf{V}_{\boldsymbol{\alpha}} = \mathbf{V}_{\boldsymbol{\alpha}_0} - \mathbf{V}_{\boldsymbol{\alpha}_0}\mathbf{D}^{\mathrm{T}}\mathbf{V}_{\mathrm{D}}\mathbf{D}\mathbf{V}_{\boldsymbol{\alpha}_0}. \tag{A.13}$$

Finally, using the conditions in Eq. (A.8) and (A.9), the χ^2 of Eq. (A.7) can be written as:

$$\begin{aligned}
\chi^2 &= (\boldsymbol{\alpha} - \boldsymbol{\alpha}_0)^{\mathrm{T}}\mathbf{V}_{\boldsymbol{\alpha}_0}(\boldsymbol{\alpha} - \boldsymbol{\alpha}_0) \\
&= (\mathbf{V}_{\boldsymbol{\alpha}_0}\mathbf{D}^{\mathrm{T}}\boldsymbol{\lambda})^{\mathrm{T}}\mathbf{D}^{\mathrm{T}}\boldsymbol{\lambda} \\
&= \boldsymbol{\lambda}^{\mathrm{T}}(\mathbf{D}\mathbf{V}_{\boldsymbol{\alpha}_0}^{\mathrm{T}}\mathbf{D}^{\mathrm{T}})\boldsymbol{\lambda} \\
&= \boldsymbol{\lambda}^{\mathrm{T}}\mathbf{V}_{\mathrm{D}}^{-1}\boldsymbol{\lambda} && \text{(A.14)} \\
&= \boldsymbol{\lambda}^{\mathrm{T}}(\mathbf{D}\delta\boldsymbol{\alpha}_0 + \mathbf{d}) && \text{(A.15)}
\end{aligned}$$

where Eq. (A.12) has been used in (A.14).
The expression for the χ^2 shows quite clearly that it is the sum of r distinct terms, one per constraint. However, it is possible to identify each of these terms with a particular constraint just in a very loose sense, since their contributions are all correlated through $\mathbf{V}_{\mathrm{D}}$.
The χ^2 value that results from Eq. (A.15) is a measure of how much the parameters have been "pulled" away from the unconstrained values to satisfy Eq. (A.2): a high χ^2 value means that the parameters have been changed a lot with respect to their starting unconstrained values. Hence, the track should be rejected by a χ^2 cut (see Sec. 6.1.2.3 and 6.1.2.5).

A.2 The 4C fitter

In the following, the general fitting algorithm described in the previous paragraph will be specialised for the case of a 4 constraints fit ($r = 4$) with mass conservation for the daughter particles. This means that the masses of the particles are fixed and cannot be modified by the fit. So each track is described just by three parameters (n_p): they are the momentum components p_x, p_y and p_z. Hence, if we denote the number of tracks (n in Sec. A.1) with n_d (number of daughters of the resonance), $\boldsymbol{\alpha}$ becomes a $3n_d \times 1$ column vector:

$$\boldsymbol{\alpha} = \begin{pmatrix} p_{x1} \\ p_{y1} \\ p_{z1} \\ \vdots \\ p_{x\,n_d} \\ p_{y\,n_d} \\ p_{z\,n_d} \end{pmatrix}. \tag{A.16}$$

$\boldsymbol{\alpha}_0$ is the vector with the unconstrained values obtained from the backpropagation of each daughter particle to its own vertex:

$$\boldsymbol{\alpha}_0 = \begin{pmatrix} p^0_{x1} \\ p^0_{y1} \\ p^0_{z1} \\ \vdots \\ p^0_{x\,n_d} \\ p^0_{y\,n_d} \\ p^0_{z\,n_d} \end{pmatrix}. \tag{A.17}$$

The set of four constraints can be written as:

$$\sum_i^{n_d} p_i^\mu - p_C^\mu = 0, \qquad \mu = x, y, z, E \tag{A.18}$$

where the sum is over the n_d daughters and p_C is the constrained 4-momentum. For example, for the decay channel described in Sec. 6.1, p_C is set to be equal to the invariant mass of $\Psi(3770)$. In detail, $\mathbf{H}(\boldsymbol{\alpha}) = \mathbf{0}$ is now:

$$\begin{aligned} H_1 &= p_{x1} + p_{x2} + p_{x3} - p_{xC} = 0 \\ H_2 &= p_{y1} + p_{y2} + p_{y3} - p_{yC} = 0 \\ H_3 &= p_{z1} + p_{z2} + p_{z3} - p_{zC} = 0 \\ H_4 &= E_1 + E_2 + E_3 - E_C = 0. \end{aligned} \tag{A.19}$$

By choosing $\boldsymbol{\alpha}_\mathrm{A} = \boldsymbol{\alpha}_0$, the $4 \times n_d$ $\mathbf{D}$ matrix (Eq. (A.3)) becomes:

$$\begin{aligned} \mathbf{D} &= \begin{pmatrix} \frac{\partial H_1(\boldsymbol{\alpha}_0)}{\partial p_{x1}} & \cdots & \frac{\partial H_1(\boldsymbol{\alpha}_0)}{\partial p_{z1}} & \frac{\partial H_1(\boldsymbol{\alpha}_0)}{\partial p_{x2}} & \cdots & \frac{\partial H_1(\boldsymbol{\alpha}_0)}{\partial p_{x3}} & \cdots \\ \frac{\partial H_2(\boldsymbol{\alpha}_0)}{\partial p_{x1}} & \vdots & \frac{\partial H_2(\boldsymbol{\alpha}_0)}{\partial p_{z1}} & \vdots & \cdots & \vdots & \cdots \\ \frac{\partial H_3(\boldsymbol{\alpha}_0)}{\partial p_{x1}} & \vdots & \frac{\partial H_3(\boldsymbol{\alpha}_0)}{\partial p_{z1}} & \vdots & \cdots & \vdots & \cdots \\ \frac{\partial H_4(\boldsymbol{\alpha}_0)}{\partial p_{x1}} & \cdots & \frac{\partial H_4(\boldsymbol{\alpha}_0)}{\partial p_{z1}} & \frac{\partial H_4(\boldsymbol{\alpha}_0)}{\partial p_{x2}} & \cdots & \frac{\partial H_4(\boldsymbol{\alpha}_0)}{\partial p_{x3}} & \cdots \end{pmatrix} \\ &= \begin{pmatrix} 1 & 0 & 0 & 1 & 0 & 0 & 1 & 0 & 0 \\ 0 & 1 & 0 & 0 & 1 & 0 & 0 & 1 & 0 \\ 0 & 0 & 1 & 0 & 0 & 1 & 0 & 0 & 1 \\ \frac{p^0_{x1}}{E^0_1} & \frac{p^0_{y1}}{E^0_1} & \frac{p^0_{z1}}{E^0_1} & \frac{p^0_{x2}}{E^0_2} & \cdots & \cdots & \cdots & \cdots & \cdots \end{pmatrix}, \end{aligned} \tag{A.20}$$

where E^0_i and $p^0_{\mu i}$ ($\mu = x, y, z$ and $i = 1, 2, \cdots, n_d$) are the energy and momentum components of each track at its vertex, as given by the track reconstruction

algorithm.
Taking into account the constraint equations (A.19), the 4×1 $\mathbf{d}$ vector of Eq. (A.4) is now:

$$\mathbf{d} = \begin{pmatrix} p^0_{x1} + p^0_{x2} + p^0_{x3} - p_{xC} \\ \vdots \\ E^0_1 + E^0_2 + E^0_3 - E_C \end{pmatrix}. \tag{A.21}$$

Because of the choice $\boldsymbol{\alpha}_\mathrm{A} = \boldsymbol{\alpha}_0$, $\delta\boldsymbol{\alpha}_\mathrm{A} = 0$; hence, from Eq. (A.14) $\chi^2 = \boldsymbol{\lambda}^\mathrm{T}\mathbf{d}$. The new track parameters $\boldsymbol{\alpha}$ are then computed with Eq. (A.10), where now $\boldsymbol{\lambda} = \mathbf{V}_D\mathbf{d}$. In the hypothesys of a 4C fit with mass conservation, the energy is then computed with:

$$E = \sqrt{p_x^2 + p_y^2 + p_z^2 + m^2}, \tag{A.22}$$

where p_i are the new momentum components, adjusted in order to satisfy the constraints and m is the unchanged initial mass value, which has been set in the particle identification step.